Microfluidic Technologies for Bioanalytical Chemistry:
Advancing Epigenetic Profiling via Chromatin Immunoprecipitation in Droplets

by

Steven Robert Doonan

A dissertation submitted in partial fulfillment
of the requirements for the degree of
Doctor of Philosophy
(Chemistry)
in The University of Michigan
2019

Doctoral Committee:

Professor Ryan C. Bailey, Chair
Associate Professor Eric Johnsen
Professor Robert T. Kennedy
Professor Brandon T. Ruotolo

Steven Robert Doonan

srdoonan@umich.edu

ORCID iD: 0000-0003-3847-0879

DEDICATION

To my wife, Ashley

ACKNOWLEDGEMENTS

First, I would like to thank my advisor, Professor Ryan C. Bailey, for his mentorship and support across the last few years (and two universities). Ryan cultivated a challenging environment where I relied on my own ideas and effort, driving me to mature as a scientist. I would also like to thank the other members of my committee, Associate Professor Eric Johnsen, Professor Robert T. Kennedy, and Professor Brandon T. Ruotolo. I am grateful to the University of Michigan community for their supportive welcome during the transition from the University of Illinois at Urbana-Champaign in 2016, particularly to Professor Kennedy for the spirit of collegiality and collaboration he fosters between the Kennedy and Bailey Labs. I would also like to express my gratitude for funding and support from the National Science Foundation Graduate Research Fellowship Program, the National Institutes of Health (Award CA191186), the Mayo-Illinois Alliance for Technology Based Healthcare, the Mayo Clinic Center for Individualized Medicine, the NIH-sponsored Midwest Cancer Nanotechnology Training Center (CA154015), and the Robert C. and Carolyn J. Springborn Endowment.

I would further like to acknowledge my friends and colleagues who significantly shaped and supported my graduate studies. I was privileged to share my time in the Bailey Lab with talented postdoctoral researchers and fellow graduate students, and I particularly want to acknowledge the other members of the droplet epigenetics team: Gloria Diaz, Dr. Richard Graybill, Jamy Lee, Melissa Lin, Dr. Vishal Sahore, Dr. Meng Sun, and Dr. Yi Xu. I am especially grateful for the opportunity to train and mentor a number of graduate and undergraduate

colleagues, including Dongkwan Lee among others. I would also like to thank Dr. Maria de la cruz Cardenosa Rubio, Benjamin Lund, Prof. Daniel McCurry, Dr. Ellen Muehl, Dr. Elizabeth Neumann, Michael Toth, and Shannon Wetzler (among others) for their continuing friendship and support. I would also like to thank Prof. R. Scott Martin for his continuing mentorship and support.

Finally, I would like to acknowledge and thank my family: my parents, Michael and Yvonne Doonan and Dale and Kathy Ebersole, and the rest of my immediate family, Tim and Lindsay Doonan, Brenton Ebersole, and Eric Ebersole. Most of all I would like to thank my wife, Ashley, for her unwavering support, and I would be remiss to exclude our dog, Elia, who is always happy to see me after a long day in the lab.

TABLE OF CONTENTS

LIST OF TABLES

TABLE

LIST OF FIGURES

FIGURE

LIST OF SUPPLEMENTARY MOVIES

SUPPLEMENTARY MOVIE

LIST OF APPENDICES

LIST OF ACRONYMS

3C	Chromosome Conformation Capture
4C	Chromosome Conformation Capture-on-Chip
5C	Chromosome Conformation Capture Carbon Copy
5caC	5-Carboxylcytosine
5fmC	5-Formylcytosine
5hmC	5-Hydroxymethylcytosine
5mC	5-Methylcytosine
ac	Acetylation
Ago	Argonaute
ATAC-seq	Assay for Transposase-Accessible Chromatin Analyzed by Deoxyribonucleic Acid Sequencing
ATP	Adenosine Triphosphate
AutoChIP	Automated Microfluidic Chromatin Immunoprecipitation
BER	Base Excision Repair
C.	Common Valve Port
C^3PE	Counter-Current Continuous Phase Extraction
CAB-seq	Chemical Modification-Assisted Bisulfite Sequencing
CAR-Wash	Coalesce-Attract-Resegment Washing
cDNA	Complementary Deoxyribonucleic Acid
CGE	Capillary Gel Electrophoresis
ChIA-PET	Chromatin Interaction Analysis by Paired-End Tag Sequencing
ChEC-seq	Chromatin Endogenous Cleavage Analyzed by Deoxyribonucleic Acid Sequencing
ChIP	Chromatin Immunoprecipitation
ChIP-exo	Chromatin Immunoprecipitation with Exonuclease Treatment
ChIP-MS	Chromatin Interacting Protein-Mass Spectrometry
ChIP-PCR	Chromatin Immunoprecipitation Analyzed by Polymerase Chain Reaction
ChIP-rx	Chromatin Immunoprecipitation with Reference Exogenous Genome
ChIP-seq	Chromatin Immunoprecipitation Analyzed by Deoxyribonucleic Acid Sequencing
COC	Cyclic Olefin Copolymer
COP	Cyclic Olefin Polymer
CUT&RUN	Cleavage Under Targets and Release Using Nuclease
DAQ	Data Acquisition Device
DI	Deionized Water
DMV	Droplet Morphometry and Velocimetry
DNA	Deoxyribonucleic Acid
DNase-seq	DNase I Digestion Analyzed by Deoxyribonucleic Acid Sequencing
DNMT	DNA Methyltransferase
DRIE	Deep Reaction Ion Etching
Drop-ChIP	Drop-Based Microfluidic Chromatin Immunoprecipitation
dsDNA	Doubled-Stranded Deoxyribonucleic Acid
EDTA	Ethylenediaminetetraacetic Acid
ELISA	Enzyme-Linked Immunosorbent Assay

DoD	Droplet-on-Demand
ESI	Electronic Supplementary Information
EWOD	Electro-Wetting on Dielectric
EZH2	Enhancer of Zeste Homolog 2
FAIRE	Formaldehyde-Assisted Isolation of Regulatory Elements
FAIRE-seq	Formaldehyde-Assisted Isolation of Regulatory Elements Analyzed by Deoxyribonucleic Acid Sequencing
fCAB-seq	5-Formylcytosine Chemically Assisted Bisulfite Sequencing
GOI	Gene of Interest
GRO-seq	Global Run-On Sequencing
HAT	Histone Acetyltransferase
HDAC	Histone Deacetylase
HMT	Histone Methyltransferase
HT-ChIP	High Throughput Automated Microfluidic Chromatin Immunoprecipitation
ID	Inner Diameter
IHEC	International Human Epigenome Consortium
lncRNA	Long Non-Coding Ribonucleic Acid
MBD	Methyl-CpG-Binding Domain
MBD2	Methyl-CpG-Binding Domain Protein 2
me	Monomethylation
me2	Dimethylation
me2a	Asymmetric Dimethylation
me2s	Symmetric Dimethylation
me3	Trimethylation
MeDIP	Methylated Deoxyribonucleic Acid Immunoprecipitation
MeDIP-seq	Methylated Deoxyribonucleic Acid Immunoprecipitation Analyzed by Deoxyribonucleic Acid Sequencing
MEMS	Microelectromechanical Systems
miRNA	Micro Ribonucleic Acid
MLPA	Multiplex Ligation-Dependent Probe Amplification
MNase	Micrococcal Nuclease
MNase-seq	Micrococcal Nuclease Digestion Analyzed by Deoxyribonucleic Acid Sequencing
MOWChIP-seq	Microfluidic-Oscillatory-Washing-Based Chromatin Immunoprecipitation Analyzed by Deoxyribonucleic Acid Sequencing
mRNA	Messenger Ribonucleic Acid
N.C.	Normally Closed Valve Port
NCI	National Cancer Institute
ncRNA	Non-Coding Ribonucleic Acid
NGS	Next-Generation Sequencing
NIH	National Institutes of Health
N.O.	Normally Open Valve Port
NSCLC	Non-Small Cell Lung Cancer
OD	Outer Diameter
oxoBS-seq	Oxidative Bisulfite Sequencing

PBS	Phosphate Buffered Saline
PC	Polycarbonate
PCR	Polymerase Chain Reaction
PDMS	Poly(dimethyl siloxane)
piRNA	Piwi-Interacting Ribonucleic Acid
PMI	Precision Medicine Initiative
PMMA	Poly(Methyl Methacrylate)
PP	Polypropylene
PRC2	Polycomb Repressive Complex 2
PTFE	Polytetrafluoroethylene
PTM	Post-Translational Modification
qPCR	Quantitative Polymerase Chain Reaction
RE	Reference Electrode
RISC	Ribonucleic Acid-Induced Silencing Complex
RNA	Ribonucleic Acid
RNA-seq	Ribonucleic Acid Sequencing
RRBS	Reduced Representation Bisulfite Sequencing
RSD	Relative Standard Deviation
RT-PCR	Reverse Transcription Polymerase Chain Reaction
SDS	Sodium Dodecyl Sulfate
SNV	Single Nucleotide Variant
TAB-seq	Tet-Assisted Bisulfite Sequencing
TAD	Topologically Associated Domain
TE	Tris-Ethylenediaminetetraacetic Acid Washing Buffer
TET	Ten-Eleven Translocation Enzyme
TRE	Transcriptional Regulatory Element
TSS	Transcription Start Site
VI	Virtual Instrument
WE	Working Electrode
WGBS	Whole-Genome Bisulfite Sequencing

LIST OF SYMBOLS

$\Delta\Delta Ct$	Change in the Threshold Cycle for the Gene of Interest Compared to the Reference Gene for the Immunoprecipitated Sample after Subtraction of the Change in the Threshold Cycle for the Gene of Interest Compared to the Reference Gene for the Input Sample
ΔCt	Change in the Threshold Cycle for the Gene of Interest Compared to the Reference Gene
ΔP	Pressure Drop
ΔV	Change in Volume
Δv	Velocity Difference
η	Viscosity
Θ	K-Channel Angle between Channel Arms
μ_0	Magnetic Permeability
ϕ	K-Channel Angle Relative to Main Channel or Droplet Volume Fraction (Context-Dependent)
B	Magnetic Field
c	Constant Defined in Context where Used
Ct	Threshold Cycle
$Ct_{GOI:Input}$	Threshold Cycle for the Gene of Interest in the Input Sample
$Ct_{GOI:IP}$	Threshold Cycle for the Gene of Interest in the Immunoprecipitated Sample
$Ct_{RG:Input}$	Threshold Cycle for the Reference Gene in the Input Sample
$Ct_{RG:IP}$	Threshold Cycle for the Reference Gene in the Immunoprecipitated Sample
d	Distance or Diameter
D	Incubation Dispersion
f	Frequency
F_d	Hydrodynamic Drag Force
F_m	Magnetic Force
Hz	Hertz
I	Incubation Time
m	Magnetic Moment
Q	Volumetric Flow Rate
r	Radius
R_H	Hydraulic Resistance
s	Second
V	Volume

ABSTRACT

Beyond the linear sequence of the genome, the epigenome dynamically controls chromatin remodeling and transcriptional poise without inducing changes in DNA sequence. These epigenetic mechanisms, particularly modifications to the histone proteins which mediate chromatin compaction, play critical roles in health and disease. To empower further successes in epigenetic therapies, current tools for understanding these systems must be improved. In particular, Chromatin Immunoprecipitation (ChIP) offers the gold standard technique for probing DNA associations with modified histones. This protocol isolates chromatin complexes (nucleosomes) for affinity purification of only those displaying the modification of interest. Final analysis of captured DNA can identify novel pathways or provide a quantitative view of current transcriptional state. Unfortunately, this assay's large sample requirements and laborious, user-dependent protocol have generally proven prohibitive to widespread clinical deployment.

This doctoral dissertation presents the development of a semi-automated, miniaturized platform for performing the ChIP assay using droplet microfluidics, capitalizing on an assay format in which pL-scale encapsulation in immiscible oil limits sample loss and accelerates mass transfer. A wide array of supporting technologies empower dynamic control over droplet composition and reaction conditions, making each droplet analogous to a reaction vessel (but for handling up to thousands of discrete volumes every second). Finally, these platforms serially process dynamic samples sizes by adjusting the total number of droplets handled, not individual reagent conditions, suggesting the potential for dynamic scalability of ChIP across a range of sample sizes.

First, the dissertation informs the direction of the work in the context of epigenetic and microfluidic challenges. Chapter I motivates opportunities and hindrances in the analytical characterization of the epigenome from the perspective of precision medicine, providing a survey of both conventional methods and emerging microfluidic techniques. Then, it outlines strategies to address technical difficulties of the ChIP protocol using droplet-based methods. Importantly, it identifies points-of-need in droplet technologies, especially for affinity purification capabilities essential to ChIP (and to other important bioassays).

Next, the dissertation describes fundamental advances in droplet microfluidic technologies. Chapter II describes the K-channel, a multifunctional, switchable, and scalable approach to improve droplet handling and chemical manipulation. K-channels performed reagent injection (0-100% of droplet volume) and magnetically biased droplet splitting (1:1 daughter droplet ratio, 96% magnetic particles retained), among other operations. Chapter III presents translation of droplet techniques into mass manufacturable thermoplastic materials, anticipating future needs in practically deploying these technologies. Chapter IV describes the Counter-Current Continuous Phase Extraction (C^3PE) module for determinant control over droplet packing fraction (50 - 85%) and applies it with the K-channel for high temporal resolution analysis (~100 ms) of flow behavior for confined droplets (example incubation time dispersions reduced by up to 50%).

Lastly, the dissertation describes a critical innovation in droplet microfluidic purifications and, empowered by it, the full development and characterization of the droplet-based ChIP technology. Chapter V introduces the Coalesce-Attract-Resegment Washing (CAR-Wash) platform for efficient droplet-mediated particle washing (greater than 100-fold dilutions achieved at 500 Hz processing with 98% particle capture) and demonstrates its efficacy in the bioanalytical context of affinity separations. Chapter VI fully realizes the droplet microfluidic ChIP platform

with automated cell lysis, chromatin digestion, immunoprecipitation, and particle washing, achieving successful application to two modified histone targets (H3K4me3 and H3K27me3). Finally, Chapter VII concludes the work and offers future directions in both technical improvements and general directions for droplet bioassay development.

Chapter I

Translational Opportunities in Precision Epigenomics and Technical Demands for Adaptation to Droplet Microfluidics

This work was partly adapted from "Translational Opportunities for Microfluidic Technologies to Enable Precision Epigenomics," a manuscript in preparation by Yi Xu, Steven R. Doonan, Tamas Ordog, and Ryan C. Bailey. Of the adapted sections, S. R. Doonan was the lead author on "EPIGENOMIC IMPLICATIONS FOR PRECISION MEDICINE." Y. Xu was the lead author on "CURENT TECHNOLOGIES FOR EPIGENOMIC PROFILING" and "*TRANSLATING EPIGENTIC TECHNOLOGIES TO A CLINICAL SETTING," including Table I.1 and Figures I.1-I.3.*

EPIGENOMIC IMPLICATIONS FOR PRECISION MEDICINE

Interchangeably referred to as precision, personalized, or individualized medicine, this exciting paradigm in modern medicine considers a patient's biochemical markers indicative of disease risk or progression in order to design an optimized prevention and treatment strategy tailored for a specific individual.[1, 2] In 2015 President Barack Obama announced the Precision Medicine Initiative (PMI), which directed additional funding to the National Institutes of Health (NIH) to bolster efforts to realize the potential of this personalized approach to medicine. In support of this mission, the National Cancer Institute (NCI) has focused on improving the understanding of inter- and intra-tumor genomic heterogeneity to advance cancer screening and

treatment. The broader vision of the PMI seeks to establish a national research cohort with longitudinally profiled multi-omic biomarker data as a reference population for future precision medicine approaches.[3] In parallel, ongoing efforts toward enhancing precision medicine aim at developing digital tools and companion diagnostics crucial to the implementation of precision therapies.[4, 5]

As a critical innovation for precision medicine, the sequencing of the human genome has led to considerable insight into the genetic hallmarks of disease; and next-generation sequencing (NGS) has led to numerous breakthroughs in terms of revealing specific tumor-driving mutations and assessing patient heterogeneity.[6] As the technology most associated with precision medicine, NGS further informs not only patient response to therapy but also pharmacogenetically-driven drug discovery.[6-9] The combination of decreasing costs and increasing throughput for NGS provided by commercially available platforms (e.g., Illumina HiSeq and NovaSeq platforms), as well as the increasing availability and sophistication of bioinformatic tools for referencing genomic data against databases (e.g., the Cancer Genome Atlas), continues to increase the power of this approach.[6, 10-13] For instance, classification of phenotypically indistinguishable cystic fibrosis patients into genetic subgroups has enabled successful targeted therapies based on each subgroup's specific molecular aberration.[14] Likewise, genetic "hotspot" analysis of non-small cell lung cancer (NSCLC) biopsies routinely guides therapeutic strategies in the clinical setting.[6] Additional successful, clinically relevant examples of precision therapies and diagnostics based on sequencing are highlighted by recent reviews.[1, 2, 6, 9, 14]

The combination of NGS with the tools of molecular genetics such as CRISPR-Cas9 genome editing has led to the elucidation of single nucleotide variants (SNVs) and other mutations in the genome contributing to diseases like obesity and breast cancer.[15-17] On the other hand, purely

genetic methods may not always provide sufficient information and context to guide clinical decisions. In the case of cancer, most sequence mutations detected in patient samples typically lack a direct role in tumorigenesis, increasing the complexity of isolating targetable and actionable information from large sequencing libraries.[8, 18, 19] Beyond the linear sequence of DNA, environmental factors may also influence phenotype and even lead to heritable diseases.[20] Perhaps the most striking example of nongenetic mechanisms shaping phenotypic diversity is the divergence of the transcriptome and other phenotypic traits in monozygotic twins occurring likely in response to environmental cues.[21, 22] Moreover, some toxins impair fertility across multiple generations after ancestral exposure even though they do not induce corresponding mutations in DNA sequence.[23] Sensitive to environmental insults, a complex regulatory network of "epigenetic" factors acts beyond the genome and can even lead to diseases such as cancer, especially when dysregulated.[24-27] In this work, we discuss the importance and opportunity held by new methods that can assess epigenetic states with a focus on guiding disease prevention, diagnosis, and therapy. We also evaluate the current state-of-the-art in terms of technologies available in the research laboratory setting, hindrances of these approaches to clinical translation, and opportunities for new tools to enable precision epigenetics.

Understanding the Epigenome

Broadly speaking, epigenetics encompasses multiple layers of interacting regulatory elements that define phenotypic variation beyond what is encoded in DNA sequence alone.[28, 29] For example, embryogenesis integrates cues from the local environment to modulate expression of genes critical to differentiation while establishing a complex network of specialized tissues from a single-celled zygote.[30-32] Moreover, the epigenetic landscape of silenced and expressed genes

established at each stage of development stably programs somatic cells and persists through multiple rounds of cell cycle and mitotic divisions.[30, 33] Some acquired epigenetic alterations may even be transmitted meiotically to germline cells and later affect future generations never directly exposed to the initiating stimuli. However stable, these epigenetically encoded traits are not irreversible, as germline reprogramming removes or remodels most parental epigenetic information during germ cell development and after fertilization as totipotent stem cells are formed.[29, 30, 32, 34, 35] These processes can now be mimicked experimentally to generate induced pluripotent stem cells, e.g., for the purposes of regenerative medicine.[36, 37] Beyond differentiation and development, epigenetic characteristics play a major role in transcriptional regulation in disease pathways, further underscoring the importance of understanding their molecular basis.[25, 38, 39]

Understanding chromatin structure is crucial to understanding the epigenome. The most fundamental unit of chromatin is the nucleosome. Nucleosomes are octameric protein complexes that each contain two copies of four histone proteins (H2A, H2B, H3, and H4).[33, 40] Around each nucleosome are ~147 base pairs (1.67 turns) of left-handed, supercoiled DNA. Nucleosomes are connected by linker DNA, and chromatin compaction is achieved by higher order assembly of nucleosomes that effectively control accessibility of particular genomic regions to transcriptional machinery.[41-43] Epigenetic modifications provide a genome-wide indexing system that, through the actions of chromatin remodelers and chaperones, regulates the use of the DNA template for transcription, replication, and repair, and they can be indicative of the functional state of chromatin during analysis.[30, 44]

The best understood level of epigenetic control is provided by DNA: cytosine modifications. Specifically, cytosine is frequently covalently modified to 5-methylcytosine (5mC),

particularly in a CG dinucleotide context. Oxidative derivatives of 5mC, 5-hydroxymethylcytosine (5hmC), 5-formylcytosine (5fC) and 5-carboxylcytosine (5caC), although less stable and less abundant, also have functional significance besides representing a path toward complete demethylation.[45-47] Cytosine methylation at relatively high CG dinucleotide sequence-content regions (so-called "CpG islands") near gene promoter sites alters the binding of transcription machinery at methyl-CpG-binding domains (MBDs), typically repressing gene expression.[42, 44] Moreover, especially low density (<10 CpG per 100 bp) "CpG deserts" also have regulatory implications.[48] The installation and maintenance of methyl groups by DNA methyltransferases (DNMTs) serve to regulate this process, in conjunction with Ten-Eleven Translocation (TET) proteins and members of the Base Excision Repair (BER) pathways, which erase these marks (with 5hmC, 5fC and 5caC being common intermediates).[44, 45, 47] Unsurprisingly, 5hmC regions most commonly associate with actively transcribed sequences, and 5hmC can even persist as a stable mark, not only as a transient intermediate from 5mC erasure pathways.[46, 47] In summary, the landscape of modified DNA bases provides a dynamic regulatory network for gene expression.

Modification of core histone proteins is a major mechanism regulating the binding strength of specific genomic sequences to nucleosomes and also poises loci for binding of transcription factors and related complexes.[31, 40, 43, 44, 49] Histone subunits exist in multiple isoforms which can exchange to and from an intracellular pool of free histones by the action of chaperone proteins. Variants such as H3.3 play critical roles in germline cell maturation and other processes by aiding in the recruitment of transcription factors and chromatin remodeling enzymes with downstream effects.[31, 40] Similarly, post-translational modifications (PTMs) to each histone subunit directly impact the binding interactions among histones, DNA, and other biomolecules. For example, the activating mark H3K9ac (acetylation of histone H3 at lysine residue 9) decreases the positive

charge of the histone, thus reducing the magnitude of its electrostatic attraction to DNA. This altered interaction can thus play a role in increasing DNA accessibility. Mono-, di-, and trimethylation (me, me2, and me3) events at lysine residues or mono- and symmetrical or asymmetrical dimethylation (me1, me2s, me2a) at arginine residues may act as activating or repressive marks by changing the steric structure of the histone-DNA associations and, as a result, changing the binding properties to transcription factors and chaperones.[43, 44, 50, 51] Writing and erasing histone marks by enzymes like histone acetyltransferases, deacetylases, and methyltransferases (HATs, HDACs, and HMTs) dynamically install and remove PTMs. Further, these enzymes contribute to complex mitotic and meiotic epigenetic inheritance pathways.[33, 44] The population of post-translationally modified histone variants, sometimes referred to as the "histone code," synergistically interacts with other epigenetic mechanisms including modified DNA bases to facilitate control over transcription, replication, and repair.[42, 44]

Whereas histones restructure chromatin to modulate DNA accessibility, non-coding RNAs (ncRNAs) may also regulate post-transcriptional processing. Some small RNAs such as Piwi-interacting RNAs (piRNAs) can recruit chromatin remodelers like Argonaute (Ago) proteins and other enzymes to modify histones.[41, 44] Others like microRNAs (miRNAs, 17-25 bases) directly affect gene expression by binding to messenger RNA (mRNA) post-transcription in conjunction with the RNA-induced silencing complex (RISC) to repress translation or degrade mRNAs.[52, 53] Interestingly, populations of small RNAs can persist in germline cells to facilitate transgenerational epigenetic effects such as gene silencing in subsequent generations.[54] An additional class of RNA, termed long non-coding RNA (lncRNA; ranging from 200 bases to 100 kilobases), can serve as a pool to sequester regulatory small RNAs and can directly participate in chromatin remodeling. Some lncRNAs competitively bind miRNAs so that they do not bind to

targeted mRNA molecules, thus reducing the level of miRNA-mediated gene repression.[52, 55] Additionally, they can recruit chromatin remodelers and interact with other lncRNAs (as well as other regulatory species such as RNA splicing enzymes).[52, 56] Ongoing work increasingly demonstrates the significance of chemical modifications to RNA bases as a mechanism for epigenetic regulation.[57, 58]

The combined actions of DNA modifications, histone protein isoforms, histone post-translational modifications, and non-coding RNAs facilitate a complex regulatory network controlling gene expression by dynamically altering the three-dimensional conformation and accessibility of chromatin in a gene-specific manner.[59-61] In conjunction with recruited adenosine triphosphate (ATP)-dependent chromatin remodelers, the downstream effects of these epigenetic factors include altering nucleosome occupancy and positioning, which manage the accessibility of transcription promoter and initiator sites to transcription factor and RNA polymerase binding.[59-63] Furthermore, this three-dimensional architecture affects DNA replication and repair and, overall, holds significant consequences for heath and disease, as we will examine in the next section.[60, 61]

Epigenetics and Disease

Because of their major role in managing chromatin states, dysregulation or aberrant function of epigenetic regulators commonly leads to serious and harmful consequences, including cancer development and progression.[55, 64-66] Aberrant genome-wide CpG hypomethylation commonly occurs in cancers due mainly to the hypomethylation of highly repetitive sequences, which comprise approximately half of the human genome.[67] Cancer-linked hypomethylation has also been linked to increased expression of several genes, and overexpression of the H3K27 HMT enhancer of zeste homolog 2 (EZH2) oncogenically dysregulates histone remodeling of tumor

suppressor genes, including *p27* and *BRCA1*.[65-67] Epigenetic repression of tumor suppressors also often arises from promoter hypermethylation of normally unmethylated CpG islands.[68] Likewise, dysregulation of the *H19* lncRNA can downregulate the tumor suppressor gene retinoblastoma and further dysregulates downstream miRNA activity in colorectal cancers.[55] Beyond cancer, epigenetic dysregulation can lead to many other diseases. For example, exposure to environmental toxins can trigger heritable changes in DNA methylation in germline cells that correlate with increased risk for obesity.[20] Some autoimmune diseases may even have a significant epigenetic component, including hyperactivity of nucleosome-remodeling HDACs that play pro-inflammatory roles and enhance destructive immune cell activity in rheumatoid arthritis.[69, 70] Dysregulation of miRNAs has also been shown to correspond to neurological disorders, such the repressive activity of overexpressed miR-182 on genes like *Adcy6* (involved in circadian rhythm) in patients with major depressive disorder.[71] While these examples encompass only a small subset of epigenetic disease pathways, the far-reaching significance of epigenetic factors to disease and human health cannot be understated.

Mirroring their multifaceted roles in disease pathology, epigenetic factors also present exciting therapeutic opportunities. Currently, most epigenetic-based therapeutic strategies focus on one of two major approaches: (1) reprogramming aberrant epigenomic regulation to reestablish homeostasis, or (2) utilizing epigenetic pathways to directly induce apoptosis or increase drug sensitivity for destruction of aberrant cells.[72] For example, HDAC inhibitors butyrate or trichostatin A promote repression and reversion of the glycolytic phenotype in cancer cells, thus repressing tumor growth and invasion.[65] Other HDAC inhibitors have also shown promising effects to reprogram dysregulated histone acetylation in neurodegenerative diseases.[65, 70, 73] In other contexts, several FDA-approved HDAC inhibitors (e.g., belinostat and vorinostat)

selectively disrupt oncogenic pathways to trigger apoptosis in cancer cells. Moreover, specific inhibition of the histone lysine methyltransferase activity of EZH2 re-sensitizes radio-resistant prostate cancer cells to radiation therapy.[74] Other epigenetic factors also provide promising therapeutic opportunities. Examples include the alteration of miRNA pathways in psychiatric disorders and leveraging DNA demethylation for breast cancer treatment.[71, 75] Furthermore, epigenetic factors may manifest critical biomarkers to enhance diagnosis, offer predictive value to guide therapies, and provide affirmative measures for monitoring patient response. For instance, a recent study successfully demonstrated a predictive association between DNA methylation profile and potential for relapse in children with acute myeloid leukemia.[76] Increasingly sophisticated bioinformatics tools, coupled to the expanding information available from reference epigenomes,[77] hold great promise for the future, especially when made widely available through repositories like the International Human Epigenome Consortium (IHEC).[78]

As efforts continue to discover epigenetic mechanisms involved in disease development, providing new therapeutic targets, the potential for epigenetically-driven precision therapies becomes increasingly within reach. However, new tools will be required to translate these basic biomolecular insights into personalized treatment regimens. The following sections describe the current state-of-the art technologies for probing epigenomic signatures that may be suggestive of particular treatments, as well as gaps—or chasms—that exist between promise and realization of precision epigenomics.

CURENT TECHNOLOGIES FOR EPIGENOMIC PROFILING

To elucidate key epigenomic mechanisms impacting human health, a number of assays have been developed to profile different aspects of the epigenome—many strongly coupled to the

rapid growth of NGS techniques. Moreover, cutting-edge analyses utilize multiple profiles of diverse epigenetic markers to obtain a more thorough understanding of the embedded epigenomic landscape and to infer causal relations among these epigenomic mechanisms.[79] These technological developments have contributed enormously to the current understanding of epigenetic regulation. In this section, we will summarize the primary methods for epigenomic analysis.

Direct Sequencing to Investigate Regulatory Noncoding RNAs

The epigenetics community has adopted RNA sequencing (RNA-seq) to reveal information regarding the roles ncRNAs play in phenotypic regulation.[80, 81] The general workflow starts with reverse transcription of a collection of RNA samples (total ribosomal RNA removed or fractionated by other means) to form a complementary DNA (cDNA) library. After ligating DNA adaptors or barcodes to one or both ends and optionally amplifying the library by polymerase chain reaction (PCR), commercial platforms sequence the (amplified) library. Following mapping of the reads to a reference genome, quantifying the number of reads mapped to a specific gene enables the assessment of the level of gene expression.[82, 83] Concentrating targets by size selection out of a total RNA sample or deconvolving the total reads generally enables direct profiling of small ncRNAs such as miRNAs and siRNAs, whereas lncRNAs may need an additional step of fragmentation to break the long sequences into shorter pieces more compatible with deep-sequencing technologies.[82, 84] Additionally, conducting RNA-seq on other RNA targets, such as mRNA, obtains high-resolution profiling information to resolve the whole transcriptome.

Applying the RNA-seq methods described above to ncRNA studies (1) demonstrated that miRNAs predominantly destabilize and decrease target protein-coding mRNA levels and reduce

protein production,[85] (2) enabled identification and quantification of translational suppression induced by siRNA and miRNA targets without relying on computational predictions,[86] and (3) revealed active transcriptional regulatory elements (TREs) and polymerase-regulator interactions over broad promoter regions via a modified RNA-seq protocol, named global run-on sequencing (GRO-seq).[87, 88] Furthermore, RNA-seq has uncovered thousands of novel lncRNAs expressed in diffuse large B cell lymphoma and predicted their potential roles in lymphomagenesis by identifying co-expressed coding genes.[89] RNA-seq also enabled identification of novel lncRNAs dysregulated in colorectal carcinogenesis.[90] As a fundamental tool for epigenetics, RNA-seq excels at discovering unannotated ncRNAs and novel isoforms to expand the global view of the transcriptome. Although it may suffer from potential bias during library construction and challenges in bioinformatic analysis, RNA-seq offers several analytical advantages including single base resolution, low background signals and large dynamic ranges spanning five orders of magnitude.[82, 83]

Chemical Treatment-Based Methods Followed by Sequencing to Detect DNA Modifications

Besides ncRNAs, epigenetic studies also target modifications to DNA bases. Prevalent methods include a toolkit of bisulfite sequencing strategies to locate and quantify DNA methylation and other variants within genomic DNA by chemically altering their structures. Whole-genome bisulfite sequencing (WGBS) treats DNA with a bisulfite reagent before sequencing to convert regular cytosine, 5fC, and 5caC to uracil, while leaving 5mC and 5hmC intact (Fig. I.1, middle workflow). Subsequent sequencing profiles genome-wide cytosine methylation and hydroxymethylation down to single nucleotide resolution.[91-95] Reduced representation bisulfite sequencing (RRBS) offers decreased cost and improved efficiency over

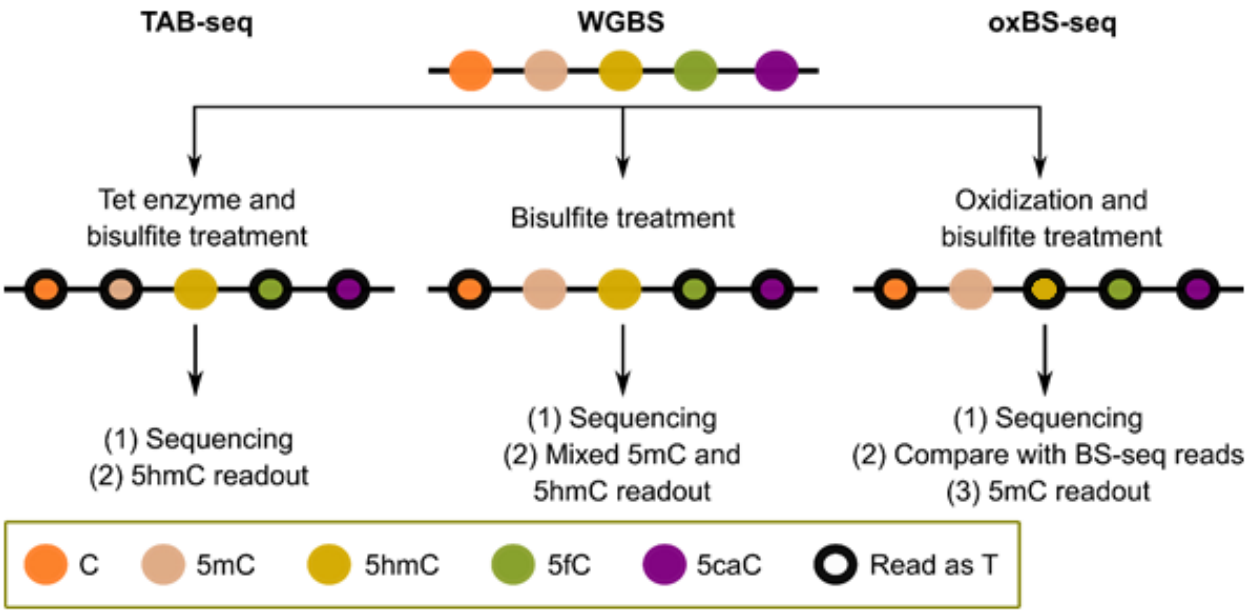

Figure I.1. Workflows of selected chemical treatment-based DNA methylation analysis methods.

WGBS by first digesting samples with restriction enzymes (e.g., *Msp*I and *Bgl*II) and then extracting appropriately-sized DNA fragments (<600 bp) to selectively enrich CpG-containing regions prior to bisulfite treatment.[96-98] As a result, the coverage of RRBS is limited to CpG-rich regions, and therefore does not as extensively cover enhancers and intronic regions compared to WGBS.[99] Additionally, Tet-assisted bisulfite sequencing (TAB-seq) specifically detects 5hmC at single-base resolution and determines its abundance at each modification site by protecting 5hmC with glycosylation and oxidizing other cytosine residues with Tet enzyme. Thus, only 5hmC remains intact after bisulfite treatment (Fig. I.1, left workflow).[100-102] 5mC can thus be detected by subtracting TAB-seq results from regular bisulfite sequencing data. A third modified bisulfite sequencing strategy, oxidative bisulfite sequencing (oxBS-Seq), differentiates 5mC and 5hmC by specifically oxidizing 5hmC before bisulfite treatment to obtain a positive readout of pure 5mC. Comparing oxBS-seq reads with those from a regular bisulfite sequencing run on the same sample infers the profile and distribution of 5hmC (Fig. I.1, right workflow).[103, 104] Unlike TAB-seq, oxBS-seq does not require expensive enzymes and avoids the potential inefficiency in

glycosylation of 5hmC or enzymatic oxidization of 5mC, which can result in false calling of 5hmC.[94, 104] In practice, directly detecting the much more abundant 5mC can increase the error of estimating 5hmC by subtraction (compared to other methods). Beyond techniques targeting 5mC and 5hmC, strategies specifically detecting 5fC, 5caC, and other DNA modifications have also emerged. Examples include 5fC chemically assisted bisulfite sequencing (fCAB-seq) for 5fC mapping and chemical modification-assisted bisulfite sequencing (CAB-seq) for 5caC mapping.[99] However, methods capable of differentiating between 5mC and its oxidative derivatives have not gained broad acceptance, due in part to reagents and protocols not yielding robust, consistent results.

Promisingly, applications of these methods have further extended our understanding of the mechanisms of DNA modification-regulated gene expression. WGBS and RRBS have been utilized to reveal DNA methylome variances induced by non-shared environmental factors,[105] map genome-wide DNA methylation patterns in mammalian ovaries,[106] and identify DNA methylome footprint during human B cell differentiation.[107] TAB-seq and oxBS-seq have exposed the biological functions of 5hmC in cellular memory reprogramming, cancer development, and other diseases.[108-111] Ongoing optimization in bisulfite sequencing-based strategies will further enable higher coverage and improved accuracy in DNA methylome mapping.

Affinity Methods to Probe DNA Modifications, Histone Modifications, and DNA-Binding Proteins

In addition to analyzing epigenetic control at the nucleic acid level using chemical treatments, epigenetic studies have widely exploited affinity-based methods to enrich modifications of interest on both DNA and DNA-associated histone proteins to elucidate

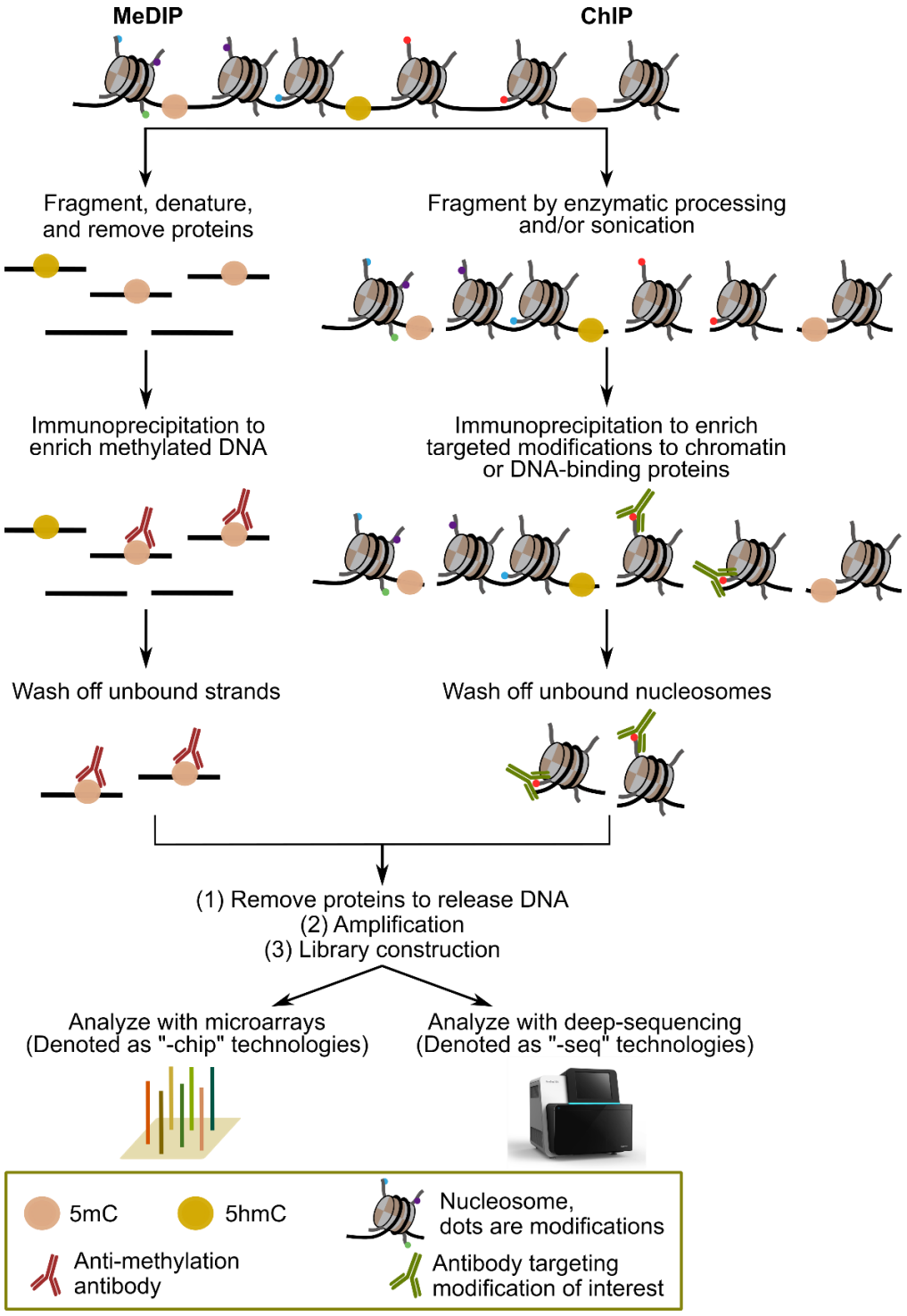

Figure I.2. Workflows of selected affinity-based chromatin modification analysis methods.

underlying biological impact.[112] Methylated DNA immunoprecipitation (MeDIP) enriches 5mC DNA regions with highly efficient binding from 5mC-specific antibodies (Fig. I.2, left workflow).

Sequencing the enriched product generates high-resolution whole-genome DNA methylation profiles (MeDIP-seq).[113, 114] Similarly, antibodies targeting 5hmC, 5fC, and 5caC locate respective modified cytosine residues, providing multiple variants of DIP-seq (i.e., hMeDIP-seq, 5fC-DIP-seq, and 5caC-DIP-seq).[115-117] Methods using the MBD of MBD protein 2 (MBD2) to precipitate methylated DNA regions can also identify DNA methylation patterns when integrated with sequencing (i.e. MBD-seq based methods).[118, 119] Compared with WGBS, TAB-seq, and oxBS-seq, which provide genome-wide methylation profiles, affinity-based methods have limited methylation coverage that is biased towards CpG-rich regions; however, MeDIP- and MBD-seq can provide information on these specific sites at low costs and high efficiency.[120, 121] Deploying these affinity-based methods has clarified the critical roles of DNA methylation and its variations involved in the mechanisms regulating differentiation, development, and carcinogenesis.[122-124]

Besides analyzing modifications to DNA, affinity-based immunoprecipitation also reveals the profiles of modifications to histones and to DNA-binding proteins (e.g., transcription factors and chromatin remodeling complexes) that influence transcriptional regulation, as well as RNA polymerase II and its covalent modifications. The gold standard to identify such protein-DNA interaction is chromatin immunoprecipitation followed by sequencing (ChIP-seq) (Fig. I.2, right workflow). The general protocol of ChIP-seq involves: (1) optional crosslinking of DNA and proteins to preserve their interactions; (2) shearing of chromatin into mono- and di-nucleosome sizes (~147 and ~300 bp, respectively) by sonication and/or micrococcal nuclease (MNase) enzymatic digestion; (3) immunocapture of the modification of interest with specific antibodies; and (4) purification of captured DNA for library preparation and sequencing.[125-127] Comparing the sequencing results of the ChIP DNA library to those of a control library obtained without specific antibody capture (otherwise following the same protocol) allows the assessment of enrichment

specificity and efficiency. Due to the size heterogeneity resulting from inconsistencies in DNA shearing and potential contamination from unbound DNA, conventional ChIP-seq suffers from low resolution in mapping the binding locations of proteins of interest, and thus may not profile them precisely and thoroughly.[94] Moreover, DNA fragmentation heterogeneity, immunoprecipitation efficiency variations, and inconsistency from other experimental steps limit direct comparisons of ChIP results derived from different cell types or differentially perturbed cells.[128] Finally, despite its popularity, this method lacks a robust normalization protocol to empower quantitative comparisons among heterogeneous samples.[128, 129]

To address these issues, notable variations of ChIP-seq have emerged. ChIP-exo utilizes exonuclease treatment to narrow the region of protein binding on ChIP DNA sequences, enhancing mapping resolution of bound locations down to the single-nucleotide level.[129] ChIP with reference exogenous genome (ChIP-Rx) allows normalization of sequencing reads across cell populations by adding a defined quantity of a reference epigenome on a per-cell basis, thus enabling quantitative comparison among multiple ChIP-seq runs.[128] Chromatin endogenous cleavage with high-throughput sequencing (ChEC-seq) exploits a fusion protein comprising a DNA-binding protein of interest and MNase to bind targeted DNA sequences and then precisely cuts only the bound regions for targeted DNA isolation for sequencing. This approach offers genome-wide high-resolution determination of protein binding sites.[130] Recently, the same group who developed ChEC-seq reported a protocol called “Cleavage Under Targets and Release Using Nuclease”, or CUT&RUN, to enable low background and base pair resolution profiling of chromatin modification and protein binding sites genome-wide.[131] This protocol utilizes a Protein A-MNase fusion to recognize antibodies bound to targeted epigenetic modifications or DNA-binding proteins, and spatially-confined nuclease activity selectively releases only the regions of chromatin

involved in the targeted interaction. Replacing the DNA-binding protein of interest with Protein A in the MNase fusion reduces the cost of the protocol and avoids potential distortions in the fused protein's structure, thus preserving its original binding affinity. In another approach, the typically high input requirements of ChIP-seq can be reduced within the range of ~10,000 cells (in the case of histone marks) to ~100,000 cells (to study transcription factor binding) by combining ChIP with hyperactive Tn5 transposase treatment that enables simultaneous DNA fragmentation and adaptor tagging (ChIPmentation; a term that combines "ChIP" with "tagmentation").[132] While limited in some contexts, ChIP-seq and the derivative methods have successfully identified and validated epigenetic factors and mechanisms related to chromatin remodeling, cellular development, disease progression, and other crucial processes.[133-136]

Within the context of analyzing the interactions of chemically modified chromatin components, an additional, complementary methodology must also be recognized: mass spectrometry. Leveraging the impressive capabilities developed for proteomic analysis (and for other "–omics"), mass spectrometry provides structural determination and quantitation of chromatin species without necessarily requiring affinity-based separations.[137-142] Thus, mass spectrometry provides one of the most attractive technologies for fundamental discovery of modified DNA bases and histone-chromatin interactions: it can probe these complexes without prior development of high affinity antibodies and in a multiplex format applicable to histones with multiple concurrent modifications.[138, 140, 142] Leveraging a combinatorial toolkit of upstream separation methods, ionization techniques, and mass analyzers facilitates comprehensive analysis of nucleosomes.[137, 140-142] Successes have included identification of novel methylated lysine interactions in the context of transcriptional repression[143] and characterization of global changes in histone methylation and acetylation in cancerous cells.[144] Further, Chromatin Interacting

Protein-Mass Spectrometry (ChIP-MS) and related approaches re-introduce antibody-based affinity separations to enrich targets for final analysis, for instance, in identifying novel transcriptional regulators interacting with X-chromosome-associated epigenetic modifications.[145] On the other hand, obtaining clinically useful data often requires DNA sequence information in addition to nucleosome structural information, but this combination can be achieved by sophisticated strategies using a gene sequence-targeted affinity purification prior to analysis.[137, 139] Moreover, the limited abundance of many epigenetic proteins, particularly in sample-limited applications, may also hinder mass spectrometry workflows (compared to the routine DNA amplification possible for low input nucleic acid analysis).[141, 142] Nonetheless, these techniques have been well suited to discovery and pathway elucidation, and they have fundamentally increased the body of epigenetic knowledge.[137, 139-142]

Enzymatic and Chemical Processing Methods Followed by Sequencing to Assess Nucleosome Distribution and Open Chromatin

In addition to chemical modifications to histone proteins, nucleosome occupancy, nucleosome positioning, and consequent chromatin accessibility all epigenetically regulate gene expression. Various methods have been used to map these important features by exploiting diverse enzymatic and chemical processing strategies to expose regulatory regions of interest from open chromatin. MNase is an endo-exonuclease that digests chromatin with minimal sequence preference into (mono-)nucleosomes by cleaving exposed DNA and DNA ends until encountering a barrier (e.g., nucleosome).[146, 147] Combining MNase digestion with high-throughput sequencing (MNase-seq) enables localization of DNA-binding proteins (e.g., transcriptional factors) and nucleosome positioning at single base pair resolution (Fig. I.3).[148] Limited exposure to MNase can

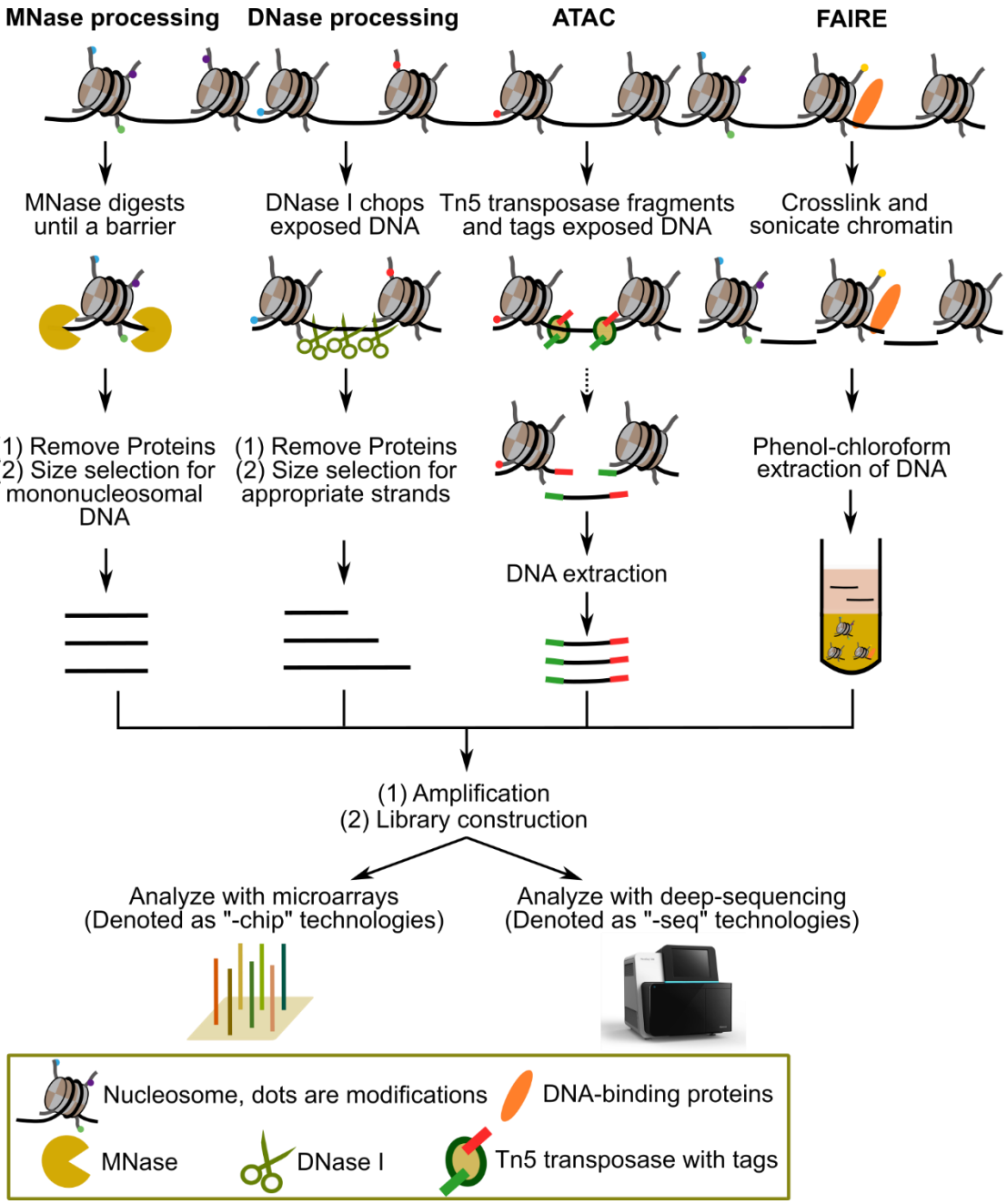

Figure I.3. Workflows of selected methods to analyze nucleosome distribution and open chromatin.

also be used for the identification of accessible, nucleosome-free DNA.[149] On the other hand, non-occluded accessible regions on genomic sequences are more often profiled using limited digestion from the endonuclease DNase I (DNase-seq) (Fig. I.3).[150] This allows the mapping of genetic *cis*-regulatory elements (e.g., promoters, enhancers, and silencers) in open chromatin structures, which

reveals dynamic changes in the acquisition and loss of the transcriptional competency of specific genomic loci.[151, 152] Both MNase-seq and DNase-seq separate enzymatic processing of chromatin from adaptor ligation/library preparation. By contrast, a relatively recently developed assay for transposase-accessible chromatin using sequencing (ATAC-seq) has emerged to utilize hyperactive Tn5 transposase to fragment and tag the genome with sequencing adaptors simultaneously (Fig. I.3).[153,154] ATAC-seq enables fast genome-wide mapping of active regulatory elements, nucleosome positioning, and chromatin accessibility simultaneously, making it an attractive method to assess the dynamic landscape of accessible DNA sequences in mammalian preimplantation embryos,[155] neural progenitor cells,[156] and human mesoderm development.[157]

Apart from enzymes, chemicals such as formaldehyde also can be used for orthogonal chromatin processing, such as formaldehyde-assisted isolation of regulatory elements (FAIRE) (Fig. I.3).[158] By crosslinking chromatin with formaldehyde prior to sonication-induced shearing, nucleosome-depleted regions obtain reduced crosslinking efficiencies when compared to nucleosome-occupied sites. Therefore, subsequent phenol-chloroform extraction enriches nucleosome-depleted DNA into the aqueous phase, serving as the sample for subsequent sequencing. FAIRE-seq provides insight on active regulatory elements abundant in open chromatin, serving as another alternative to DNase-seq and ATAC-seq without relying on enzymatic digestion.[159]

Applied individually or in combination, these methods have enhanced the community's understanding of the genome-wide dynamics of and relationships between nucleosome occupancy and chromatin remodeling during processes such as disease development, including human hematopoiesis, leukemia progression, and oncogenic state formation.[160-163]

Hybridization-Based Technologies

Sequencing-based studies have revolutionized our understanding of epigenetic regulation. Unfortunately, translating these protocols to large clinical cohorts can prove challenging in terms of cost, throughput, reproducibility, and complexity of bioinformatic analysis. A desire for efficient and cost-effective sample analysis can therefore favor alternative approaches that rely on hybridization-based technologies instead of sequencing readouts,[98] though at the cost of dramatically reduced genomic depth. Oligonucleotide microarrays simultaneously interrogate thousands to millions of transcripts, enabling transcriptome-wide expression profiling.[164] The general protocol includes reverse transcribing RNA targets to labeled cDNA (e.g., with fluorescent tags) followed by introducing the cDNA onto a microarray for hybridization with complementary DNA probes. After washing steps to remove nonspecific binding, scanning the microarrays quantifies hybridized targets based on signals from appended tags, allowing assessment of expression levels. Compared to sequencing, microarray-based techniques are more sensitive in detecting regulatory RNAs expressed at low abundance (e.g., lncRNAs): different RNAs hybridize to the probes independently, while highly abundant mRNA would dominate the sequencing reads and impede quantification in sequencing-based methods.[165] Capitalizing on this feature, applications of oligonucleotide microarrays excel at ncRNA profiling, including evaluating the regulatory roles of lncRNAs in cancer development and assessing the role of miRNAs in molecular pathways of disease progression.[166, 167] An impressive recent example even includes a 6.9 million-feature oligonucleotide array studying the human transcriptome in clinical studies with higher sensitivity than RNA-seq analysis performed in parallel.[168]

Microarray methods have also garnered wide popularity in detecting DNA methylation and histone modifications when assessing the progression and effects of adiposity,[169] quantifying

metabolic contributions to tumor development,[170] and mapping DNA methylome footprint during B cell differentiation.[107] This popularity is reflected in the existence of many types of commercial kits available to researchers, representative products among which are the Infinium Methylation Assays from Illumina. Infinium HumanMethylation450 BeadChip Kit (450K array) provided more than 485,000 methylation sites per sample at single-nucleotide resolution across the genome. Upon bisulfite treatment, the assay interrogated these sites with two probes differentiating methylated and unmethylated loci, allowing analysis of up to 96 samples simultaneously.[171] Fruitful DNA methylation profiling results have emerged since the epigenetic research community widely embraced the 450K array, and updated versions of this assay are now available.[172] For example, the Infinium Methylation EPIC Kit (EPIC array), almost doubles quantifiable methylation sites to over 850,000. The EPIC array significantly increases genomic coverage, particularly with more probes targeting methylations at enhancers while maintaining the ease of analysis and affordability from 450K array.[172] Moreover, combining microarrays with immunoprecipitation or chemical processing of chromatin enables tiling array techniques including ChIP-chip, MeDIP-chip, and DNase-chip ("chip" indicates microarray read-out). After targeting and isolating DNA associated with the modification of interest via ChIP, bisulfite treatment, or other chemical modification methods, purified DNA hybridizes with complementary probes for microarray scanning and detection. Common applications of these arrays include identifying specialized chromatin domains in transcriptional regulation,[173] identifying protein markers for psychiatric disorder development,[174] and marking cell-specific epigenomic sites.[175]

Cross-linking-Based Chromatin Conformation Assays

Beyond nucleic acid-protein interactions, higher-order three-dimensional nuclear organization further affects cellular interpretation of genomic information.[176, 177] The development of chromosome conformation capture (3C) and 3C-derived methods such as chromosome conformation capture-on-chip (4C), chromosome conformation capture carbon copy (5C), Hi-C, and chromatin interaction analysis by paired-end tag sequencing (ChIA-PET) have greatly enhanced the exploration of higher-order structural features of chromatin to an unprecedented extent.[177] 3C uses restriction endonuclease enzymes (e.g., *Eco*RI) to digest crosslinked and isolated nuclei, and intramolecular ligation links loci that are linearly separated but in close three-dimensional proximity. Quantitative PCR (qPCR) detects the ligated products after reverse-crosslinking and determines the frequency of interactions between any two genomic loci.[178] Results can be expressed relative to data obtained in corresponding sequences of chromatin-free DNA incorporated into bacterial artificial chromosomes. 4C combines 3C with microarrays or sequencing to search genome-wide for DNA loci that interact with a given locus.[179] 5C starts with building a 3C library of fragmented DNA and then applies multiplex ligation-dependent probe amplification (MLPA) to the 3C templates to determine interactions between multiple loci simultaneously either with microarrays or high-throughput sequencing.[180] Hi-C adjusts the 3C protocol slightly by marking the ends of digested DNA with a biotinylated nucleotide and pulling down only biotinylated and ligated DNA with streptavidin-coated magnetic beads, followed by deep sequencing. By mapping Hi-C reads to the genome, interactions between all fragments generate a matrix of ligation frequencies.[181] Lastly, ChIA-PET integrates ChIP with 3C by purifying DNA fragments with an antibody targeting a protein of interest to only detect interactions between loci associated with that specific protein.[182] 3C and 3C-based methods have revealed many three-dimensional epigenetic regulatory features, including (1) topologically associated

domains (TADs) and their functions in controlling the contact of enhancers with target genes,[183] (2) chromosomal rearrangements under both balanced and dynamic conditions with the discovery of a novel leukemogenic translocation partner of the T cell receptor,[184] and (3) the X chromosome topological remodeling and regulation of chromosome-wide gene expression.[185]

To conclude this section, the methods described above provide an invaluable toolbox for the analytical characterization of the epigenome, and Table I.1 summarizes these key approaches.

TRANSLATING EPIGENTIC TECHNOLOGIES TO A CLINICAL SETTING

Among the epigenetic marks accessible to the analytical methods introduced in this work, DNA methylation is the most commonly studied epigenetic marker in mammalian genomes.[186] Commercially available assays targeting DNA methylation aim to increase automation and reduce user dependence in clinical settings.[187, 188] Because of the relative maturity of those techniques, this section will instead outline other research efforts to date for the analysis of protein-DNA epigenetic interactions as well as chromatin conformation with the goal of ultimately translating these technologies into a clinical setting for empowering precision medicine.

Limitations of ChIP-seq and Variants

While being the traditional workhorse to probe protein-nucleic acid interactions, limitations of ChIP-seq prevent its routine clinical implementation, and the importance of these interactions to health and development was outlined earlier in this chapter. One major challenge is the large input sample size requirement. Traditionally, ChIP-seq requires more than 10^6 cells as starting material per analysis of one target to ensure effective enrichment of related DNA. This is unfeasible for clinical biopsies containing fewer than 10^3 cells or samples of rare cell

Table I.1. Achievements and Limitations of Current Technologies for Epigenetic Studies in the Context of Precision Medicine.

Technologies	Achieved Information	Limitations to Precision Medicine
RNA-seq	*Coding and non-coding RNAs*	(1) Intensive data processing (2) Bias from RNA fragmentation and sequencing library construction
WGBS	DNA 5mC and 5hmC	(1) No differentiation between 5mC and 5hmC (2) High sequencing cost
RRBS	DNA 5mC and 5hmC, mainly from CpG islands	(1) No differentiation between 5mC and 5hmC (2) Limited coverage of methylation
TAB-seq	DNA 5hmC	(1) Use of expensive Tet enzyme (2) Potential inefficiency in 5hmC glycosylation or 5mC oxidization leading to false calling
oxBS-seq	DNA 5mC	(1) Intensive sequencing depth and data processing from two required parallel sequencing runs
MeDIP-seq and variants	DNA methylation, can target 5mC, 5hmC, 5fC, and 5caC individually	(1) Low resolution (2) Antibody cross-activity (3) Bias towards highly methylated regions
MBD-seq	DNA methylation, especially in CpG-rich regions	(1) Low resolution (2) Limited coverage (3) Bias towards highly methylated regions
ChIP-seq and variants	Profiles of DNA-binding proteins and modifications to DNA and histones	(1) Large Input Requirements (2) Specificity and sensitivity depend on high-quality antibodies (3) Lack of automation (operator dependence)
MNase-seq	Nucleosome positioning	(1) Bias towards AT-rich regions (2) Need for high sequencing depth
DNase-seq	Regulatory regions and chromatin accessibility	(1) Bias from DNase I digestion (2) Need for high sequencing depth (3) May miss some distal regulatory regions
FAIRE-seq	Regulatory regions and chromatin accessibility	(1) Lower enrichment of targets compared to DNase-seq (2) May miss some promoter regions
ATAC-seq	Nucleosome positioning, chromatin accessibility, and transcription factor binding sites	(1) Bias towards nucleosomes around regulatory regions
Oligonucleotide microarrays (e.g., RNA profiling, 450 kit, ChIP-chip, MeDIP-chip, and DNase-chip)	Low abundance regulatory RNAs, DNA-protein interactions, DNA modifications, etc.	(1) Limited throughput by the number of array probes (2) Low resolution (3) Limited coverage
3C and variants	Interactions between gene loci and three-dimensional chromatin conformation	(1) Interference in reading from nonspecific co-localization of almost any two loci (2) Failure to detect dynamics and cell-to-cell variations of chromosome folding

populations.[126, 127] A second challenge of ChIP-seq is its inability to profile cellular heterogeneity. Lysis, digestion, and analysis of cells are commonly performed in bulk followed by the

aggregation of DNA from all cells, obscuring possible rare signals from low-abundance abnormal or novel features. Additionally, ChIP-seq suffers from poor robustness and low reproducibility as it relies largely on operator skills and reagent quality, especially antibody specificity. ChIP-seq experiments also require high quality chromatin and, therefore, are only typically amenable to fresh or frozen cell/chromatin samples—although methods modified for use in formalin-fixed, paraffin-embedded samples have been published.[189, 190] Finally, ChIP-seq is inherently low throughput as it investigates one target per sample (by using only one antibody). When combined, these factors complicate the use of conventional ChIP-seq in both routine clinical practice and longitudinal studies on large populations, making it less amenable to profiling a wide range of healthy and abnormal samples.[98]

Efforts have been made to improve the conventional ChIP DNA preparation workflow in bulk by reducing required cell numbers, shortening DNA preparation time, and improving automation and throughput. Early attempts included keeping multiple steps in the same tube and adapting ChIP to 96-well plates to reduce sample loss during material transfers and to simplify manual processing.[191-193] Unfortunately, fully user-independent automation of the entire protocol coupled to an efficient approach for applying ChIP-seq to clinical samples with small numbers of (scarce) cells has yet to be achieved. Improvements in throughput and analysis speed are also needed to facilitate monitoring of multiple epigenomic targets, especially in the context of possible synergetic effects and dynamic changes related to disease development. To summarize, an ideal, clinically-friendly ChIP-seq platform would automatically process patient samples containing varying numbers of cells with little pre-treatment and deliver results with high confidence, high accuracy, and high reproducibility. Such a platform would provide a reliable information source for diagnostic and prognostic guidance.

Promising Approaches of Automated DNA-Protein Interaction Analysis

Recent research efforts have turned to microfluidic tools as powerful alternatives to macroscale methods for automating ChIP-seq. Microfluidics features miniaturization of reagent volume, parallelization of multiple samples, and automation of an integrated workflow, which are all especially well-suited to sample-constrained, labor-intensive, and operator-dependent epigenetic analyses.[194] Particularly due to microscale device sizes and features, microfluidics facilitates single cell handling and analysis, making it a fundamentally enabling tool for the investigation of single cell epigenomic heterogeneities confounded by macroscale methods. The toolbox of single cell manipulation and processing on microfluidics has been expanding over the years with the emergence of promising proof-of-concept studies including highly efficient single cell encapsulation in microfluidic droplets,[195] high-throughput single cell reverse transcription PCR (RT-PCR),[196, 197] and single-cell sequencing with comparable read count and improved sensitivity compared to tube-based protocols.[198, 199] Although these methods still have limitations such as bias in reaction efficiency associated with minute sample amounts,[198] these principles have enabled many exciting studies aimed at facilitating microfluidic DNA-protein interaction analysis.

The Quake group pioneered the application of microfluidic techniques to automated, low-input epigenomic profiling. They developed automated microfluidic ChIP (AutoChIP) allowing enrichment of ChIP DNA from 2,000 cells and demonstrated higher precipitation efficiency than conventional ChIP.[200, 201] AutoChIP's multi-layered and valve-actuated ring structures controlled sample loading, bead washing, and elution of DNA. By multiplexing AutoChIP structures they obtained a high throughput, automated microfluidic device for ChIP (HTChIP) capable of processing 10,000-cell equivalent chromatin samples in each parallel structure, running 14 ChIP experiments and 2 controls simultaneously.[202] Though AutoChIP and HTChIP demonstrate

automated enrichment and washing, the fixed ring structure volumes limited their applications to a determinate sample size. Moreover, HTChIP did not start directly with cells to automate cell lysis or chromatin fragmentation. This pre-processing and defined sample volume may limit the applicability for some clinical applications, but the work represents a pioneering initial approach to microfluidic ChIP.

The Lu lab has also investigated epigenomic assays for small cell populations by exploiting microfluidic chamber structures. Using a valve-actuated microfluidic chamber to control magnetic bead packing, cell lysate loading, and captured DNA elution, they developed microfluidic oscillatory washing–based ChIP-seq (MOWChIP-seq) to capture targeted DNA from 100-cell chromatin equivalents for sequencing in the context of discovering new enhancer regions.[203] Further integration of sonication and immunoprecipitation enabled on-chip shearing of chromatin in addition to DNA capture.[204] They also fabricated multiple microfluidic beds on one chip to carry out ChIP targeting two marks in parallel.[205] Additionally, by immobilizing antibodies directly to the channel surface for flow-based target capture, they developed SurfaceChIP-seq to investigate histone marks in the mouse prefrontal cortex and cerebellum.[206] These strategies further automated the ChIP workflow; but MOWChIP-seq's fixed chamber structure again limited this microfluidic epigenetic platform's capability in processing flexible sample sizes (as any changes in sample size may require labor-intensive re-optimization of immunocapture conditions). Nonetheless, these devices have improved throughput and plexity while reducing input requirements for microfluidic ChIP.

Besides continuous flow microfluidics, the Weitz lab and colleagues have applied droplet microfluidics to achieve automated single-cell ChIP-seq (Drop-ChIP) that can handle samples with indeterminate sizes and process thousands of cells individually within minutes.[207] Starting with

single cell encapsulation followed by simultaneous introduction of chromatin fragmentation and DNA immunocapture reagents to cell-containing droplets, Drop-ChIP used DNA barcoding to uniquely label chromatin from different cells. Therefore, it was able to analyze a mixture of three different cell types at single-cell resolution using deconvoluted chromatin state mapping, leading to cell subpopulation elucidation.[207] The specificity and information content accuracy were high, as ~50% of reads could be aligned to known positive sites, and coverage of aggregated reads from 50 cells was comparable to conventional profiles. On the other hand, the coverage per cell was sparse, comprising on the order of 1000 unique reads. Additionally, this device only automated cell lysis, chromatin digestion, and indexing with DNA barcodes; the protocol manually completed immunoprecipitation and ChIP DNA extraction off the device. Furthermore, potential repetitions or other errors in DNA barcoding could confound the final results.

The Bailey lab recently described a strategy to automate chromatin fragmentation for MNase-seq utilizing droplet microfluidics to process cell samples directly, and their approach yielded high quality nucleosome mapping profiles.[208] In this technique, cells were directly encapsulated in microdroplets at a junction that simultaneously introduced a combined cell lysis and enzymatic chromatin digestion reagent flow. On-chip processing was mediated by delay channels to define the reaction time for chromatin processing, terminated by a final injection of MNase quenching buffer (containing EDTA as a chelating agent to inhibit the Ca^{2+}-dependent nuclease). This microfluidic device showed the capability to tolerate different sample sizes, making it amenable toward future clinical deployment with variable sample quantities; however, the approach has not yet demonstrated single cell resolution. Promisingly, these and related advances in droplet microfluidic technologies are being translated into mass-manufacturable

thermoplastic materials, bringing them closer to at-scale manufacturing and fulfilling their promise for clinical distribution and implementation.[209, 210]

Despite their respective limitations, these promising examples show the potential of microfluidics to facilitate fully automated, low-input (and single-cell) epigenomic studies in a clinical setting. When reliable and rapid analysis of patients' epigenomes becomes clinically routine, the enhanced understanding available will offer insights on the unique combination of epigenomic marks that play crucial roles in disease pathways in individual patients. Thus, these technologies will guide diagnostic, therapeutic, and prognostic decisions, furthering the advance of precision medicine.

DROPLET MICROFLUIDICS: EXPLORING THE CAPABILITIES OF SEGMENTED FLOW BIOASSAYS

Droplet microfluidics provide an exciting opportunity in automated analysis of DNA-protein interactions using ChIP. Following seminal works from Quake and Ismagilov, droplet (or segmented flow) techniques emerged as a promising method for controlling networks of small volume samples (fL to nL per droplet) for bioassay and materials applications.[211-213] Segmented flow systems possess a number of advantageous differences compared to more traditional, laminar flow-based microfluidics. By compartmentalizing each sample (the dispersed phase) in an immiscible, typically fluorinated oil (the continuous phase), unique samples remain discretized during analysis with minimal to no material transfer through the oil phase between droplets or with the microdevice walls. Therefore, droplet microfluidic devices can reproducibly and rapidly handle large numbers of heterogeneous sample volumes with minimal material loss or contamination.[214-217] Fluorosurfactant addition further promotes droplet stability by organizing at the dispersed

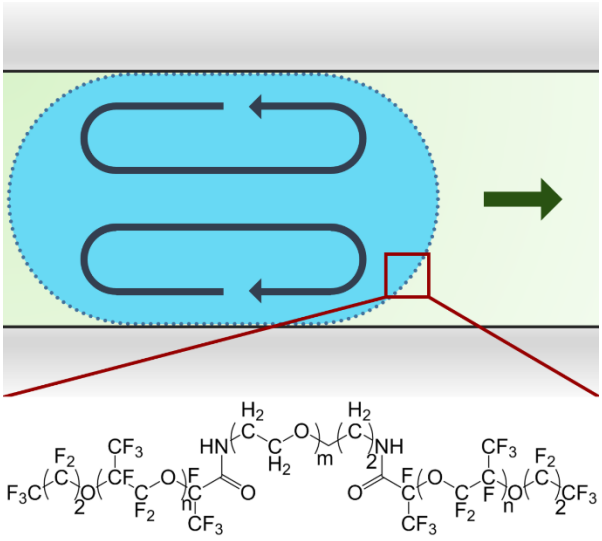

Figure I.4. Simple droplet dynamics during flow in an enclosed microchannel. Major mixing vortices within the droplet (dark blue arrows) are oriented counter to the flow direction (green arrow) where in contact with channel walls (gray). The fluorinated oil (light green)-aqueous droplet interface (dotted line) is stabilized by fluorosurfactants (example shown in inset, $10 \leq n \leq 60$ for perfluorinated polyether units, $4 \leq m \leq 10$ for polyethylene glycol units). Figure components are not to scale.

phase-continuous phase interface and decreasing surface tension (Fig. I.4).[218, 219] However stable, individual droplet volumes still remain accessible for a range of unit operations to enable useful chemistry and biochemistry, as will be discussed below. Moreover, the internally recirculating vortices present in a flowing, wall-bounded droplet promote extremely efficient mass and heat transfer, with complete mixing frequently achieved on the sub-second timescale.[212, 214, 215, 217] Finally, continuously flowing droplets are facilely scalable. Serial droplet processing reproducibly acts on each individual droplet volume, so scaling to larger samples only requires production and handling of more droplets. Droplet microfluidics therefore present an attractive option for developing a robust, automated, and dynamically scalable ChIP workflow.

A growing toolkit of unit operations enables a diversity of chemistry in segmented flow microfluidics, and these unit operations will be crucial to developing a droplet-based ChIP method. Droplet formation commonly takes the form of T-Junction (Fig. I.5a) or hydrodynamic flow

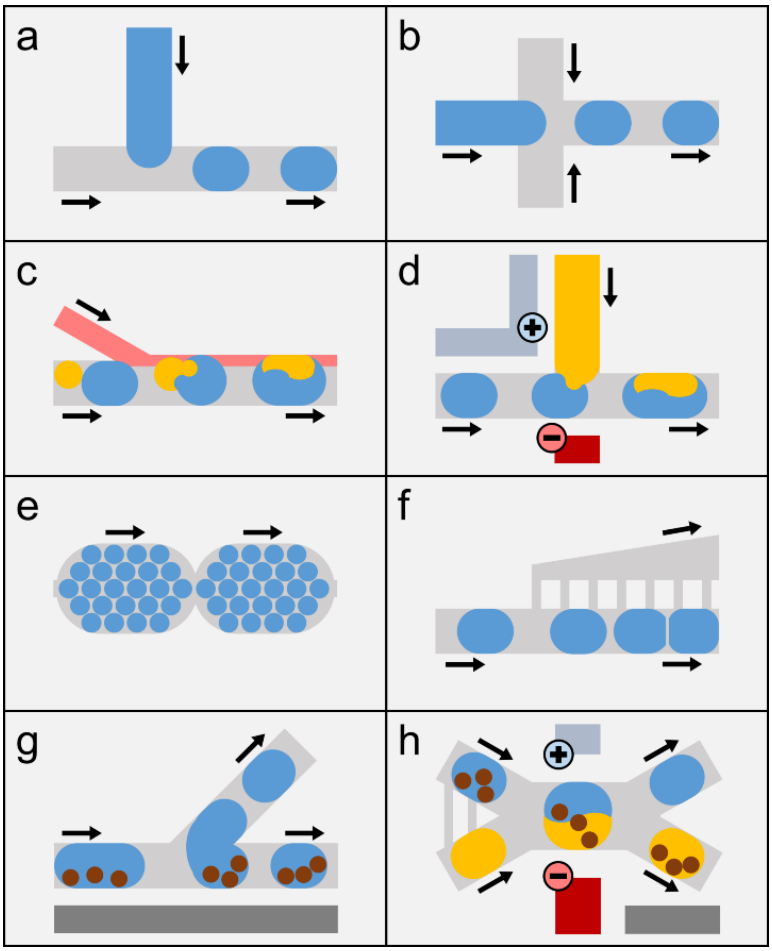

Figure I.5. Selected droplet unit operations. a) The T-junction forms droplets at the interface of two orthogonally directed, immiscible flows. b) The hydrodynamic flow focusing structure segments the dispersed phase with two symmetric and orthogonal continuous phase flows. c) Pairwise droplet fusion uses a continuous phase-miscible chemical destabilizing agent or other means to merge synchronized droplets. d) Direct injection forces reagent flow into passing droplets during temporary interface fusion under the influence of local electric field. e) Delay channels accommodate droplet populations in large-volume, continuously flowing chambers to mediate on-device reaction time. f) Specialized drain channel structures selectively extract the continuous phase to alter droplet packing. g) Droplet splitting at the channel bifurcation in the presence of a magnetic field gradient concentrates magnetic particles in one of the daughter droplets, and the other daughter droplet only contains decanted supernatant. h) The washing module fuses synchronized sample and washing buffer droplets using electric field, a magnetic field gradient collects magnetic particles in the washing buffer portion of the fused droplet, and fission at the channel bifurcation re-divides the volume back into constituent parts. For all panels, light blue and dark yellow objects represent dispersed phase elements, light gray objects represent continuous phase elements, light red objects represent chemically-modified continuous phase elements, blue-grey and dark red objects represent electric field elements (example polarities indicated), brown circles represent magnetic particles, dark gray objects represent magnetic field elements, and black arrows indicate flow direction (for adjacent elements). Figure components are not to scale.

focusing (Fig. I.5b) configurations capable of production at up to kHz frequencies for highly monodisperse droplets.[211, 212, 216, 217, 220] Changing channel geometry and the relative flow rates of the continuous and dispersed phases alters droplet size, spacing, and generation frequency across predictable trends.[220, 221] Adaptations of these fundamental structures have increased production beyond tens of kHz,[222] have integrated sophisticated inertial strategies for individual cell and particle encapsulation,[223] and have enabled on demand combinatorial production.[224-226] Further, tailoring channel surface chemistry selects which fluid acts as the continuous phase and even enables production of multilamellar emulsion structures.[217, 227]

Encapsulating samples with reagents may be sufficient for simple processing, but adding additional chemical and physical controls on-chip creates opportunities for more sophisticated assays. After formation, desired droplets can be synchronized and merged to mediate the next step in a chemical workflow (Fig. I.5c). By including a mismatch in alternating droplet sizes (smaller droplets move faster until being trapped behind larger, wall-bounded neighbors) or by using ladder-like networks of pressure-equalizing channels and other structures, droplets can be brought together.[228-233] Then, introducing a chemical destabilizer (like a coalescence-initiating, oil-miscible co-flow) can fuse contacting droplets as a means of reagent introduction.[233] Alternately, electric fields induce a local dielectric force on polarizable droplet components, thus providing sufficient disruption to droplet stability to promote fusion of adjacent volumes.[228, 229, 232, 234] These electric fields can be delivered on-chip via conventional electrode materials, or a simple alternative approach charges microchannels filled with sufficiently conductive electrolyte solution, reducing the cost and difficulty of fabricating devices with integrated electric fields.[235] Although this class of reagent addition operation efficiently isolates heterogeneous sample droplet volumes, it can be

technically challenging to achieve high fidelity synchronization to prevent a fraction of droplets from experiencing inaccurate processing.[228, 232, 234]

Direct injection strategies take a different approach to introducing reagents into pre-formed droplet volumes. Instead of fusion between paired droplets, direct injection occurs at the interface between the droplet flow and a dispersed phase-miscible continuous reagent stream. As each droplet passes the junction with the reagent stream, reagent flow enters the droplet, increasing its total volume and correspondingly altering its composition (Fig. I.5d).[213, 236, 237] Changing the flow rate of the reagent proportionally adjusts volume injected. Like droplet fusion, this technique also commonly relies on destabilizing forces (most commonly electric field) to promote temporary droplet-reagent stream fusion, and continuously moving droplets separate from the reagent stream after flow pushes them past the interface. In contrast to pairwise droplet synchronization and fusion, direct injection represents an arguably simpler system: the droplet sample is brought past a stationary reagent flow instead of coordinating two independently moving species. Simplicity of function notwithstanding, this technique has two key limitations. First, flow instabilities during routine operation can lead to aberrant formation of independent reagent droplets when reagent fluid is ejected into the main channel out of phase with the presence of passing droplets. Under these circumstances adjacent droplets may consequently receive non-standard injection volumes. The "picoinjector" represents a direct injection variant addressing this problem.[237] By including a tapered nozzle feature, the picoinjector induces a stabilizing Laplace pressure from the tapered curvature of the reagent stream, and flow of reagents only occurred if both droplets and electric field were present. Practically, however, the picoinjector module may still experience aberrant and non-standard injections, if at reduced incidence compared to its predecessors.[238] Second, direct injection necessitates that all sample droplets temporarily merge with the same reagent stream.

While injections into passing droplets ensure that reagent volume is flowing continuously toward the droplet train, merging leads to diffusive and convective forces at the interface. Therefore, net flow drives reagent fluid into the droplet, but these mixing forces simultaneously drive some portion of the original droplet into the reagent stream. Later droplets may thus be injected with material from previous droplets. For heterogeneous droplet processing under stringent conditions, conventional approaches to direct injection may yield unaccepted cross-contamination.[236] Despite these limitations, direct injection strategies provide a popular and easy to implement strategy for reagent addition. See Chapters II and III for additional discussion.

After establishing conditions for in-droplet chemistry, chemical reactions need sufficient time to occur. Long term incubations (hours to days) are routinely managed by collecting droplets and reinjecting them for additional on-device processing when desired, but even generally successful strategies result in a fraction of lost or mishandled droplets.[229] Shorter term incubations (seconds to minutes) are most frequently mediated by relatively large cross-sectional area "delay channels" (Fig. I.5e).[239] These features are capable of dynamic storage for large droplet volumes while minimizing the corresponding increases in hydraulic resistance which would result from solely increasing channel length to accommodate more droplets. Incubation time is proportional to the number of droplets packed in a given feature and inversely proportional to the droplet processing frequency, so changing droplet conditions correspondingly alters incubation performance. In particular, a range of approaches have been developed to adjust droplet packing by selective extraction of the continuous phase (mediated by droplet-retaining micropillar structures, Fig. I.5f).[239-241] Continuous phase extraction includes an additional benefit: densely packed droplets can be uniformly respaced with fresh continuous phase after incubation for robust downstream processing. Unfortunately, these extraction modules function best under narrow

ranges of droplet flow conditions and otherwise yield droplet breakup and sample loss. Moreover, tools for controlling and analytically characterizing droplet-to-droplet incubation time reproducibility (directly affecting reaction yield and efficiency) have been limited to poor time resolution, potentially obscuring significant physical phenomena.[239, 240] Certainly for many applications, these methods prove sufficient for mediating on-device reactions, but improvements to these technologies will improve in-droplet reaction precision and fundamental understanding of multiphase flows. See Chapter IV for additional discussion.

Introducing on-chip magnetic fields creates another opportunity for droplet unit operations: deterministic material control orthogonal to flow forces.[242, 243] Capitalizing on a wealth of available surface chemistries, magnetic particles capture and selectively immobilize sample material for workflows involving solid phase extraction, immunoassays, and others.[243-245] Buffer and reagent exchange around sample-bound particles enables washing operations (to remove off-target components) as well as sophisticated multistep chemistries. In the context of droplet microfluidics, the most common magnetic particle manipulation strategy involves flowing a droplet train toward a channel bifurcation to split each droplet into two daughter droplets (Fig. I.5g). In the presence of a directional magnetic field gradient, magnetic particles concentrate in one droplet hemisphere prior to the division, and, thus, they segregate into only the daughter droplet closest to the magnet during fission. Under ideal conditions the other daughter droplet contains only unbound supernatant material, subject to further processing and analysis or discarded as waste.[246] Innovations to this core approach have tailored droplet splitting and magnetic capture through asymmetric fission regimes capable of more efficiently decanting supernatant,[247] and some even show dynamic selection of splitting fraction based on flow conditions, not solely bifurcation geometry.[248, 249] Unfortunately, these technologies operate at relatively poor throughput (0.5-30

Hz processing frequency) and typically leave 10% or more supernatant remaining. Chiefly, this limitation is due to relative magnetic force on particles (often with low, variable magnetic content per particle) compared to opposing hydrodynamic forces generated by internal convective flows and turbulence during fission.[242] Combinations of these magnetic operations have been demonstrated, coupled to washing buffer direct injection for replenishing droplet volume, but errors propagate as washing effectiveness per operation exponentially decreases.[250] Nonetheless, this technique has been successfully implemented for several simple bioassays, and even droplet splitting and selective droplet extraction without magnetic enrichment provide valuable sampling methods.[243, 244, 250-252] See Chapters II, III, and V for additional discussion.

Combining the concepts of pairwise droplet fusion and magnetically biased droplet fission, an additional droplet-mediated particle washing approach has been described (Fig. I.5h).[230] In this technique, droplets with magnetic particle-bound sample (and free contaminants) are synchronized with a train of washing buffer droplets. At the channel region where the two droplet populations come into contact, local electric field fuses paired droplets while a strong magnetic field gradient deflects the beads toward the washing buffer side. Immediately downstream, a channel bifurcation re-divides the two original droplets from each other. Effectively, this module transfers particles from the original droplet to the washing buffer droplet, and washing efficiency depends on mixing and nonspecific material transfer during the merger between sample and buffer droplets. While technologically innovative (and, perhaps, representing the first truly integrated in-droplet particle washing unit operation), this technique has not been widely implemented. Besides the practical challenges in robust droplet synchronization and fusion, the demands of magnetophoretically migrating particles between the paired droplets during brief fusion restrict throughput to only a few volumes per second.[230] See Chapter V for additional discussion.

This work does not attempt to include a comprehensive description of every droplet technology or application, and several excellent reviews include additional techniques for droplet sorting,[253] ferrofluid applications,[254] acoustic manipulations,[255] and more.[217, 243] Instead, this discussion seeks to offer a practical perspective on the droplet toolkit immediately relevant to bioassay prototyping. In summary, a number of basic unit operations have been established to varying degrees of maturity for integration into sophisticated biochemical workflows, and additional innovations may solve current limitations hindering the practical adoption of these techniques.

DROPLET MICROFLUIDIC-MEDIATED ChIP: TECHNOLOGICAL CHALLENGES

Ultimately, conventional ChIP can be subdivided into a set of unit operations which must be achieved in a microdroplet format for assay translation. At a simplified level, sample introduction represents droplet formation, potentially compartmentalizing a single cell per droplet. Reagents for cell lysis, enzymatic chromatin digestion, digestion quenching, and antibody-bead loading, as well as washing buffers, must be added to the droplet reaction volume at appropriate times through methods like pairwise fusion or direct injection. Reactions progress via incubation in delay channel structures or through off-device incubation and later reinjection onto the next module. Immunoprecipitation and washing for selective target enrichment could be mediated by any of the existing magnetic droplet manipulation modes. This initial outline does, however, ignore many of the technological limitations for droplets described above as well as certain practical considerations in effective droplet bioassay development.

The principle impediment to the combination of these components for an integrated, automated ChIP-in-droplets platform (as described above) originates in the number of operations

required. Each reagent addition step during ChIP processing represents an additional geometrical, electrical, and flow component on device, yielding a complicated network of mutually perturbing features and fluid flows.[250, 256] Isolating these operations on simplified, separate devices multiplies the number of droplet transfers between devices, leading to sample loss at each step.[229] Failure to do so, however, increases droplet-to-droplet handling variance as errors and flow instabilities propagate among serial operations, and complicated, extended flow channels may require impractically high pressures to drive flow.[256] These difficulties are further compounded by the composition of many key ChIP buffers. Detergents play vital roles in cell lysis for making chromatin accessible, and they help to decrease non-specific retention during immunoprecipitation and washing.[257-263] In segmented flow, however, detergents decrease droplet stability, generating opportunities for sample loss and droplet breakup (which constitutes an example of unit operation-disrupting flow perturbation). Further within the context of immunoprecipitation in droplets, uniformly introducing dense, iron oxide-rich magnetic particles into microscale flow is opposed by gravity-driven sedimentation.[264] Even after particle addition, stringent washing of particles for selective enrichment represents perhaps the greatest challenge. ChIP protocols commonly exchange particles through four buffers to deliver a gradient of ionic strength and detergent conditions. Decanting 99% of droplet supernatant for high purity washing requires several droplet splitting and washing buffer additions per buffer, and poorer washing decreases ChIP enrichment. Therefore, this initial strategy for ChIP washing might necessitate a few tens of droplet operations (serial fission and direct injection). Such an approach would likely be impossible and would certainly exclude any resulting technology from use by non-experts. Overall, these considerations highlight the difficulty of adapting complex bioassays into a miniaturized, high throughput droplet format and suggest areas in need of innovation.

Promisingly, the Bailey Lab's droplet-based chromatin preparation platform described earlier in this chapter not only enabled MNAse-seq but also provided a starting point to enable cell processing through chromatin digestion in droplets. .[208] It ultimately formed the basis of the first module for performing ChIP using droplet microfluidics, although it did not integrate on-device immunoprecipitation or washing for affinity purification of targeted chromatin species. These capabilities (immunoprecipitation and washing) thus demand technical innovations in droplet processing before the realization of droplet-based ChIP. In this work, I will describe the development of technologies for supporting this microfluidic epigenetic assay and its final demonstration after component integration. See Chapter VI for additional discussion.

CONCLUSIONS

Over the years, increased efforts have aimed to elucidate the epigenomic mechanisms of pathogenesis to provide insights for diagnosis and treatment. While many assays have profiled ncRNA expression, DNA methylation, histone modifications, and other chromatin-regulating molecules, ongoing efforts must focus on translating these basic research techniques to clinical settings. Due to current drawbacks, ChIP-seq in particular struggles to assess biopsy samples containing small cell numbers. This limits its application in routine analysis for prognosis, diagnosis, and treatment. While microfluidics has provided improved automation and reduced reagent consumption, current microfluidic ChIP approaches still suffer from sample size restriction due to determinate microfluidic devices, complicated microfluidic operation, and lack of automation of the entire ChIP process from cell input to analytical readout. As a promising starting point for the development of an automated ChIP system meeting many of these needs, the droplet microfluidic techniques outlined here demonstrate capabilities in sample compartmentalization,

reagent addition, and selective material concentration and extraction. Nonetheless, additional innovations will be necessary to fully adapt the protocol, particularly in the context of in-droplet affinity-based purification. Encouraged by the potential of initial studies, the application of microfluidics tools to clinical epigenetic profiling promises to fundamentally transform the field of precision medicine.

ACKNOWLEDGEMENTS

We gratefully acknowledge financial support from the National Institutes of Health (NIH CA191186), the Mayo-Illinois Alliance for Technology Based Healthcare, the Mayo Clinic Center for Individualized Medicine, and the NIH-sponsored Midwest Cancer Nanotechnology Training Center (CA154015). S.R.D. was supported by a National Science Foundation Graduate Research Fellowship.

REFERENCES

1. L. R. Cardon and T. Harris, *Hum. Mol. Gen.*, 2016, **25**, R166-R172.
2. A. A. Friedman, A. Letai, D. E. Fisher and K. T. Flaherty, *Nat. Rev. Cancer*, 2015, **15**, 747-756.
3. F. S. Collins and H. Varmus *N. Engl. J. Med.*, 2015, **372**, 793-795.
4. R. Bhargava and A. Madabhushi, *Annu. Rev. Biomed. Eng.*, 2016, **18**, 387-412.
5. E. H. Rubin, J. D. Allen, J. A. Nowak and S. E. Bates, *Clin. Cancer Res.*, 2014, **20**, 1419-1427.
6. L. Dong, W. Wang, A. Li, R. Kansal, Y. Chen, H. Chen and X. Li, *Curr. Genomics*, 2015, **16**, 253-263.
7. S. Roychowdhury and A. M. Chinnaiyan, *J. Clin. Oncol.*, 2013, **31**, 1866-1873.
8. Y. Zhang, H. C. Su and M. J. Lenardo, *Nat. Immunol.*, 2015, **16**, 1001-1004.

9. S. A. Dugger, A. Platt and D. B. Goldstein, *Nat. Rev. Drug Discov.*, 2018, **17**, 183-196.

10. M. D. M. Leiserson, F. Vandin, H.-T. Wu, J. R. Dobson, J. V. Eldridge, J. L. Thomas, A. Papoutsaki, Y. Kim, B. Niu, M. McLellan, M. S. Lawrence, A. Gonzalez-Perez, D. Tamborero, Y. Cheng, G. A. Ryslik, N. Lopez-Bigas, G. Getz, L. Ding and B. J. Raphael, *Nat. Genet.*, 2015, **47**, 106-114.

11. Y. Yuan, E. M. Van Allen, L. Omberg, N. Wagle, A. Amin-Mansour, A. Sokolov, L. A. Byers, Y. Xu, K. R. Hess, L. Diao, L. Han, X. Huang, M. S. Lawrence, J. N. Weinstein, J. M. Stuart, G. B. Mills, L. A. Garraway, A. A. Margolin, G. Getz and H. Liang, *Nat. Biotechnol.*, 2014, **32**, 644-652.

12. M. S. Lawrence, P. Stojanov, C. H. Mermel, J. T. Robinson, L. A. Garraway, T. R. Golub, M. Meyerson, S. B. Gabriel, E. S. Lander and G. Getz, *Nature*, 2014, **505**, 495-501.

13. E. A. Ashley, A. J. Butte, M. T. Wheeler, R. Chen, T. E. Klein, F. E. Dewey, J. T. Dudley, K. E. Ormond, A. Pavlovic, A. A. Morgan, D. Pushkarev, N. F. Neff, L. Hudgins, L. Gong, L. M. Hodges, D. S. Berlin, C. F. Thorn, K. Sangkuhl, J. M. Hebert, M. Woon, H. Sagreiya, R. Whaley, J. W. Knowles, M. F. Chou, J. V. Thakuria, A. M. Rosenbaum, A. W. Zaranek, G. M. Church, H. T. Greely, S. R. Quake and R. B. Altman, *Lancet*, 2010, **375**, 1525-1535.

14. E. A. Ashley, *Nat. Rev. Genet.*, 2016, **17**, 507-522.

15. M. Claussnitzer, S. N. Dankel, K.-H. Kim, G. Quon, W. Meuleman, C. Haugen, V. Glunk, I. S. Sousa, J. L. Beaudry, V. Puviindran, N. A. Abdennur, J. Liu, P.-A. Svensson, Y.-H. Hsu, D. J. Drucker, G. Mellgren, C.-C. Hui, H. Hauner and M. Kellis, *N. Engl. J. Med.*, 2015, **373**, 895-907.

16. M. Arnedos, C. Vicier, S. Loi, C. Lefebvre, S. Michiels, H. Bonnefoi and F. Andre, *Nat. Rev. Clin. Oncol.*, 2015, **12**, 693-704.

17. K. Ford, D. McDonald and P. Mali, *J. Mol. Biol.*, 2018, DOI: 10.1016/j.jmb.2018.06.034.

18. Y. B. Khotskaya, G. B. Mills and K. R. M. Shaw, *ANNU. REV. MED.*, 2017, **68**, 113-125.

19. D. Tripathy, K. Harnden, K. Blackwell and M. Robson, *BMC Medicine*, 2014, **12**, 140.

20. M. K. Skinner, M. Manikkam, R. Tracey, C. Guerrero-Bosagna, M. Haque and E. E. Nilsson, *BMC Medicine*, 2013, **11**, 228.

21. L. Roos, J. van Dongen, C. G. Bell, A. Burri, P. Deloukas, D. I. Boomsma, T. D. Spector and J. T. Bell, *Clin. Epigenetics*, 2016, **8**, 7.

22. Z. Xiang, Y. Yang, C. Chang and Q. Lu, *J. Autoimmun.*, 2017, **83**, 43-50.

23. E. E. Nilsson and M. K. Skinner, *Biol. Reprod.*, 2015, **93**, 145, 141-148.

24. M. K. Skinner, *BMC Medicine*, 2014, **12**, 153.

25. C. Plass, S. M. Pfister, A. M. Lindroth, O. Bogatyrova, R. Claus and P. Lichter, *Nat. Rev. Genet.*, 2013, **14**, 765-780.

26. P. Polak, R. Karlic, A. Koren, R. Thurman, R. Sandstrom, M. S. Lawrence, A. Reynolds, E. Rynes, K. Vlahovicek, J. A. Stamatoyannopoulos and S. R. Sunyaev, *Nature*, 2015, **518**, 360-364.

27. G. Almouzni, L. Altucci, B. Amati, N. Ashley, D. Baulcombe, N. Beaujean, C. Bock, E. Bongcam-Rudloff, J. Bousquet, S. Braun, B. B.-d. Paillerets, M. Bussemakers, L. Clarke, A. Conesa, X. Estivill, A. Fazeli, N. Grgurević, I. Gut, B. T. Heijmans, S. Hermouet, J. Houwing–Duistermaat, I. Iacobucci, J. Ilaš, R. Kandimalla, S. Krauss-Etschmann, P. Lasko, S. Lehmann, A. Lindroth, G. Majdič, E. Marcotte, G. Martinelli, N. Martinet, E. Meyer, C. Miceli, K. Mills, M. Moreno-Villanueva, G. Morvan, D. Nickel, B. Niesler, M. Nowacki, J. Nowak, S. Ossowski, M. Pelizzola, R. Pochet, U. Potočnik, M. Radwanska, J. Raes, M. Rattray, M. D. Robinson, B. Roelen, S. Sauer, D. Schinzer, E. Slagboom, T. Spector, H. G. Stunnenberg, E. Tiligada, M.-E. Torres-Padilla, R. Tsonaka, A. V. Soom, M. Vidaković and M. Widschwendter, *BMC Genomics*, 2014, **15**, 487.

28. A. D. Goldberg, C. D. Allis and E. Bernstein, *Cell*, 2007, **128**, 635-638.

29. M. K. Skinner, *Genome Biol. Evol.*, 2015, **7**, 1296-1302.

30. T. Chen and S. Y. R. Dent, *Nat. Rev. Genet.*, 2014, **15**, 93-106.

31. D. Filipescu, S. Müller and G. Almouzni, *Annu. Rev. Cell Dev. Biol.*, 2014, **30**, 615-646.

32. Y. Atlasi and H. G. Stunnenberg, *Nat. Rev. Genet.*, 2017, **18**, 643-658.

33. A. Corpet and G. Almouzni, *Trends Cell Biol.*, 2009, **19**, 29-41.

34. M. K. Skinner, *Nat. Rev. Endocrinol.*, 2016, **12**, 68-70.

35. E. Heard and Robert A. Martienssen, *Cell*, 2014, **157**, 95-109.

36. K. Takahashi and S. Yamanaka, *Cell*, 2006, **126**, 663-676.

37. G. Wang, R. Weng, Y. Lan, X. Guo, Q. Liu, X. Liu, C. Lu and J. Kang, *Sci. Rep.*, 2017, **7**, 39527.

38. M. L. Suvà, N. Riggi and B. E. Bernstein, *Science*, 2013, **339**, 1567-1570.

39. A. Kinnaird, S. Zhao, K. E. Wellen and E. D. Michelakis, *Nat. Rev. Cancer*, 2016, **16**, 694-707.

40. K. Sarma and D. Reinberg, *Nat. Rev. Mol. Cell Biol.*, 2005, **6**, 139-149.

41. D. Holoch and D. Moazed, *Nat. Rev. Genet.*, 2015, **16**, 71-84.

42. J. Du, L. M. Johnson, S. E. Jacobsen and D. J. Patel, *Nat. Rev. Mol. Cell Biol.*, 2015, **16**, 519-532.

43. A. J. Bannister and T. Kouzarides, *Cell Res.*, 2011, **21**, 381-395.

44. C. D. Allis and T. Jenuwein, *Nat. Rev. Genet.*, 2016, **17**, 487-500.

45. A. C. Drohat and C. T. Coey, *Chem. Rev.*, 2016, **116**, 12711-12729.

46. P. Brazauskas and S. Kriaucionis, *Nat. Chem.*, 2014, **6**, 1031-1033.

47. L. I. Kroeze, B. A. van der Reijden and J. H. Jansen, *BBA-REV. CANCER*, 2015, **1855**, 144-154.

48. M. K. Skinner and C. Guerrero-Bosagna, *BMC Genomics*, 2014, **15**, 692.

49. V. G. Allfrey, R. Faulkner and A. E. Mirsky, *Proc. Natl. Acad. Sci. U. S. A.*, 1964, **51**, 786-794.

50. A. P. Feinberg, M. A. Koldobskiy and A. Gondor, *Nat. Rev. Genet.*, 2016, **17**, 284-299.

51. H. Huang, S. Lin, B. A. Garcia and Y. Zhao, *Chem. Rev.*, 2015, **115**, 2376-2418.

52. K. Katsushima and Y. Kondo, *Front Genet.*, 2014, **5**.

53. R. M. Graybill and R. C. Bailey, *Anal. Chem.*, 2016, **88**, 431-450.

54. L. Houri-Zeevi and O. Rechavi, *Trends Genet.*, 2017, **33**, 46-57.

55. E. A. Gibb, C. J. Brown and W. L. Lam, *MOL. CANCER*, 2011, **10**, 38.

56. S. Leone and R. Santoro, *FEBS Lett.*, 2016, **590**, 2342-2353.

57. J. Song and C. Yi, *ACS Chem. Biol.*, 2017, DOI: 10.1021/acschembio.6b00960.

58. Y. Zhang, X. Zhang, J. Shi, F. Tuorto, X. Li, Y. Liu, R. Liebers, L. Zhang, Y. Qu, J. Qian, M. Pahima, M. Yan, Z. Cao, X. Lei, Y. Cao, H. Peng, S. Liu, Y. Wang, H. Zheng, R. Woolsey, D. Quilici, Q. Zhai, L. Li, T. Zhou, W. Yan, F. Lyko, Q. Zhou, E. Duan and Q. Chen, *Nat. Cell Biol.*, 2018, **20**, 535-540.

59. B. Bartholomew, *Annu. Rev. Biochem.*, 2014, **83**, 671-696.

60. O. Bell, V. K. Tiwari, N. H. Thomä and D. Schübeler, *Nat. Rev. Genet.*, 2011, **12**, 554-564.

61. C. Jiang and B. F. Pugh, *Nat. Rev. Genet.*, 2009, **10**, 161-172.

62. K. Struhl and E. Segal, *Nat. Struct. Mol. Biol.*, 2013, **20**, 267-273.

63. F. Mueller-Planitz, H. Klinker and P. B. Becker, *Nat. Struct. Mol. Biol.*, 2013, **20**, 1026-1032.

64. X.-h. Shen, P. Qi and X. Du, *Mod. Pathol.*, 2015, **28**, 4-13.

65. C. C. Wong, Y. Qian and J. Yu, *Oncogene*, 2017, DOI: 10.1038/onc.2016.485, 1-16.

66. P. Chi, C. D. Allis and G. G. Wang, *Nat. Rev. Cancer*, 2010, **10**, 457-469.

67. M. Ehrlich, *Epigenomics*, 2009, **1**, 239-259.

68. S. B. Baylin, *Nat. Clin. Pract. Oncol.*, 2005, **2 Suppl 1**, S4-11.

69. C.-g. Miao, Y.-y. Yang, X. He and J. Li, *Cell. Signal.*, 2013, **25**, 875-882.

70. K. J. Falkenberg and R. W. Johnstone, *Nat. Rev. Drug Discov.*, 2014, **13**, 673-691.

71. A. Luoni and M. A. Riva, *Pharmacol. Ther.*, 2016, **167**, 13-27.

72. P. A. Jones, J. P. Issa and S. Baylin, *Nat. Rev. Genet.*, 2016, **17**, 630-641.

73. S. A. Ganai, S. Banday, Z. Farooq and M. Altaf, *Pharmacol. Ther.*, 2016, **166**, 106-122.

74. C. Peitzsch, M. Cojoc, L. Hein, I. Kurth, K. Mäbert, F. Trautmann, B. Klink, E. Schröck, M. P. Wirth, M. Krause, E. A. Stakhovsky, G. D. Telegeev, V. Novotny, M. Toma, M. Muders, G. B. Baretton, F. M. Frame, N. J. Maitland, M. Baumann and A. Dubrovska, *Cancer Res.*, 2016, **76**, 2637-2651.

75. J. S. K. Bell, J. D. Kagey, B. G. Barwick, B. Dwivedi, M. T. McCabe, J. Kowalski and P. M. Vertino, *Epigenetics*, 2016, **11**, 273-287.

76. M. Zampini, C. Tregnago, V. Bisio, L. Simula, G. Borella, E. Manara, C. Zanon, F. Zonta, V. Serafin, B. Accordi, S. Campello, B. Buldini, A. Pession, F. Locatelli, G. Basso and M. Pigazzi, *Leukemia*, 2018, **32**, 1124-1134.

77. R. Beekman, V. Chapaprieta, N. Russinol, R. Vilarrasa-Blasi, N. Verdaguer-Dot, J. H. A. Martens, M. Duran-Ferrer, M. Kulis, F. Serra, B. M. Javierre, S. W. Wingett, G. Clot, A. C. Queiros, G. Castellano, J. Blanc, M. Gut, A. Merkel, S. Heath, A. Vlasova, S. Ullrich, E. Palumbo, A. Enjuanes, D. Martin-Garcia, S. Bea, M. Pinyol, M. Aymerich, R. Royo, M. Puiggros, D. Torrents, A. Datta, E. Lowy, M. Kostadima, M. Roller, L. Clarke, P. Flicek, X. Agirre, F. Prosper, T. Baumann, J. Delgado, A. Lopez-Guillermo, P. Fraser, M. L. Yaspo, R. Guigo, R. Siebert, M. A. Marti-Renom, X. S. Puente, C. Lopez-Otin, I. Gut, H. G. Stunnenberg, E. Campo and J. I. Martin-Subero, *Nat. Med.*, 2018, **24**, 868-880.

78. F. Albrecht, M. List, C. Bock and T. Lengauer, *Nucleic Acids Res.*, 2016, **44**, W581-586.

79. S. H. Stricker, A. Koferle and S. Beck, *Nat. Rev. Genet.*, 2017, **18**, 51-66.

80. M. U. Kaikkonen, M. T. Lam and C. K. Glass, *Cardiovasc. Res.*, 2011, **90**, 430-440.

81. E. Machiela, A. Popkie and L. F. Sempere, *Personalized Epigenetics*, 2015, DOI: 10.1016/b978-0-12-420135-4.00004-8, 83-122.

82. Z. Wang, M. Gerstein and M. Snyder, *Nat. Rev. Genet.*, 2009, **10**, 57-63.

83. Y. Han, S. Gao, K. Muegge, W. Zhang and B. Zhou, *Bioinform. Biol. Insights*, 2015, **9**, 29-46.

84. A. Chu, G. Robertson, D. Brooks, A. J. Mungall, I. Birol, R. Coope, Y. Ma, S. Jones and M. A. Marra, *Nucleic Acids Res.*, 2016, **44**, e3.

85. H. Guo, N. T. Ingolia, J. S. Weissman and D. P. Bartel, *Nature*, 2010, **466**, 835-840.

86. C. Addo-Quaye, T. W. Eshoo, D. P. Bartel and M. J. Axtell, *Curr. Biol.*, 2008, **18**, 758-762.

87. L. J. Core, J. J. Waterfall and J. T. Lis, *Science*, 2008, **322**, 1845-1848.

88. C. G. Danko, S. L. Hyland, L. J. Core, A. L. Martins, C. T. Waters, H. W. Lee, V. G. Cheung, W. L. Kraus, J. T. Lis and A. Siepel, *Nat. Methods*, 2015, **12**, 433-438.

89. A. Verma, Y. Jiang, W. Du, L. Fairchild, A. Melnick and O. Elemento, *Genome Med.*, 2015, **7**, 110.

90. A. Yamada, P. Yu, W. Lin, Y. Okugawa, C. R. Boland and A. Goel, *Sci. Rep.*, 2018, **8**, 575.

91. R. Shapiro, R. E. Servis and M. Welcher, *J. Am. Chem. Soc.*, 1970, **92**, 422-424.

92. M. J. Ziller, K. D. Hansen, A. Meissner and M. J. Aryee, *Nat. Methods*, 2015, **12**, 230-232.

93. H. Hayatsu, Y. Wataya, K. Kai and S. Iida, *Biochemistry*, 1970, **9**, 2858-2865.

94. J. Shin, G. L. Ming and H. Song, *Nat. Neurosci.*, 2014, **17**, 1463-1475.

95. M. Frommer, L. E. McDonald, D. S. Millar, C. M. Collis, F. Watt, G. W. Grigg, P. L. Molloy and C. L. Paul, *Proc. Natl. Acad. Sci. U. S. A.*, 1992, **89**, 1827-1831.

96. A. Meissner, A. Gnirke, G. W. Bell, B. Ramsahoye, E. S. Lander and R. Jaenisch, *Nucleic Acids Res.*, 2005, **33**, 5868-5877.

97. H. Gu, Z. D. Smith, C. Bock, P. Boyle, A. Gnirke and A. Meissner, *Nat. Protoc.*, 2011, **6**, 468-481.

98. H. Yan, S. Tian, S. L. Slager, Z. Sun and T. Ordog, *Am. J. Epidemiol.*, 2016, **183**, 96-109.

99. N. Plongthongkum, D. H. Diep and K. Zhang, *Nat. Rev. Genet.*, 2014, **15**, 647-661.

100. S. Ito, L. Shen, Q. Dai, S. C. Wu, L. B. Collins, J. A. Swenberg, C. He and Y. Zhang, *Science*, 2011, **333**, 1300-1303.

101. M. Yu, G. C. Hon, K. E. Szulwach, C. X. Song, P. Jin, B. Ren and C. He, *Nat. Protoc.*, 2012, **7**, 2159-2170.

102. M. Yu, G. C. Hon, K. E. Szulwach, C. X. Song, L. Zhang, A. Kim, X. Li, Q. Dai, Y. Shen, B. Park, J. H. Min, P. Jin, B. Ren and C. He, *Cell*, 2012, **149**, 1368-1380.

103. M. J. Booth, M. R. Branco, G. Ficz, D. Oxley, F. Krueger, W. Reik and S. Balasubramanian, *Science*, 2012, **336**, 934-937.

104. M. J. Booth, T. W. Ost, D. Beraldi, N. M. Bell, M. R. Branco, W. Reik and S. Balasubramanian, *Nat. Protoc.*, 2013, **8**, 1841-1851.

105. S. Busche, X. Shao, M. Caron, T. Kwan, F. Allum, W. A. Cheung, B. Ge, S. Westfall, M. M. Simon, A. Barrett, J. T. Bell, M. I. McCarthy, P. Deloukas, M. Blanchette, G. Bourque, T. D. Spector, M. Lathrop, T. Pastinen and E. Grundberg, *Genome Biol.*, 2015, **16**, 290.

106. X. L. Yuan, N. Gao, Y. Xing, H. B. Zhang, A. L. Zhang, J. Liu, J. L. He, Y. Xu, W. M. Lin, Z. M. Chen, H. Zhang, Z. Zhang and J. Q. Li, *Sci. Rep.*, 2016, **6**, 22138.

107. M. Kulis, A. Merkel, S. Heath, A. C. Queiros, R. P. Schuyler, G. Castellano, R. Beekman, E. Raineri, A. Esteve, G. Clot, N. Verdaguer-Dot, M. Duran-Ferrer, N. Russinol, R. Vilarrasa-Blasi, S. Ecker, V. Pancaldi, D. Rico, L. Agueda, J. Blanc, D. Richardson, L. Clarke, A. Datta, M. Pascual, X. Agirre, F. Prosper, D. Alignani, B. Paiva, G. Caron, T. Fest, M. O. Muench, M. E. Fomin, S. T. Lee, J. L. Wiemels, A. Valencia, M. Gut, P. Flicek, H. G. Stunnenberg, R. Siebert, R. Kuppers, I. G. Gut, E. Campo and J. I. Martin-Subero, *Nat. Genet.*, 2015, **47**, 746-756.

108. P. Yu, L. Ji, K. J. Lee, M. Yu, C. He, S. Ambati, E. C. McKinney, C. Jackson, C. A. Baile, R. J. Schmitz and R. B. Meagher, *PloS One*, 2016, **11**, e0154949.

109. C. J. Mariani, J. Madzo, E. L. Moen, A. Yesilkanal and L. A. Godley, *Cancers*, 2013, **5**, 786-814.

110. A. Zhubi, Y. Chen, E. Dong, E. H. Cook, A. Guidotti and D. R. Grayson, *Transl. Psychiatry*, 2014, **4**, e349.

111. X. Li, Y. Liu, T. Salz, K. D. Hansen and A. Feinberg, *Genome Res.*, 2016, **26**, 1730-1741.

112. Y. Obata, Y. Furusawa and K. Hase, *Immunol. Cell Biol.*, 2015, **93**, 226-232.

113. M. Weber, J. J. Davies, D. Wittig, E. J. Oakeley, M. Haase, W. L. Lam and D. Schubeler, *Nat. Genet.*, 2005, **37**, 853-862.

114. T. A. Down, V. K. Rakyan, D. J. Turner, P. Flicek, H. Li, E. Kulesha, S. Graf, N. Johnson, J. Herrero, E. M. Tomazou, N. P. Thorne, L. Backdahl, M. Herberth, K. L. Howe, D. K. Jackson, M. M. Miretti, J. C. Marioni, E. Birney, T. J. Hubbard, R. Durbin, S. Tavare and S. Beck, *Nat. Biotechnol.*, 2008, **26**, 779-785.

115. G. Ficz, M. R. Branco, S. Seisenberger, F. Santos, F. Krueger, T. A. Hore, C. J. Marques, S. Andrews and W. Reik, *Nature*, 2011, **473**, 398-402.

116. E. A. Raiber, D. Beraldi, G. Ficz, H. E. Burgess, M. R. Branco, P. Murat, D. Oxley, M. J. Booth, W. Reik and S. Balasubramanian, *Genome Biol.*, 2012, **13**, R69.

117. L. Shen, H. Wu, D. Diep, S. Yamaguchi, A. C. D'Alessio, H. L. Fung, K. Zhang and Y. Zhang, *Cell*, 2013, **153**, 692-706.

118. D. Serre, B. H. Lee and A. H. Ting, *Nucleic Acids Res.*, 2010, **38**, 391-399.

119. S. Kangaspeska, B. Stride, R. Metivier, M. Polycarpou-Schwarz, D. Ibberson, R. P. Carmouche, V. Benes, F. Gannon and G. Reid, *Nature*, 2008, **452**, 112-115.

120. X. Xing, B. Zhang, D. Li and T. Wang, *Methods Mol. Biol.*, 2018, **1708**, 209-246.

121. K. A. Aberg, R. F. Chan, L. Xie, A. A. Shabalin and E. van den Oord, *Methods Mol. Biol.*, 2018, **1708**, 171-189.

122. S. N. Kamdar, L. T. Ho, K. J. Kron, R. Isserlin, T. van der Kwast, A. R. Zlotta, N. E. Fleshner, G. Bader and B. Bapat, *Clin. Epigenetics*, 2016, **8**, 32.

123. C. M. Greco, P. Kunderfranco, M. Rubino, V. Larcher, P. Carullo, A. Anselmo, K. Kurz, T. Carell, A. Angius, M. V. Latronico, R. Papait and G. Condorelli, *Nat. Commun.*, 2016, **7**, 12418.

124. Y. Li, K. J. Hamilton, T. Wang, L. A. Coons, W. N. Jefferson, R. Li, Y. Wang, S. A. Grimm, J. T. Ramsey, L. Liu, K. E. Gerrish, C. J. Williams, P. A. Wade and K. S. Korach, *Proc. Natl. Acad. Sci. U. S. A.*, 2018, **115**, E4189-E4198.

125. D. S. Johnson, A. Mortazavi, R. M. Myers and B. Wold, *Science*, 2007, **316**, 1497-1502.

126. G. Robertson, M. Hirst, M. Bainbridge, M. Bilenky, Y. Zhao, T. Zeng, G. Euskirchen, B. Bernier, R. Varhol, A. Delaney, N. Thiessen, O. L. Griffith, A. He, M. Marra, M. Snyder and S. Jones, *Nat. Methods*, 2007, **4**, 651-657.

127. A. Barski, S. Cuddapah, K. Cui, T. Y. Roh, D. E. Schones, Z. Wang, G. Wei, I. Chepelev and K. Zhao, *Cell*, 2007, **129**, 823-837.

128. D. A. Orlando, M. W. Chen, V. E. Brown, S. Solanki, Y. J. Choi, E. R. Olson, C. C. Fritz, J. E. Bradner and M. G. Guenther, *Cell Rep.*, 2014, **9**, 1163-1170.

129. H. S. Rhee and B. F. Pugh, *Cell*, 2011, **147**, 1408-1419.

130. G. E. Zentner, S. Kasinathan, B. Xin, R. Rohs and S. Henikoff, *Nat. Commun.*, 2015, **6**, 8733.

131. P. J. Skene and S. Henikoff, *eLife*, 2017, **6**.

132. C. Schmidl, A. F. Rendeiro, N. C. Sheffield and C. Bock, *Nat. Methods*, 2015, **12**, 963-965.

133. Y. Kitagawa, N. Ohkura, Y. Kidani, A. Vandenbon, K. Hirota, R. Kawakami, K. Yasuda, D. Motooka, S. Nakamura, M. Kondo, I. Taniuchi, T. Kohwi-Shigematsu and S. Sakaguchi, *Nat. Immunol.*, 2016, DOI: 10.1038/ni.3646.

134. R. Mathur, B. H. Alver, A. K. San Roman, B. G. Wilson, X. Wang, A. T. Agoston, P. J. Park, R. A. Shivdasani and C. W. Roberts, *Nat. Genet.*, 2016, DOI: 10.1038/ng.3744.

135. C. Wang, J. E. Lee, B. Lai, T. S. Macfarlan, S. Xu, L. Zhuang, C. Liu, W. Peng and K. Ge, *Proc. Natl. Acad. Sci. U. S. A.*, 2016, **113**, 11871-11876.

136. M. Imbeault, P. Y. Helleboid and D. Trono, *Nature*, 2017, **543**, 550-554.

137. R. Noberini, G. Sigismondo and T. Bonaldi, *Epigenomics*, 2016, **8**, 429-445.

138. X. Wang, S. Sidoli and B. A. Garcia, in *Epigenetic Technological Applications*, ed. Y. G. Zheng, Academic Press, Boston, 2015, DOI: https://doi.org/10.1016/B978-0-12-801080-8.00004-1, pp. 55-78.

139. M. Wierer and M. Mann, *Hum. Mol. Genet.*, 2016, **25**, R106-R114.

140. J. Simithy, S. Sidoli and B. A. Garcia, *PROTEOMICS*, 2018, **18**, 1700309.

141. H. C. Beck, in *Bioinformatics Methods in Clinical Research*, ed. R. Matthiesen, Humana Press, Totowa, NJ, 2010, DOI: 10.1007/978-1-60327-194-3_13, pp. 263-282.

142. K. A. Janssen, S. Sidoli and B. A. Garcia, in *Methods in Enzymology*, ed. A. K. Shukla, Academic Press, 2017, vol. 586, pp. 359-378.

143. M. Vermeulen, H. C. Eberl, F. Matarese, H. Marks, S. Denissov, F. Butter, K. K. Lee, J. V. Olsen, A. A. Hyman, H. G. Stunnenberg and M. Mann, *Cell*, 2010, **142**, 967-980.

144. M. F. Fraga, E. Ballestar, A. Villar-Garea, M. Boix-Chornet, J. Espada, G. Schotta, T. Bonaldi, C. Haydon, S. Ropero, K. Petrie, N. G. Iyer, A. Pérez-Rosado, E. Calvo, J. A. Lopez, A. Cano, M. J. Calasanz, D. Colomer, M. Á. Piris, N. Ahn, A. Imhof, C. Caldas, T. Jenuwein and M. Esteller, *Nat. Genet.*, 2005, **37**, 391-400.

145. C. I. Wang, A. A. Alekseyenko, G. LeRoy, A. E. H. Elia, A. A. Gorchakov, L.-M. P. Britton, S. J. Elledge, P. V. Kharchenko, B. A. Garcia and M. I. Kuroda, *Nat. Struct. Mol. Biol.*, 2013, **20**, 202.

146. T. R. Butt, D. B. Jump and M. E. Smulson, *Proc. Natl. Acad. Sci. U. S. A.*, 1979, **76**, 1628-1632.

147. J. Allan, R. M. Fraser, T. Owen-Hughes and D. Keszenman-Pereyra, *J. Mol. Biol.*, 2012, **417**, 152-164.

148. J. G. Henikoff, J. A. Belsky, K. Krassovsky, D. M. MacAlpine and S. Henikoff, *Proc. Natl. Acad. Sci. U. S. A.*, 2011, **108**, 18318-18323.

149. A. Lorzadeh, M. Bilenky, C. Hammond, D. Knapp, L. Li, P. H. Miller, A. Carles, A. Heravi-Moussavi, S. Gakkhar, M. Moksa, C. J. Eaves and M. Hirst, *Cell Rep.*, 2016, **17**, 2112-2124.

150. L. Song and G. E. Crawford, *CSH Protocols*, 2010, **2010**, pdb prot5384.

151. A. P. Boyle, S. Davis, H. P. Shulha, P. Meltzer, E. H. Margulies, Z. Weng, T. S. Furey and G. E. Crawford, *Cell*, 2008, **132**, 311-322.

152. H. H. He, C. A. Meyer, S. S. Hu, M. W. Chen, C. Zang, Y. Liu, P. K. Rao, T. Fei, H. Xu, H. Long, X. S. Liu and M. Brown, *Nat. Methods*, 2014, **11**, 73-78.

153. J. D. Buenrostro, P. G. Giresi, L. C. Zaba, H. Y. Chang and W. J. Greenleaf, *Nat. Methods*, 2013, **10**, 1213-1218.

154. J. D. Buenrostro, B. Wu, H. Y. Chang and W. J. Greenleaf, *Curr. Protoc. Mol. Biol.*, 2015, **109**, 21 29 21-29.

155. J. Wu, B. Huang, H. Chen, Q. Yin, Y. Liu, Y. Xiang, B. Zhang, B. Liu, Q. Wang, W. Xia, W. Li, Y. Li, J. Ma, X. Peng, H. Zheng, J. Ming, W. Zhang, J. Zhang, G. Tian, F. Xu, Z. Chang, J. Na, X. Yang and W. Xie, *Nature*, 2016, **534**, 652-657.

156. J. Xu, A. C. Carter, A. V. Gendrel, M. Attia, J. Loftus, W. J. Greenleaf, R. Tibshirani, E. Heard and H. Y. Chang, *Nat. Genet.*, 2017, **49**, 377-386.

157. P. W. Koh, R. Sinha, A. A. Barkal, R. M. Morganti, A. Chen, I. L. Weissman, L. T. Ang, A. Kundaje and K. M. Loh, *Sci. Data*, 2016, **3**, 160109.

158. P. G. Giresi, J. Kim, R. M. McDaniell, V. R. Iyer and J. D. Lieb, *Genome Res.*, 2007, **17**, 877-885.

159. P. G. Giresi and J. D. Lieb, *Methods*, 2009, **48**, 233-239.

160. J. Mieczkowski, A. Cook, S. K. Bowman, B. Mueller, B. H. Alver, S. Kundu, A. M. Deaton, J. A. Urban, E. Larschan, P. J. Park, R. E. Kingston and M. Y. Tolstorukov, *Nat. Commun.*, 2016, **7**, 11485.

161. V. I. Risca, S. K. Denny, A. F. Straight and W. J. Greenleaf, *Nature*, 2016, DOI: 10.1038/nature20781.

162. M. de Dieuleveult, K. Yen, I. Hmitou, A. Depaux, F. Boussouar, D. Bou Dargham, S. Jounier, H. Humbertclaude, F. Ribierre, C. Baulard, N. P. Farrell, B. Park, C. Keime, L. Carriere, S. Berlivet, M. Gut, I. Gut, M. Werner, J. F. Deleuze, R. Olaso, J. C. Aude, S. Chantalat, B. F. Pugh and M. Gerard, *Nature*, 2016, **530**, 113-116.

163. M. R. Corces, J. D. Buenrostro, B. Wu, P. G. Greenside, S. M. Chan, J. L. Koenig, M. P. Snyder, J. K. Pritchard, A. Kundaje, W. J. Greenleaf, R. Majeti and H. Y. Chang, *Nat. Genet.*, 2016, **48**, 1193-1203.

164. M. Sarwat and M. M. Yamdagni, *Crit. Rev. Biotechnol.*, 2016, **36**, 191-203.

165. Y. Shi and J. Shang, *Methods Mol. Biol.*, 2016, **1402**, 43-61.

166. M. H. Lu, B. Tang, S. Zeng, C. J. Hu, R. Xie, Y. Y. Wu, S. M. Wang, F. T. He and S. M. Yang, *Oncogene*, 2016, **35**, 3524-3534.

167. G. Rai, R. Rai, A. H. Saeidian and M. Rai, *Immunol. Res.*, 2016, **64**, 14-24.

168. W. Xu, J. Seok, M. N. Mindrinos, A. C. Schweitzer, H. Jiang, J. Wilhelmy, T. A. Clark, K. Kapur, Y. Xing, M. Faham, J. D. Storey, L. L. Moldawer, R. V. Maier, R. G. Tompkins, W. H. Wong, R. W. Davis and W. Xiao, *Proc. Natl. Acad. Sci. U. S. A.*, 2011, **108**, 3707-3712.

169. S. Wahl, A. Drong, B. Lehne, M. Loh, W. R. Scott, S. Kunze, P. C. Tsai, J. S. Ried, W. Zhang, Y. Yang, S. Tan, G. Fiorito, L. Franke, S. Guarrera, S. Kasela, J. Kriebel, R. C. Richmond, M. Adamo, U. Afzal, M. Ala-Korpela, B. Albetti, O. Ammerpohl, J. F. Apperley, M. Beekman, P. A. Bertazzi, S. L. Black, C. Blancher, M. J. Bonder, M. Brosch, M. Carstensen-Kirberg, A. J. de Craen, S. de Lusignan, A. Dehghan, M. Elkalaawy, K. Fischer, O. H. Franco, T. R. Gaunt, J. Hampe, M. Hashemi, A. Isaacs, A. Jenkinson, S. Jha, N. Kato, V. Krogh, M. Laffan, C. Meisinger, T. Meitinger, Z. Y. Mok, V. Motta, H. K. Ng, Z. Nikolakopoulou, G. Nteliopoulos, S. Panico, N. Pervjakova, H. Prokisch, W. Rathmann, M. Roden, F. Rota, M. A. Rozario, J. K. Sandling, C. Schafmayer, K. Schramm, R. Siebert, P. E. Slagboom, P. Soininen, L. Stolk, K. Strauch, E. S. Tai, L. Tarantini, B. Thorand, E. F. Tigchelaar, R. Tumino, A. G. Uitterlinden, C. van Duijn, J. B. van Meurs, P. Vineis, A. R. Wickremasinghe, C. Wijmenga, T. P. Yang, W. Yuan, A. Zhernakova, R. L. Batterham, G. D. Smith, P. Deloukas, B. T. Heijmans, C. Herder, A. Hofman, C. M. Lindgren, L. Milani, P. van der Harst, A. Peters, T. Illig, C. L. Relton, M. Waldenberger, M. R. Jarvelin, V. Bollati, R. Soong, T. D. Spector, J. Scott, M. I. McCarthy, P. Elliott, J. T. Bell, G. Matullo, C. Gieger, J. S. Kooner, H. Grallert and J. C. Chambers, *Nature*, 2017, **541**, 81-86.

170. M. Mehrmohamadi, L. K. Mentch, A. G. Clark and J. W. Locasale, *Nat. Commun.*, 2016, **7**, 13666.

171. J. Sandoval, H. Heyn, S. Moran, J. Serra-Musach, M. A. Pujana, M. Bibikova and M. Esteller, *Epigenetics*, 2014, **6**, 692-702.

172. R. Pidsley, E. Zotenko, T. J. Peters, M. G. Lawrence, G. P. Risbridger, P. Molloy, S. Van Djik, B. Muhlhausler, C. Stirzaker and S. J. Clark, *Genome Biol.*, 2016, **17**, 208.

173. S. Tashiro, T. Handa, A. Matsuda, T. Ban, T. Takigawa, K. Miyasato, K. Ishii, K. Kugou, K. Ohta, Y. Hiraoka, H. Masukata and J. Kanoh, *Nat. Commun.*, 2016, **7**, 10393.

174. A. Luoni, R. Massart, V. Nieratschker, Z. Nemoda, G. Blasi, M. Gilles, S. H. Witt, M. J. Suderman, S. J. Suomi, A. Porcelli, G. Rizzo, L. Fazio, S. Torretta, A. Rampino, A. Berry, P. Gass, F. Cirulli, M. Rietschel, A. Bertolino, M. Deuschle, M. Szyf and M. A. Riva, *Transl. Psychiatry*, 2016, **6**, e943.

175. G. E. Crawford, S. Davis, P. C. Scacheri, G. Renaud, M. J. Halawi, M. R. Erdos, R. Green, P. S. Meltzer, T. G. Wolfsberg and F. S. Collins, *Nat. Methods*, 2006, **3**, 503-509.

176. J. Dekker, M. A. Marti-Renom and L. A. Mirny, *Nat. Rev. Genet.*, 2013, **14**, 390-403.

177. E. de Wit and W. de Laat, *Genes Dev.*, 2012, **26**, 11-24.

178. J. Dekker, K. Rippe, M. Dekker and N. Kleckner, *Science*, 2002, **295**, 1306-1311.

179. M. Simonis, P. Klous, E. Splinter, Y. Moshkin, R. Willemsen, E. de Wit, B. van Steensel and W. de Laat, *Nat. Genet.*, 2006, **38**, 1348-1354.

180. J. Dostie, T. A. Richmond, R. A. Arnaout, R. R. Selzer, W. L. Lee, T. A. Honan, E. D. Rubio, A. Krumm, J. Lamb, C. Nusbaum, R. D. Green and J. Dekker, *Genome Res.*, 2006, **16**, 1299-1309.

181. J. M. Belton, R. P. McCord, J. H. Gibcus, N. Naumova, Y. Zhan and J. Dekker, *Methods*, 2012, **58**, 268-276.

182. M. J. Fullwood, M. H. Liu, Y. F. Pan, J. Liu, H. Xu, Y. B. Mohamed, Y. L. Orlov, S. Velkov, A. Ho, P. H. Mei, E. G. Chew, P. Y. Huang, W. J. Welboren, Y. Han, H. S. Ooi, P. N. Ariyaratne, V. B. Vega, Y. Luo, P. Y. Tan, P. Y. Choy, K. D. Wansa, B. Zhao, K. S. Lim, S. C. Leow, J. S. Yow, R. Joseph, H. Li, K. V. Desai, J. S. Thomsen, Y. K. Lee, R. K. Karuturi, T. Herve, G. Bourque, H. G. Stunnenberg, X. Ruan, V. Cacheux-Rataboul, W. K. Sung, E. T. Liu, C. L. Wei, E. Cheung and Y. Ruan, *Nature*, 2009, **462**, 58-64.

183. M. Franke, D. M. Ibrahim, G. Andrey, W. Schwarzer, V. Heinrich, R. Schopflin, K. Kraft, R. Kempfer, I. Jerkovic, W. L. Chan, M. Spielmann, B. Timmermann, L. Wittler, I. Kurth, P. Cambiaso, O. Zuffardi, G. Houge, L. Lambie, F. Brancati, A. Pombo, M. Vingron, F. Spitz and S. Mundlos, *Nature*, 2016, **538**, 265-269.

184. M. Simonis, P. Klous, I. Homminga, R. J. Galjaard, E. J. Rijkers, F. Grosveld, J. P. Meijerink and W. de Laat, *Nat. Methods*, 2009, **6**, 837-842.

185. E. Crane, Q. Bian, R. P. McCord, B. R. Lajoie, B. S. Wheeler, E. J. Ralston, S. Uzawa, J. Dekker and B. J. Meyer, *Nature*, 2015, **523**, 240-244.

186. G. Zhang and S. Pradhan, *IUBMB life*, 2014, **66**, 240-256.

187. D. S. Paul, A. E. Teschendorff, M. A. Dang, R. Lowe, M. I. Hawa, S. Ecker, H. Beyan, S. Cunningham, A. R. Fouts, A. Ramelius, F. Burden, S. Farrow, S. Rowlston, K. Rehnstrom, M. Frontini, K. Downes, S. Busche, W. A. Cheung, B. Ge, M. M. Simon, D. Bujold, T. Kwan, G. Bourque, A. Datta, E. Lowy, L. Clarke, P. Flicek, E. Libertini, S. Heath, M. Gut, I. G. Gut, W. H. Ouwehand, T. Pastinen, N. Soranzo, S. E. Hofer, B. Karges, T. Meissner, B. O. Boehm, C. Cilio, H. Elding Larsson, A. Lernmark, A. K. Steck, V. K. Rakyan, S. Beck and R. D. Leslie, *Nat. Commun.*, 2016, **7**, 13555.

188. R. L. Hood, L. C. Schenkel, S. M. Nikkel, P. J. Ainsworth, G. Pare, K. M. Boycott, D. E. Bulman and B. Sadikovic, *Sci. Rep.*, 2016, **6**, 38803.

189. M. Fanelli, S. Amatori, I. Barozzi and S. Minucci, *Nat. Protoc.*, 2011, **6**, 1905-1919.

190. P. Cejas, L. Li, N. K. O'Neill, M. Duarte, P. Rao, M. Bowden, C. W. Zhou, M. Mendiola, E. Burgos, J. Feliu, J. Moreno-Rubio, H. Guadalajara, V. Moreno, D. Garcia-Olmo, J. Bellmunt, S. Mullane, M. Hirsch, C. J. Sweeney, A. Richardson, X. S. Liu, M. Brown, R. A. Shivdasani and H. W. Long, *Nat. Med.*, 2016, **22**, 685-691.

191. R. Blecher-Gonen, Z. Barnett-Itzhaki, D. Jaitin, D. Amann-Zalcenstein, D. Lara-Astiaso and I. Amit, *Nat. Protoc.*, 2013, **8**, 539-554.

192. J. A. Dahl and P. Collas, *Nucleic Acids Res.*, 2008, **36**, e15.

193. J. A. Dahl and P. Collas, *STEM CELLS*, 2007, **25**, 1037-1046.

194. C. A. Aguilar and H. G. Craighead, *Nat. Nanotechnol.*, 2013, **8**, 709-718.

195. J. F. Edd, D. Di Carlo, K. J. Humphry, S. Koster, D. Irimia, D. A. Weitz and M. Toner, *Lab Chip*, 2008, **8**, 1262-1264.

196. A. K. White, M. VanInsberghe, O. I. Petriv, M. Hamidi, D. Sikorski, M. A. Marra, J. Piret, S. Aparicio and C. L. Hansen, *Proc. Natl. Acad. Sci. U. S. A.*, 2011, **108**, 13999-14004.

197. S. C. Kim, I. C. Clark, P. Shahi and A. R. Abate, *Anal. Chem.*, 2018, **90**, 1273-1279.

198. A. M. Streets, X. Zhang, C. Cao, Y. Pang, X. Wu, L. Xiong, L. Yang, Y. Fu, L. Zhao, F. Tang and Y. Huang, *Proc. Natl. Acad. Sci. U. S. A.*, 2014, **111**, 7048-7053.

199. A. M. Klein, L. Mazutis, I. Akartuna, N. Tallapragada, A. Veres, V. Li, L. Peshkin, D. A. Weitz and M. W. Kirschner, *Cell*, 2015, **161**, 1187-1201.

200. A. R. Wu, J. B. Hiatt, R. Lu, J. L. Attema, N. A. Lobo, I. L. Weissman, M. F. Clarke and S. R. Quake, *Lab Chip*, 2009, **9**, 1365-1370.

201. A. R. Wu and S. R. Quake, *CSH Protocols*, 2016, **2016**, pdb prot084996.

202. A. R. Wu, T. L. Kawahara, N. A. Rapicavoli, J. van Riggelen, E. H. Shroff, L. Xu, D. W. Felsher, H. Y. Chang and S. R. Quake, *Lab Chip*, 2012, **12**, 2190-2198.

203. Z. Cao, C. Chen, B. He, K. Tan and C. Lu, *Nat. Methods*, 2015, **12**, 959-962.

204. Z. Cao and C. Lu, *Anal. Chem.*, 2016, **88**, 1965-1972.

205. T. W. Murphy, Y. P. Hsieh, S. Ma, Y. Zhu and C. Lu, *Anal. Chem.*, 2018, **90**, 7666-7674.

206. S. Ma, Y. P. Hsieh, J. Ma and C. Lu, *Sci. Adv.*, 2018, **4**, eaar8187.

207. A. Rotem, O. Ram, N. Shoresh, R. A. Sperling, A. Goren, D. A. Weitz and B. E. Bernstein, *Nat. Biotechnol.*, 2015, **33**, 1165-1172.

208. Y. Xu, J. H. Lee, Z. Li, L. Wang, T. Ordog and R. C. Bailey, *Lab on a chip*, 2018, **18**, 2583-2592.

209. V. Sahore, S. R. Doonan and R. C. Bailey, *Anal. Methods*, 2018, **10**, 4264-4274.

210. S. R. Doonan and R. C. Bailey, *Anal. Chem.*, 2017, **89**, 4091-4099.

211. T. Thorsen, R. W. Roberts, F. H. Arnold and S. R. Quake, *Phys. Rev. Lett.*, 2001, **86**, 4163-4166.

212. H. Song, J. D. Tice and R. F. Ismagilov, *Angew. Chem. Int. Ed.*, 2003, **42**, 768-772.

213. H. Song, D. L. Chen and R. F. Ismagilov, *Angew. Chem. Int. Ed.*, 2006, **45**, 7336-7356.

214. S.-Y. Teh, R. Lin, L.-H. Hung and A. P. Lee, *Lab on a chip*, 2008, **8**, 198-220.

215. S. Mashaghi, A. Abbaspourrad, D. A. Weitz and A. M. van Oijen, *Trends Anal. Chem.*, 2016, **82**, 118-125.

216. T. S. Kaminski and P. Garstecki, *Chem. Soc. Rev.*, 2017, **46**, 6210-6226.

217. L. Shang, Y. Cheng and Y. Zhao, *Chem. Rev.*, 2017, **117**, 7964-8040.

218. C. Holtze, A. C. Rowat, J. J. Agresti, J. B. Hutchison, F. E. Angile, C. H. J. Schmitz, S. Koster, H. Duan, K. J. Humphry, R. A. Scanga, J. S. Johnson, D. Pisignano and D. A. Weitz, *Lab Chip*, 2008, **8**, 1632-1639.

219. J.-C. Baret, *Lab Chip*, 2012, **12**, 422-433.

220. S. L. Anna, N. Bontoux and H. A. Stone, *Appl. Phys. Lett.*, 2003, **82**, 364-366.

221. P. Garstecki, M. J. Fuerstman, H. A. Stone and G. M. Whitesides, *Lab Chip*, 2006, **6**, 437-446.

222. E. Amstad, M. Chemama, M. Eggersdorfer, L. R. Arriaga, M. P. Brenner and D. A. Weitz, *Lab Chip*, 2016, **16**, 4163-4172.

223. D. J. Collins, A. Neild, A. deMello, A.-Q. Liu and Y. Ai, *Lab Chip*, 2015, **15**, 3439-3459.

224. U. Tangen, G. A. Minero, A. Sharma, P. F. Wagler, R. Cohen, O. Raz, T. Marx, T. Ben-Yehezkel and J. S. McCaskill, *Biomicrofluidics*, 2015, **9**, 044103.

225. U. Tangen, A. Sharma, P. Wagler and J. S. McCaskill, *Biomicrofluidics*, 2015, **9**, 014119.

226. R. Lin, J. S. Fisher, M. G. Simon and A. P. Lee, *Biomicrofluidics*, 2012, **6**, 024103-024103-024110.

227. C.-X. Zhao, *Adv. Drug Deliv. Rev.*, 2013, **65**, 1420-1446.

228. L. Mazutis, J.-C. Baret, P. Treacy, Y. Skhiri, A. F. Araghi, M. Ryckelynck, V. Taly and A. D. Griffiths, *Lab Chip*, 2009, **9**, 2902-2908.

229. M. Lee, J. W. Collins, D. M. Aubrecht, R. A. Sperling, L. Solomon, J.-W. Ha, G.-R. Yi, D. A. Weitz and V. N. Manoharan, *Lab on a chip*, 2014, **14**, 509-513.

230. H. Lee, L. Xu and K. W. Oh, *Biomicrofluidics*, 2014, **8**, 044113.

231. L. Mazutis and A. D. Griffiths, *Lab Chip*, 2012, **12**, 1800-1806.

232. L. Xu, H. Lee, R. Panchapakesan and K. W. Oh, *Lab Chip*, 2012, **12**, 3936-3942.

233. I. Akartuna, D. M. Aubrecht, T. E. Kodger and D. A. Weitz, *Lab Chip*, 2015, **15**, 1140-1144.

234. M. Zagnoni, G. Le Lain and J. M. Cooper, *Langmuir*, 2010, **26**, 14443-14449.

235. A. Sciambi and A. R. Abate, *Lab Chip*, 2014, **14**, 2605-2609.

236. L. Li, J. Q. Boedicker and R. F. Ismagilov, *Anal. Chem.*, 2007, **79**, 2756-2761.

237. A. R. Abate, T. Hung, P. Mary, J. J. Agresti and D. A. Weitz, *Proc. Natl. Acad. Sci. U. S. A.*, 2010, **107**, 19163-19166.

238. M. Rhee, Y. K. Light, S. Yilmaz, P. D. Adams, D. Saxena, R. J. Meagher and A. K. Singh, *Lab Chip*, 2014, **14**, 4533-4539.

239. L. Frenz, K. Blank, E. Brouzes and A. D. Griffiths, *Lab Chip*, 2009, **9**, 1344-1348.

240. W. G. Cochrane, A. L. Hackler, V. J. Cavett, A. K. Price and B. M. Paegel, *Anal. Chem.*, 2017, **89**, 13227-13234.

241. J. R. Haliburton, S. C. Kim, I. C. Clark, R. A. Sperling, D. A. Weitz and A. R. Abate, *Biomicrofluidics*, 2017, **11**, 034111-034111.

242. M. A. M. Gijs, *Microfluid. Nanofluid.*, 2004, **1**, 22-40.

243. M. Serra, D. Ferraro, I. Pereiro, J. L. Viovy and S. Descroix, *Lab Chip*, 2017, **17**, 3979-3999.

244. R. Gao, Z. Cheng, A. J. deMello and J. Choo, *Lab on a Chip*, 2016, **16**, 1022-1029.

245. A. H. C. Ng, U. Uddayasankar and A. R. Wheeler, *Anal. Bioanal. Chem.*, 2010, **397**, 991-1007.

246. D. Lombardi and P. S. Dittrich, *Anal. Bioanal. Chem.*, 2011, **399**, 347-352.

247. E. Brouzes, T. Kruse, R. Kimmerling and H. H. Strey, *Lab Chip*, 2015, **15**, 908-919.

248. B. Verbruggen, K. Leirs, R. Puers and J. Lammertyn, *Microfluid. Nanofluid.*, 2015, **18**, 293-303.

249. B. Verbruggen, T. Tóth, M. Cornaglia, R. Puers, M. A. M. Gijs and J. Lammertyn, *Microfluid. Nanofluid.*, 2015, **18**, 91-102.

250. X. Pan, S. Zeng, Q. Zhang, B. Lin and J. Qin, *ELECTROPHORESIS*, 2011, **32**, 3399-3405.

251. J. Nie and R. T. Kennedy, *Anal. Chem.*, 2010, **82**, 7852-7856.

252. L. M. Fidalgo, G. Whyte, D. Bratton, C. F. Kaminski, C. Abell and W. T. S. Huck, *Angew. Chem. Int. Ed.*, 2008, **47**, 2042-2045.

253. I. C. Clark and A. R. Abate, *Lab Chip*, 2017, **17**, 2032-2045.

254. R.-J. Yang, H.-H. Hou, Y.-N. Wang and L.-M. Fu, *Sens. Actuators B Chem.*, 2016, **224**, 1-15.

255. W. Connacher, N. Zhang, A. Huang, J. Mei, S. Zhang, T. Gopesh and J. Friend, *Lab Chip*, 2018, **18**, 1952-1996.

256. K. W. Oh, K. Lee, B. Ahn and E. P. Furlani, *Lab Chip*, 2012, **12**, 515-545.

257. R. Blecher-Gonen, Z. Barnett-Itzhaki, D. Jaitin, D. Amann-Zalcenstein, D. Lara-Astiaso and I. Amit, *Nat. Protoc.*, 2013, **8**, 539.

258. P. Chi, C. D. Allis and G. G. Wang, *Nat. Rev. Cancer*, 2010, **10**, 457.

259. J. A. Dahl and P. Collas, *Nat. Protoc.*, 2008, **3**, 1032-1045.

260. J. A. Dahl and P. Collas, in *Chromatin Immunoprecipitation Assays: Methods and Protocols*, ed. P. Collas, Humana Press, Totowa, NJ, 2009, DOI: 10.1007/978-1-60327-414-2_4, pp. 59-74.

261. G. D. Gilfillan, T. Hughes, Y. Sheng, H. S. Hjorthaug, T. Straub, K. Gervin, J. R. Harris, D. E. Undlien and R. Lyle, *BMC Genomics*, 2012, **13**, 645.

262. J. D. Nelson, O. Denisenko and K. Bomsztyk, *Nat. Protoc.*, 2006, **1**, 179-185.

263. M. Adli and B. E. Bernstein, *Nat. Protoc.*, 2011, **6**, 1656.

264. A. K. Price, A. B. MacConnell and B. M. Paegel, *Anal. Chem.*, 2014, **86**, 5039-5044.

Chapter II

K-Channel: A Multi-Functional Architecture for Dynamically Re-Configurable Sample Processing in Droplet Microfluidics

Reproduced with permission from Doonan, S.R., and Bailey, R.C. "K-Channel: A Multifunctional Architecture for Dynamically Reconfigurable Sample Processing in Droplet Microfluidics." *Analytical Chemistry* **2017**, *89*(7): 4091-4099. *Copyright 2017 American Chemical Society. Available at* https://pubs.acs.org/articlesonrequest/AOR-VdtzC4qKdUPafeffyhi9 *and* doi: 10.1021/acs.analchem.6b05041.

INTRODUCTION

In contrast to bulk approaches or continuous flow microfluidics, droplet microfluidic systems compartmentalize samples and reagents into nano- to femtoliter-sized reactors in an immiscible oil.[1-3] By segmenting flow into discrete plugs separate from each other and from device walls, these systems minimize sample loss from adsorption to channels or tubing, and enable generation of libraries containing thousands of individually addressable reaction volumes.[4-6] Capitalizing on rapid mass and heat transfer in droplets, droplet microfluidic devices have been applied to synthesis and nanotechnology.[7, 8] Furthermore, droplet dimensions are especially suitable for analysis of small biological samples or even single cells, and adjusting operation times to handle variable numbers of droplets accommodates a range of sample volumes.[9-11] Notable recent work leverages droplet microfluidic systems as miniaturized instruments for

immunoassays,[12, 13] epigenetic analysis,[14] and directed molecular evolution,[15] among other applications.

In order to achieve complex biochemical processing in droplets, devices must demonstrate a number of capabilities. Droplet or plug formation often occurs at T-junction and flow focusing structures.[16, 17] Picoinjection[18-20] or droplet fusion[21] add reagents into sample droplets. Droplet reactions incubate in delay channels[22] or off-device followed by reinjection.[23] Droplet splitting samples from or parallelizes reactions.[24-26] Coupled with antibody-functionalized magnetic beads, droplet splitting can even selectively concentrate samples and remove waste volume.[13, 27-31] Overall, these well-characterized approaches provide a toolkit for in-droplet chemistry, and recent reviews highlight the broad range of droplet techniques and applications.[7, 8, 17, 32, 33]

Realizing the potential of droplet microfluidics will require overcoming certain limitations. For instance, many droplet operations occur in highly specialized geometries, and optimizing performance for a particular chemical system (such as changing the volume of fluid injected or removed) may necessitate fabricating a device with modified dimensions. Soft lithography enables rapid prototyping, but the multiple device iterations needed to optimize an in-droplet assay can still lead to high time and monetary costs.[34] An additional challenge includes the sensitivity of droplet manipulations like injection to flow instabilities and contamination. Because these techniques often rely on a single inlet channel for injected reagent delivery, pressure fluctuations during extended device operation significantly move the equilibrium position of the injection interface (changing injection magnitude), and any material extracted from droplets during injection may contaminate later droplets.[19, 35, 36] Finally, common biochemical techniques like ELISA typically require washing samples on a solid phase like antibody-conjugated magnetic beads,[37] but only limited efforts have demonstrated analogous processes in continuously flowing droplets at

low throughput (1-5 droplets per second) compared to many other droplet operations (100-1000 droplets per second).[38, 39] Therefore, the clear need exists to engineer versatile and robust droplet manipulation modules that simplify assay optimization and enable in-droplet washing.

With these considerations in mind, a promising approach to creating more robust droplet systems with useful, novel functions has been "cross-channel"-style geometries. As a pioneering first example, Chen *et al.* developed the "chemistrode," a probe for delivering nL droplets via one channel and collecting sample droplets with the second across the parallel surface being interogated.[40] Later examples have integrated miniaturized cross-channel architectures into fully self-contained droplet systems, typically as a means of droplet formation. Lin *et al.* used a cross-channel flow of a cell suspension past an oil channel to generate single cell-containing droplets-on-demand (DoD) upon nearby PDMS valve triggering.[41] This structure stably maintained the aqueous cell suspension-oil interface before and after valve actuation. More recently, a similar approach adapted a cross-channel structure which dispersed flow instabilities through the cross-channel to improve droplet formation reproducibility.[36] A serial array of similar modules also served as a combinatorial droplet generator for DNA library assembly.[6, 42] Other variations on cross-channel flow interfaced to droplets have been specialized to single operations.[38, 43]

Aiming to develop a simple, easily switchable module for droplet manipulation, we have explored cross-channel interfaces that support droplet generation and sampling modes beyond those previously reported.[6, 36, 40-43] By adding features such as on-chip electric and magnetic fields, our "K-channel" device enables a range of useful droplet processing steps such as reagent injection, volume extraction, droplet splitting, magnetic bead capture, and more. Importantly, our approach allows dynamic tuning of a single device among these different functional operations simply by adjusting external device operating conditions, such as applied pressure, electric field,

and fluid composition. Moreover, continuous cross-channel flow greatly reduces the chance for cross-contamination inherent in previous approaches.[19, 35] Finally, we demonstrate the versatility of the K-channel module to create a two-step washing device consisting of magnetic bead-concentrating droplet splitting followed by water injection, and realize robust device operation at nearly two orders of magnitude higher droplet frequency than previous reports.[38, 39]

EXPERIMENTAL SECTION

Microfluidic Device Fabrication

PDMS microfluidic devices bonded to a glass substrate were formed via conventional soft lithography using SU8-2025 Photoresist (MicroChem Corp.) masters on 3'' silicon wafers (WRS Materials).[34] Photomasks were designed in AutoCAD (Autodesk) and printed as transparencies (CAD/Art Services). Prior to use, masters were treated with (tridecafluoro-1,1,2,2-tetrahydrooctyl)trichlorosilane (Gelest, Inc.) under vacuum for 2-4 hours. PDMS was mixed 10:1 (RTV615A:RTV615B) (Momentive) and cured for 1 hour at 70 °C. PDMS molds were removed from the master and punched with 20 Ga needles to create ports. PDMS molds and glass slides (Cover Glass, Thickness 1 ½, 22 x 40 mm, Corning, Inc.) were bonded following oxygen plasma activation (PDC-32G, Harrick Plasma). Devices were incubated at 70 °C overnight and treated with 1% (tridecafluoro-1,1,2,2-tetrahydrooctyl)trichlorosilane in FC-40 (Sigma Aldrich). All channels were 40 μm in height.

Fluid Flow

Fluids were driven by a home-built pressure controller. Briefly, a custom gas manifold (VWR International) distributed N_2 through a parallel regulator array (VWR International) into an

array of LHDA0531115H solenoid valves (The Lee Company). Valves were actuated by a NI PCIe-6251 Multifunction Data Acquisition device (National Instruments) interfaced via LabView (National Instruments). Upon valve actuation, pressure was delivered into the headspace of sample vials via stainless steel fittings (New England Small Tube). Fluid flowed from pressurized vials through #30 AWG PTFE tubing (Cole Parmer) inserted directly into device ports. Typical pressures were 65 kPa for the continuous phase, 60 kPa for the dispersed phase, and 20-90 kPa for the cross-channel fluid. Typical droplet volumes were 100-200 pL, and droplets were usually produced at 300-500 Hz.

For all experiments, the continuous phase was 3M™ Novec™ 7500 Engineered Fluid (The 3M Company) with 2% poly(ethylene glycol) di-(krytox-FSH amide) (Ran Biotechnologies, Inc.) surfactant. For geometry characterization (Figures II.2, II.3, II.S1, II.S2, and II.S3 and Supplementary Movies SMII.1, SMII.2, SMII.3, and SMII.4) and for serial K-channels (Movie SMII.6), the dispersed phase was food dye (McCormick & Company) in water, and the fluid in the K-channel was identical either to the continuous phase (for droplet splitting) or to the dispersed phase (for other operations). Injection with pulsed electric field (Movie SMII.5) used water as the dispersed phase and 1 mM fluorescein (Sigma Aldrich) in water as the K-channel fluid. For material exchange characterization (Figure II.4 and Movie SMII.7), the dispersed phase was 200 μM fluorescein in water, and the fluid in the K-channel was water. For the enzyme characterization (Movie SMII.8), β-galactosidase (Life Technologies Corporation) converted resorufin β-D-galactopyranoside (ThermoFisher Scientific) into fluorescent resorufin in 1X phosphate buffered saline with 0.5% bovine serum albumin. Where indicated, an electric field (25-35 VAC) was supplied to 3 M NaCl in electrode channels[20] or to 250 μm Pt wires submerged in solution vials

by a Tenma 72-6628 DC Regulated Power Supply (MCM Electronics) modified with a DC to AC inverter. Electric field pulses were actuated manually or by a LabView interface.

Magnetic Bead Capture and Washing

Embedded magnet devices were fabricated as described above with the addition of a magnet that was positioned along guide features on the master prior to pouring PDMS. The magnet was removed to form a guide hole in the PDMS mold after curing. Magnets were 1/2'' x 1/4'' x 1/8'' N52 (magnetized through thickness) (K&J Magnetics, Inc.). Prior to device operation, an array of 8 magnets was positioned along the guide hole to form a block of 4 magnets above and 4 magnets below the glass slide (total dimensions 1/2'' x 1/2'' x 1/2''). The magnetization of this array was along the plane of the glass slide in the direction of the main channel side of the K-channel.

1-3 μm paramagnetic bead samples (Protein A Magnetic Beads, New England Biolabs) were washed with buffer (50 mM Trizma HCl at pH 7.5, 150 mM NaCl, 5 mM EDTA, 0.5% IGEPAL CA-630, 1% Triton X-100), suspended in Optiprep Density Gradient Medium (Sigma Aldrich), and filtered through a microfluidic device with 10-15 μm pores to remove contaminating particles and large aggregates prior to use.

Droplet Imaging and Analysis

Microfluidic devices were imaged by an M80 stereo microscope (Leica Microsystems) or a DMi8 light microscope (Leica Microsystems) using a Phantom Miro eX2 high speed camera (Vision Research). Videos and images were typically collected at 1000-6000 fps. For geometry and material exchange characterization, droplet size and frequency were analyzed using Droplet

Morphometry and Velocimetry (DMV) software, courtesy of Amar Basu (Wayne State University, Detroit, MI).[44] Fluorescent analysis was carried out using ImageJ (NIH) to monitor pixel intensity followed by processing by an in-house macro. All plots use N = 3 devices in which at least N = 30 droplets were measured on each device at each experimental condition.

Magnetic bead analysis was performed semi-manually in ImageJ to track droplet size and magnetic particles in droplets across the detection channel (see Figure II.S4). Bead capture analysis (Figure II.5) tracked 300 main channel and 300 waste channel droplets (N = 100 droplets for each of N = 3 devices) and bead washing analysis (Figure II.6) tracked 180 droplets (N = 20 droplets for N = 3 time points for N = 3 operations: droplet formation, splitting, and injection) across multiple frames to reduce error from beads obscured by droplet edges and from aberrations due to extra-droplet satellites and channel defects.

RESULTS AND DISCUSSION

K-Channel Design

The K-channel is formed by the intersection of a continuous flow cross-channel with a segmented flow main channel (Figure II.1). This junction resembles a capital letter "K" turned on its side, and also typically includes nearby electrode channels.[20] As droplets pass the intersection, the flow through the cross-channel predictably modifies them based on applied conditions. These operations include, but are not limited to, injecting fluid from the cross-channel into droplets, extracting fluid from droplets into the cross-channel, maintaining a stable interface without altering

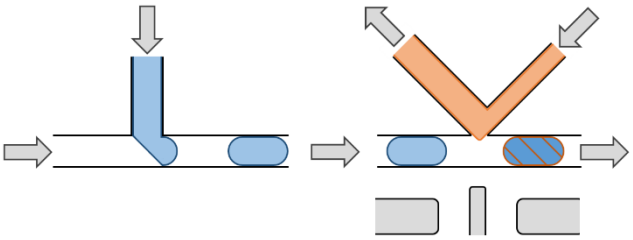

Figure II.1. K-channel device operation. Arrows indicate flow directions. After forming at a T-junction (left), droplets (blue) flow through the main channel to the K-channel element (right). The K-channel fluid (orange), an aqueous or an oil phase, flows through the cross-channel in an anti-parallel direction relative to main channel flow. An electric field may be supplied via the electrode channels (gray) to destabilize passing droplets. Through the interaction at the K-channel, droplet size, number, composition, and spacing can be altered.

droplets, using oil (instead of aqueous) cross-channel flow to split droplets, and adding or extracting oil to change droplet spacing. For operations such as injection and extraction, droplets merge with the cross-channel flow temporarily during destabilization via a local electric field, and the continuously flowing cross-channel washes away extracted material to reduce the risk of droplet-to-droplet contamination. While approaches like picoinjection use a single inlet flow channel to add reagents,[19, 35] the K-channel inlet-outlet functions to partially disperse flow instabilities so that operations are less sensitive to instabilities arising during extended operation. As a consequence of its versatility and robustness, K-channel devices and arrays of K-channels demonstrate significant potential for rational design and dynamic reconfiguration of complex droplet reaction sequences.

Fundamental K-Channel Operations

K-channel behavior with aqueous flow through the cross-channel follows the Hagen-Poiseuille Equation:[45]

$$Q = \Delta P / R_H \qquad (1)$$

where Q is the volumetric flow rate through a system volume, ΔP is the pressure drop across the system volume, and R_H is the hydraulic resistance of the system volume derived from the viscosity, the channel length, and the channel cross-sectional area.

Selecting the junction of the cross-channel with the droplet channel as the system volume specifically describes the K-channel:

$$Q_J = \Delta P_J / R_{H,J} \quad (2)$$

where Q_J is the flow through the junction (from the cross-channel into the main channel), ΔP_J is the pressure drop across the junction, and $R_{H,J}$ is the hydraulic resistance of the junction. $Q_J > 0$ corresponds to injection, $Q_J < 0$ corresponds to extraction, and $Q_J = 0$ corresponds to no net droplet volume change.

The pressures for droplet formation applied to the oil continuous phase, ΔP_C, and to the aqueous dispersed phase, ΔP_D, are held constant. Assuming constant hydraulic resistance for a single device at equilibrium, varying the pressure applied to the K-channel inlet, ΔP_K, leads to:

$$\Delta P_J = c_1 * \Delta P_K + c_2 \quad (3)$$

where c_1 and c_2 are constants derived from ΔP_C, ΔP_D, and the hydraulic resistances of the device. Clearly, ΔP_J is directly proportional to ΔP_K. Substituting Equation 3 into Equation 2:

$$Q_J = c_3 * \Delta P_K + c_4 \quad (4)$$

where c_3 and c_4 are constants derived in the same manner as c_1 and c_2. Thus, Q_J is also directly proportional to ΔP_K. Because it alters the sign and magnitude of Q_J, changing ΔP_K enables injecting into or extracting from droplets over a working range of volumes.

Removing the destabilizing electric field establishes a relatively high $R_{H,J}$ based on the Laplace pressure of the aqueous-oil interface.[19] Under a limited range of pressure conditions, this can be exploited to approximate $Q_J = 0$, where a robust droplet-K-channel fluid interface prevents volume exchange between droplets and the aqueous cross-channel flow. At slightly lower pressures (where $Q_J < 0$ and $|Q_J|$ is small) oil may stream out from the main channel into the K-channel outlet to decrease the spacing between droplets. Significant deviations from $Q_J = 0$ result in irregular droplet splitting (for $Q_J < 0$) or new droplet formation from the cross-channel fluid (for $Q_J > 0$). On the other hand, oil flow (instead of aqueous flow) through the cross-channel can lead to both dispersed and continuous phase removal through the K-channel (droplet splitting and oil removal) when $Q_J < 0$. For $Q_J > 0$ with oil flow, additional oil enters the main channel to increase the spacing between droplets.

Figure II.2 displays the fundamental K-channel operations described by this model. Representing a typical device geometry, the 40 μm wide main channel (flowing left to right) intersects with the cross channel (flowing right to left) using a 25 μm wide inlet channel (right) and a 40 μm wide outlet channel (left). Droplets formed upstream at a T-Junction under constant pressure. While manipulating the pressure at the K-channel inlet, relatively high pressure (85 kPa) injected orange dye from the cross-channel into passing droplets in the presence of an electric field (Figure II.2a and Movie SMII.1). Decreasing the pressure (45 kPa) extracted fluid from droplets into the cross-channel in the presence of an electric field (Figure II.2b and Movie SMII.2).

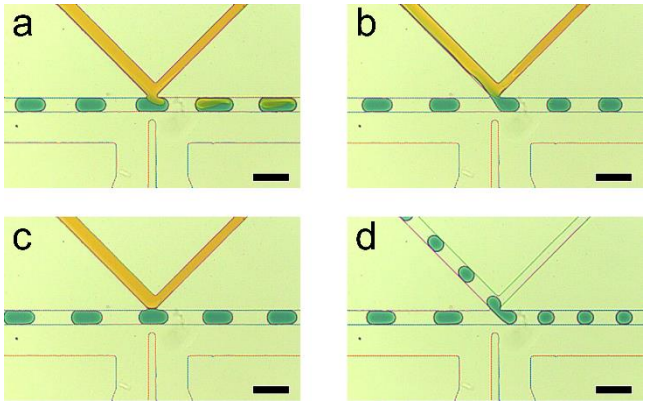

Figure II.2. Multiple K-channel operations on a single device. Droplets flow left to right. The K-channel continuous phase flows right to left. a) High K-channel pressure with electric field injects into droplets. b) Low K-channel pressure with electric field extracts from droplets. c) Moderate K-channel pressure without electric field maintains the droplet-K-channel interface. d) Low K-channel pressure without electric field splits droplets under oil flow. (scale bars = 100 µm)

Moderate pressure (73 kPa) without electric field created a stable and robust droplet-cross-channel interface (Figure II.2c and Movie SMII.3). Finally, oil flow with low pressure (20 kPa) and without electric field yielded droplet splitting (Figure II.2d and Movie SMII.4). As Figure II.2 demonstrates, changing the applied conditions (pressure, electric field, fluid), enabled a wide range of operations, not only with a single geometry, but by a single device, a novel capability which will be useful in designing and optimizing modular droplet microfluidic assays.

Device Architecture Characterization

The performance of the K-channel over typical operating conditions is shown in Figure II.3. All data was collected using a standard K-channel geometry (see Figure II.2) unless otherwise noted. In Figure II.3a, the net change in droplet volume due to interaction with the aqueous phase in the K-channel across a range of K-channel pressure is plotted. Depending on the applied pressure, up to 50% of droplet volume could be extracted and up to 100% of droplet volume could be injected. Additionally, in the absence of an applied electric field, a stable interface between

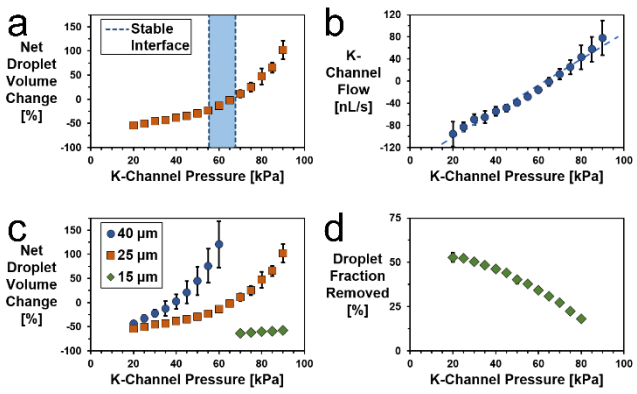

Figure II.3. K-channel operation characterization. a) Net droplet volume change becomes more positive with increasing applied K-channel pressure. In the highlighted region, a stable droplet-K-channel fluid interface occurs in the absence of an applied electric field. b) K-channel volumetric flow rate into droplets is directly proportional to applied pressure (R^2 = 0.981). c) Increasing the K-channel inlet hydraulic resistance (by decreasing the inlet channel width from 40 µm to 25 µm to 15 µm) decreases net droplet volume change. d) Increasing applied K-channel pressure reduces the droplet fraction removed during oil flow-induced droplet splitting.

droplets and the K-channel (in which droplet volume and composition were unaffected) was supported over a ~12 kPa range. At the lower pressures of this stable interface range, oil was selectively removed from the main channel, decreasing droplet spacing but leaving droplet composition and volume unchanged (see Figure II.S1). While operating in this stable range, pulsed application of the electric field enabled injections into fractions of the total droplet population (Movie SMII.5). The number of droplets receiving injections was defined by the droplet frequency and the duration of the applied electric field. Importantly, injection and material transfer only occurred in the presence of the electric field, so droplets passing the K-channel before or after the electrical pulse were unaltered. This performance was robust across multiple replicates of each device geometry (N = 3).

Equation 4 predicts that fluid flow from the cross-channel into droplets should be directly proportional to the pressure applied to the K-channel inlet, but it is clear that net droplet volume change does not follow a linear trend (Figure II.3a). Because droplet formation and the K-channel are controlled via applied pressure, changing the pressure at one inlet changes the relative pressure

drop and, therefore, volumetric flow rate, across every channel in the device. Thus, droplet frequency and, to a lesser extent, droplet volume decrease as the K-channel pressure increases.[16] By taking the product of the net change in volume per droplet, $\Delta V_{Net,Droplet}$, and the droplet frequency, f, at each pressure, we obtained approximate values for the volumetric flow rate from the cross-channel into droplets, Q_J:

$$Q_J = \Delta V_{Net,Droplet} * f \quad (5)$$

Plotting this flow rate versus K-channel pressure yielded a linear relationship (R^2 = 0.981) consistent with the model (Figure II.3b). Minor deviations from linearity are not surprising given limitations of the single phase, laminar flow-based Hagen-Poiseuille-based model,[45] which also does not account for any oil extraction from the inter-droplet spacing during K-channel operation.

While changing pressure enabled a range of operations, K-channel behavior can also be tuned by varying the geometry. Most significantly, altering hydraulic resistances (by changing the K-channel inlet width across a range of sizes from 15 µm to 40 µm) adjusted performance (Figure II.3c). As the width decreased, the channel hydraulic resistance increased, so a greater fraction of the pressure drop occurred across the length of the inlet channel instead of across the junction between the cross-channel and the main channel. Flow into droplets became more negative at each pressure. On the other hand, flow into droplets increased when the hydraulic resistance of the K-channel outlet increased (data not shown). For this reason, the standard K-channel geometry (25 µm inlet, 40 µm outlet) is asymmetrical: changing cross-channel flow direction (40 µm inlet, 25 µm outlet) selects between two ranges for K-channel pressures on a single device when desired. Nonetheless, flow direction does not intrinsically affect net droplet volume change. A symmetric

K-channel with 40 μm wide inlet and outlet channels did not significantly differ in performance with flow direction at 95% confidence (Student's t-Test, Figure II.S2). Likewise, changing the angular orientations of the cross-channels had little effect (Figure II.S3) relative to changing channel widths. By altering the geometry, K-channels can be rationally designed to provide desired operations in a chosen pressure range.

The K-channel also provides a simple method for tunable droplet splitting. Adjusting the pressure on the K-channel altered droplet splitting so that 15-50% of the droplet (1:5 – 1:1 daughter droplet ratio) was diverted into the cross-channel in each splitting step (Figure II.3d). This method provides an advantage over many previously described droplet splitting regimes: it does not require prototyping a new device with a different ratio of hydraulic resistances to adjust the size of daughter droplets,[24, 25] a capability not widely demonstrated by existing methods.[26, 28] At high K-channel pressure, oil was injected into the main channel to increase droplet spacing, but droplets did not split (data not shown).

Finally, K-channel devices are not limited to single operations. Instead, serial or parallel K-channels can enable multistep sequences on a single device. For example, two K-channels were operated in series (Movie SMII.6). Water droplets formed upstream were injected with yellow dye at the first K-channel, mixed and incubated through a serpentine region, and injected with black dye at the second K-channel. Adjusting the length and geometry of the channel between the two K-channel injections tunes reaction time.[22] Moreover, tandem operations need not be identical, so droplets could first be injected with reagent at one K-channel, then split at the next K-channel, etc. As noted above, adjusting the pressure on one K-channel modifies the flow through every channel.[45] Therefore, careful attention will be necessary to design multistep devices to orient multiple K-channel geometries such that they operate under mutually compatible pressures;

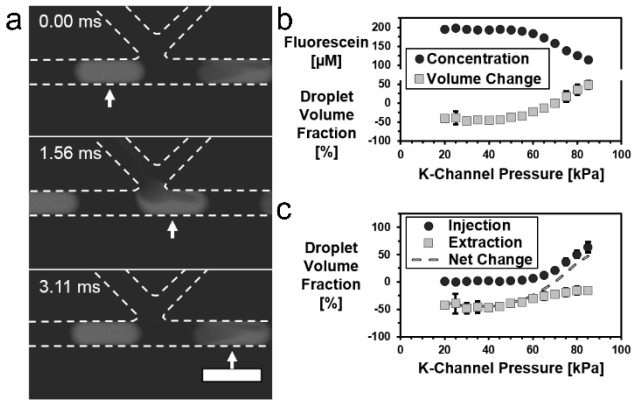

Figure II.4. K-channel material exchange. During K-channel operations that merge droplets with the continuous aqueous phase, bi-directional exchange of material occurs. a) The K-channel extracts fluorescein from droplets as it injects water. Continuous flow through the K-channel washes away extracted fluorescein to reduce the likelihood for droplet-to-droplet cross-contamination. The white arrow highlights the position of a single droplet across subsequent frames. b) Monitoring the net change in droplet volume and fluorescein concentration at the K-channel enables c) decoupling of the relative magnitudes of water injection, fluorescein extraction, and net volume change (the sum of injection and extraction) at each K-channel pressure. (scale bar = 100 μm)

however, the versatility of this geometry allows for the potential for dynamic reconfiguration.

Contamination and Bidirectional Material Exchange

During injection and extraction, the droplet-K-channel fluid interface collapses temporarily. Droplets mix and exchange with the K-channel fluid in a mass transfer process governed by the pressure drop across the K-channel, diffusion, and convective turbulence during fluid merger and breakup. While any injection technique which transiently fuses droplets with a reagent stream will extract some fraction of droplet material into the injected fluid, the K-channel explicitly addresses the inter-droplet contamination that may result. Leveraging the continuous flow through the cross-channel, the K-channel significantly reduces the risk of contamination from re-injecting extracted material from one droplet into later droplets. In Figure II.4a (Movie SMII.7), the fluid passing the K-channel decreases 85% in fluorescent intensity between injection events at 300 Hz, indicating efficient clearing of extracted material. When desired, this can be improved by

decreasing droplet frequency or increasing cross-channel linear flow rate to replace a greater fraction of cross-channel volume. Other injection methods lack the direct capability to flush out accumulated contaminants between injection events.[18, 19, 35] Though continuous replacement of fluid through the K-channel does increase reagent consumption, the versatility of the design allows for the reduction/elimination of cross-contamination depending upon the application.

Besides monitoring the net volume change per droplet, $\Delta V_{Net,Droplet}$, decoupling the volumes simultaneously injected, $V_{Injected}$, and extracted, $V_{Extracted}$, informs an understanding of droplet composition following K-channel operations:

$$\Delta V_{Net,Droplet} = V_{Injected} + V_{Extracted} \qquad (6)$$

In order to quantitatively characterize simultaneous material exchange during K-channel operations, droplet volume changes and fluorescence intensity were measured for water injection into fluorescein droplets (Figure II.4b). This information, coupled with Equation 6, was used to decouple injection and extraction components (Figure II.4c):

$$[Droplet]_F = [Droplet]_0 * (V_0 + V_{Extracted}) / V_F \qquad (7)$$

where $[Droplet]_F$ and $[Droplet]_0$ are the final and initial fluorescein concentrations in the droplet, and V_F and V_0 are the final and initial droplet volumes.

While the injection or extraction terms dominated at high or low pressures, respectively, performance at intermediate pressures included significant contributions from injected and extracted volumes. For instance, intermediate pressure conditions simultaneously added and

removed approximately 20% of droplet material. Therefore, it is critical to account for bidirectional material exchange when designing droplet reaction sequences to ensure that intended reagent concentrations are reached. Notwithstanding, in cases where cross contamination or bidirectional material transfer are unacceptable risks, techniques like droplet fusion and droplet splitting are alternative strategies.

Biochemical Compatibility

Besides characterizing the physical responses of K-channel devices to internal and external perturbations, we also wanted to demonstrate the amenability of K-channel systems to biochemical droplet manipulations. Based on the extended dynamic range and ease of tuning for K-channel injections, we envision that K-channel devices could be especially suitable for precise measurement of enzyme kinectics.[5, 7] For example, K-channel devices can routinely scan across a range of substrate injection volumes into enzyme-containing droplets. Coupled to the rapid internal convection of in-droplet mixing, this approach should enable rapid determination of enzyme velocities.[46, 47] To this end, we confirmed the bio-compatibility of K-channel operations for this purpose by monitoring the action of β-galactosidase on K-channel-injected substrate (resorufin β-D-galactopyranoside) in a downstream incubation region (Movie SMII.8). As mentioned previously, the increased reagent consumption via K-channel flow may make this approach poorly suited to studying some enzyme systems, but careful assay design can minimize substrate consumption.

Superparamagnetic Bead Capture and Sample Washing

In characterizing performance and material exchange, it is clear that the K-channel offers significant versatility in modifying droplet size and composition. Up to this point, we have presented K-channel operations which interact non-selectively with droplet contents. However, some reaction sequences must include selective steps like concentrating samples, decanting supernatants, and buffer exchange. To these ends, magnetic beads present an opportunity for capturing samples on a functionalized solid phase subject both to fluid flow and to applied magnetic field. Recently examples have integrated on-chip magnetic fields to concentrate and manipulate bead-bound samples, typically by splitting droplets and collecting beads in one of the two daughter droplets.[13, 27-31, 38, 39] We have expanded magnetic bead capture to take advantage of the simple tunability (1:1 to 1:5 daughter droplet ratio) and high throughput (200-500 Hz) of K-channel droplet splitting.

The K-channel device was modified to incorporate an array of N52 magnets 250 μm away from the main channel-cross-channel intersection (Figure II.5a). As droplet-encapsulated superparamagnetic beads approached the K-channel, the magnetic force concentrated them toward one side of the droplet as:

$$F_m = (1/\mu_0) * (m * \nabla)B \qquad (8)$$

where F_m is the magnetic force on a point-like magnetic dipole (bead), μ_0 is the magnetic permeability of a vacuum, m is the magnetic moment of the dipole (assumed to be saturated and position independent in the vicinity of the magnet), and B is the magnetic field.[28, 48]

When performing magnetic bead operations in droplets, uniform magnetic bead encapsulation is of particular interest. Bead encapsulation in the presence of a magnetic field has

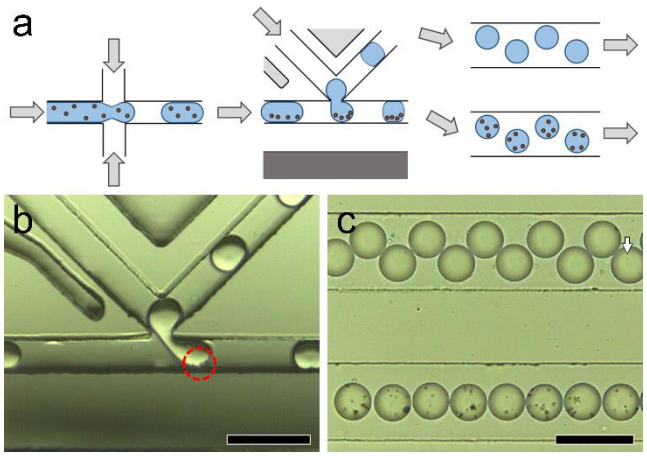

Figure II.5. Magnetic bead capture. a) Schematic of bead capture device. Arrows indicate flow directions. Magnetic bead (brown) containing droplets (blue) form at a flow focusing geometry (left) followed by droplet splitting under oil flow at a K-channel (middle). During droplet splitting, a magnet (dark gray) pulls beads into only one of the two daughter droplets. Electrode channels (light gray) are not enabled during this operation. After droplet splitting, waste droplets without magnetic beads (upper) and sample droplets with magnetic beads (lower) flow to the detection channels (right). b) The nearby magnet pulls beads (circled in red) into one of the two daughter droplets during droplet splitting at the K-channel. c) The detection channels show high incidence (96%) of magnetic beads in the sample droplets (lower channel) and low incidence (4%) of magnetic bead loss (white arrow) into waste droplets (upper channel). (scale bar = 100 µm)

been shown to result in ordering and chain formation that lead to variance in per droplet bead abundance.[27] To this end, we displaced the droplet-forming flow focusing structure 1 cm from the leading edge of the magnet. A serpentine mixer directly upstream of encapsulation also contributed to the disruption of chain formation. Finally, we compensated for gravity-based bead settling and aggregation by shortening the tubing connection to the device (5 cm) and by adding Optiprep Density Gradient Medium (Sigma Aldrich) to the bead suspension. This decreased magnetic bead settling, and first passing beads through a 15 µm pore microfluidic device removed contaminants and large aggregates prior to use. Overall, 10 ± 3 superparamagnetic beads (1-3 µm diameter) were encapsulated per droplet.

As droplets approached the magnet, beads were selectively pulled into the lower hemisphere of the droplet (away from the K-channel intersection), and, after droplet splitting, the

majority of beads were retained in the main channel. Daughter droplets flowed through a serpentine mixer to recirculate beads before passing into a detection channel region. Figures II.5b-c provide representative examples of bead capture at the K-channel (Movie SMII.9) and at the detection channels (Movie SMII.10). Under these conditions, K-channel droplet splitting retained 96 ± 1% of magnetic beads when removing 50 ± 1% of droplet volume at a droplet frequency of 380 ± 20 Hz. (See Figure II.S4 for a detailed description of magnetic bead capture analysis.) While some devices have reported larger droplet fractions removed (60-90%) or higher capture efficiencies (98-100%), K-channel magnetic separation proceeds at droplet frequencies more than an order of magnitude faster than these approaches (0.5-30 Hz).[27-29] We anticipate that K-channel bead retention would be similarly improved by velocity reduction to increase the residence time for beads in the magnetic field. Ongoing work seeks to concentrate magnetic beads in smaller droplet fractions per splitting event.

Given the versatile range of K-channel operations, we expanded our K-channel devices to include a full sample washing mode. Figure II.6 (Movie SMII.11) demonstrates how magnetic bead-laden droplets passing through the device (Figure II.6a) split at the first K-channel (Figure II.6b), are respaced at an oil channel (Figure II.6c), and double upon water injection at the second K-channel (Figure II.6d). By removing 46 ± 2 % of droplet volume during splitting followed by injecting 93 ± 7 % of remaining daughter droplet volume, the washing device effected a net concentration decrease of 48 % with only a net volume increase of 7 % across the device. Importantly, droplet washing at 200 ± 10 Hz successfully retained 98 ± 5 % of encapsulated magnetic beads. While Electrowetting on Dielectric (EWOD) devices routinely manipulate small droplet populations or single droplets at a time through washing steps,[49] very few examples have interfaced this technique into continuously flowing droplets.[38, 39] This K-channel approach

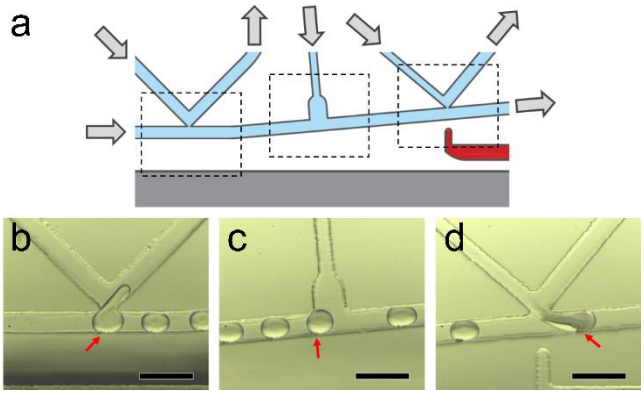

Figure II.6. Magnetic Bead Washing. (a) Schematic of washing device. Light gray arrows indicate flow direction. After magnetic bead encapsulation in droplets (not shown) droplets (b) split at the leftmost K-channel under parallel oil flow, (c) respace at an oil channel, and (d) double in size upon injection at the rightmost K-channel using parallel water flow in an electric field (supplied by red electrode channels in schematic). Magnetic beads (highlighted by red arrows) are pulled toward the magnet (dark gray in schematic) and are retained during operations. (scale bars = 100 μm)

provides a rapid (200 Hz), highly efficient (98% retention), and tunable washing strategy for continuously flowing droplet microfluidic systems.

CONCLUSIONS

Broadly speaking, methods for fluid manipulation within droplet microfluidics typically rely upon monofunctional device components that have limited capacity to be dynamically controlled. In contrast, the K-channel is a multifunctional tool that in a single design can accomplish a wide range of common droplet operations. Droplets can be injected into, extracted from, split, and respaced. Integration of a magnet even allows selective sample manipulation in droplet splitting and washing operations. As a modular building block, parallel and serial combinations of K-channels can be interfaced to perform sophisticated chemical and biochemical reaction sequences. Furthermore, we anticipate that K-channel's robustness, ease of tuning, and versatility in changing operations will be very attractive features, especially in using this device as a fundamentally enabling tool for rapid optimization of on-chip chemistry.

ACKNOWLEDGEMENTS

We gratefully acknowledge financial support from the National Institute of Health (CA191186) and the Mayo-Illinois Alliance for Technology-Based Healthcare. S.R.D. was supported by the National Science Foundation Graduate Research Fellowship Program and by a Robert C. and Carolyn J. Springborn Fellowship (University of Illinois at Urbana-Champaign). We also thank Professor Amar Basu (Wayne State University) for access to Droplet Morphometry and Velocimetry (DMV) software, Daniel A. McCurry (University of Illinois at Urbana-Champaign) for help in developing LabView software for controlling pressure-driven flow, Jamy Lee (University of Michigan) for assistance with enzyme chemistry in droplets, and Richard M. Graybill (University of Illinois at Urbana-Champaign) for helpful discussions.

REFERENCES

1. T. Thorsen, R. W. Roberts, F. H. Arnold and S. R. Quake, *Physical Review Letters*, 2001, **86**, 4163-4166.
2. H. Song, J. D. Tice and R. F. Ismagilov, *Angewandte Chemie International Edition*, 2003, **42**, 768-772.
3. T. M. Squires and S. R. Quake, *Reviews of Modern Physics*, 2005, **77**, 977-1026.
4. S.-Y. Teh, R. Lin, L.-H. Hung and A. P. Lee, *Lab on a Chip*, 2008, **8**, 198-220.
5. M. T. Guo, A. Rotem, J. A. Heyman and D. A. Weitz, *Lab on a Chip*, 2012, **12**, 2146-2155.
6. U. Tangen, G. A. Minero, A. Sharma, P. F. Wagler, R. Cohen, O. Raz, T. Marx, T. Ben-Yehezkel and J. S. McCaskill, *Biomicrofluidics*, 2015, **9**, 044103.
7. S. Mashaghi, A. Abbaspourrad, D. A. Weitz and A. M. van Oijen, *TrAC Trends in Analytical Chemistry*, 2016, **82**, 118-125.
8. A. Armada-Moreira, E. Taipaleenmaki, F. Itel, Y. Zhang and B. Stadler, *Nanoscale*, 2016, **8**, 19510-19522.

9. J. F. Edd, D. Di Carlo, K. J. Humphry, S. Koster, D. Irimia, D. A. Weitz and M. Toner, *Lab on a Chip*, 2008, **8**, 1262-1264.

10. H. N. Joensson and H. Andersson Svahn, *Angewandte Chemie International Edition*, 2012, **51**, 12176-12192.

11. E. X. Ng, M. A. Miller, T. Jing and C.-H. Chen, *Biosensors and Bioelectronics*, 2016, **81**, 408-414.

12. B. Teste, A. Ali-Cherif, J. L. Viovy and L. Malaquin, *Lab on a Chip*, 2013, **13**, 2344-2349.

13. R. Gao, Z. Cheng, A. J. deMello and J. Choo, *Lab on a Chip*, 2016, **16**, 1022-1029.

14. A. Rotem, O. Ram, N. Shoresh, R. A. Sperling, A. Goren, D. A. Weitz and B. E. Bernstein, *Nat. Biotechnol.*, 2015, **33**, 1165-1172.

15. A. C. Larsen, M. R. Dunn, A. Hatch, S. P. Sau, C. Youngbull and J. C. Chaput, *Nat. Commun.*, 2016, **7**.

16. P. Garstecki, M. J. Fuerstman, H. A. Stone and G. M. Whitesides, *Lab on a Chip*, 2006, **6**, 437-446.

17. P. Zhu and L. Wang, *Lab Chip*, 2017, **17**, 34-75.

18. L. Li, J. Q. Boedicker and R. F. Ismagilov, *Analytical Chemistry*, 2007, **79**, 2756-2761.

19. A. R. Abate, T. Hung, P. Mary, J. J. Agresti and D. A. Weitz, *Proceedings of the National Academy of Sciences*, 2010, **107**, 19163-19166.

20. A. Sciambi and A. R. Abate, *Lab on a Chip*, 2014, **14**, 2605-2609.

21. I. Akartuna, D. M. Aubrecht, T. E. Kodger and D. A. Weitz, *Lab Chip*, 2015, **15**, 1140-1144.

22. L. Frenz, K. Blank, E. Brouzes and A. D. Griffiths, *Lab on a Chip*, 2009, **9**, 1344-1348.

23. M. Lee, J. W. Collins, D. M. Aubrecht, R. A. Sperling, L. Solomon, J.-W. Ha, G.-R. Yi, D. A. Weitz and V. N. Manoharan, *Lab on a Chip*, 2014, **14**, 509-513.

24. L. Ménétrier-Deremble and P. Tabeling, *Physical Review E*, 2006, **74**, 035303.

25. J. Nie and R. T. Kennedy, *Analytical Chemistry*, 2010, **82**, 7852-7856.

26. M. Yamada, S. Doi, H. Maenaka, M. Yasuda and M. Seki, *J. Colloid Interface Sci.*, 2008, **321**, 401-407.

27. E. Brouzes, T. Kruse, R. Kimmerling and H. H. Strey, *Lab on a Chip*, 2015, **15**, 908-919.

28. B. Verbruggen, T. Tóth, M. Cornaglia, R. Puers, M. A. M. Gijs and J. Lammertyn, *Microfluidics and Nanofluidics*, 2015, **18**, 91-102.

29. B. Verbruggen, K. Leirs, R. Puers and J. Lammertyn, *Microfluidics and Nanofluidics*, 2015, **18**, 293-303.

30. D. Lombardi and P. S. Dittrich, *Analytical and Bioanalytical Chemistry*, 2011, **399**, 347-352.

31. H. Lee, L. Xu, B. Ahn, K. Lee and K. W. Oh, *Microfluidics and Nanofluidics*, 2012, **13**, 613-623.

32. Z. Zhu and C. J. Yang, *Acc. Chem. Res.*, 2017, **50**, 22-31.

33. T. S. Kaminski, O. Scheler and P. Garstecki, *Lab Chip*, 2016, **16**, 2168-2187.

34. Y. Xia and G. M. Whitesides, *Angewandte Chemie International Edition*, 1998, **37**, 550-575.

35. M. Rhee, Y. K. Light, S. Yilmaz, P. D. Adams, D. Saxena, R. J. Meagher and A. K. Singh, *Lab on a Chip*, 2014, **14**, 4533-4539.

36. Y. Ding, X. Casadevall i Solvas and A. deMello, *Analyst*, 2015, **140**, 414-421.

37. A. H. C. Ng, U. Uddayasankar and A. R. Wheeler, *Analytical and Bioanalytical Chemistry*, 2010, **397**, 991-1007.

38. H. Lee, L. Xu and K. W. Oh, *Biomicrofluidics*, 2014, **8**, 044113.

39. X. Pan, S. Zeng, Q. Zhang, B. Lin and J. Qin, *ELECTROPHORESIS*, 2011, **32**, 3399-3405.

40. D. Chen, W. Du, Y. Liu, W. Liu, A. Kuznetsov, F. E. Mendez, L. H. Philipson and R. F. Ismagilov, *Proceedings of the National Academy of Sciences*, 2008, **105**, 16843-16848.

41. R. Lin, J. S. Fisher, M. G. Simon and A. P. Lee, *Biomicrofluidics*, 2012, **6**, 024103-024103-024110.

42. U. Tangen, A. Sharma, P. Wagler and J. S. McCaskill, *Biomicrofluidics*, 2015, **9**, 014119.

43. G. T. Roman, M. Wang, K. N. Shultz, C. Jennings and R. T. Kennedy, *Analytical Chemistry*, 2008, **80**, 8231-8238.

44. A. S. Basu, *Lab on a Chip*, 2013, **13**, 1892-1901.

45. K. W. Oh, K. Lee, B. Ahn and E. P. Furlani, *Lab on a Chip*, 2012, **12**, 515-545.

46. J. Lim, O. Caen, J. Vrignon, M. Konrad, V. Taly and J.-C. Baret, *Biomicrofluidics*, 2015, **9**, 034101.

47. D. Hess, A. Rane, A. J. deMello and S. Stavrakis, *Anal. Chem.*, 2015, **87**, 4965-4972.

48. M. A. M. Gijs, *Microfluidics and Nanofluidics*, 2004, **1**, 22-40.

49. N. M. Lafrenière, J. M. Mudrik, A. H. C. Ng, B. Seale, N. Spooner and A. R. Wheeler, *Analytical Chemistry*, 2015, **87**, 3902-3910.

SUPPLEMENTARY INFORMATION

The supplementary information in its original format (including videos) may be accessed online at doi: 10.1021/acs.analchem.6b05041.

Supplementary Movie SMII.1. K-channel injection. High K-channel pressure with electric field injects fluid into droplets. The K-channel flows from right to left.

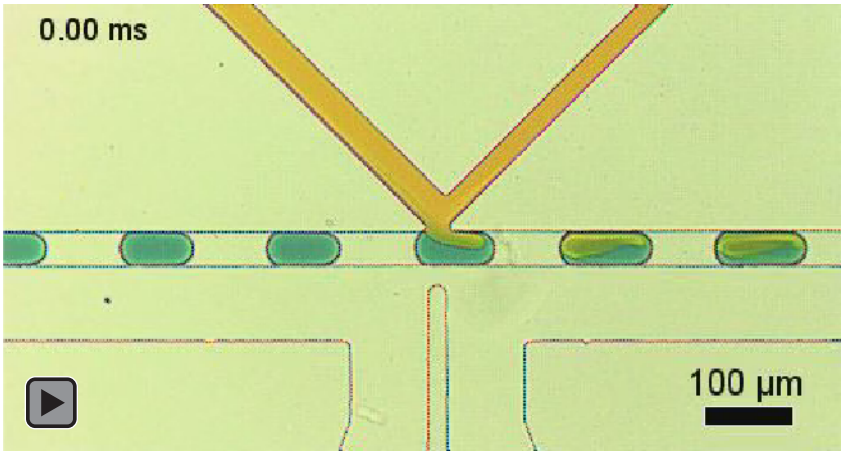

Supplementary Movie SMII.2. K-channel extraction. Low K-channel pressure with electric field extracts fluid from droplets. The K-channel flows from right to left.

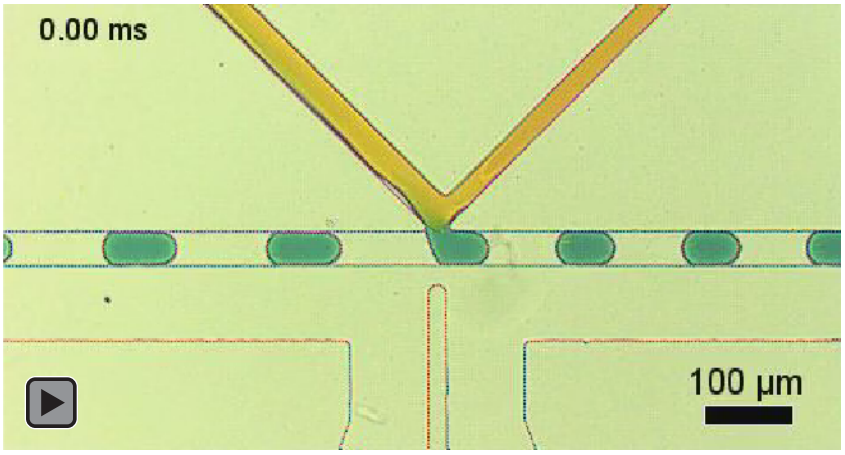

Supplementary Movie SMII.3. K-channel stable interface. Moderate K-channel pressure without electric field establishes a stable droplet-K-channel interface. The K-channel flows from right to left.

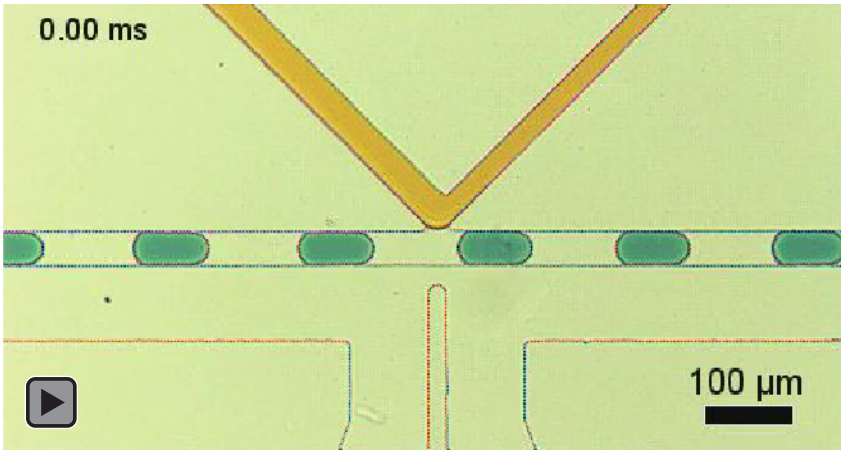

Supplementary Movie SMII.4. K-channel droplet splitting. Low K-channel pressure without electric field splits droplets. Oil flows from right to left across the K-channel.

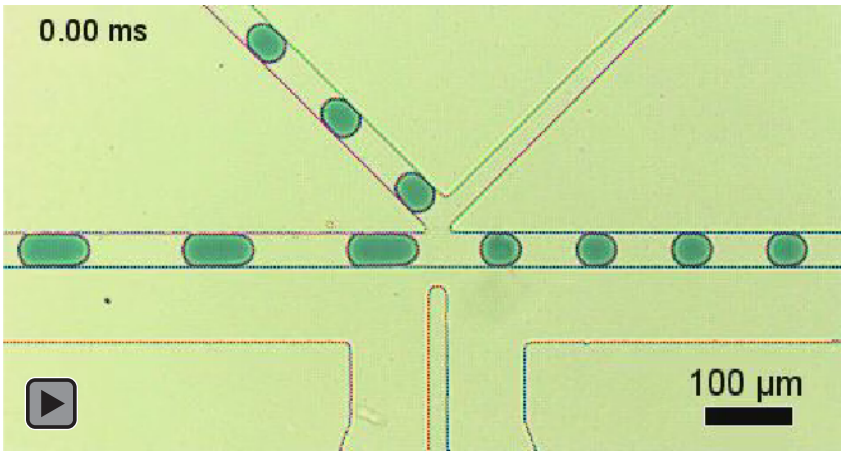

Supplementary Movie SMII.5. Injection with pulsed electric field. If the device is in the pressure range for forming a stable droplet-K-channel interface, temporarily applying the electric field can inject into a subset of the total water droplet population (originally non-fluorescent). The duration of the electric field pulse is controlled manually or by an in-house LabView application.

Supplementary Movie SMII.6. Serial K-channel operation. Two K-channels inject reagents into droplets in the presence of electric fields at each K-channel. The leftmost K-channel flows left to right, and the rightmost K-channel flows right to left. Serial K-channels may also perform non-identical operations (i.e., injection followed by droplet splitting).

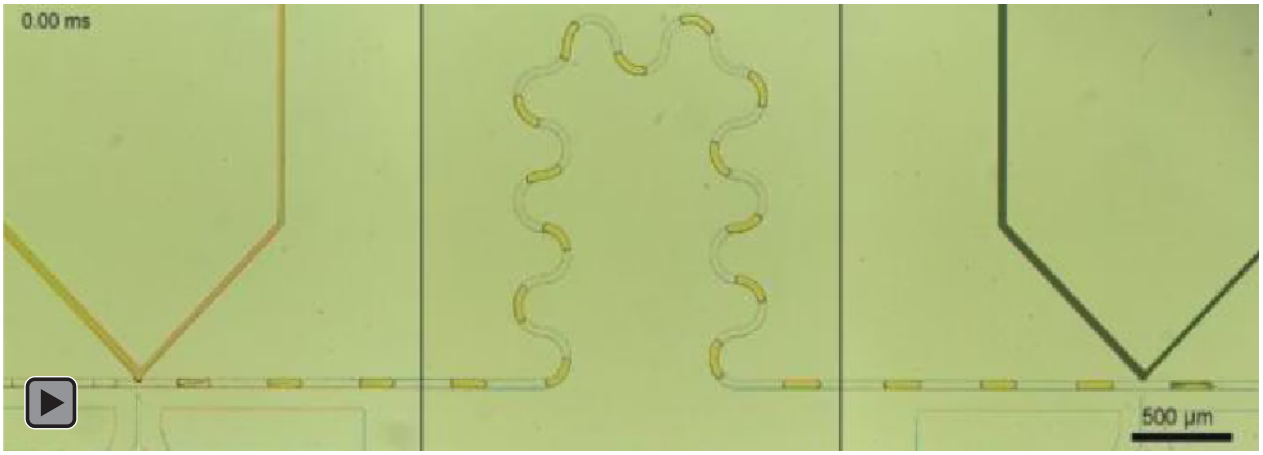

Supplementary Movie SMII.7. K-channel material exchange. As water injects into passing droplets, the K-channel extracts fluorescein from the droplets. Continuous flow through the K-channel (right to left) reduces the risk for droplet-to-droplet cross-contamination by washing away extracted fluorescein.

Supplementary Movie SMII.8. K-channel-enabled enzyme chemistry. Visualizing the downstream incubation region demonstrates β-galactosidase activity on K-channel-injected resorufin β-D-galactopyranoside in droplets (flowing left to right). Fluorescence intensity increases as the concentration of fluorescent product increases in each droplet. Adjusting the magnitude of K-channel injection doses enzyme droplets with desired substrate quantities.

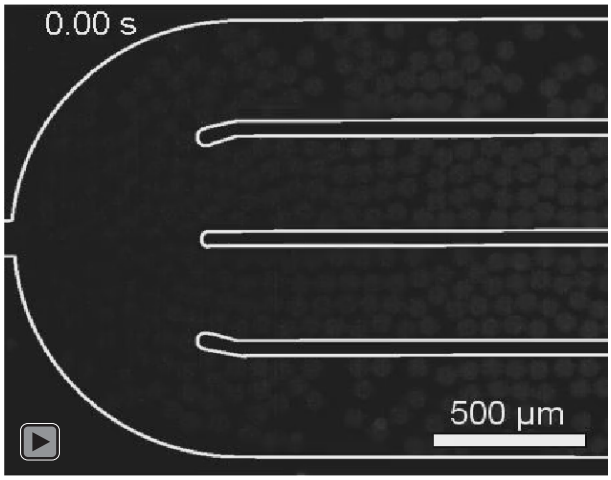

Supplementary Movie SMII.9. K-channel magnetic bead capture. An assembly of 1/2'' x 1/4'' x 1/8'' N52 magnets positioned ~250 µm from the K-channel pulls magnetic beads away from the K-channel as low K-channel pressure without electric field splits droplets. As a result, most magnetic beads concentrate in main channel droplets (lower), and few escape into waste droplets (upper). Oil flows from left to right across the K-channel.

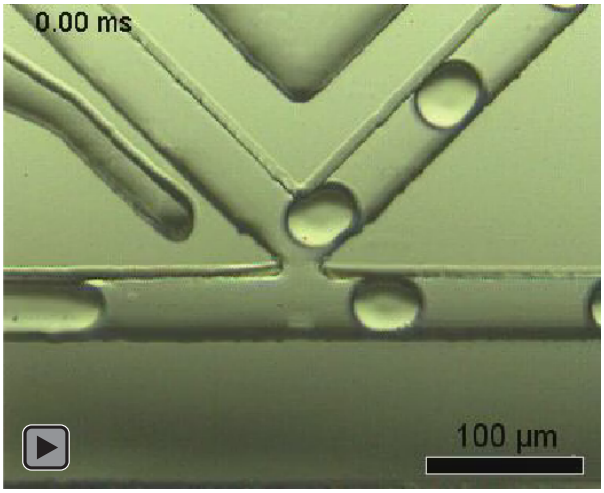

Supplementary Movie SMII.10. Magnetic bead detection. After magnetic bead capture, main channel droplets with captured magnetic beads (lower) and waste channel droplets with lost magnetic beads (upper) flow through a slower velocity, larger cross-section channel further removed from the magnet (to reduce marginalization of the beads) for analysis.

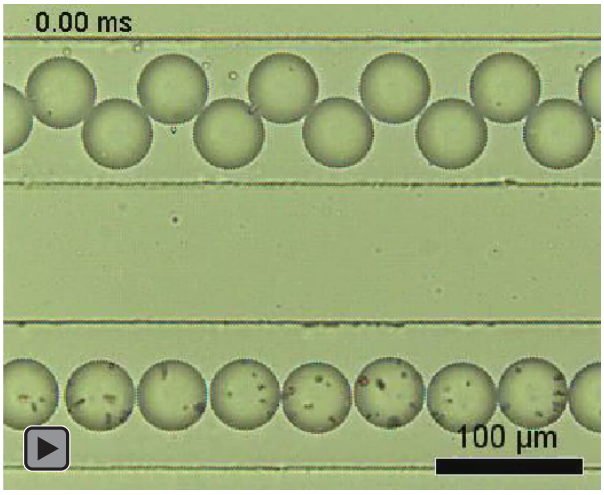

Supplementary Movie SMII.11. Magnetic bead washing. Droplet splitting removes 46 ± 1 % of droplet volume (leftmost panel), an oil channel respaces droplets (center panel), and water injection (left to right K-channel flow) adds 93 ± 7 % of remaining droplet volume (rightmost panel) at 200 Hz on a single device. During this sequence, 98 ± 5 % of droplet-encapsulated superparamagnetic beads were retained, initial droplet concentration was reduced by 48 %, and droplet volume increased by only 7 %.

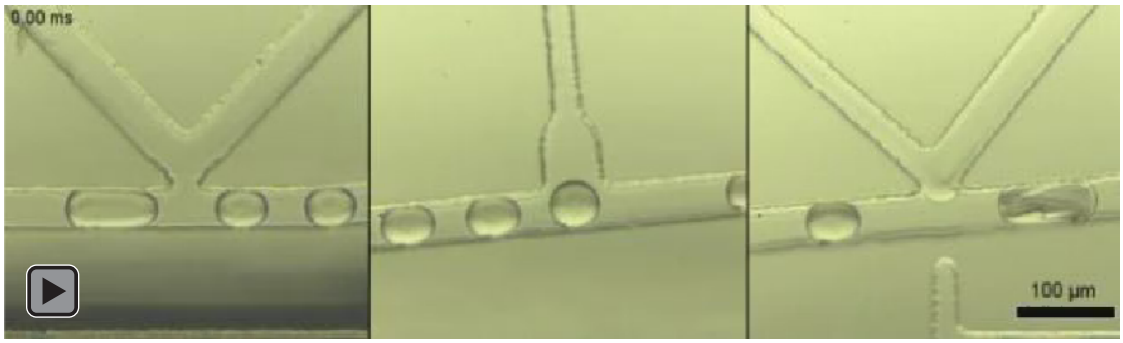

SUPPLEMENTARY FIGURES

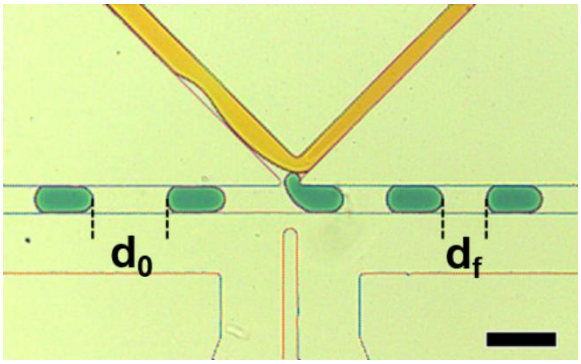

Figure II.S1. K-channel oil extraction. Droplets flow left to right. The K-channel aqueous phase flows right to left, and no electric field is applied. For low pressures within the range of stable droplet-K-channel interface formation, a fraction of the oil selectively extracts through the K-channel. In this example, the original distance between droplets, d_0, is reduced by 40% to the final distance, d_f. Droplet volume and composition are unaffected. (scale bar = 100 µm)

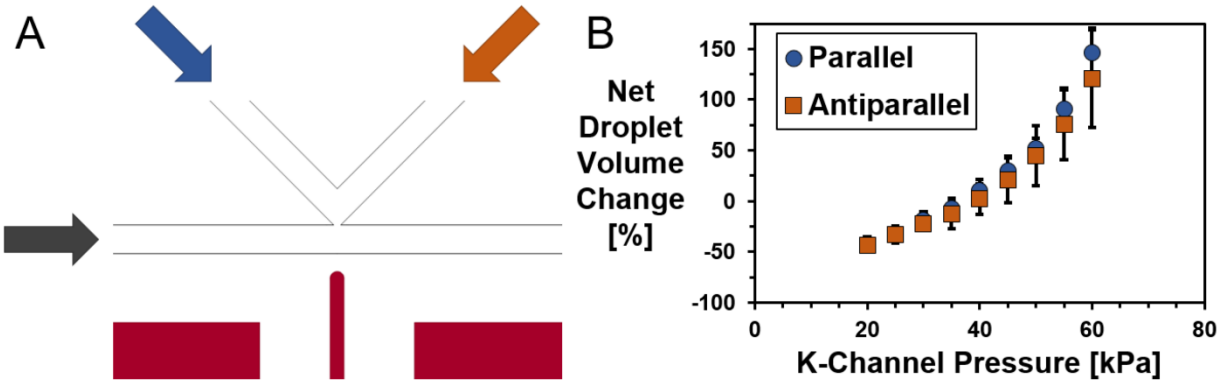

Figure II.S2. Directional independence of K-channel operations. a) Parallel (blue) and antiparallel (orange) arrows indicate flow through a symmetric K-channel relative to droplet flow (dark gray) arrow. b) Net volume change for each applied K-channel pressure does not vary significantly with flow direction for a symmetrical K-channel device.

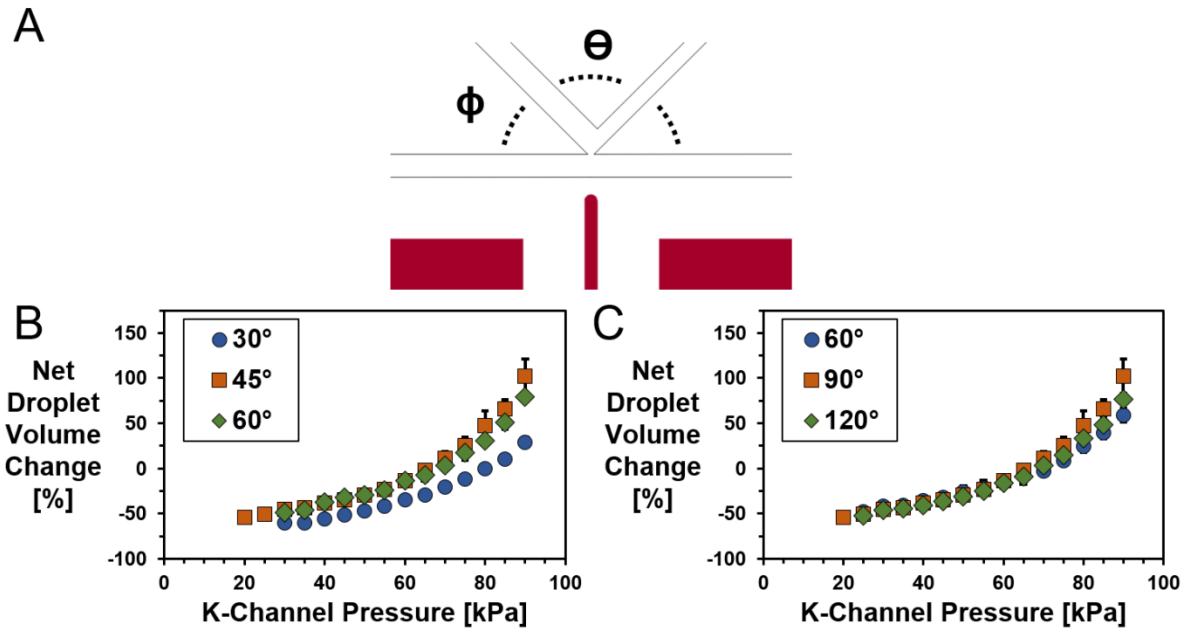

Figure II.S3. K-channel cross-channel angle characterization. a) K-channel schematic highlighting the angle between the cross-channel and the main channel, ϕ, and the angle between the two side channels, Θ. b) Varying angle ϕ has little effect on K-channel performance. c) Varying angle Θ does not significantly impact K-channel performance.

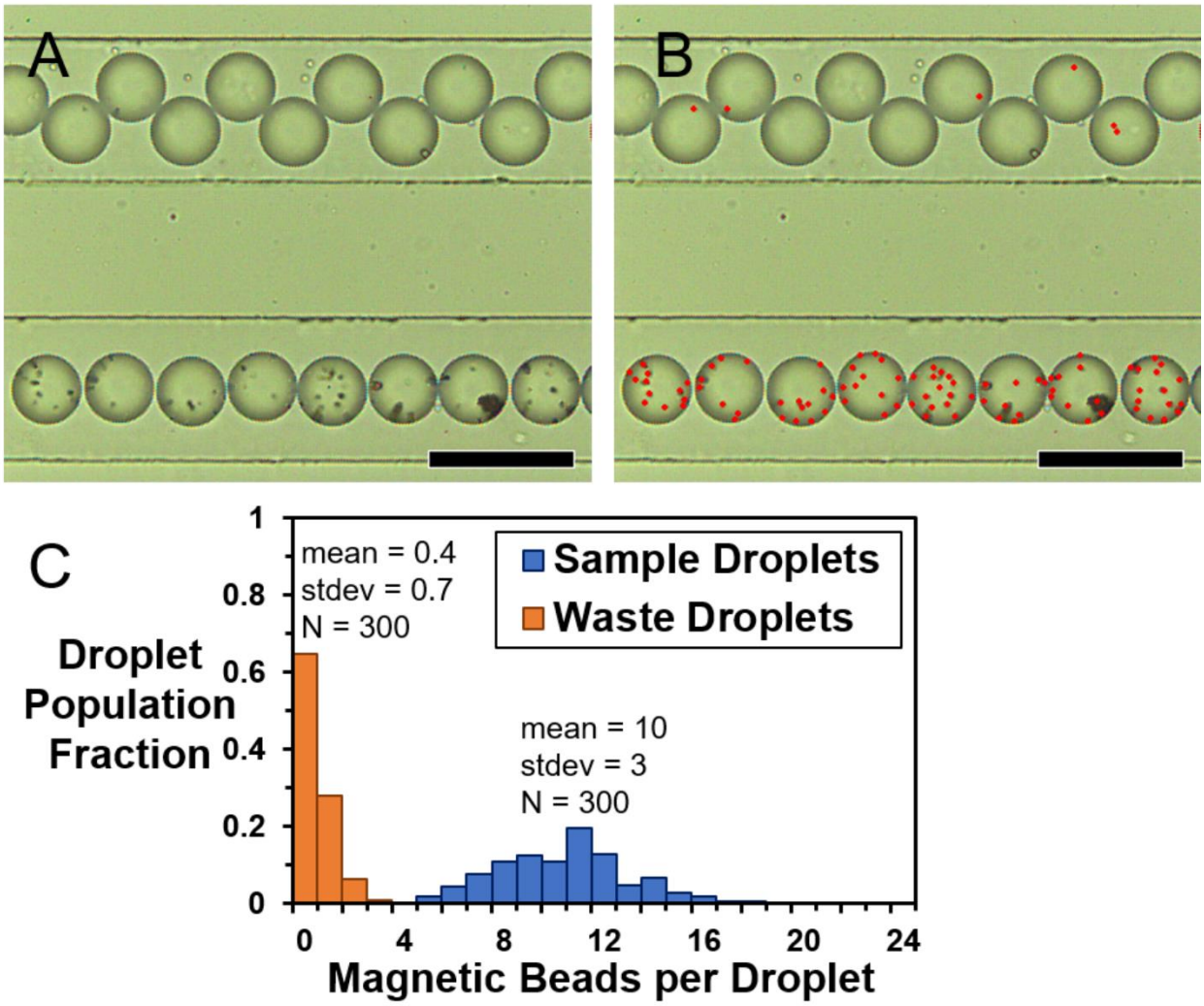

Figure II.S4. Magnetic bead quantitation. (a) Original image of detection region. (b) Red dots highlight magnetic beads or magnetic bead aggregates. Each independently circulating body (single particles and aggregates of many particles) is counted as one magnetic bead entity. By monitoring each droplet across the entire detection region, magnetic beads from the fringes of droplets can be detected, and aqueous extra-droplet satellites and channel defects can be discriminated from magnetic beads. (c) Histogram of magnetic bead distribution in main channel sample droplets and in waste channel droplets. For each droplet population, N = 3 devices with N = 100 droplets for each device. (scale bars = 100 μm)

Chapter III

Droplet Microfluidics in Thermoplastics: Device Fabrication, Droplet Generation, and Content Manipulation Using Integrated Electric and Magnetic Fields

Reproduced from Sahore, V., Doonan, S.R., and Bailey, R.C. "Droplet Microfluidics in Thermoplastics: Device Fabrication, Droplet Generation, and Content Manipulation Using Integrated Electric and Magnetic Fields." *Analytical Methods* **2018**, *10*: 4264-4274. *with permission from the Royal Society of Chemistry*. *Available at* doi: 10.1039/C8AY01474D.

INTRODUCTION

Droplet microfluidic devices segment samples of interest into small-scale volumes (often fL to nL) encapsulated within an immiscible carrier fluid. Sample segmentation has multiple analytical advantages including minimized sample loss to channel fouling and low reagent consumption. Additionally, inert carrier oil prevents significant cross-contamination among sample volumes, and the small length scales and flow characteristics inside droplets enhance mass-transport, thus making them suitable for applications using limited sample volumes and requiring fast reactions.[1-4] Accordingly, droplets have found utility in a variety of integrated (bio)chemical analyses such as single-cell protein profiling,[5] genome sequencing,[6] chromatin digestion and nucleosome positioning determination,[7] enzyme-modulator screening,[8, 9] protease activity determination,[10] and polymerase chain reaction of single-copy DNA molecules.[11] Droplets are primarily generated using T-junction[12] and flow-focusing configurations,[13] and integrated

downstream operations have been developed to add reagents,[14, 15] incubate reactions,[16] merge and split droplets,[15, 17, 18] or use electric and magnetic fields to sort droplets of interest.[19-21]

Initially, droplet microfluidic devices were tested in different materials including poly(dimethyl siloxane) (PDMS),[22] urethane,[23] and thermoplastics,[12, 24, 25] with PDMS emerging as the most popular due to the ease of fabrication via soft-lithography techniques.[6, 11, 16, 26] Moreover, rapid prototyping of PDMS and amenability to the complex, integrated designs needed for droplet analysis have further established PDMS as the material of choice for most droplet microfluidic architectures.[27, 28] These PDMS droplet devices have well-characterized surface chemistries, but they are not suitable for large-scale production and have some limitations in terms of solvent compatibility and changes in material surface properties over time.[29, 30] Other conventional materials for prototyping, such as silicon[31] and glass,[32] have also been used to make microfluidic devices, however, the material hardness, inability to be thermo-molded, and high manufacturing costs present potential limitations for their usage in applications requiring mass production.

Mass manufacturable thermoplastics take advantage of well-characterized and stable chemistries and are the material of choice for many large-volume, disposable consumables, including many within the healthcare marketplace.[33] Depending upon the critical dimensions and required channel quality, techniques such as laser engraving,[34] hot embossing,[35] and injection molding[36] are capable of imprinting micro-channels into thermoplastic materials. Importantly, these all have high-volume production capability. Laser engraving is the simplest method with rapid prototyping potential, however, the quality of native engraved channels, including channel roughness and uniformity, is often insufficient and requires additional chemical processing steps to make them suitable for droplet microfluidic operations.[37] Hot embossing and injection molding

techniques both use a master mold from which micro-channel features can be transferred into moldable thermoplastics. Typically, master fabrication employs state-of-the-art semiconductor processing techniques such as photolithography, deep reactive ion etching (DRIE), and electroplating to generate complex designs with critical dimensions in micron to sub-micron scales suitable for droplet microfluidic operations.[38, 39]

Commonly used thermoplastics for microfluidic applications are poly(methyl methacrylate) (PMMA), cyclic olefin polymer (COP), polycarbonate (PC), and polypropylene (PP). PMMA and COP are interesting materials—particularly as an intermediate step between prototyping and mass production—due to their moderate-cost, easy availability, and excellent optical transparency. The amenability of PMMA and COP to hot embossing and injection molding, the low bonding temperatures required for PMMA and COP layers, and the compatibility of PMMA and COP with standard chip-to-world microfluidic interconnects further make them compelling materials for fabricating complex designs needed for droplet microfluidic operations.[40] Moreover, well-studied surface properties of PMMA and COP facilitate the introduction of hydrophobic surface modifications critical to stable droplet generation and manipulation.[41, 42]

Beyond droplet generation,[12, 13] the range of useful droplet manipulations includes direct reagent injection into droplets[14, 15] and droplet splitting to parallelize reactions or remove waste,[15, 43, 44] among others,[1] providing needed control over in-droplet chemistry. While these operations have been well characterized in PDMS, translation of droplet technologies into thermoplastics for mass fabrication depends on robustly demonstrating these processes in thermoplastic devices. Droplets form at T-junctions, direct injection occurs via electrically-mediated picoinjectors,[14] and splitting occurs at channel bifurcations.[44, 45] More recently, we developed a multifunctional K-channel geometry for manipulating droplets and leveraged it for not only direct injections but also

for selective droplet decanting and washing steps via integrated magnetic field that concentrated in-droplet magnetic beads during droplet splitting operations.[15] To realize these components in thermoplastics, it is critical to establish material compatibility with required electric and magnetic fields as well as to fundamentally replicate channel features with spatial resolution and fidelity comparable to PDMS. Ideally, droplet microfluidic device components would be tested both individually and as integrated devices to broadly demonstrate the applicability of thermoplastic materials for sophisticated droplet microfluidic analyses.

In this work, we have developed a fabrication workflow to produce droplet microfluidic devices in mass-manufacturable thermoplastics, integrating droplet generation, electric field-assisted reagent injection, and droplet splitting with magnetic bead collection. Silicon masters were fabricated using photolithography and DRIE. Then microfluidic channels were hot embossed into PMMA and COP using this template, followed by solvent-assisted low-temperature bonding and ultraviolet light-assisted hydrophobic modification of channel surfaces. After fabrication, several essential droplet microfluidic functions were demonstrated in PMMA. A simple T-junction design was used to show stable droplet generation without surface wetting. Next, electric field-assisted reagent injection into passing droplets was demonstrated using both picoinjector and K-channel configurations. Subsequently, magnetic field compatibility was evaluated with K-channel-based droplet splitting for magnetic bead concentration. These operations were then combined to realize an integrated magnetic bead-in-droplet washing device with both electric and magnetic fields to demonstrate the suitability of this fabrication workflow to enable robust droplet microfluidic applications in thermoplastic materials. Finally, we used the integrated microfluidic devices made in COP to perform an in-droplet β-Galactosidase enzymatic assay and demonstrated their potential

for (bio)chemical applications. These complex devices provide an early translational step in engineering mass-fabricated thermoplastic devices for integrated in-droplet (bio)chemical assays.

EXPERIMENTAL SECTION

Chemicals and Materials

Bare silicon wafers were obtained from University Wafers (Boston, MA). 1.5 mm and 2 mm thick poly (methyl methacrylate), PMMA, sheets were purchased from Evonik (Sanford, ME). 1 mm and 2 mm thick cyclic olefin polymer, COP, ZEONOR 1060 R sheets were purchased from Zeon Specialty Materials (San Jose, CA). Fluorinert FC 40, optiprep density gradient medium, 10-μm size streptavidin-functionalized magnetic beads, and biotin-β-Galactosidase were purchased from Sigma Aldrich (Milwaukee, WI). Novec 7500 Engineered Fluid was from 3M (Maplewood, MN). Fluorosurfactant-008 for droplet stabilization was purchased from RAN Biotechnologies (Beverly, MA). Potassium hydroxide pellets and resorufin-β-D-galactopyranoside were from Thermo Fisher Scientific (Waltham, MA). Food coloring dyes were obtained from McCormick (Baltimore, MD). Heptadecafluoro-1,1,2,2-tetrahydrodecyltrichlorosilane used for PMMA and COP channel surface modification was purchased from Gelest (Morrisville, PA). All solutions were passed through Nylon syringe filters (0.2 μm pore size) from VWR International (Radnor, PA) to remove particulates. NdFeB permanent magnets were purchased from K&J Magnetics, Inc. (Pipersville, PA). All aqueous solutions were prepared in 18 MΩ deionized water purified using a Barnstead GenPure water purifying system from Thermo Scientific (Waltham, MA).

Device Design and Fabrication

Devices were designed using AutoCAD, and the masks were printed on transparent thin film sheets (CAD/Art Services, Bandon, OR). Five different designs comprising the T-junction; picoinjector; electrical K-channel; magnetic K-channel; and integrated T-junction, electrical K-channel and magnetic K-channel configurations were tested. All the designs were initially tested using PMMA, and subsequently after initial testing, the enzymatic assay was performed with the integrated devices manufactured in COP. All channels (except the wider K-channel side with 150 μm width) were 100 μm in width. K-channel and picoinjector junctions with the main channel had 100 μm and 50 μm wide openings, respectively. Typical channel lengths were 1.3 to 7.5 cm. Electrode channels were spaced 100 μm from the main channel, and the permanent magnet was spaced 500 μm from the main channel. All device inlets were 1.2 mm in diameter.

Microfluidic channels were hot embossed into 1.5 mm thick PMMA or 1 mm thick COP sheets using silicon masters according to the overall workflow described in Figure III.1. To generate masters, 4" bare silicon wafers were spin coated with SPR220 photoresist (Dow Chemical, Midland, MI) and exposed to UV light (MA-6/BA-6 Mask and Bond Aligner, SUSS MicroTec, Garching, Germany) through the appropriate photomask. After a pre-development bake the wafers were developed using AZ726 metal ion free developer. Developed wafers were etched with deep reactive ion etching (STS Peagasus4, SPTS Technologies, Newport, UK) with etching gas, SF_6, at 400 sccm; passivation layer gas, C_2F_6, at 200 sccm; for 100 ± 10 cycles; and 7 or 6 min. To remove the photoresist mask and residual polymer the etched wafers were cleaned using oxygen plasma: 800 sccm at 800 W and 150°C for 6 min (YES CV200RFS, Yield Engineering Systems, Livermore, CA). Cleaned wafers were then diced (ADT 7100 Dicing Saw, Advanced Dicing Technologies, Yokneam, Israel) to obtain the individual silicon masters. To reduce the feature roughness the diced masters were etched with 40% KOH at 70°C for 5 min. Before

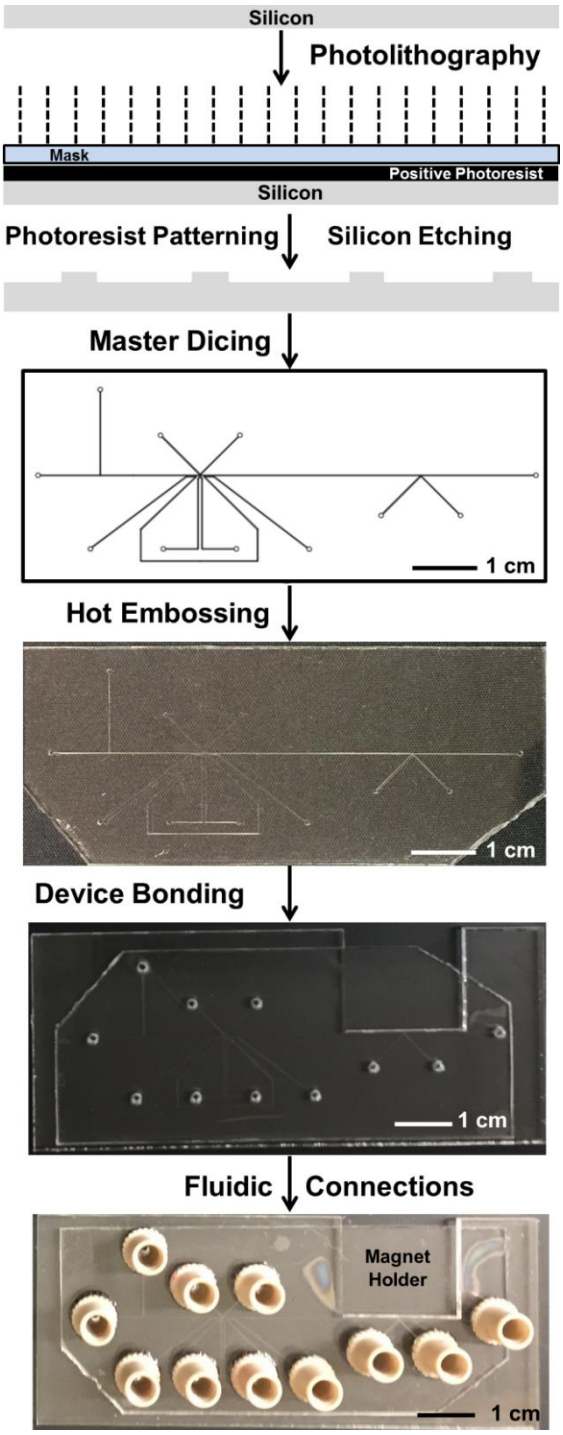

Figure III.1. Device manufacturing in poly(methyl methacrylate) (PMMA) or cyclic olefin polymer (COP) through hot embossing using silicon masters fabricated by photolithography and deep reactive ion etching processes.

embossing, the silicon masters were ultrasonically cleaned for 10 min each using acetone, IPA and DI water, respectively.

Hot embossing was performed on PMMA or COP using an in-house procedure. A 1.5 mm thick PMMA or 1 mm thick COP sample was aligned against the silicon master, and a glass slide was positioned on each side of the pair, followed by a copper plate for each side. This assembly was firmly clamped together with C-clamps (McMaster, Aurora, OH).[46, 47] The complete clamp assembly was placed inside an oven (Thermo Scientific) at 135°C for 26 min for embossing, and at 90°C for 10 min followed by cooling to room temperature over 30 min to complete de-embossing.

For each embossed device, fluidic inlets (1.2 mm diameter) were drilled through another 2 mm thick PMMA sample using a CO_2 laser cutter (Universal Laser Systems, Scottsdale, AZ) or 2 mm thick COP sample using the drill press (Cameron Micro Drill Presses, Sonora, CA). The position of these inlets complemented the channel geometry of the corresponding embossed sample. For the magnetic K-channel and integrated devices a rectangular slot was also cut in this layer to hold the permanent magnet. Drilled samples were flattened at 110°C for 26 min for PMMA and 20 min for COP in the oven using the clamping assembly mentioned above (but with no silicon template in the assembly).

PMMA layers were bonded using solvent-assisted low-temperature bonding[48] and COP layers were bonded using the solvent-less high temperature bonding.[46] Briefly, corresponding PMMA layers (the embossed channel portion and the drilled inlet portion) were bathed in ethanol for 10 min, dried, and aligned together in a clamping assembly as referenced above. Bonding occurred in the oven at 80°C for 1-2 h, and the exact processing time depends upon the total bonding area (device size). COP layers were bonded at 110°C for 20 min using the same procedure mentioned above but without using the ethanol/solvent bathing step. Bonded PMMA and COP device edges were sealed using acetonitrile and cyclohexane, respectively, as the solvents, and

channels were thoroughly vacuum cleaned using isopropanol and DI water. Commercially available NanoPort interconnects (Idexx Corporation, Westbrook, ME) were attached to PMMA and COP using epoxy and cured overnight.

Device Characterization and Operation

The quality of the hot embossed channels was determined using scanning electron microscopy (SEM) imaging (LEO 1455VP, Carl Zeiss AG, Oberkochen, Germany), after sputtering a thin layer of gold (Cressington Scientific Instruments, Watford, UK) onto the devices. Channel quality was also verified with optical microscopy and flow-through of isopropanol and DI water prior to droplet experiments. Profilometry (Dektak XT, Bruker, Tucson, AZ) was also used to measure the embossed channel depth and uniformity.

To reduce dispersed phase surface wetting and to sustain stable droplet formation, the device channels of PMMA and COP devices were hydrophobically modified. Briefly, the channels were selectively exposed to UV light (Clearstone Technologies, Hopkins, MN) for 10 min by masking the non-channel regions with electrical tape. The exposed channels were treated with 10 mM heptadecafluoro-1,1,2,2-tetrahydrodecyltrichlorosilane diluted in FC 40 for 2 h at a flow rate of 2-5 μL/min. Devices were then cleaned using FC 40 for 30 min at 10 μL/min and DI water for 30 min at 20 μL/min. Modified device channels were then dried under vacuum for 30 min.

In all experiments, the carrier oil continuous phase was 2% Fluorosurfactant-008 in Novec 7500 Engineered Fluid. Water was the dispersed phase, except for experiments using suspensions of 10 μm diameter streptavidin coated magnetic microparticles (Sigma Aldrich, Milwaukee, WI) in optiprep density gradient medium (to reduce bead sedimentation). For picoinjector and K-channel injections, black dye or yellow dye (for contrast without obscuring beads in integrated

devices) was injected. The continuous phase oil was flowed through the K-channel for magnetic bead enrichment during droplet splitting. For β-galactosidase assay, the streptavidin-magnetic beads were derivatized with biotin-β-galactosidase for 1 h, at 4°C in phosphate buffer saline (PBS), 0.5 % bovine serum albumin (BSA) at pH 7.4. After binding, the bead contents were thoroughly washed using PBS, 0.5 % BSA, pH 7.4 buffer, and the beads were re-suspended in optiprep solution for on-chip loading. Resorufin-β-D-galactopyranoside in PBS, 0.5 % BSA, pH 7.4 buffer was used as the substrate solution for the electrical K-channel injection.

A custom pressure-driven flow system supported by LabView (National Instruments, Austin, TX) was used to control the fluid flow through microchannels.[15] Regulated N_2 gas delivered to the headspace of sample vials forced fluid flow through 24 gauge Teflon tubing (Cole Palmer, Vernon Hills, IL) connected to the device through NanoPort interconnects, and flow rates for each solution were proportional to gas pressure. Typical applied pressures were from 10-40 kPa. An electric field (~40 VAC) was supplied by a custom DC to AC inverter to charge the 3 M NaCl in water-filled electrode channels.[49] A magnetic field was applied with a stack of four 0.4T NdFeB (0.5" x 0.25" x 0.125") permanent magnets placed inside the rectangular slot in the top PMMA and COP layers. Droplet microfluidic operations were recorded using a high-speed camera (VEO 640L, Vision Research, Inc., Wayne, NJ) connected to a DMi8 microscope (Leica Microsystems, Wetzlar, Germany). Fluorescent images for the β-galactosidase enzyme assay were collected using a Texas Red Filter Cube installed on the microscope. Data was analyzed using ImageJ software (National Institutes of Health, Bethesda, MD) to monitor droplet volume, droplet frequency, and magnetic bead position. Each experiment was repeated on at least three different devices from each design and all reported values include at least N = 25 droplets for each condition to demonstrate representative performance.

RESULTS AND DISCUSSION

Device Manufacturing

Manufacturing devices with design complexity and channel dimensions comparable to PDMS is critical for adopting droplet microfluidic operations in thermoplastics. Initially, several materials were considered, including PMMA, COP, PC, and PP for this application. However, PMMA and COP were selected for their low cost, wide availability, and application-compatible physical properties (surface chemistry, optical window, and electromagnetic permittivity).[40] Early attempts using laser engraved PMMA were unsatisfactory due to high channel roughness and poor control over channel depth and uniformity, and additionally, with COP, the material melting was an issue using the CO_2 laser cutter. Even after post-process smoothing of PMMA channels, the devices could not support stable droplet operations. We then selected hot embossing, and established an in-house procedure to manufacture devices in PMMA and COP at lower set-up cost and reduced equipment requirements compared to injection molding.

Silicon dioxide-silicon masters were originally fabricated using photolithography and wet etching techniques. Master fabrication worked well for simple, straight-channel designs; however, orientation-dependent over-etching interfered with more complex geometries.[50] To overcome this problem, DRIE was successfully employed to generate isotropically etched features with high fidelity on silicon wafers. To reduce effects from scalloped features and surface roughness, which are associated with DRIE and could affect hot embossing yield, a 5 min KOH etching step was added that improved the de-molding yield of imprinted PMMA and COP. SEM imaging data in Figure III.2 demonstrates the quality of imprinted T-junction, picoinjector, and K-channel features in PMMA. Profilometry measurements gave a feature height of 30 ± 4 μm for deep reactive ion

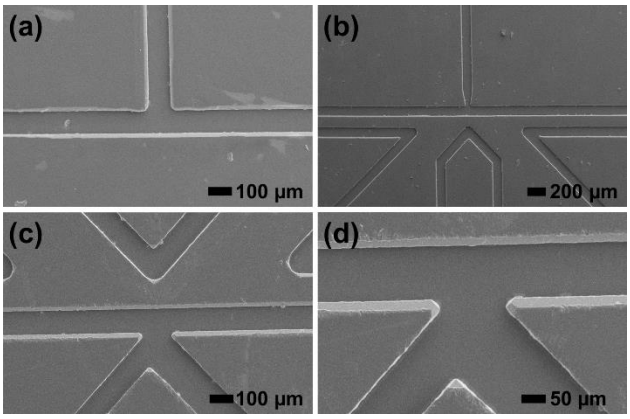

Figure III.2. Scanning electron micrographs of hot embossed droplet microfluidic device components in PMMA. a) T-junction; b) Picoinjector; and c) and d) K-channel with working and reference electrodes.

etched silicon masters and channel depth of 29 ± 3 µm for hot embossed PMMA microchannel, with high embossing yield and uniform feature transfer. The observed small deviations in feature height and channel depth among templates is primarily due to the different number of cycles (100 ± 10 cycles) used for different instances of wafer processing using DRIE. Moreover, a small variation in hot embossed channel depth (33 ± 0.3 µm, n = 5 measurement locations) across a single device confirms uniform pressure application during the embossing procedure.

Next, the inlet PMMA and COP layer was bonded to the imprinted channel layer. There are a variety of techniques that can be used for PMMA-PMMA bonding.[51] Ultimately, thermal bonding above the glass transition temperature of PMMA proved challenging for maintaining the channel quality, so solvent-assisted bonding at low temperatures was used instead, whereas the high temperature bonding was used for the COP device fabrication. With our existing pressure system set-up, we safely applied 100 kPa without any bonding failure. This applied pressure is limited by the system's mechanical parts, but we believe, depending upon the microfluidic requirements, the applied pressure can be increased further to sustain the fluid flow. The channel smoothness and bonding worked well to support pressure-driven flow, as evidenced in the SEM, optical microscope, and solvent flow through studies. For reliable world-to-chip connections,

commercially available microfluidic interconnects (Nanoports) were bonded to the devices with epoxy.

Wetting of PMMA and COP device channels by the aqueous phase interferes with stable droplet generation. Initially, plasma oxidation was used to modify the channel walls before reaction with heptadecafluoro-1,1,2,2-tetrahydrodecyltrichlorosilane to introduce a hydrophobic coating; however, unreliable oxygen plasma across the entire device footprint led to coating defects. To overcome this problem, UV-assisted activation of the channels[46, 52] was used preceding treatment with heptadecafluoro-1,1,2,2-tetrahydrodecyltrichlorosilane suspended in FC 40. This surface modification procedure allowed for stable droplet generation and subsequent complex device operation, as described below.

Droplet Generation Using a T-Junction

Droplet generation is the first step in most droplet microfluidic device operations, and, therefore, a commonly-used T-junction geometry (Figure III.3a) was a first test objective for PMMA channels. As shown in Figure III.3b and III.3c, the water droplets suspended in fluorinated carrier oil were generated successfully. In this example, droplets had volumes of 330 ± 15 pL (n = 25 droplets) and were generated at 1.2 Hz frequency for further manipulation (see Supplementary Movie SMIII.1), but changing flow conditions (i.e. applied pressures) could alter volume and frequency to desired parameters.

Reagent Picoinjection

For adding reagents to pre-formed droplets to initiate in-droplet chemistry, direct injection advantageously does not require the added complexity of droplet train synchronization required

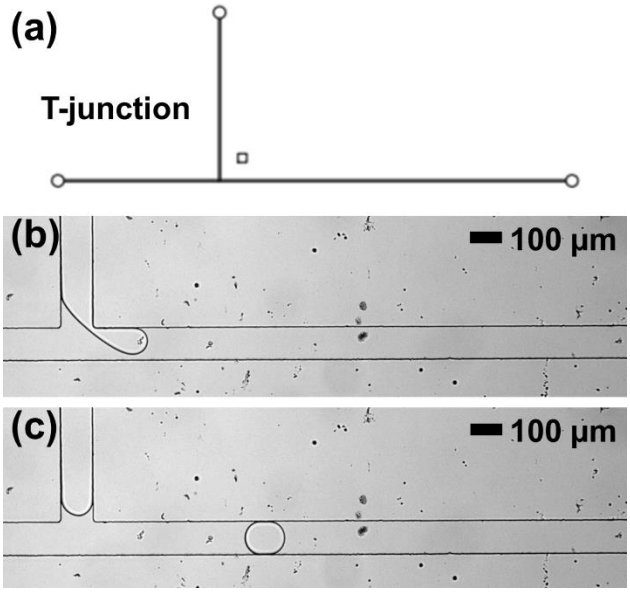

Figure III.3. a) Device design for the T-junction droplet microfluidic operation in thermoplastic devices. b) Droplet generation at a T-junction fabricated in PMMA via embossing. c) Droplet flowing downstream of the T-junction down the main channel.

by approaches that pair and fuse sample and reagent droplets.[14, 17] One such geometry for direct injection, the picoinjector, uses an electro-pneumatic mechanism to force fluid into passing droplets at the picoinjector-droplet (aqueous-aqueous) interface in the presence of an electric field, which disturbs the boundary between the approaching droplet and the aqueous phase in the injector channel.[14] The applied pressure on the picoinjected fluid determines the amount of fluid injected. This operation in thermoplastic devices requires the penetration of electric field through PMMA, supplied through saline-filled electrode channels in our device. Considering the electrical properties of PMMA and limitations of embossing channels in PMMA (feature size and spacing, etc.), a picoinjector device with 200 µm spacing between the boundary of the working electrode channel and the main droplet channel-picoinjector junction was designed (Figure III.4a). To demonstrate picoinjector operation, we injected black dye into passing water droplets to enable visualization, as shown in Figure III.4c (also see Supplementary Movie SMIII.2). Figures III.4b and III.4d show the droplet before and after the picoinjection. In this device operation, 70 ± 10 pL

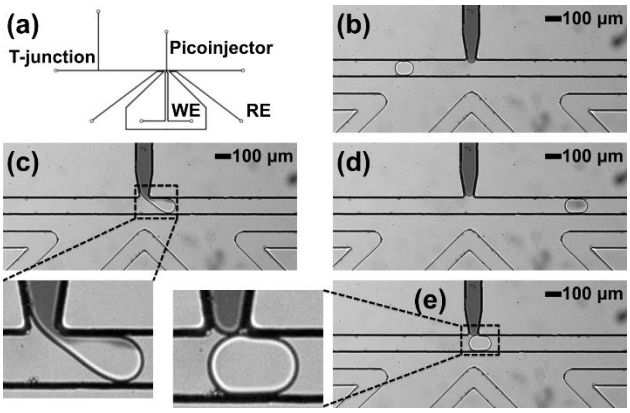

Figure III.4. Picoinjector operation in PMMA for reagent injection into droplets. a) Picoinjector device design in thermoplastic material. b) Droplet flowing down a channel before the picoinector. c) Droplet immediately leaving the picoinjector in the presence of applied electric field and a zoomed image showing disruption of the droplet interface and exchange of fluid between the aqueous phases of the picoinjector and the droplet due to the applied electric field. d) Droplet flowing down the main channel after picoinjection. e) Droplet passing the picoinjector in the absence of applied electric field and a zoomed image showing no fluid exchange between the picoinjector and the passing droplet. WE: working electrode; RE: reference electrode.

(or 23%) black dye was successfully injected into the input droplets of 310 ± 10 pL, but changing picoinjector channel flow conditions (i.e. applied pressures) could alter the injected fluid volume. In the absence of electric field, the droplets do not interact and there is not dye (fluid) transfer, as shown in Figure III.4e. Overall, this data demonstrates both effective electric field application and fabrication with sufficient fidelity to enable picoinjection in PMMA, a useful direct reagent injection operation in droplet microfluidics.

Reagent Injection Using the Multifunctional K-Channel

Next, we tested the multifunctional K-channel design in reagent injection mode. This droplet manipulation scheme also relies on an electro-pneumatic direct injection mechanism, but stabilizes flow and reduces droplet-droplet cross-contamination by continuously flowing fresh reagent past the junction with the main channel.[15] This device, shown in Figure III.5a, included a K-channel structure instead of the picoinjector but was otherwise identical in critical features

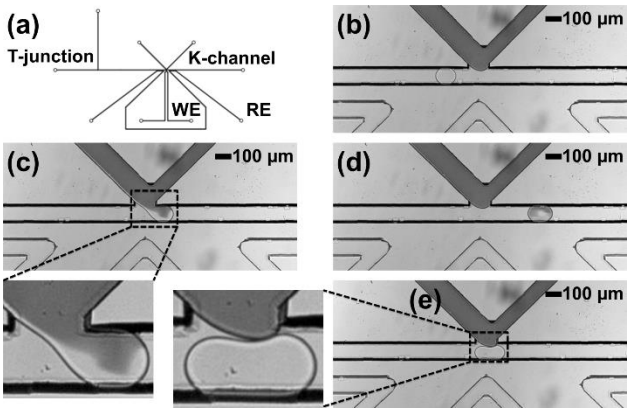

Figure III.5. K-channel operation in PMMA for reagent injection into the droplet. a) K-channel device design. b) Flow of droplet in the main channel before K-channel injection. c) Flow of droplet across the K-channel in the presence of applied electric field and zoomed image showing disruption of boundary and exchange of fluid between the aqueous phases of the K-channel and the droplet due to the applied electric field. d) Flow of droplet in the main channel after K-channel injection. e) Flow of droplet across the K-channel in the absence of applied electric field and zoomed image showing no fluid exchange between the K-channel and the passing droplet. WE: working electrode; RE: reference electrode.

(channel length and cross-section, T-junction geometry, electrode channel structure, etc.). While a single K-channel device can be reconfigured between injecting reagents and extracting droplet volume, this first demonstration focused on electro-pneumatic fluid addition. Considering the K-channel architecture, there is an exchange of a small volume between the droplet and the K-channel, however overall there is a net volume that is injected into the droplet from the K-channel. This injected volume is calculated based upon the size difference between the droplet approaching K-channel and the one leaving K-channel. For effective reagent injection, black dye was flowed through the K-channel from narrow-to-wide channel size direction such that the black dye was injected into the water droplets, as shown in Figure III.5c (also see Supplementary Movie SMIII.3). Figures III.5b and III.5d show the droplet before and after the K-channel injection, respectively. In this device operation, 85 ± 20 pL (or 20%) black dye was successfully injected into input droplets of 415 ± 20 pL, but changing K-channel channel flow conditions (i.e. applied pressures) could alter the injected fluid volume or could also initiate the extraction of fluid volume from

droplets. When an electric field is not applied, as shown in Figure III.5e, there is no interaction between the K-channel aqueous phase and the passing droplet, and hence, no injection of dye into the droplet. Overall, the results from both picoinjector and K-channel operations not only fundamentally confirm that PMMA transmits sufficient electric field to enable electrically-mediated droplet processing, but also that PMMA does not intrinsically change the performance of higher order droplet functions.

Droplet Splitting and Magnetic Bead Enrichment Using the Multifunctional K-Channel

The K-channel also supports another useful droplet operation: droplet splitting. Droplet splitting can not only parallelize a single reaction volume into two daughter volumes, but can also enrich magnetic beads into one daughter droplet when coupled with a local magnetic field. Therefore, sample associated with the magnetic bead (perhaps through antibody- or nucleotide sequence-based recognition and binding) is selectively concentrated in one daughter droplet, while the other daughter droplet can be discarded or otherwise manipulated. Therefore, this process can remove waste volume from a droplet while enriching bead-bound sample.[15, 43, 44] For magnetic bead-containing droplet processing, this K-channel device was designed with 500 μm spacing between the main channel and the permanent magnet, as shown in Figure III.6a. To optimize magnetic bead loading and counter bead sedimentation, droplets were formed from a suspension of magnetic beads in optiprep density gradient medium. In this example, fluorinated oil was flowed through the K-channel from wide-to-narrow channel size direction, and the applied pressure-dependent flow rate through this element selected the droplet splitting ratio. Importantly, as shown in Figure III.6c, the daughter droplet in the main channel carried all the beads due to the presence of magnetic field, which pulled the beads to the lower boundary of the initial droplet prior to the

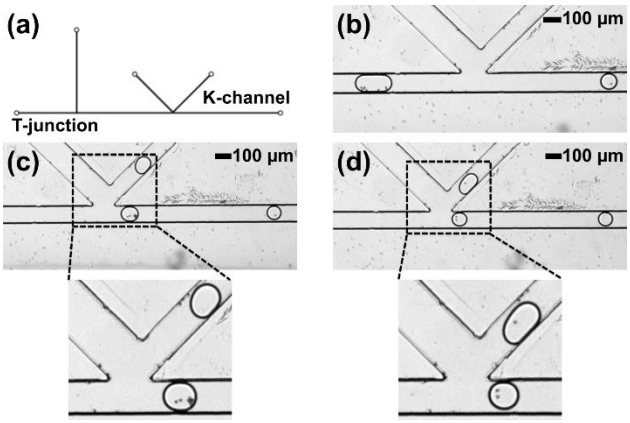

Figure III.6. K-channel operation in PMMA for droplet splitting and magnetic bead concentration. a) K-channel device design. b) Flow of droplets in the main channel before and after splitting using a K-channel. c) Droplet immediately after splitting at the K-channel in the presence of applied magnetic field and zoomed image of split droplets with magnetic concentration of beads in the main channel and an empty droplet in the K-channel. d) Droplet splitting at the K-channel in the absence of applied magnetic field and zoomed image showing no magnetic concentration: both droplets contain magnetic beads.

splitting event (see Supplementary Movie SMIII.4). The daughter droplet split into the K-channel outlet did not contain any beads. Figure III.6b shows droplets before and after splitting in the main channel. In this device operation, 285 ± 30 pL (or 59 %) of the droplet volume was removed from 480 ± 15 pL input droplets along with the successful retention of all magnetic beads under these conditions, but increasing the proportion of the droplet removed increases the chance of bead loss. In contrast, in the absence of a magnetic field, the magnetic beads are randomly distributed within each droplet volume, as shown in Figure III.6d where they are found in both fractions of the split input droplet. This result further demonstrates the compatibility of PMMA thermoplastic devices with established droplet operations in the context of droplet splitting and magnetic field permeation.

Multi-Step Droplet Processing Using Thermoplastic Microfluidics: Integrated Droplet Generation, Reagent Injection, and Magnetic Bead Enrichment

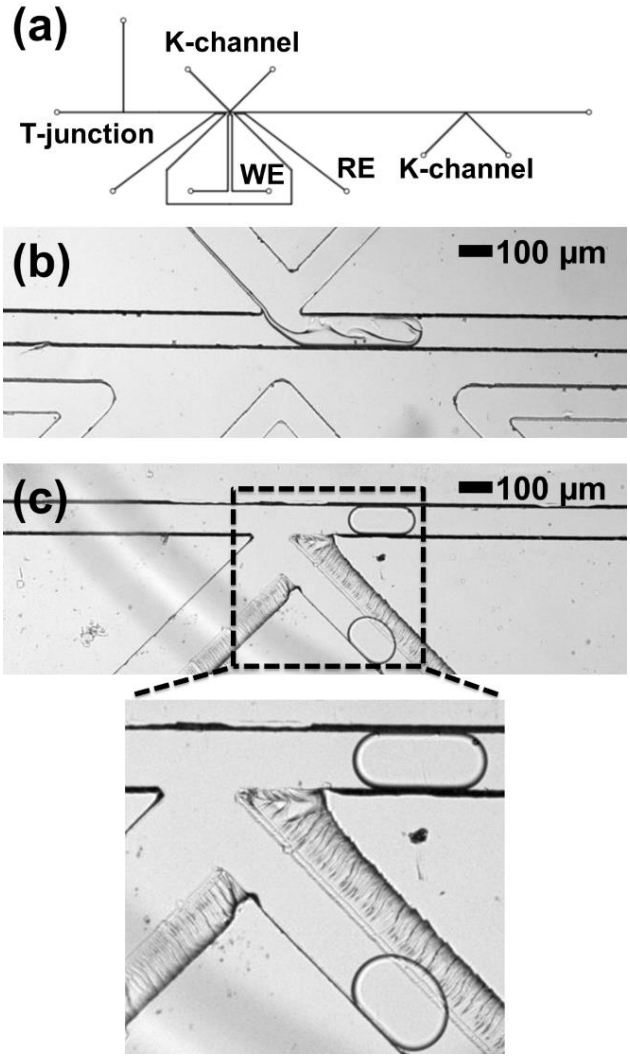

Figure III.7. Integrated device operation in PMMA for droplet generation, injection, and magnetic splitting. a) Device design for the integrated device. b) Dilute dye injection at K-channel in the presence of applied electric field. c) Droplet splitting at K-channel and magnetic concentration in the presence of applied magnetic field and zoomed image showing the droplet containing magnetic beads in the main channel and the empty droplet in the K-channel. WE: working electrode; RE: reference electrode.

As a next demonstration to establish the ability of thermoplastic microfluidic devices to support higher-order component integration for multi-step sample processing, droplet generation, electrical K-channel injection, and magnetic K-channel droplet splitting operations were performed sequentially on a single device, as shown in Figure III.7a. Magnetic bead-containing optiprep-in-oil droplets were first generated at the T-junction, followed by injection of dye at the

first K-channel, as shown in Figure III.7b. At the second K-channel the magnetic splitting operation collected magnetic beads in the main channel daughter droplet only (Figure III.7c). A zoomed in image provides a closer view of the droplet splitting to show the final position of captured magnetic beads. In this integrated device, input droplets of 755 ± 30 pL size were first injected with 375 ± 35 pL of dye solution (a 50 % volume increase), followed by the removal of a total of 525 ± 30 pL (a 46 % reduction in droplet volume) via droplet splitting (see Supplementary Movie SMIII.5). We observed a small fabrication defect in the second K-channel, which was probably due to the melted PMMA displaced during the embossing process, that was not completely removed during the subsequent device fabrication steps. We do not expect this defect to significantly affect the droplet manipulation as can be clearly seen through the droplet movement in Supplementary Movie SMIII.5. .By including formation, injection, and magnetic enrichment components in series, this device washes the beads in the droplets, exchanging the droplet fluid composition while retaining the bead sample. While a proof-of-concept experiment, combining serial modules encompassing both electric and magnetic field components clearly demonstrates the ability of PMMA thermoplastic microfluidic devices made via hot embossing to support multi-step droplet processing capabilities with equivalent performance to conventional PDMS devices.

As a final demonstration, we applied the integrated washing device to perform a simple in-droplet enzymatic activity and sampling assay. For this application, we expanded our material selection capabilities to COP and successfully performed needed droplet operations without significant deviations from PMMA channel quality or performance. For this demonstration, we captured biotinylated β-galactosidase on the surface of streptavidin-coated magnetic beads, then loaded the enzyme-functionalized beads into droplets in the integrated COP device. Upon substrate

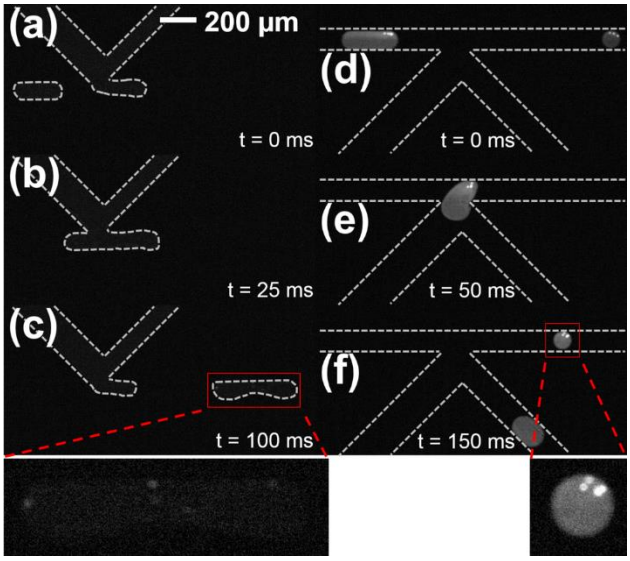

Figure III.8. Fluorescence imaging of the in-droplet β-galactosidase enzymatic assay in integrated microfluidic devices manufactured in cyclic olefin polymer (COP). a) Droplets loaded with biotinylated-β-galactosidase bound to streptavidin coated magnetic beads approach the substrate injection K-channel showing very low background fluorescence. b) K-channel-mediated resorufin-β-D-galactopyranoside substrate injection in the presence of applied electric field initiates the chemical reaction. c) Immediately after injection, weak fluorescence localized near magnetic beads indicates initial formation of fluorescent resorufin product (see expanded inset). d) Downstream imaging after ~2.6 s incubation demonstrates additional product formation and mixing throughout the droplet. e) Droplet splitting at the K-channel localizes magnetic-bead bound enzymes in the main channel portion. f) After splitting, the magnetic-bead bound enzyme remains in the main channel for additional reaction or downstream processing (see expanded inset), while the K-channel collects a portion of the product.

injection at the first K-channel (resorufin-β-D-galactopyranoside), the enzyme reaction initiated. Figures III.8a-b show low background fluorescence from substrate and bead samples prior to injection, but fluorescent resorufin product immediately formed upon injection, as evidenced from weak fluorescence localized near the beads in Figure III.8c. After ~2.6 s reaction time in the channel, Figure III.8d shows a significant increase in fluorescence both near enzyme-coated beads and delocalized throughout the droplet, indicating reaction progress. Finally, K-channel splitting samples a portion of the product for immediate collection at this time point, and bead-bound enzyme was retained in the main channel portion by local magnetic field for additional reaction or other processing (see Supplementary Movie SMIII.6). With this proof-of-concept experiment,

combining both electric and magnetic field components to process an in-droplet enzymatic process, we clearly demonstrated our ability to apply these thermoplastic microfluidic devices to multi-step (bio) chemical assays.

CONCLUSIONS

We have reported a fabrication workflow to manufacture droplet microfluidic devices in thermoplastics and have demonstrated successful operation of several key droplet manipulation operations. Photolithography followed by deep reactive ion etching was used to fabricate silicon masters that facilitated high performance hot embossing. This approach was utilized to create individual microfluidic components supporting droplet generation at a T-junction, reagent injection using both picoinjector and K-channel designs, and volume removal and magnetic bead enrichment using the K-channel. In addition to demonstrating the compatibility of PMMA and COP thermoplastic for droplet microfluidics in terms of channel size and surface properties, these devices also showed that electric and magnetic field-based droplet actuation can be achieved comparably to devices in PDMS. This work is the first to report multi-step droplet manipulations in thermoplastics and therefore lays the groundwork for the translation of droplet microfluidic devices from PDMS-based prototypes into materials systems that are poised for mass production.

ACKNOWLEDGEMENTS

We gratefully acknowledge the National Institutes of Health (Grant No. CA191186) for supporting this work. SRD acknowledges support from the National Science Foundation Graduate Research Fellowship Program. Support from the University of Michigan's Lurie Nanofabrication Facility and University of Michigan College of Literature, Science, and the Arts Machine Shop is

also greatly appreciated. We also thank Prof. Adam Matzger (University of Michigan, Department of Chemistry) for providing access to the CO_2 laser cutter and Prof. Robert Kennedy for access to the drill press.

REFERENCES

1. T. S. Kaminski and P. Garstecki, *Chemical Society Reviews*, 2017, **46**, 6210-6226.

2. L. R. Shang, Y. Cheng and Y. J. Zhao, *Chemical Reviews*, 2017, **117**, 7964-8040.

3. M. T. Guo, A. Rotem, J. A. Heyman and D. A. Weitz, *Lab on a Chip*, 2012, **12**, 2146-2155.

4. A. B. Theberge, F. Courtois, Y. Schaerli, M. Fischlechner, C. Abell, F. Hollfelder and W. T. S. Huck, *Angewandte Chemie-International Edition*, 2010, **49**, 5846-5868.

5. P. Shahi, S. C. Kim, J. R. Haliburton, Z. J. Gartner and A. R. Abate, *Scientific Reports*, 2017, **7**.

6. F. Lan, B. Demaree, N. Ahmed and A. R. Abate, *Nature Biotechnology*, 2017, **35**, 640-+.

7. Y. Xu, J.-H. Lee, Z. Li, L. Wang, T. Ordog and R. C. J. L. o. a. C. Bailey, 2018.

8. E. D. Guetschow, D. J. Steyer and R. T. Kennedy, *Analytical Chemistry*, 2014, **86**, 10373-10379.

9. E. D. Guetschow, S. Kumar, D. B. Lombard and R. T. Kennedy, *Analytical and Bioanalytical Chemistry*, 2016, **408**, 721-731.

10. A. K. Price, A. B. MacConnell and B. M. Paegel, *Analytical Chemistry*, 2016, **88**, 2904-2911.

11. Y. Schaerli, R. C. Wootton, T. Robinson, V. Stein, C. Dunsby, M. A. A. Neil, P. M. W. French, A. J. deMello, C. Abell and F. Hollfelder, *Analytical Chemistry*, 2009, **81**, 302-306.

12. J. H. Xu, S. W. Li, J. Tan, Y. J. Wang and G. S. Luo, *Aiche Journal*, 2006, **52**, 3005-3010.

13. P. Garstecki, H. A. Stone and G. M. Whitesides, *Physical Review Letters*, 2005, **94**.

14. A. R. Abate, T. Hung, P. Mary, J. J. Agresti and D. A. Weitz, *Proceedings of the National Academy of Sciences of the United States of America*, 2010, **107**, 19163-19166.

15. S. R. Doonan and R. C. Bailey, *Analytical Chemistry*, 2017, **89**, 4091-4099.

16. L. Frenz, K. Blank, E. Brouzes and A. D. Griffiths, *Lab on a Chip*, 2009, **9**, 1344-1348.

17. M. Lee, J. W. Collins, D. M. Aubrecht, R. A. Sperling, L. Solomon, J. W. Ha, G. R. Yi, D. A. Weitz and V. N. Manoharan, *Lab on a Chip*, 2014, **14**, 509-513.

18. I. Akartuna, D. M. Aubrecht, T. E. Kodger and D. A. Weitz, *Lab on a Chip*, 2015, **15**, 1140-1144.

19. K. Ahn, C. Kerbage, T. P. Hunt, R. M. Westervelt, D. R. Link and D. A. Weitz, *Applied Physics Letters*, 2006, **88**.

20. L. Mazutis, J. Gilbert, W. L. Ung, D. A. Weitz, A. D. Griffiths and J. A. Heyman, *Nature Protocols*, 2013, **8**, 870-891.

21. Y. J. Sung, J. Y. H. Kim, H. I. Choi, H. S. Kwak and S. J. Sim, *Scientific Reports*, 2017, **7**.

22. J. D. Tice, H. Song, A. D. Lyon and R. F. Ismagilov, *Langmuir*, 2003, **19**, 9127-9133.

23. T. Thorsen, R. W. Roberts, F. H. Arnold and S. R. Quake, *Physical Review Letters*, 2001, **86**, 4163-4166.

24. T. Nisisako, T. Torii and T. Higuchi, *Lab on a Chip*, 2002, **2**, 24-26.

25. J. H. Xu, G. S. Luo, S. W. Li and G. G. Chen, *Lab on a Chip*, 2006, **6**, 131-136.

26. J. C. McDonald and G. M. Whitesides, *Accounts of Chemical Research*, 2002, **35**, 491-499.

27. D. C. Duffy, J. C. McDonald, O. J. A. Schueller and G. M. Whitesides, *Analytical Chemistry*, 1998, **70**, 4974-4984.

28. A. Rotem, O. Ram, N. Shoresh, R. A. Sperling, A. Goren, D. A. Weitz and B. E. Bernstein, *Nature Biotechnology*, 2015, **33**, 1165-U1191.

29. J. N. Lee, C. Park and G. M. Whitesides, *Analytical Chemistry*, 2003, **75**, 6544-6554.

30. D. Bodas and C. Khan-Malek, *Sensors and Actuators B-Chemical*, 2007, **123**, 368-373.

31. V. Sahore and I. Fritsch, *Analytical Chemistry*, 2013, **85**, 11809-11816.

32. R. F. Gerhardt, A. J. Peretzki, S. K. Piendl and D. Belder, *Analytical Chemistry*, 2017, **89**, 13030-13037.

33. H. Becker and C. Gartner, *Microchip Diagnostics: Methods and Protocols*, 2017, **1547**, 3-21.

34. S. C. Wang, C. Y. Lee and H. P. Chen, *Journal of Chromatography A*, 2006, **1111**, 252-257.

35. H. Becker and U. Heim, *Sensors and Actuators a-Physical*, 2000, **83**, 130-135.

36. U. M. Attia, S. Marson and J. R. Alcock, *Microfluidics and Nanofluidics*, 2009, **7**, 1-28.

37. Z. K. Wang, H. Y. Zheng, R. Y. H. Lim, Z. F. Wang and Y. C. Lam, *Journal of Micromechanics and Microengineering*, 2011, **21**.

38. D. A. Mair, E. Geiger, A. P. Pisano, J. M. J. Frechet and F. Svec, *Lab on a Chip*, 2006, **6**, 1346-1354.

39. M. B. Esch, S. Kapur, G. Irizarry and V. Genova, *Lab on a Chip*, 2003, **3**, 121-127.

40. P. N. Nge, C. I. Rogers and A. T. Woolley, *Chemical Reviews*, 2013, **113**, 2550-2583.

41. B. Subramanian, N. Kim, W. Lee, D. A. Spivak, D. E. Nikitopoulos, R. L. McCarley and S. A. Soper, *Langmuir*, 2011, **27**, 7949-7957.

42. S. J. Hwang, M. C. Tseng, J. R. Shu and H. H. Yu, *Surface & Coatings Technology*, 2008, **202**, 3669-3674.

43. B. Verbruggen, T. Toth, M. Cornaglia, R. Puers, M. A. M. Gijs and J. Lammertyn, *Microfluidics and Nanofluidics*, 2015, **18**, 91-102.

44. E. Brouzes, T. Kruse, R. Kimmerling and H. H. Strey, *Lab on a Chip*, 2015, **15**, 908-919.

45. Y. C. Tan, J. S. Fisher, A. I. Lee, V. Cristini and A. P. Lee, *Lab on a Chip*, 2004, **4**, 292-298.

46. V. Sahore, M. Sonker, A. V. Nielsen, R. Knob, S. Kumar and A. T. Woolley, *Analytical and Bioanalytical Chemistry*, 2018, **410**, 933-941.

47. M. Sonker, E. K. Parker, A. V. Nielsen, V. Sahore and A. T. Woolley, *Analyst*, 2018, **143**, 224-231.

48. N. Ling, J. S. Lee and N. Y. Lee, *Sensors and Actuators a-Physical*, 2017, **265**, 168-173.

49. A. Sciambi and A. R. Abate, *Lab on a Chip*, 2014, **14**, 2605-2609.

50. H. Seidel, L. Csepregi, A. Heuberger and H. Baumgartel, *Journal of the Electrochemical Society*, 1990, **137**, 3612-3626.

51. C. W. Tsao and D. L. DeVoe, *Microfluidics and Nanofluidics*, 2009, **6**, 1-16.

52. X. H. Sun, W. C. Yang, T. Pan and A. T. Woolley, *Analytical Chemistry*, 2008, **80**, 5126-5130.

SUPPLEMENTARY INFORMATION

The supplementary information in its original format (including videos) may be accessed online at doi: 10.1039/C8AY01474D.

Supplementary Movie SMIII.1. Water droplet generation at the T-junction.

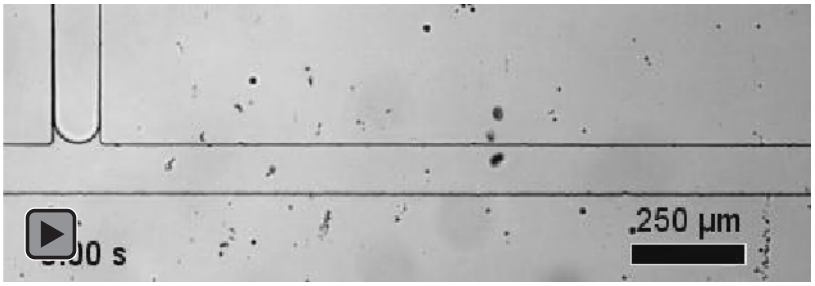

Supplementary Movie SMIII.2. Droplets flow past the picoinjector where dye injects in the presence of electric field.

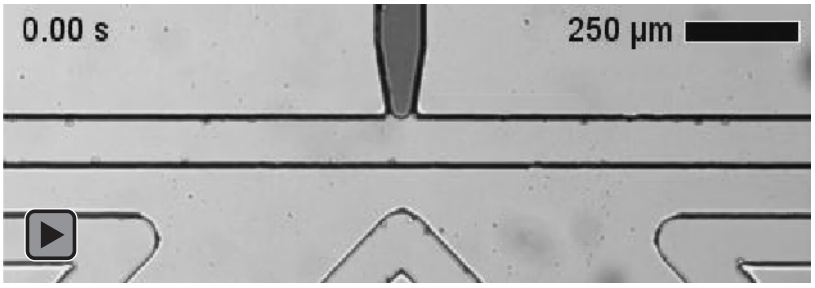

Supplementary Movie SMIII.3. Droplets flow past the K-channel where dye injects in the presence of electric field.

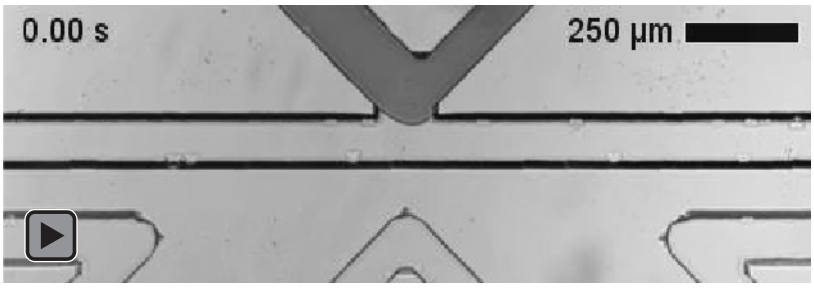

Supplementary Movie SMIII.4. Droplets split at the K-channel, and applied magnetic field concentrates magnetic beads in the main channel (lower) daughter droplets. Some droplets do not have magnetic beads before splitting due to bead sedimentation during loading.

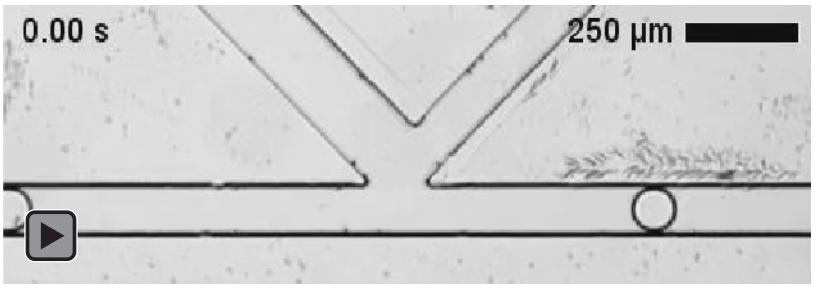

Supplementary Movie SMIII.5. In the first part of the video, the upstream (first) K-channel injects dye into droplets in the presence of electric field. In the second part of the video, dye-injected droplets split at the downstream (second) K-channel, and magnetic field concentrates beads into the main channel (upper) daughter droplets.

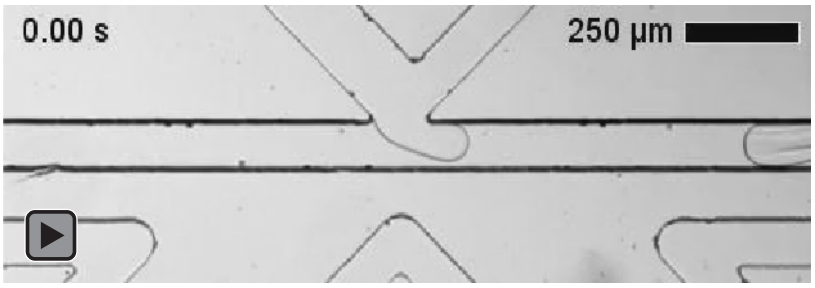

Supplementary Movie SMIII.6. In the first part of the fluorescence video, the upstream (first) K-channel injects resorufin-β-D-galactopyranoside substrate into the droplets containing β-galactosidase-magnetic bead complexes in the presence of electric field to initiate the reaction. In the second part of the video, these droplets (now also containing significant resorufin product) split at the downstream (second) K-channel, and magnetic field concentrates bead-bound enzyme into the main channel (upper) daughter droplets.

SUPPLEMENTARY FIGURE

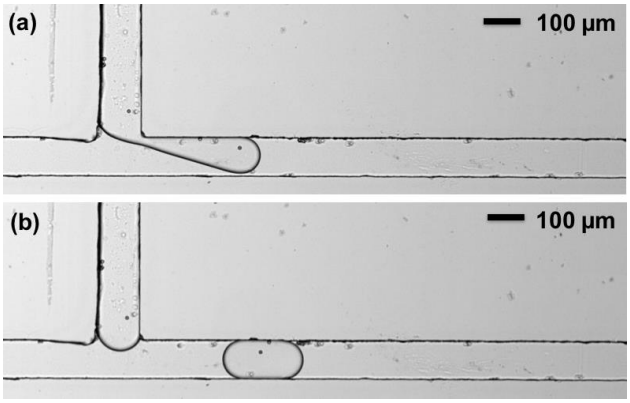

Figure III.S1. a) Droplet generation at the T-junction of an integrated device fabricated in cyclic olefin polymer (COP) via embossing. b) Magnetic beads containing droplet flowing downstream of the T-junction down the main channel.

Chapter IV

C^3PE: Counter-Current Continuous Phase Extraction for Improved Precision of in-Droplet Chemical Reactions

Adapted from a Manuscript in Preparation by Steven R. Doonan, Melissa Lin, Dongkwan Lee, Jamy Lee, and Ryan C. Bailey.

INTRODUCTION

Droplet microfluidic technologies enable continuous, automated, and high throughput (up to 1000s of droplets per second) processing and analysis of non-deterministic sample volumes.[1, 2] By encapsulating samples in miniature volumes (fL-nL) surrounded by immiscible (often fluorinated) oils and stabilized by specially tailored surfactants, each droplet acts as an individually addressable reactor. Compartmentalization in these volumes limits sample loss via non-specific adsorption to tubing and channel walls and favorably increases the rate of internal mixing.[3-5] As this technology has become more broadly implemented within a range of material systems[6] and contexts, such as genomic and epigenomic analyses,[7-9] immunoassays,[10] and (bio)material applications,[11] the accompanying suite of droplet formation and manipulation techniques has similarly grown. Flow focusing and T-junction structures form mono-disperse droplets at high frequencies.[12, 13] Specialty architectures enable gradient generation,[14] deterministic droplet pairing and fusion,[15-17] direct injection into droplets,[18, 19] and dielectrophoretically-[20] or acoustically-mediated[21] droplet sorting. Other techniques tether recognition molecules to in-droplet magnetic

particles, enabling sample capture and purification.[18, 22-25] A number of reviews profile droplet technologies in detail.[2, 26, 27]

While these techniques manipulate droplet size, position, and composition, fully realizing the potential of in-droplet chemistry requires interfacing serial combinations of modules to establish reaction conditions and to provide time for the reactions to occur.[3] Incubating droplets statically on-[28] or off-chip[15] provides hours or longer of reaction time, although ensuring droplet stability during collection, storage, and recovery can be technically challenging.[5] On the other hand, on-chip incubation relies on elongated stretches of large cross-section features like delay channels, thereby increasing total device volume while limiting the corresponding increases in hydraulic resistance and back-pressure. Importantly, the design and implementation of such features should not only take total incubation time into account but must also consider droplet flow uniformity. Thus, it is critical to ensure homogenous conditions to limit inter-droplet variance in reaction performance, particularly to achieve high precision in using time-sensitive chemistry.[29, 30]

Packing is central to control over droplet incubation. The volume fraction of the droplets, φ, describes the relative portion of the total channel volume occupied by droplets. Beyond directly controlling the number of droplets packed into a given microchannel, φ also affects flow characteristics and droplet motions, consequentially altering in-droplet reaction performance.[30, 31] Through selective continuous phase removal, on-device oil extraction provides a practical method to usefully manipulate φ in particular channel regions.[17, 29, 31] This operation lends itself to two principle applications, controlling droplet incubation time and enabling uniform respacing. First, increased φ at fixed droplet size and frequency leads to proportionally greater residence time for each droplet within an incubation module.[29-31] Second, useful multistep chemistry often requires

several reaction steps separated by intermediary incubation periods. Extracting oil before incubation with uniform oil re-addition afterwards minimizes deviations in droplet spacing due to stochastic droplet-oil redistribution in large cross-section incubation channels.[29] Because many useful downstream operations (such as direct injection and pairwise droplet merging) often depend on droplet spacing uniformity, retaining excess oil through the entire reaction sequence limits the practical implementation of multistep in-droplet reactions.[15, 17, 30] Overall, control of φ through oil extraction can afford significant control over in-droplet reaction performance.

Limited examples of oil extraction have been employed for droplet applications. The most common motif for on-chip oil extraction leverages micropillar structures.[17, 29, 31] As flow enters these modules, oil exits through the narrow gaps between pillars, but surfactant-stabilized droplets are occluded unless high flow forces distort and fragment droplets through these apertures. Multilayer fabrication approaches have also been included to improve droplet retention by decreasing drain channel height to more closely match reduced width.[17, 31] In addition, including active oil extraction flow rate control using gravity- or pump-based methods provides dynamic selection of final φ.[17] These devices have empowered efficient droplet packing for droplet synchronization or for obtaining incubation times up to a few tens of minutes.[17, 29, 31] Nonetheless, they presented specialized examples tailored to targeted droplet sizes, frequencies, and final φ. There has not yet been an example of a single architecture demonstrating dynamically selectable final φ without droplet breakup for a broad range of droplet sizes and frequencies.

Here, we present an oil extraction method, the Counter-Current Continuous Phase Extraction (C^3PE) module, which leverages a single microfluidic architecture to deterministically modulate φ. Not only could this device realize a wide distribution of φ, but we also showed exceptional compatibility with a range of initial droplet volumes without causing droplet fission

and sample loss. Additionally, operation was effective for droplets at frequencies from 40 to 200 Hz. We then labeled defined droplet subpopulations via electro-fluidic injection to probe the flow characteristics of droplets in incubation channels as a function of φ at high temporal resolution compared to previous methods.[29, 31] This facilitated an understanding of the relationship between droplet packing density and the duration and uniformity of on-chip incubation. We also characterized the effects of channel geometry and oil viscosity as examples where using this approach lent additional insight into optimizing the precision of in-droplet reaction times. Finally, we applied these principles to monitoring in-droplet β-galactosidase activity in an extended reactor volume to demonstrate significantly improved reaction performance, validating conclusions derived from our incubation tracking model. We envision this versatile approach will be applicable to a range of in-droplet chemistries and will ultimately lead to both an expanded microfluidic toolkit and more reproducible droplet handling.

EXPERIMENTAL SECTION

Fabrication

All devices were fabricated in 5:1 poly(dimethyl siloxane) (PDMS) (RTV615, Momentive) molded around SU8 2025 (Microchem) features on silicon wafers (University Wafer). Master molds were created via conventional soft lithography with 40 μm channel height.[32] Devices were designed in AutoCAD (Autodesk), and photomasks were sourced from CAD/Art Services, Inc. PDMS devices were irreversibly sealed to glass coverslips (Corning) after punching holes for fluidic connections with a 30 ga needle and activation by oxygen plasma (PDC-32G, Harrick

Plasma). Microchannels were treated with 1% tridecafluoro-1,1,2,2-tetrahydrooctyl trichlorosilane (Gelest, Inc.) in Fluoroinert FC-40 (The 3M Company) prior to use.

Device Operation

A pressure-driven flow system delivered fluids on-chip. For this system, a custom manifold (VWR) distributed high pressure N_2 gas to an array of regulators. Gas flow continued through tygon tubing to a solenoid valve array (LHDA0531115H, The Lee Company) controlled by an in-house LabView program (National Instruments) that delivered selected gas pressures to the head space of solution-filled vials through stainless steel fittings (New England Small Tube). This pressure drove fluids from the vials through 20 cm lengths of #30 PTFE tubing (Cole Parmer) connected directly to device inlet ports. Changing pressures (measured at the regulators for each fluid line) proportionally adjusted the corresponding fluid flow rates (20-80 kPa typical pressures yielding flows on the order of µL/min).

The continuous phase oil for droplet formation and oil extraction channels was a mixture of Fluoroinert FC-40 (typically 80%) with Novec 7500 Engineered Fluid (typically 18%) (The 3M Company) and 2% 008-Fluorosurfacant to stabilize droplets (Ran Biotechnologies). Oil kinetic viscosity measurements were collected using a No. 75 Cannon-Manning Semi-Micro Type for Transparent Liquids viscometer operated at room temperature (Cannon Instrument Company). For characterization and droplet tracking experiments, the dispersed phase for droplet formation was water, and the K-channel fluid was black food dye (McCormick). Typical droplet volumes were ~150 pL, and typical droplet frequencies were ~100-200 Hz. All solutions were passed through a 0.2 µm syringe filter prior to use. For enzyme activity experiments, the dispersed phase was 500 µM resorufin-β-D-galactopyranoside (Thermo Fisher Scientific) in 1X PBS with 0.5% BSA, pH

7.4. The K-channel delivered the enzyme sample, a slurry of 10 μm diameter streptavidin-coated magnetic microparticles (Sigma Aldrich) resuspended in OptiPrep Density Gradient Medium (Sigma Aldrich). Microparticles were previously incubated for 1 h with β-galactosidase-biotin (Sigma Aldrich) in 1X PBS with 0.5% BSA, pH 7.4.

A custom DC to AC inverter supplied ~40 VAC electric field for transient K-channel dye injections. The electric field was applied via in-device 3M NaCl solution-filled electrode channels. Precise electric field pulse timing was controlled via LabView interfaced directly to the inverter.

Imaging and Analysis

A DMi8 microscope platform (Leica Microsystems) coupled to a VEO 640L high speed camera (Vision Research, Inc.) enabled bright-field and fluorescence imaging of droplet performance. Fluorescence images were collected using a TXR Cube Filter (Leica Microsystems). Videos were analyzed via ImageJ to monitor droplet size, position, frequency, φ, and fluorescence intensity. φ was measured in straight channel segments where droplets flowed single file and was calculated as the ratio of droplet area to the total channel area from the leading edge of one droplet to the leading edge of the next. Oil extraction plots represent at least N = 20 droplets measured for each condition tested, and incubation tracking experiments evaluated at least three droplet tagging pulses per each of three devices used under each condition. Incubation time was calculated by finding the average and standard deviation among all incubation times corresponding to each tagged droplet sub-population for each condition. Incubation dispersion was calculated by first finding the relative standard deviation for each tagged droplet sub-population and then finding the average and standard deviation of these values for each condition (see the Supplementary Information for the detailed incubation analysis method). For plots of geometry and oil viscosity

variants versus incubation time and dispersion, the same standard dataset was included, representing single lane incubation with high oil viscosity. Statistical significance was assessed using an F-test to compare the variances among different incubation test datasets (as described in the ESI) and by using a two-sample Student's t-test to assess incubation time relative standard deviation (RSD) values.

For the β-galactosidase enzyme assay, videos were collected to visualize the final 1 mm of the incubation channel while opening the shutter to the exposure source (to minimize photobleaching). Droplet intensity was measured for droplets containing only one bead across three trials for each condition tested, and each trial included at least 15 droplets, contingent on stochastic bead distribution. Between trials, packing fraction was verified, and flow conditions were adjusted as needed to compensate for flow perturbations across the extended channel. Fluorescence dispersion was evaluated by finding the RSD of fluorescence intensity for each trial. For each condition, the average and standard deviation among these RSDs was calculated. Finally, the two conditions were compared using a two-sample Student's t-test. To generate the histogram, droplet intensity values from each trial were normalized to the overall average intensity for each condition, and points were weighted so that each trial represented 33% of the total area per condition. The superimposed fit lines assumed a normal distribution centered at each average intensity with standard deviations calculated from the reported RSD values from each condition.

RESULTS AND DISCUSSION

C^3PE Operating Principles

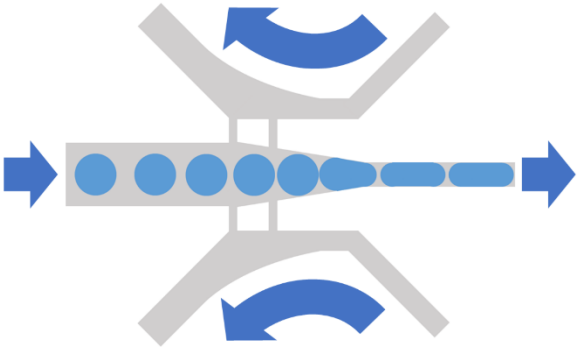

Figure IV.1. C^3PE Operating Schematic. As the droplets (light blue) flow into the module, the higher pressure in the main channel relative to the counter-current oil flows drives oil into the cross-channel to increase droplet volume fraction (arrows indicate flow direction).

The Counter-Current Continuous Phase Extraction (C^3PE) module consisted of two symmetric cross-channels linked to the droplet-containing main channel by an array of narrow apertures (Fig. IV.1). As droplets entered the system, oil drained out through the narrow apertures which blocked droplet passage. Importantly, counter-current, antiparallel oil flows through the cross-channels (relative to droplet flow direction) provided an active control element to adjust extraction performance in response to droplet size, initial φ, and desired final φ, among other parameters. At relatively low cross-channel oil flow rates and pressures, a net pressure difference drove more oil from the higher pressure main channel into the cross-channels, removing it from the sample emulsion.

A combination of principles made fluid removal specific to the oil phase (Fig. IV.2a-b, Supplementary Movie SMIV.1). Narrow connecting channels blocked the passage of droplets unless the net force toward cross-channels overcame the Laplace pressure from severe droplet curvature through narrow apertures.[17, 19] Additionally, hydrodynamic (lift) forces provided a focusing force toward the center of the channel for droplets of smaller diameter than the channel width.[33] Moreover, because the lateral forces toward each cross-channel balanced at the center of the channel, the system minimized the net force felt by droplets toward either cross-channel. Due

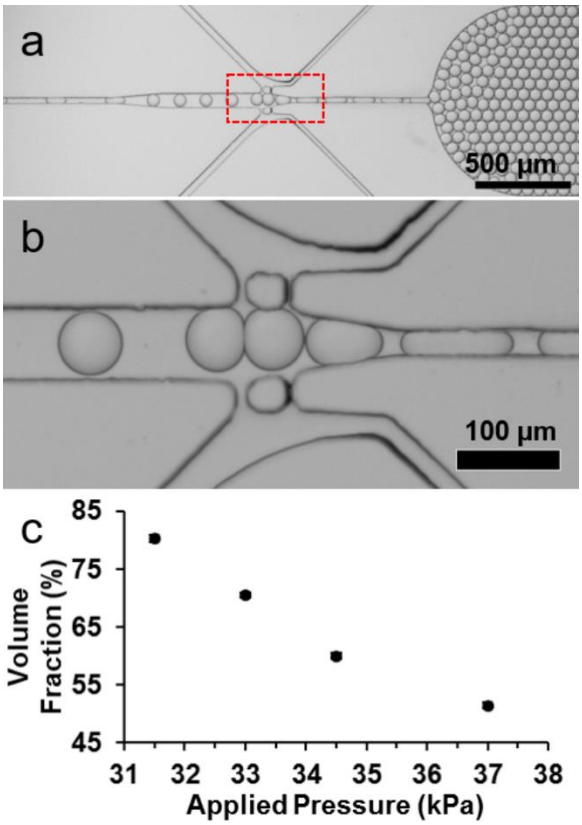

Figure IV.2. Oil Extraction Operation. a) Water droplets (flowing left to right) pass the C^3PE module and pack at high φ downstream. b) Sample droplets are selectively retained in the main channel using micropillar structures and a balance of symmetrically applied forces. c) Final φ decreases with increasing pressure applied to oil-filled cross-channels, and error bars represent N = 20 droplets.

to the central symmetry of forces on droplets, fluid removal via C^3PE preferentially eliminated peripheral oil first. This symmetry reduced the need to employ higher complexity fabrication-based strategies (such as shorter channel heights for only the connecting channels) to prevent droplet loss.[17, 31] In summary, this single-layer module reproducibly extracted oil from passing droplets to increase φ because it successfully counterbalanced forces that might fragment droplets.

Adjusting oil extraction cross-channel flow rates (by manipulating pressure-driven flow) controlled the direction and magnitude of oil flow through the connecting apertures (Fig. IV.2c). Using lower cross-channel oil pressures created a greater net pressure difference from the main channel to the oil extraction channels, leading to greater flow of main channel oil into the cross-

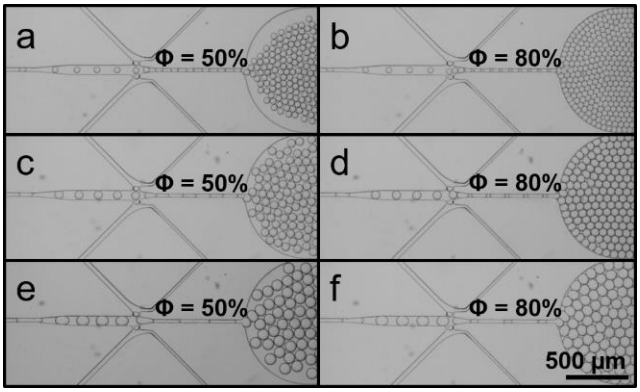

Figure IV.3. Droplet Size Versatility. The C^3PE device is broadly compatible with many input droplet volumes, manipulating a-b) small (75 pL), c-d) medium (130 pL), and e-f) large (230 pL) droplets without droplet breakup and sample loss for tunable final φ (50% and 80% shown).

channels. For example, this module yielded a final φ of up to 80% at low oil cross-channel pressures without droplet break-up (150 pL each, 100 Hz generation frequency). Further extraction was possible but presented a higher likelihood of instabilities as forces on droplets increased (higher droplet frequencies were demonstrated in later examples). Conversely, higher cross-channel oil pressures and flow rates limited oil flow out of the main channel (decreasing final φ). While the exact pressure values depended primarily on the oil cross-channel dimensions, on oil viscosity, and on the pressures driving other on-device flows, careful control of these cross-channel flows effectively selected φ.

This ability to extract oil from the main channel while minimizing droplet stresses empowered the platform to access a range of droplet sizes (Fig. IV.3 and Supplementary Fig. IV.S1). For small, loosely spaced droplets (Fig. IV.3a-b and Supplementary Fig. IV.S1a), low initial values for φ necessitated very low cross-channel oil pressures for effective oil extraction. The increased oil flow from the main channel exerted larger forces on the droplets. In this case, Laplace pressure from increased droplet curvature (smaller radius) further stabilized the system against droplet fission.[17] Increasing droplet size necessitated higher cross-channel pressures to compensate for the lower relative oil fraction in initial droplets (Fig. IV.3c-f). Additionally, the

symmetry of forces applied to droplets toward the cross-channels expanded the use of this module to even larger, less stable droplet sizes, which were processed without fission (Supplementary Fig. IV.S1b). Accessing droplets beyond the 7-fold size range demonstrated here may require scaling of channel features, and extreme input conditions can destabilize operation. Nonetheless, dynamic control of flow parameters empowered this monolayer device to adapt to a broader range of initial and final droplet packing states beyond those shown by any single previous example.

K-Channel-Mediated Droplet Labeling

In order to investigate the effects of φ on time-dependent droplet systems, we developed a model device where droplets passed into a delay-type incubation channel after oil extraction. The uniformity of chemical reaction progress across a droplet population should directly correlate with the homogeneity of droplet incubation time, termed "dispersion."[29] Droplet behavior and residence time was evaluated in this model system's incubation channel as a function of φ and additional parameters to better profile the physical principles that lead to incubation dispersion.

To more easily monitor droplet trajectories through the incubation channel, a K-channel module[18] was included upstream of the C^3PE geometry (Fig. IV.4a, Supplementary Movie SMIV.2). The K-channel's precisely balanced cross-channel flow of aqueous black dye injected a small volume of dye into passing droplets only when the adjacent saline electrodes were charged.[18, 34] Using high dye concentrations ensured droplet size did not appreciably increase while still generating sufficient optical contrast. This on-demand control over electric field timing provided a method for generating discrete, trackable populations of black-dyed droplets amongst the total water droplet population (Fig. IV.4b). Because droplets and the K-channel- stream only fused and exchanged material in the presence of the interface-destabilizing electric field, changing the length

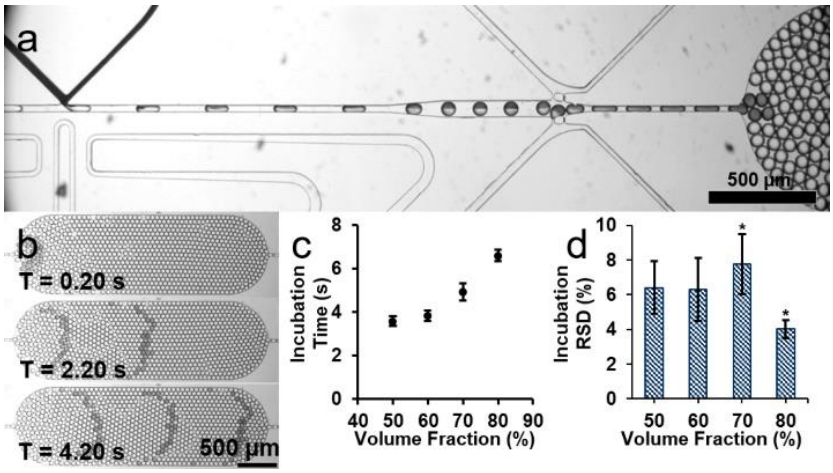

Figure IV.4. Droplet Tracking and Incubation. a) The K-channel (leftmost feature, saline electrode channels below) deterministically injects black dye into a water droplet sub-population before the droplets undergo oil extraction and incubation. Injection only occurs when the electrodes are charged. b) Dyed droplets follow a parabolic trajectory in the incubation channel (φ = 70%, flowing left to right). c) Incubation time increases with increasing φ. d) The relative standard deviations of the incubation times at both φ = 70% and φ = 80% differ significantly from the values at all other packings (95% confidence).

of time during which the electrodes were charged determined how many sequential droplets were labelled with dye. For example, pulses 100-250 ms in duration commonly injected into 15-40 droplets (depending on droplet generation frequencies, typically 150-200 Hz). Droplets passing the K-channel before or after the electrical pulse were unaffected, as were up- and downstream operations, which were shielded from the field by grounding channels.[18] In summary, short electric field pulses for K-channel injections provided a high temporal resolution tool for studying the behavior of droplet flow through incubation channels and represented a sophisticated alternative to previous techniques varying input droplet composition.[29, 31]

Volume Fraction and Incubation Characterization

Leveraging this model system, the effects of the oil extraction module on droplet incubation were evaluated. A detailed description of the analysis method is presented in the Supplementary Information. For these experiments, a smaller incubation volume (providing

generally less than 10 s of incubation) with all droplets confined within a single plane was chosen. This channel provided a simple model system with easily monitored droplets to avoid obscuring core phenomena with confounds from an overly large or complex incubation feature.

Fundamentally, increasing droplet packing for droplets of fixed size and frequency leads to proportionally greater residence time per droplet in a given incubation volume. In practice, incubation time increases can compound due to increased downstream hydraulic resistance from more densely packed droplets in the incubation channel. This resistance decreases upstream flow rates and droplet generation frequency (185 Hz at $\varphi = 50\%$ decreased to 175 Hz at $\varphi = 80\%$ in one example). Nonetheless, this compounding effect has lesser significance to incubation time than the number of droplets packed in the channel. Overall, the K-channel-coupled C^3PE platform dynamically selected incubation times, nearly doubling values from $\varphi = 50\%$ (3.6 s) to $\varphi = 80\%$ (6.6 s) for a fixed channel volume (Fig. IV.4c).

Modulating droplet packing significantly alters the character of droplet motions within the incubation region, leading to changes in the incubation dispersion, evaluated in this work as the relative standard deviation (RSD) of each droplet population's incubation time. This dispersion is due to dis-uniform droplet motions throughout the channel volume, driving some droplets into trajectories which take relatively longer or shorter times. For instance, changing the channel cross-sectional area plays a major role in incubation dispersion because droplets flowing in a confined, single-file channel experience fewer degrees of freedom in their motions than those flowing through a region with lateral dimensions much larger than the droplet diameter. Incubation dispersion can further compound when increased channel heights permit significant motions. We limited this study to monitoring effectively two-dimensional droplet flows through relatively confined channels, resulting in smaller incubation dispersions[29] with simplified flow behavior.

Using this system, we monitored incubation dispersion as altering φ passed droplets through different regimes (Fig. IV.4d). At very high φ (80%, Supplementary Movie SMIV.3), droplets approached maximal packing and organized into a hexagonal lattice. In this jammed state, droplets in the rigid array moved at a uniform linear velocity across the incubation channel.[30] Primarily, incubation deviations for individual droplets arose from shuffling and defects in the lattice,[31] especially at the regions where the channel cross section changed. It is also at these regions of channel expansion and contraction where droplets crossing the channel center followed a shorter path length (than those which travel around the periphery) and could exit the channel first, hence the parabolic pattern in the dyed droplet population. As φ decreased (70%, Supplementary Movie SMIV.4), the prevalence of flaws in the lattice increased, leading to droplet shuffling and whole faces of the lattice shifting relative to one another. At the channel periphery, loosely packed droplets in contact with walls moved the slowest, and this condition had the highest dispersion. At even lower φ (50%, Supplementary Movie SMIV.5), rafts of uniformly-moving droplet lattice transiently formed and broke up near the center of the channel, driven by hydrodynamic forces. Moreover, because a larger portion of the channel became occupied by loosely packed droplets, flow velocity at the edges increased as freely moving droplets flowed through the lower resistance streamlines. Therefore, droplets on the edges still traversed a longer path length but did so at a higher linear velocity. These results agreed with previous work[29] to help confirm the validity of this incubation monitoring workflow as well as to verify that the C^3PE module did not generate any unexpected flow disruptions.

Channel Geometry: Subdivisions

For continuous (not segmented) flow through a microchannel, subdividing the channel cross-section into parallel channels can correspondingly subdivide the parabolic flow profile through it into a series of parallel, smaller parabolic profiles. For segmented flow systems, the key factor in performance for this geometry was not actually the re-scaling of the laminar flow profile closer to the critical dimensions (i.e., diameter) of droplets, but instead that droplets in the subdivided channels had less opportunity to move laterally.[29] Although narrowing channels to flow droplets single file should theoretically yield the lowest dispersion (no droplet lateral motion), we chose a 4-fold divided approach. This not only simplified fabrication (larger channels are more tolerant of small defects), but also limited the increases in hydraulic resistance and back-pressure which can make very narrow channels prohibitively resistive to be practical for longer incubations.

In our 4-fold sub-divided channel the width of each sub-channel restricted more than four droplets from flowing side-by-side. The total incubation times were not greatly affected (Fig. IV.5a), and, as expected, reduced lateral motions within each sub-channel were qualitatively observed compared to the bulk channel. On the other hand, significantly higher dispersion under most values of φ were measured (Fig. IV.5b). At low φ (50%), hydrodynamic forces focus incoming droplets near the center of the channel,[33, 35] leading to asymmetry among sub-channel packings (Fig. IV.5c). The higher viscosity of densely packed droplets in the midline channels caused slower flow, so droplets exited peripheral channels first. At high φ (80%), droplets experienced little shuffling even in the absence of sub-division-induced confinement, so the incidence of droplets overtaking each other was already low, largely eliminating the purpose of the sub-division. In this case, however, flow at channel bifurcations exerted approximately balanced forces toward both possible flow directions. This balance temporarily trapped some droplets at bifurcation points, thus leading to the observed dispersion increase (Fig. IV.5d). These

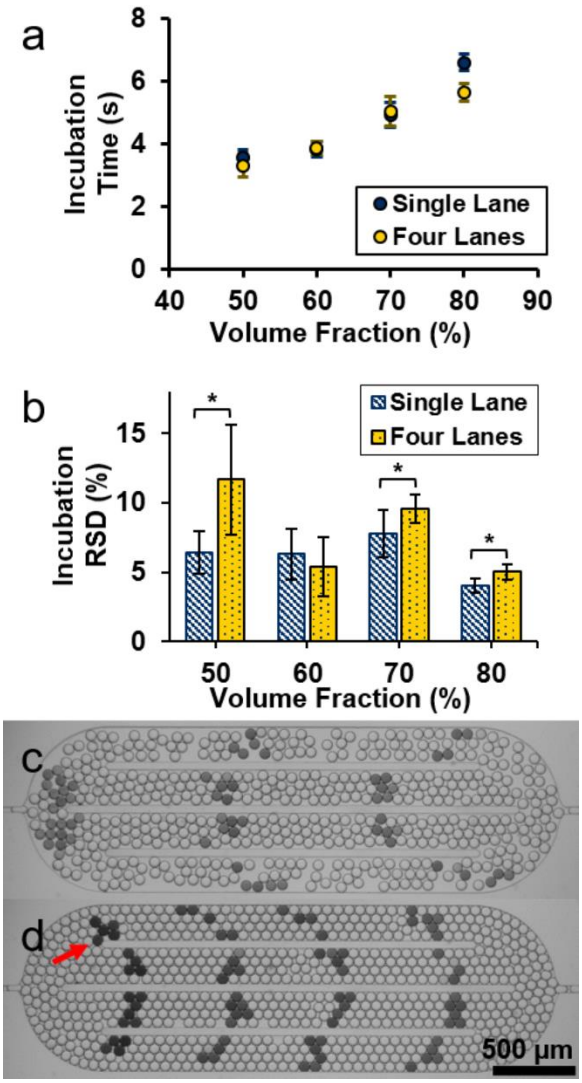

Figure IV.5. Channel Subdivisions Decrease Incubation Uniformity. a) Incubation time varies little between an undivided (single lane) and a subdivided channel (four lanes) of identical size. b) At low φ, incubation distribution is significantly increased (at 95% confidence) for the subdivided channel due to packing and velocity heterogeneities among lanes. At high φ, incubation distribution is significantly increased due to bifurcation-driven disordering. c) At low φ (50%), hydrodynamic forces focus droplets toward innermost channels, increasing hydraulic resistance in those channels. Outer channels experience faster flow. d) At high φ (80%), opposing forces at channel bifurcations can temporarily trap droplets (example highlighted by red arrow). Flow in images is left to right.

results consistently showed poorer performance for the subdivided channel, but additional investigation may enable optimization of channel inlets and bifurcation points.

Oil Viscosity

Viscosity plays a major role in droplet flow, proportionally changing flow rates under fixed pressures and altering flow segmentation characteristics. The fluorinated oil continuous phase further provides the medium through which droplet trajectories determine incubation time and dispersion, so we examined the relationship between oil viscosity and incubation performance. As expected, increasing the viscosity of the oil phase (by changing its blending ratio) generated slower-moving droplets with longer incubation times under similar flow conditions and droplet sizes (Fig. IV.6a).

Beyond routine effects from viscosity-induced flow rate changes, incubation dispersion as a function of oil viscosity was evaluated. Dispersion originates from heterogeneous droplet motions, so we hypothesized that altering the medium through which these motions occur should also alter incubation uniformity. Correspondingly, increasing the rigidity of the packed droplet lattice using high oil viscosity reduced dis-uniform droplet motions, decreasing incubation dispersion at high φ (80%) (Fig. IV.6b). Interestingly, the opposite trend was observed at intermediate φ (60-70%), where higher oil viscosity increased dispersion. Under intermediate packing conditions, center-directed hydrodynamic forces were generally insufficient to hold the droplets into a central lattice. Therefore, examining the flow character of loosely packed droplets at the periphery revealed significant contributions to dispersion (particularly for droplets moving more slowly than the central population).[29, 33, 35] In cases where these droplets had less resistance to slide past each other and were not rigidly trapped in contact with the walls, the low viscosity oil streams enabled many peripheral droplets to travel at higher velocity through longer peripheral flow paths (Fig. IV.6c-d). This effect significantly reduced dispersion compared to using higher viscosity oil. At low φ (50%), even the highest viscosity oil condition entered the loose-packed regime where peripheral droplets traveled faster than central ones, and no significant differences

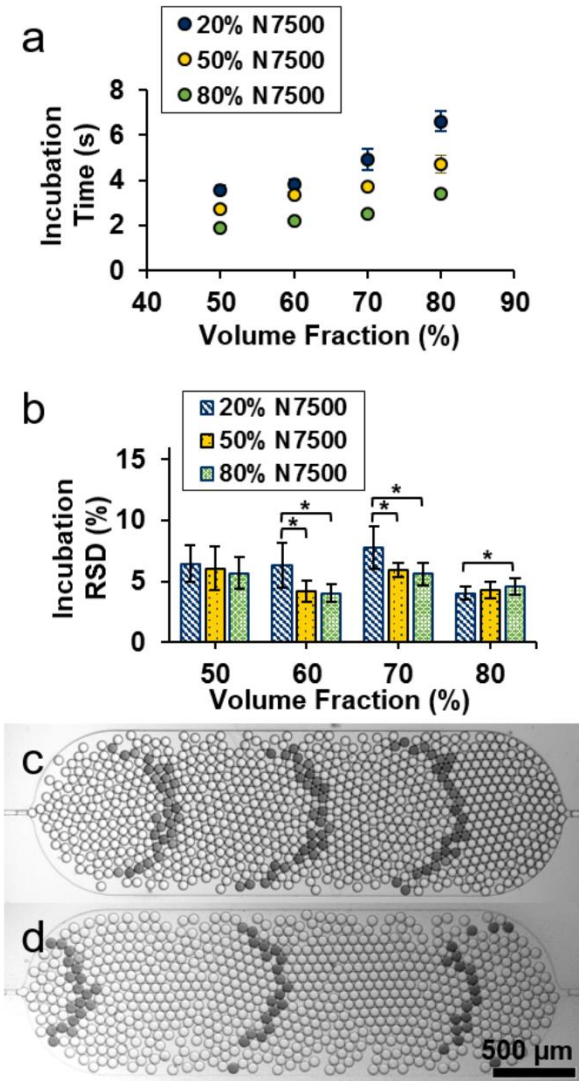

Figure IV.6. Oil Viscosity Dependence of Incubation Time and Distribution. a) Increased Novec 7500 (N7500):Fluoroinert FC-40 ratio decreases viscosity to decrease average incubation times. b) At intermediate φ, high viscosity oil limits droplet lateral motions, trapping peripheral droplets in slow, wall-bounded streamlines, significantly (95% confidence) increasing incubation distribution. At high φ, lower viscosity oil provides less resistance to the disturbance of close-packed droplet lattices and thus significantly increases incubation distribution. c) Peripheral droplets under high viscosity conditions (20% Novec 7500, φ = 60%) lag further behind the central population than (d) those under low viscosity conditions (80% Novec 7500, φ = 60%). For 20%, 50%, and 80% Novec 7500, η = 2.04, 1.46, and 1.08 cSt, respectively.

in incubation dispersion were observed. These results provide an initial demonstration of the significant role oil viscosity plays in droplet motions in the context of controlling incubation uniformity.

B-Galactosidase Reaction Optimization

Finally, we wanted to confirm that the incubation guidelines derived by the simple incubation model system would apply meaningfully to a biochemical reaction in droplets with more practically useful incubation times. Because of its broad deployment as an enzymatic amplification strategy (when coupled to a suitable antibody) in enzyme-linked immunoassays, we chose β-galactosidase. In this context, control over enzyme incubation directly affects the final fluorescent product signal (generally proportional to analyte concentration in an immunoassay), and devising a meaningful, accurate, and precise in-droplet immunoassay will thus require high precision incubation for effective analyte quantitation. We used a K-channel injection of streptavidin beads bound to β-galactosidase-biotin to stochastically deliver discrete loadings of enzyme into resorufin-β-D-galactopyranoside substrate droplets (Fig. IV.7a-b). Following oil extraction, droplets incubated in an extended delay channel, and droplet packing and flow behavior were confirmed using brightfield imaging to ensure that packing performance would be representative of results from prior droplet tracking experiments. At the end of the incubation channel, fluorescent imaging monitored turnover of fluorescent resorufin product in droplets containing only one enzyme-coated bead (Fig. IV.7c-d). Higher fluorescence intensities observed in droplets containing multiple beads (representing accelerated reactions) confirmed that substrate was not depleted within the reactions measured. As expected, droplets at lower packing ($\varphi = 55\%$) incubated for shorter time (~45 s) and had lower average fluorescence intensity than those incubated at higher packing ($\varphi = 85\%$, ~70 s incubation). Droplets at the sub-optimal packing condition ($\varphi = 55\%$) also showed significantly greater fluorescence dispersion (RSD = 10 ± 2%) compared to optimal packing ($\varphi = 85\%$, RSD = 6.0 ± 0.8%). These results are in good agreement with the conclusions from our droplet tracking model. In summary, leveraging the C^3PE module

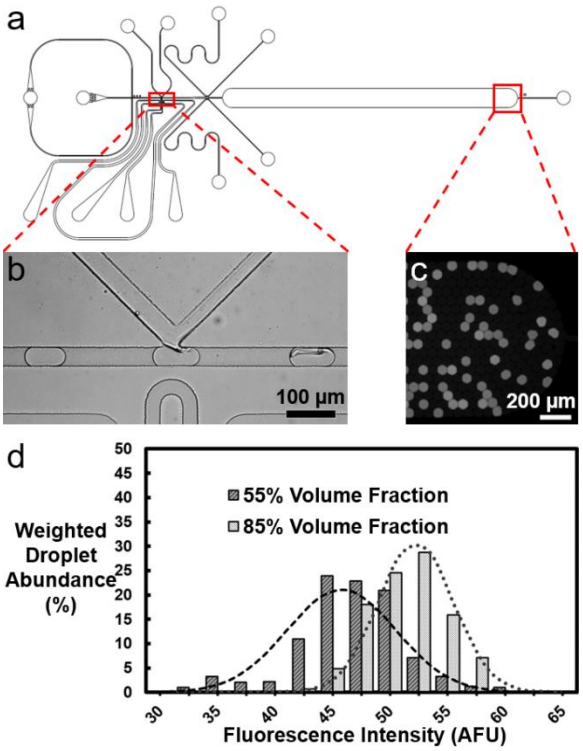

Figure IV.7. β-Galactosidase Incubation Optimization. a) Incubation dependence of an enzyme reaction in droplets was monitored using sequential resorufin β-D-galactopyranoside substrate droplet formation, b) K-channel-mediated bead-bound β-galactosidase injection, oil extraction, and c) extended incubation with fluorescent visualization. d) A normalized histogram of single bead-containing droplet fluorescent intensities demonstrates that increased fluorescent resorufin product formation with a significantly more uniform distribution was achieved at high packing conditions (φ = 85%, incubation time ~70 s, RSD = 6.0 ± 0.8%) compared to sub-optimal incubation conditions (φ = 55%, incubation time ~45 s, RSD = 10 ± 2%). Gaussian overlays assume a normal distribution and represent the reported values for each population's relative standard deviation (RSD).

both increased fluorescent product yield and decreased droplet-to-droplet variability. Further, these results suggest that similar manipulations of the other parameters tested (like channel geometry and oil viscosity) will be comparably effective in influencing the uniformity of (bio)chemical reactions in droplets.

CONCLUSIONS

In this work, the C^3PE microfluidic architecture leveraged symmetric oil countercurrent flow structures to efficiently extract oil from sample emulsions without droplet breakup, even at

high packing fractions. Moreover, adjusting external pressures applied to the module selected the final value for φ, and compatibility was demonstrated across a range of input droplet conditions. Adding a K-channel-mediated injection strategy enabled a robust droplet tracking approach that allowed for characterization of droplet behavior in incubation channels at high temporal resolution. By altering parameters such as φ, channel sub-divisions, and oil viscosity, both the overall incubation time and the relative dispersion of incubation times within each droplet population were dynamically adjusted. Finally, monitoring β-galactosidase activity in an extended incubation application demonstrated that the trends derived from the simple model can be meaningfully applied to in-droplet biochemistry. This extraction geometry, especially when coupled to the incubation monitoring approach, represents a valuable fundamental tool for controlling and understanding droplet flow behavior—particularly in the context of time-dependent chemistry.

ACKNOWLEDGEMENTS

We gratefully acknowledge financial support from the National Institutes of Health (NIH CA191186). S.R.D. was supported by the National Science Foundation Graduate Research Fellowship Program. M.L. was supported by the Pfizer Undergraduate Summer Research Award (University of Michigan). We also want to thank Prof. Robert Kennedy and Dr. Brian Shay (University of Michigan) for assistance with viscosity measurements.

REFERENCES

1. T. Thorsen, R. W. Roberts, F. H. Arnold and S. R. Quake, *Phys Rev Lett*, 2001, **86**, 4163-4166.
2. L. Shang, Y. Cheng and Y. Zhao, *Chemical Reviews*, 2017, **117**, 7964-8040.
3. H. Song, J. D. Tice and R. F. Ismagilov, *Angew Chem, Int Ed*, 2003, **42**, 768-772.

4. T. M. Squires and S. R. Quake, *Rev Mod Phys*, 2005, **77**, 977-1026.

5. J.-C. Baret, *Lab Chip*, 2012, **12**, 422-433.

6. V. Sahore, S. R. Doonan and R. C. Bailey, *Anal Methods*, 2018, **10**, 4264-4274.

7. F. Lan, B. Demaree, N. Ahmed and A. R. Abate, *Nat Biotechnol*, 2017, **35**, 640-646.

8. R. Zilionis, J. Nainys, A. Veres, V. Savova, D. Zemmour, A. M. Klein and L. Mazutis, *Nat Protoc*, 2016, **12**, 44-73.

9. Y. Xu, J.-H. Lee, Z. Li, L. Wang, T. Ordog and R. C. Bailey, *Lab Chip*, 2018, **18**, 2583-2592.

10. N. Choi, J. Lee, J. Ko, J. H. Jeon, G.-e. Rhie, A. J. deMello and J. Choo, *Anal Chem*, 2017, **89**, 8413-8420.

11. H. Huang, Y. Yu, Y. Hu, X. He, O. Berk Usta and M. L. Yarmush, *Lab Chip*, 2017, **17**, 1913-1932.

12. S.-Y. Teh, R. Lin, L.-H. Hung and A. P. Lee, *Lab Chip*, 2008, **8**, 198-220.

13. P. Garstecki, M. J. Fuerstman, H. A. Stone and G. M. Whitesides, *Lab on a Chip*, 2006, **6**, 437-446.

14. M. Sun and S. A. Vanapalli, *Anal Chem*, 2013, **85**, 2044-2048.

15. M. Lee, J. W. Collins, D. M. Aubrecht, R. A. Sperling, L. Solomon, J.-W. Ha, G.-R. Yi, D. A. Weitz and V. N. Manoharan, *Lab Chip*, 2014, **14**, 509-513.

16. M. T. Chung, D. Nunez, D. Cai and K. Kurabayashi, *Lab Chip*, 2017, **17**, 3664-3671.

17. J. R. Haliburton, S. C. Kim, I. C. Clark, R. A. Sperling, D. A. Weitz and A. R. Abate, *Biomicrofluidics*, 2017, **11**, 034111.

18. S. R. Doonan and R. C. Bailey, *Anal Chem*, 2017, **89**, 4091-4099.

19. A. R. Abate, T. Hung, P. Mary, J. J. Agresti and D. A. Weitz, *Proc Natl Acad Sci U S A*, 2010, **107**, 19163-19166.

20. L. Mazutis, J. Gilbert, W. L. Ung, D. A. Weitz, A. D. Griffiths and J. A. Heyman, *Nat Protoc*, 2013, **8**, 870-891.

21. S. Li, X. Ding, F. Guo, Y. Chen, M. I. Lapsley, S.-C. S. Lin, L. Wang, J. P. McCoy, C. E. Cameron and T. J. Huang, *Anal Chem*, 2013, **85**, 5468-5474.

22. E. Brouzes, T. Kruse, R. Kimmerling and H. H. Strey, *Lab Chip*, 2015, **15**, 908-919.

23. B. Verbruggen, K. Leirs, R. Puers and J. Lammertyn, *Microfluid Nanofluid*, 2015, **18**, 293-303.

24. S. R. Doonan, M. Lin and R. C. Bailey, *Lab Chip*, 2019, DOI: 10.1039/C9LC00125E.

25. D. Lombardi and P. S. Dittrich, *Anal Bioanal Chem*, 2011, **399**, 347-352.

26. H.-D. Xi, H. Zheng, W. Guo, A. M. Ganan-Calvo, Y. Ai, C.-W. Tsao, J. Zhou, W. Li, Y. Huang, N.-T. Nguyen and S. H. Tan, *Lab Chip*, 2017, **17**, 751-771.

27. P. C. Gach, K. Iwai, P. W. Kim, N. J. Hillson and A. K. Singh, *Lab Chip*, 2017, **17**, 3388-3400.

28. A. Huebner, D. Bratton, G. Whyte, M. Yang, A. J. deMello, C. Abell and F. Hollfelder, *Lab Chip*, 2009, **9**, 692-698.

29. L. Frenz, K. Blank, E. Brouzes and A. D. Griffiths, *Lab Chip*, 2009, **9**, 1344-1348.

30. P. Mary, A. R. Abate, J. J. Agresti and D. A. Weitz, *Biomicrofluidics*, 2011, **5**, 024101.

31. W. G. Cochrane, A. L. Hackler, V. J. Cavett, A. K. Price and B. M. Paegel, *Anal Chem*, 2017, **89**, 13227-13234.

32. Y. Xia and G. M. Whitesides, *Angew Chem, Int Ed*, 1998, **37**, 550-575.

33. B. Kaoui, G. H. Ristow, I. Cantat, C. Misbah and W. Zimmermann, *Phys Rev E*, 2008, **77**, 021903.

34. A. Sciambi and A. R. Abate, *Lab Chip*, 2014, **14**, 2605-2609.

35. K. S. Jayaprakash, U. Banerjee and A. K. Sen, *Langmuir*, 2016, **32**, 2136-2143.

36. A. S. Basu, *Lab Chip*, 2013, **13**, 1892-1901.

37. Z. Z. Chong, S. B. Tor, A. M. Gañán-Calvo, Z. J. Chong, N. H. Loh, N.-T. Nguyen and S. H. Tan, *Microfluid Nanofluid*, 2016, **20**, 66.

SUPPLEMENTARY INFORMATION

Supplementary Movie SMIV.1. Oil extraction operation increased final droplet volume fraction to 80%.

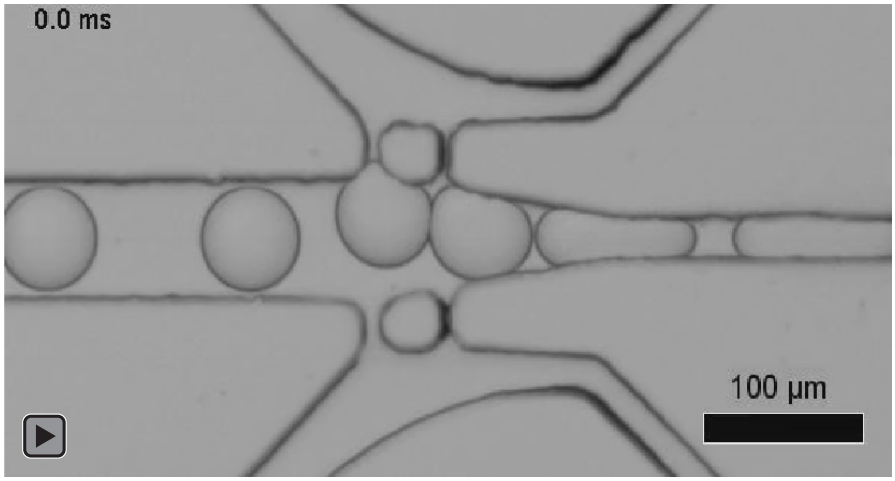

Supplementary Movie SMIV.2. The upstream K-channel injected black dye into sequential passing droplets when the electrodes were charged to generate dyed subpopulations for oil extraction followed by incubation analysis.

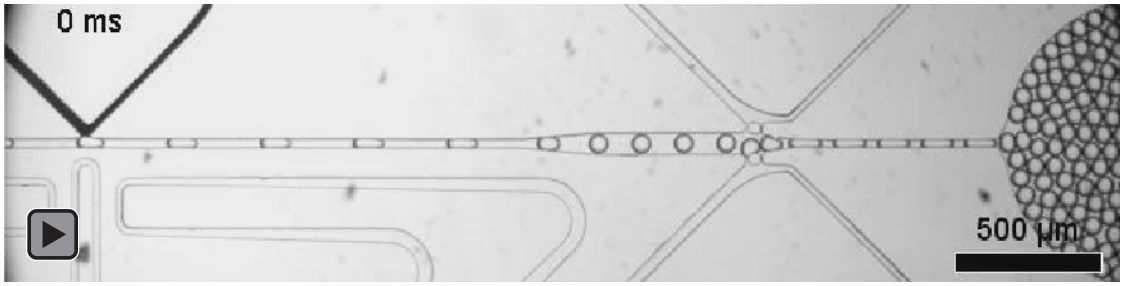

Supplementary Movie SMIV.3. Droplets tagged with black dye (125 ms electric field pulses) traversed the incubation channel at high volume fraction (80%). Droplets traveled at a fairly uniform linear velocity in the lattice, so peripheral droplets with the longest flow paths tended to exit the channel last.

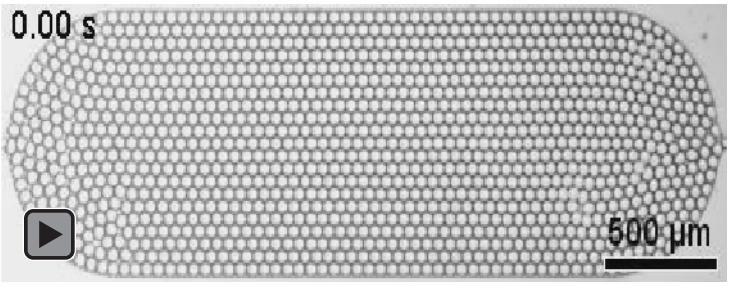

Supplementary Movie SMIV.4. Droplets tagged with black dye (125 ms electric field pulses) traversed the incubation channel at intermediate volume fraction (70%). Flaws and rearrangements occurred in high abundance in the central droplet lattice, and peripheral droplets were trapped in slow streamlines.

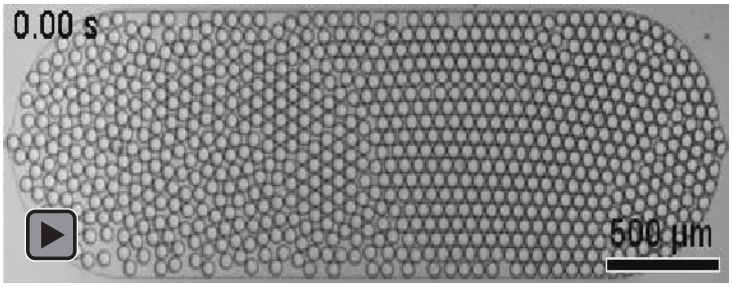

Supplementary Movie SMIV.5. Droplets tagged with black dye (125 ms electric field pulses) traversed the incubation channel at low volume fraction (50%). Loosely packed peripheral droplets traveled at higher linear velocities across a longer flow path compared to central droplets.

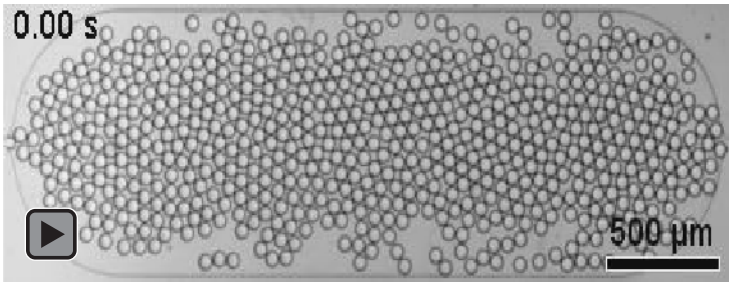

Incubation Tracking and Analysis Method

After adding a K-channel for tagging sequential droplet populations with dye, a simple and robust method for analyzing incubation performance in terms of absolute incubation time and distribution of incubation times within each population was developed. Continuously monitoring each droplet through its entire trajectory improves qualitative understanding of flow phenomena but can prove challenging to implement for large numbers of droplets. Specifically, manual tracking would be prohibitively time-consuming, and optical tracking methods often rely on thresholding and background subtractions that suffer for large footprint and inhomogeneously illuminated incubation channels (due to microscope field of view, shadows from tubing, etc.). Further, automated discrimination and tracking of droplets becomes increasingly difficult with increased packing densities. While sophisticated tracking programs have been demonstrated in prior work,[36, 37] an analysis method independent of individual droplet flow-paths was developed.

For this alternative method, the time at which each dyed droplet enters the incubation channel was first determined. Next, the time at which each tagged droplet exits the incubation channel was measured. Importantly, the specific trajectory of each droplet in the incubation channel was ignored and droplets were not indexed from entry to exit. The averages and standard

deviations of all entry and exit times were then used to calculate average incubation time, I, and the associated error was propagated to find the final standard deviation corresponding to the incubation dispersion, D.

This analysis only holds if initial droplet order does not significantly contribute to D. To verify this, we constructed two test datasets from the entry and exit times which represent the boundary conditions for incubation dispersion. For the first dataset, "Forward," it was assumed that droplet order was maintained from entry to exit, and for the second dataset, "Reverse," the assumption was that droplet order was inverted from entry to exit. These two cases represent the minimum and maximum contributions to dispersion from initial droplet order. The difference between entry and exit times corresponding to each droplet in the assigned orders was then calculated and statistically evaluated:

$$I_{Forward} = I = I_{Reverse} \qquad \text{Eq. S1}$$

$$D_{Forward} < D < D_{Reverse} \qquad \text{Eq. S2}$$

Average incubation times are equal (eq. 1) because they represent a different order of mathematical operations without fundamentally changing the calculation. On the other hand, incubation distributions range from $D_{Forward}$ to $D_{Reverse}$ as a function of droplet order (eq. 2). When $D_{Forward}$ and $D_{Reverse}$ do not significantly differ (F-test, 95% confidence threshold), this analysis holds, so there is no significant contribution from droplet order to incubation dispersion. As the labeled population becomes smaller (shorter K-channel electric field pulses), droplet order plays a correspondingly smaller role.

Overall, while individually tracking the motion of each droplet through the entire delay channel may add valuable information about flow characteristics, this analysis technique provides a simple and rapid alternative which eliminates the need for complex droplet-tracking software and still generates a quantitative understanding of incubation time and dispersion.

SUPPLEMENTARY FIGURE

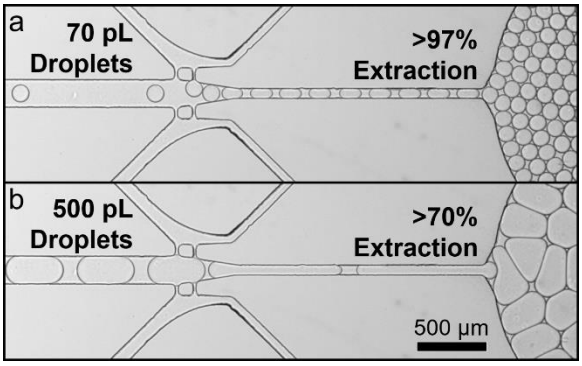

Figure IV.S1. Expanded Droplet Size Versatility. The C^3PE device can accommodate large differences in droplet size (limited here by the stability of upstream droplet formation). a) Small (70 pL, 100 Hz) and b) large (500 pL, 40 Hz) droplets are processed without sample loss.

Chapter V

Droplet CAR-Wash: Continuous Picoliter-Scale Immunocapture and Washing

Reproduced from Doonan, S.R., Lin, M., and Bailey, R.C. "Droplet CAR-Wash: Continuous Picoliter-Scale Immunocapture and Washing." *Lab on a Chip* **2019**, *19*, 1589-1598. *with permission from the Royal Society of Chemistry. Available at* doi: 10.1039/C9LC00125E.

INTRODUCTION

Droplet microfluidics have enabled revolutionary miniaturization capabilities for chemistry and biochemistry. By compartmentalizing samples in oil, two-phase segmented flow systems enable the automated handling of discretized samples through complex operations at rates of up to several kHz.[1-4] Individual droplets (fL-nL in volume) experience rapid mass transfer due to internal convective flows and short mixing distances, enhancing the speed and efficiency of in-droplet chemistry.[2, 3, 5] By leveraging fluorinated oils and optimized surfactants, these systems allow stable droplet production, extended storage, and sophisticated manipulation to provide performance analogous to or exceeding that of many bulk assays.[6] Further, the power of handling large numbers of discrete, often heterogeneous sample volumes through miniaturized, rapid processing has uniquely poised droplet microfluidics at the forefront of several exciting biochemical developments. As recent examples, droplet technologies have achieved single-nucleus RNA sequencing,[7] epigenetic analysis of nucleosome positioning,[8] and directed enzyme

evolution,[9] among other implementations. A number of reviews profile notable droplet applications in detail.[2, 4, 10-12]

Beyond these developments, integrating solid phase sample capture and manipulation can significantly extend the capabilities of microfluidics.[4, 13-16] This class of sample processing is ubiquitous in chemistry and biochemistry, retaining selected targets on a solid phase by immobilizing antibodies or complementary oligonucleotide sequences, by manipulating surface chemistry, or by using other approaches while allowing for the exchange or washing of buffers, reagents, and off-target species.[17-21] Clearly, sample immobilization and washing via interactions with a solid phase provides a range of important opportunities in synthesis, pre-concentration, extraction, and analytical measurements.[4, 13, 15] For example, a powerful bioanalytical technique, the (heterogeneous phase) immunoassay, leverages a sequence of washing and reagent exchange steps to provide an important method for clinical protein quantitation.[13, 18] To empower these capabilities in integrated droplet-based microfluidic devices, magnetic fields have provided a popular choice of flow-orthogonal force for selective manipulation of the solid phase.[4, 13, 16] Successful techniques include magnetic droplet translation through a series of co-flowing laminar reagent streams for applying polyelectrolyte surface coatings,[22, 23] magnetic tweezers for immobilizing bead volumes while exchanging reagent droplets around them for multistep bioassays,[24, 25] and additional examples of ferrofluid dispersed or continuous phase components for droplet generation and manipulation.[26, 27] These approaches have demonstrated efficient and selective magnetic phase manipulation for a range of applications, but additional capabilities are needed to fully adapt solid phase (bio)chemical techniques into droplet microfluidics.

Unfortunately for continuously flowing droplet technologies a key deficiency remains. Although well-characterized strategies in a range of material systems[28] continuously and reliably

form droplets and add reagents using T-junctions,[29] pairwise droplet fusion,[14] picoinjectors,[30] and other modules,[2, 3, 31, 32] approaches for selective sample capture and washing have faced serious limitations. The most prevalent scheme for in-droplet sample purification combines droplet splitting with a channel-adjacent magnetic field, concentrating magnetic bead-tethered sample in only one of the daughter droplets. A range of variations on this approach have achieved limited success within a few analytical applications. Examples have demonstrated high magnetic bead recovery, removal of up to 95% of starting waste volume through droplet splitting asymmetry, and/or low to modest throughput (0.5-200 Hz droplet frequencies).[17, 31, 33-37] Nonetheless, this approach can require serial droplet splitting and reagent addition operations (with exponentially decreasing effect) to reach higher washing purity, increasing device complexity while decreasing throughput.[35, 36] Lee *et al.* proposed an interesting alternative: collecting magnetic beads in a washing buffer droplet during temporary fusion with the original bead-laden sample droplet.[14] This was followed by nearly immediate breakup into the two original component droplets. While this device achieved approximately 25-fold dilution and bead transfer into collected droplets with little sample loss, it was also hindered by reduced throughput (3 Hz reported) and the added complexity of droplet synchronization for pairwise fusion and breakup. Finally, Alorabi *et al.* showed an impressive example of magnetic washing using multilaminar flow for magnetic droplet processing.[22] This device demonstrated effective washing by magnetically pulling entire ferrofluid droplets across orthogonally flowing washing buffer streams during a sophisticated layer by layer surface functionalization, in contrast to the discrete washing volumes involved in other droplet washing strategies. Recent reviews profile the breadth of solid phase manipulations in droplets, including alternative washing technologies to the continuously flowing droplet systems described here.[4, 13] These alternatives include micropillar and microwell-based devices,[38, 39] acoustic and

magnetic systems for temporary bead trapping (like those described above),[24, 25, 40] and digital microfluidic (DMF) strategies.[41] Such techniques, however, sacrifice the throughput and mixing characteristics common to continuously flowing droplet systems. A clear need for high speed, high efficiency in-droplet washing technologies remains.

In this work we sought to develop an efficient washing device without compromising simplicity of operation and droplet processing throughput. Our "Coalesce-Attract-Resegment Wash" (CAR-Wash) approach leverages a combination of electric and magnetic fields to fuse input droplets and then generate new droplets from a continuous washing buffer flow while capturing magnetic particles selectively in those final droplets. Thus, we realized greater than 100-fold dilution of the original droplets with minimal magnetic particle loss. Importantly, this technique operates at hundreds of Hz droplet frequencies, making it compatible with the high frequencies of many other droplet operations. Finally, we applied this technique to wash away a small molecule inhibitor to restore enzyme activity and to perform a selective protein enrichment and purification from cell lysate.

EXPERIMENTAL SECTION

Microfluidic Device Preparation

Devices were fabricated using standard soft lithography.[42] In brief, SU8 2025 Negative Epoxy Photoresist (MicroChem Corp.) was spin coated to 40 μm thickness on silicon wafers (University Wafer). Devices were designed in AutoCAD software (Autodesk, Inc.) and sourced as transparencies (CAD/Art Services, Inc.) for use in photolithography. After wafer baking and development, masters were surface treated under vacuum with tridecafluoro-1,1,2,2-

tetrahydrooctyl trichlorosilane (Gelest, Inc.) prior to use. A 5:1 base:curing agent ratio was used to fabricate PDMS (RTV615, Momentive Performance Materials, Inc.) devices that were bonded to glass cover slips (Sigma Aldrich) via oxygen plasma activation (PDC-32G, Harrick Plasma, Inc.) after punching inlet ports with a 30 gauge needle. All channels were 40 μm in depth and 40-200 μm in width. Devices were treated with 1% tridecafluoro-1,1,2,2-tetrahydrooctyl trichlorosilane in Fluoroinert FC-40 (Sigma Aldrich) prior to use.

Flow Control

Flow control on-device used a custom pressure controller. Nitrogen gas was directed through a splitting manifold to an array of two-stage regulators (VWR International) which selected applied pressures. From the regulators, gas was directed into a network of LHDA0531115H solenoid valves (The Lee Company) actuated by LabView via a NI PCIe-6251 Multifunction Data Acquisition Device (National Instruments Corporation). Finally, this gas was delivered through stainless steel pins (New England Small Tube Corporation) into the headspace of solution-filled reservoir vials connected to microfluidic device inlets through lengths of #30 PTFE tubing (Cole-Parmer). Applied pressures were between 10 and 100 kPa, yielding typical flow rates on the scale of μL/min. For example, the 500 Hz operation shown in Figure V.2 applied 55 kPa to the washing buffer, 45 kPa to the oil co-flow, 65 kPa to the input droplets, and 10 kPa to the waste outlet. This resulted in approximate flow rates of 75 μL/min for washing buffer, 8.5 μL/min for the oil co-flow, and 4.5 μL/min for input droplets.

Electric and Magnetic Fields

Electric field was generated using a custom inverter to apply ~45 VAC (36 kHz) to the device. Electric field was connected via a submerged platinum wire in the washing buffer reservoir and via a syringe with 3M NaCl used to fill saline electrode channels (40 μm channel depth).[43] Magnetic field was provided by an array of eight grade N52 NdFeB 1/2" x 1/4" x 1/8" magnets (K&J Magnetics, Inc.) positioned 200-500 μm from the channel using microfabricated alignment marks, and magnetization was directed toward the separation channel.

Reagents and Sample Preparation

Magnetic beads were Streptavidin Microparticles, 10 μm particle size (Sigma Aldrich), or Protein G Dynabeads, 2.8 μm particle size (Thermo Fisher Scientific). Beads were rinsed in water or buffer and re-suspended prior to use. For device characterization experiments, magnetic beads were re-suspended in 1 mM fluorescein (Sigma Aldrich) in water with 60% Optiprep (Sigma Aldrich) and 20% PBS, and the washing buffer was PBS. The fluorescent standard for these experiments was 10 μM fluorescein in PBS, and the continuous phase oil was 1% or 2% 008-Fluorosurfactant (Ran Biotechnologies, Inc.) in Novec 7500 (The 3M Company).

For the enzyme inhibition assay, 10 μg β-Galactosidase-biotin labeled from *Escherichia coli* (Sigma Aldrich) was incubated on 10 μm streptavidin microparticles for 2 hours then washed to remove unbound enzyme and re-suspended in 60% optiprep with 40% PBS and 0.2% BSA. Substrate (used as washing buffer) was 500 nM resorufin-β-D-galactopyranoside (Thermo Fisher Scientific) prepared in PBS, 0.5% BSA. Initial droplets or substrate with inhibitor also contained 1 mM isopropyl β-D-1-thiogalactopyranoside (IPTG) (Thermo Fisher Scientific) as indicated.

For the fluorescent protein enrichment assay, the cells were HeLa with Green Fluorescent Protein-Histone H2B (GFP-H2B) fusion expressed. Briefly, the cell sample processing procedure

included bulk lysis and enzymatic chromatin digestion of ~250,000 cells in detergent-rich Lysis and Digestion Buffers with Micrococcal Nuclease (New England BioLabs) as described previously.[8] mCherry (BioVision, Inc.) was added to 3.3 µg/mL for the final cell lysate suspension. Anti-GFP beads were prepared using 10 µm streptavidin microparticles with 4.5 µg GFP Rabbit anti-Jellyfish, Polyclonal Antibody (Thermo Fisher Scientific) following biotinylation of the antibody according to manufacturer's protocols (EZ-Link Sulfo-NHS-LC-Biotin, Thermo Fisher Scientific). After overnight incubation in 10 mM HEPES, 150 mM NaCl, 50 mM EDTA, 0.1% PEG, pH 7.4, beads were manually washed and re-suspended in a fresh aliquot of the same buffer to remove unbound antibodies. This buffer was also used as the washing buffer during device operation.

Data Collection and Analysis

Images were collected using a VEO 640L high speed camera (Vision Research, Inc.) connected to a DMi8 light microscope (Leica Microsystems). Fluorescent imaging was performed using a FITC filter cube for the green channel and a TXR filter cube for the red channel (Leica Microsystems). Image processing and analysis were performed using ImageJ software (NIH). Droplet size, spacing, and frequency and magnetic particle position were manually determined from brightfield images. Flow rates were calculated from droplet size, spacing, and frequency and particle velocity down the channel length. For evaluating magnetic migration velocity, particle trajectories were divided into five bins based on particle starting position in the y (magnet-oriented) direction. Magnetic migration velocity calculations compared the average velocity values for each bin after discarding the bin containing the washing buffer-oil co-flow interface (where magnetically-induced particle migration was restricted by the interface). Representative

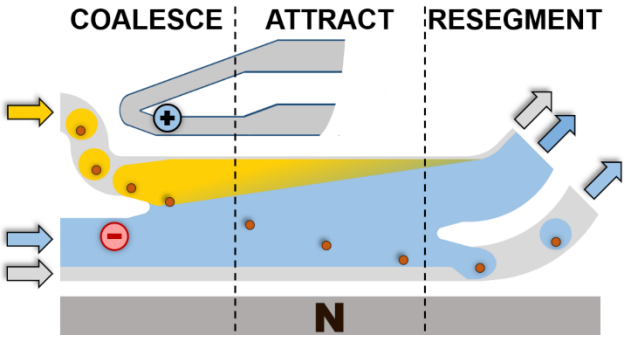

Figure V.1. The CAR-Wash technique electrocoalesces input droplets using electric field applied across the washing buffer stream and a nearby ground electrode. Next, a channel-adjacent permanent magnet attracts sample-enriched magnetic beads across the buffer stream while flow forces confine waste material to the original streamline. An oil co-flow prevents bead trapping at the channel wall and, at the end of the module, resegments droplets in washing buffer for further manipulations. Arrows indicate flow directions.

fluorescent images in figures were uniformly adjusted in brightness by fluorescent channel for ease of visualization, but quantitative data were obtained from the original images. For device characterization, droplet fluorescence localization plots average N = 20 time-points each, and the final plots were smoothed using a five point moving average. Plots of intensity values for the enzyme inhibition and fluorescent protein enrichment assays provide representative results for at least N = 50 droplets or beads for each reported sub-population. Statistical significance was assessed using a two sample Student's t-Test with a 95% confidence significance threshold (significance indicated by a dashed red line or an asterisk in plots).

RESULTS AND DISCUSSION

CAR-Wash Operating Principles

To provide a simple, robust, and effective droplet-based magnetic purification and washing method, we developed the "Coalesce-Attract-Resegment Wash" (CAR-Wash) platform. The main operating principles for this technique are highlighted in Figure V.1. Droplets containing the

magnetic bead solid phase enter the device and are subject to a destabilizing electric field. This field triggers droplet coalescence with a parallel washing buffer stream and can be generated on-device by directly charging a suitably conductive washing buffer and/or through conventional electrolyte-filled microchannel features.[43] As the boundaries between each input droplet and the washing buffer fuse, superparamagnetic beads escape the original droplet volume under the attractive influence of a channel-adjacent permanent magnet. While the laminar flow condition confines the input droplet fluid to its original streamline with relatively little mixing into the buffer flow, magnetic beads fully translate across the channel width. An oil co-flow provides a moving boundary to stop beads from reaching the channel wall while keeping them moving toward the end of the module. In the absence of this co-flow, beads may be trapped under the combined influence of maximum magnetic field and minimum orthogonal flow forces in the near-zero slip flow at the channel wall. Finally, the majority of channel flow diverts to waste (containing the input droplet volume and much of the washing buffer), and the streamline with magnetic beads segments into new droplets in combination with the oil co-flow. The abrupt local decrease in channel cross section and dispersed phase flow rate drives stable droplet formation in a dripping regime (under typical flow conditions).[32] Resegmented bead-containing droplets (now comprised of washing buffer) are suitable for further downstream processing, including, but not limited to, additional CAR-Wash operations for sequential buffer exchange.

Beyond this qualitative description of CAR-Wash operation, we also examined the physical principles interacting with parameters such as magnetic field, flow conditions, and magnetic bead identity. Each contributes to magnetic particle trajectory through the device, so we probed the effects of these parameters on the relative magnitudes of each force and the relative magnitudes of each force per unit particle mass (in examining different bead sizes). First, the

magnetic component of particle motion under a constant, high magnetic field is described under conditions of uniformly saturated magnetization throughout the particle:

$$\mathbf{F_m} = \left(\frac{1}{\mu_0}\right)(\mathbf{m} \cdot \nabla)\mathbf{B} \quad \text{eq. 1}$$

Where $\mathbf{F_m}$ is the magnetic force, μ_0 is the permeability of the medium, and **m** is the magnetic moment of the particle within the gradient of magnetic field, **B**.[13, 16, 23] The magnetic moment of the particle is directly proportional to its volume (for uniformly saturated magnetization), so the relative magnitude of the magnetic force per unit mass is constant for different particle sizes (assuming uniform particle density). On the other hand, the primary flow-derived force in the system, the hydrodynamic drag force, is directly proportional to particle radius for a spherical particle:

$$\mathbf{F_d} = 6\,\pi\,\boldsymbol{\eta}\,\boldsymbol{r}\,\Delta\mathbf{v} \qquad \text{eq. 2}$$

Where $\mathbf{F_d}$ is the hydrodynamic drag force, $\boldsymbol{\eta}$ is the fluid viscosity, $\boldsymbol{r}$ is the particle radius, and $\Delta\mathbf{v}$ is the velocity difference in fluid and particle motions.[4, 16, 23] Because volume and mass scale with the cube of the radius for a sphere of uniform density, the relative hydrodynamic drag force per unit particle mass decreases with increasing particle size.

These equations give insight about the key parameters in magnetic particle capture within the CAR-Wash. As applied magnetic field or particle magnetic moment increase, the magnetic force correspondingly increases to more effectively capture particles. These effects are achieved by using a stronger magnet or particles with a higher magnetization. Slower washing buffer flows

decrease hydrodynamic drag forces pushing particles through the channel, resulting in shorter channel lengths traversed during magnetic migration across the channel width.[4, 16] Additionally, larger particles experience a greater relative magnetic force compared to hydrodynamic drag force due to the relations discussed for eq. 1 and 2. Therefore, hydrodynamic drag forces opposing magnetically-induced motions across washing buffer streamlines have lower relative magnitudes for larger particles. Other forces like hydrodynamic lift (focusing particles toward equilibrium positions within the washing buffer's flow profile) have lower magnitude in this system compared to the magnetic force and the hydrodynamic drag force. While the lift force may oppose the magnetic force in a particle size-, particle position-, and flow velocity-dependent manner, a detailed mathematical treatment of this phenomena in the washing buffer flow bounded by immiscible, co-flowing oil streams is beyond the scope of this work.[44, 45]

From these relationships, we can infer that magnetic bead capture is most efficient with 1) high magnetic field, 2) large, highly magnetic particles, and 3) relatively slow washing buffer flow velocity toward the waste stream. These demands must be balanced to provide a practically useful device in the context of washing efficiency, throughput, and versatility.

CAR-Wash Performance Characterization

We first evaluated the module with high (≥20 %) magnetite content 10 μm diameter particles. This provided both ease of visualization and high effectiveness for the applied magnetic field in translating beads across the channel. Figure V.2a and Supplementary Movie SMV.1 show a representative example of CAR-Wash operation. As reinjected bead-loaded droplets enter the module (550 Hz, 141 ± 1 pL each), electric field applied across the washing buffer and an adjacent saline electrode channel triggered coalescence. The standard design for the platform also included

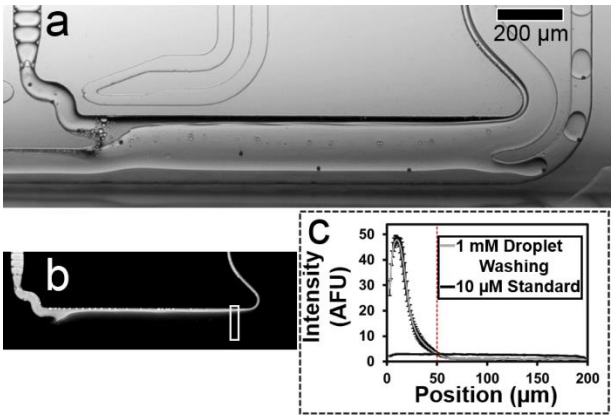

Figure V.2. CAR-Wash Operation. a) Micrograph of the module coalescing and resegmenting droplets at >500 Hz each. Electric field was applied across the PBS washing buffer to the adjacent grounded saline electrode channel. The 10 µm magnetic beads are visible as small, black particles, and flow is generally left to right. b) Loading input droplets with fluorescein enables localization of free waste material from input droplets. c) Plot of the intensity of the channel cross-section prior to the bifurcation between the waste stream and the resegmentation stream (region of interest indicated by the white box in the previous image). The fluorescent signal in the channel when washing 1 mM fluorescein droplets is statistically indistinguishable from a 100-fold diluted standard (10 µM fluorescein) at position = 50 µm (red dashed line, channel bifurcation occurs at position = 120 µm). Error bars on each trace represent 20 fluorescent profiles.

a second electrode feature nearby to enable washing into lower conductivity buffers, but directly charging the washing buffer most efficiently oriented the electric field to coalescence incoming droplets. Electrocoalescence and local turbulence generated and trapped small satellite volumes, particularly at high frequency, but these micron-sized droplet fragments very rarely contained magnetic beads, especially when using 10 µm particles. Satellites usually flowed out through the waste channel with no discernable effect on performance or bead recovery. After droplet coalescence, beads magnetophoretically traversed the channel width until reaching the washing buffer-oil co-flow interface, and they were effectively re-encapsulated in washing buffer droplets (560 Hz, 189 ± 2 pL each). Monitoring more than 4,000 beads at input and output droplet frequencies of ~500 Hz demonstrated greater than 98% successful bead capture into final droplets.

While obtaining specific droplet frequencies required balancing pressure and flow conditions for the washing buffer, oil, droplet, waste, and sample collection lines, the CAR-Wash

could also achieve robust operation across a range of conditions. Adjusting these relative flow rates could independently select droplet frequencies and final droplet size, as shown in Supplementary Movie SMV.2. This flexibility may prove beneficial when using beads originating from non-identical sample droplets: relatively faster output frequencies produced more empty droplets and reduced the incidence of bead co-encapsulation from different input droplets. Moreover, changing flow conditions also adjusted magnetic particle trajectories. Faster flows displaced particles further down the magnetophoresis channel region during magnetic migration but did not significantly change migration speed in the direction of the magnet, as shown in Figure V.S1. From this observation, we hypothesize that effective magnetic particle capture using higher operating frequencies with higher flow rates may be obtainable in the future by lengthening the magnetophoresis channel region correspondingly. In summary, several flow and device parameters influenced operation, but magnetic capture and overall performance were generally quite stable under many different flow conditions, and devices were routinely operated for >1 hour.

Next, the washing efficiency was evaluated. Specifically, we wanted to confirm effective exclusion of free material from the original droplets in the final bead-containing droplets. To test this characteristic, we added 1 mM fluorescein to starting droplets, enabling fluorescent monitoring of the content of the original droplets throughout the module as shown in Figure V.2b. Uniformly flowing a 10 μM fluorescein standard through the device at comparable flow rates provided a reference representing fluorescence intensity at 100-fold dilution. Figure V.2c shows the results of plotting time-averaged profiles of the fluorescent channel cross section when operating the module and when collecting the fluorescent reference. Promisingly, the channel's fluorescence intensity became statistically indistinguishable from the reference even before the position where the channel bifurcated to divert a fraction of the flow into droplet resegmentation

(50 µm position vs. 120 µm for channel bifurcation). Interestingly, positions closer to the channel bifurcation showed significantly lower fluorescence intensity compared to the reference, indicating effective dilution greater than 100-fold in final droplets. Although flow rate and geometry adjustments altered the exact channel position corresponding to the 100-fold dilution threshold, this result demonstrated that the CAR-Wash platform provided highly efficient removal of free species.

Compared to related continuously flowing magnetic droplet approaches, the CAR-Wash platform demonstrates a number of advantages. Our technique cannot discretely collect dynamically selectable portions of sample droplets, a feature shown by some tunable droplet splitting approaches,[31, 33-35] but it exceeds the other capabilities of previous droplet splitting platforms in the context of washing for sample purification. Specifically, exchanging >99% of droplet volume (as confirmed by fluorescent characterization) surpassed even the highest reported proportion of droplet splitting (95%)[35] and more closely resembled the continuously flowing washes of co-laminar approaches.[22, 23] Therefore, highly efficient removal of unbound species was achieved without complex sequential splitting and dilution operations.[36] While maintaining bead capture efficiency (>98%) comparable to these technologies, throughput (~500 Hz) was significantly greater than most splitting examples (0.5-30 Hz)[17, 33-37] and surpassed our previous work in this area (200 Hz).[31] Compared to Lee *et al.*'s synchronized washing design, our system shows similar advantages in volume exchange (~96% reported) and throughput (3 Hz reported).[14] Importantly for applications with heterogeneous droplets (perhaps containing single cells, etc.), Lee *et al.*'s system discretely paired sample and washing buffer droplets to ensure that beads from unique sample droplets did not mix in final droplets, and we can achieve this result by offsetting input and output droplet frequencies.

CAR-Wash Bead Input Versatility

We next re-engineered the device to accommodate alternative magnetic particles. Depending on properties such as surface coating and binding capacity, bead requirements can vary by assay, and previous magnetic droplet assays have employed a range of particle identities.[14, 17, 31, 33-37] Therefore, we anticipated highest utility for the CAR-Wash if applicable within the limitations of other commercially available beads, particularly those with low magnetic content per bead. Figure V.3a provides the schematic of the modified CAR-Wash module for handling smaller 2.8 μm Dynabeads with 14% reported magnetite content. The chief modification was the extension of the magnetophoresis region by more than five-fold compared to the original device to compensate for the lower proportion magnetite observed in these particles. Increased residence time for Dynabeads through the extended channel (at relatively fixed flow rates) was necessary to fully capture beads which were less rapidly deflected by the magnet as shown in Figure V.3b. Next, Figure V.3c shows deflected particles re-encapsulated in new droplets at the end of the magnetophoresis region, and the added flow focusing oil channels stabilized this terminal operation. This added feature was necessary to compensate for less stable flow across the longer co-flow capture region, largely originating from variance in reinjected droplets but exaggerated by the extended co-flow distance. Without the added flow focusing structure, resegmentation of droplets sometimes generated irregular droplet sizes or did not occur at all (co-flow only). Monitoring $N > 1000$ Dynabeads at droplet input and output frequencies $\geq$200 Hz yielded higher than 99% bead recovery. Finally, repeating the fluorescent droplet characterization method described earlier for this device indicated reaching the 100-fold dilution threshold at the 60 μm channel position (with channel bifurcation still occurring at 120 μm, Figure V.3d-e). Therefore, this CAR-Wash variant retained the advantages in throughput and waste removal efficiency of the

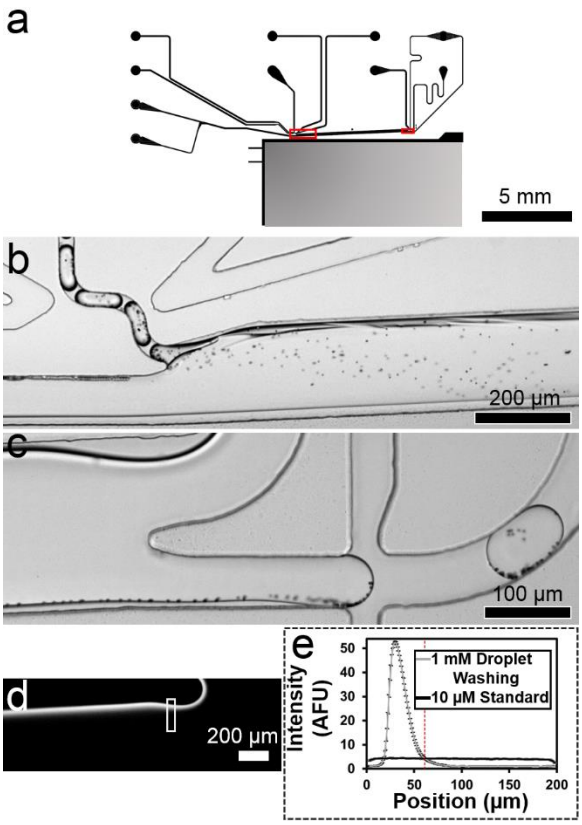

Figure V.3. CAR-Wash Application to Alternative Particles. a) Extending the magnetic capture region increases the utility of the module for particles with lower magnetic loading. Red boxes indicate regions of interest shown in following panels. b) Micrograph of the module coalescing input droplets at ~250 Hz. Electric field was applied across the PBS washing buffer to the adjacent grounded saline electrode channel. 2.8 µm magnetic Dynabeads are evident as small, black particles in high abundance, and flow is generally left to right. c) High magnification micrograph of the module resegmenting droplets downstream at ~200 Hz with efficient Dynabead recovery, stabilized by an additional flow focusing structure. d) Loading input droplets with fluorescein enables localization of free waste material from input droplets. e) Plot of the intensity of the channel cross-section prior to the bifurcation between the waste stream and the resegmentation stream (region of interest indicated by the white box in the previous image). The fluorescent signal in the channel when washing 1 mM fluorescein droplets is statistically indistinguishable from a 100-fold diluted standard (10 µM fluorescein) at position = 60 µm (red dashed line, channel bifurcation occurs at position = 120 µm). Error bars on each trace represent 20 fluorescent profiles.

original design in comparison to previous magnetic washing examples while still achieving effective particle capture.[14, 31, 33-36] In summary, this modification slightly increased footprint and operating complexity, but it established comparable performance for smaller, lower magnetic

content particles, widening the device's potential application space and extending general usability.

CAR-Wash Enzyme Inhibition Reversal

Beyond profiling the physical performance of the CAR-Wash approach, we also wanted to demonstrate biochemical utility for the device. As an initial application, we chose to monitor washing-mediated inhibition reversal for β-galactosidase activity in cleaving resorufin-β-D-galactopyranoside to free fluorescent resorufin product. Tethering biotinylated enzyme to the surface of 10 μm streptavidin beads added the magnetic handle, and isopropyl β-D-1-thiogalactopyranoside (IPTG—a well-characterized non-hydrolyzable substrate analog for β-galactosidase) served as a competitive inhibitor in initial droplets. Therefore, the CAR-Wash module provided a means to wash bead-bound β-galactosidase for IPTG removal. Enzyme activity was monitored through production of fluorescent resorufin, and fully recovered enzyme function relative to uninhibited and inhibited controls indicated successful washing.

Figure V.4a outlines the schematic for device operation. Droplets loaded with β-galactosidase-conjugated beads and IPTG were first washed through the original 10 μm magnetic bead CAR-Wash platform with input and output frequencies near 200 Hz and final droplet volumes between 260 and 300 pL. Output droplets flowed through a short loop of connecting tubing to provide ~20 s of incubation while delivering them to a secondary device for dynamic imaging within a planar microchannel. To provide an uninhibited control, Figure V.4b shows bright fluorescence in collected droplets during operation without inhibitor in the initial droplets or final washing buffer. Serving as an inhibited control, weakly fluorescent droplets in Figure V.4c were continuously exposed to IPTG in both initial droplets and in the final washing buffer. Next, Figure

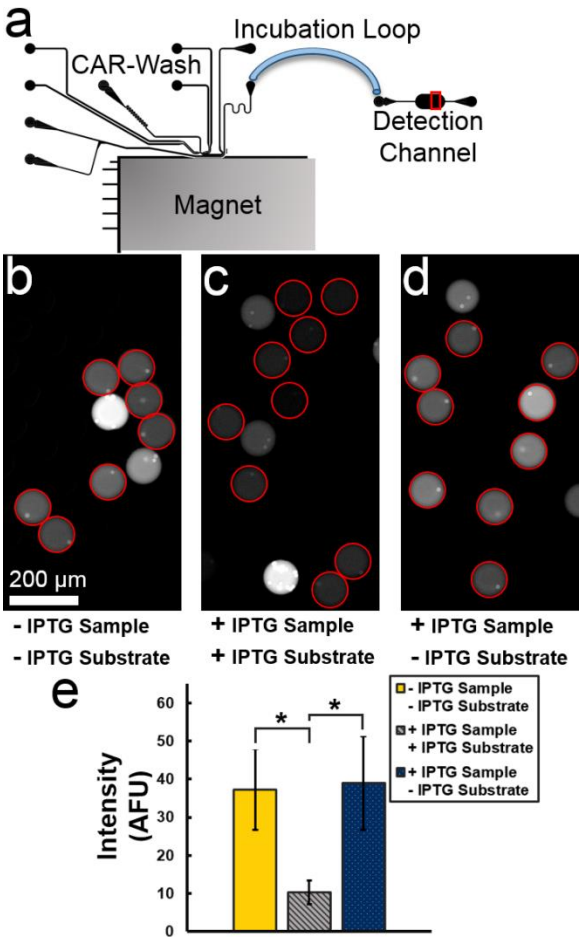

Figure V.4. Washing Reverses IPTG Inhibition of β-Galactosidase Activity. a) Droplets containing bead-bound β-galactosidase incubated with 1 mM IPTG were washed into PBS and resorufin-β-D-galactopyranoside substrate using the standard CAR-Wash module. Droplets were imaged on the planar Detection Channel device after ~20 s of dynamic incubation accomplished via a 4 cm Incubation Loop of connecting tubing. The red box indicates the region of interest for subsequent images. b) Inhibitor-free control droplets (IPTG neither in original sample droplets nor in final washing buffer with substrate) generated fluorescent resorufin product. Droplets with higher bead loadings typically gave greater signal. c) Inhibited control droplets (IPTG both in original sample droplets and in final washing buffer with substrate) generated little fluorescent product. d) IPTG-containing sample droplets were washed into IPTG-free washing buffer with substrate. Comparable fluorescent product formation relative to the inhibitor-free control indicates inhibitor removal by washing. e) Measuring the fluorescence of only single bead droplets (outlined in red) confirmed that washing fully recovered activity in the originally inhibited system (Panel d) compared to uninhibited and inhibited controls (Panels b and c, respectively). The inhibited control (Panel c) differed significantly in intensity from the other conditions.

V.4d shows bright fluorescence in final droplets when washing away IPTG from the initial droplets. To standardize enzyme loading per droplet, quantitative measurements of droplet

intensities in Figure V.4e only included data for single bead-containing droplets (circled in red in the images) since droplets with multiple beads appear to have more enzyme than can be inhibited by the provided concentration of inhibitor. Crucially, the washed system with initial IPTG did not differ significantly in fluorescence intensity from the uninhibited control, indicating full enzyme activity after washing. On the other hand, the inhibited control showed significantly lower fluorescence than the two other populations, corresponding to competitive inhibition by IPTG. Because washing succeeded in fully recovering β-galactosidase activity after inhibition, this result verified that the CAR-Wash platform could efficiently remove small molecules in a biologically relevant context.

Selective Protein Enrichment via CAR-Wash

Finally, we wanted to highlight the capabilities of the CAR-Wash platform by demonstrating affinity-based protein enrichment and separation. We chose a HeLa cell line expressing a green fluorescent protein-histone H2B (GFP-H2B) fusion in the nucleus to provide a target protein to fluorescently monitor and because selective enrichment of chromatin-associated targets provides the basis of many important epigenetic bioassays.[24] After manual cell lysis and enzymatic chromatin digestion to increase the accessibility of GFP-H2B, we added mCherry to the cell lysate as an off-target fluorescent protein to be removed during washing in addition to other, non-fluorescent lysate components. Anti-GFP antibody-functionalized magnetic particles selectively captured GFP-H2B prior to magnetic washing. Detection of bead-associated fluorescence in green and red channels indicated the abundance of GFP-H2B and mCherry, respectively, at each stage of the enrichment assay.

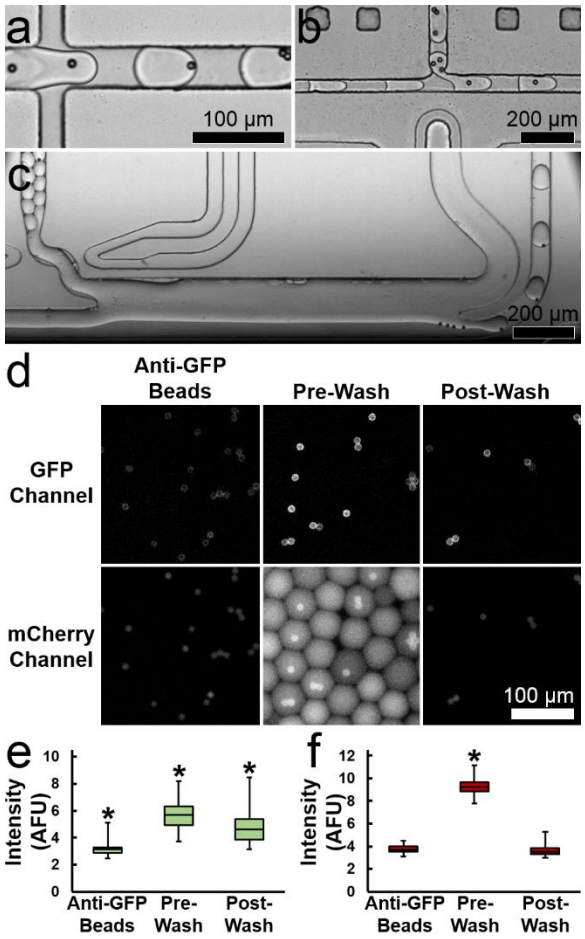

Figure V.5. Selective Enrichment of GFP-H2B from Cell Lysate. a) Anti-GFP antibody-functionalized beads were pre-emulsified into droplets at ~4 kHz to limit sedimentation. b) The bead emulsion was injected into HeLa cell lysate droplets with added mCherry. c) After 1 hour of off-chip incubation, droplets were processed via the CAR-Wash module. For all devices, flow was generally left to right. d) Droplet populations were fluorescently imaged in green and red channels under static conditions including the functionalized bead emulsion (Anti-GFP Beads), the sample droplets with beads and lysate after incubation but prior to washing (Pre-Wash), and the final sample droplets with beads after washing (Post-Wash). Beads are visible in each panel as bright spots. e) For the green fluorescent channel, the Pre-Wash population was significantly brighter than the original Anti-GFP Beads, indicating the presence of GFP-H2B. Similarly, the Post-Wash population was significantly brighter than the original Anti-GFP Beads, demonstrating enrichment and retention of GFP-H2B after washing. The Post-Wash population was slightly, but significantly less bright than the Pre-Wash population, suggesting incomplete GFP-H2B recovery. f) For the red fluorescent channel, the Pre-Wash population was significantly brighter than the original Anti-GFP Beads due to the presence of mCherry added to the cell lysate. Importantly, the Post-Wash population was not significantly brighter than the original Anti-GFP Beads, indicating mCherry removal by washing.

Figure V.5 includes the workflow for the enrichment assay. First, magnetic beads with surface-tethered anti-GFP antibody were rapidly encapsulated in droplets using a simple flow

focusing device at ~4 kHz (Figure V.5a). This approach reduced a common problem in deploying solid phase particles onto microfluidic assays: gravity-driven settling of dense beads results in a rapid decrease in their effective concentration, preventing efficient loading.[46] By emulsifying the entire bead population in the span of a few minutes, the beads remained in suspension for subsequent processing. Next, the lysate sample was encapsulated in droplets, and loading the bead emulsion on-chip at high packing fraction enabled electrode-mediated direct injection of beads into lysate droplets (Figure V.5b). Bead injection was subject to Poisson statistics and not completely uniform, but integrating sophisticated bead loading approaches in future applications could conceivably ensure uniform bead delivery.[47] Following off-device incubation to allow for target binding, bead-laden droplets were processed via the original 10 μm bead-handling CAR-Wash (Figure V.5c) prior to final imaging. This washing portion of the assay demonstrated another key advantage of the platform. Because the only input requirement for CAR-Wash was that droplets fuse with the washing buffer (which constituted the majority of flow through the module), performance was relatively insensitive to input droplet size and spacing uniformity. In particular, coalescence did not require precise coordination or synchronization between droplet and buffer flows.[14] Therefore, this technology interfaced well with detergent-enabled bioassays, such as the inclusion here of detergent-lysed HeLa in droplets. For other washing approaches, detergent-associated instability and partial channel wetting may cause size or spacing heterogeneities that disrupt the uniformity of droplet synchronization or compromise control of droplet splitting.

Droplets from each portion of the assay were statically imaged in a planar microchannel (Figure V.5d). In both green and red channels, low native fluorescence from antibody-functionalized beads resulted in background signal, but inclusion of GFP-H2B and mCherry when adding cell lysate greatly increased fluorescence intensities before washing, especially the

fluorescent signal localized to the surface of the beads via specific and non-specific interactions. After washing, antibody-antigen interactions retained GFP-H2B on bead surfaces while mCherry was washed away, returning red channel fluorescence to background levels. In the green fluorescence channel, significantly higher intensities for pre-wash and post-wash beads compared to the original beads indicated successful GFP-H2B enrichment and retention during washing (Figure V.5e). Post-wash beads did have slightly but statistically significantly lower fluorescence than pre-wash beads, suggesting some fraction of sample loss from low antibody-antigen affinity, inconsistent GFP-H2B binding capacity among beads, or the presence of other confounds. Other washing-based droplet assays have reported similar instances of sample loss,[14, 36] so it is clear that future CAR-Wash applications beyond this proof of concept implementation will also require careful optimization to maximize sample capture and retention on magnetic particles. Crucially, red fluorescence from mCherry peaked upon lysate loading before washing, but original beads and beads after washing did not differ significantly from each other in fluorescence intensity (Figure V.5f). This result verified that washing effectively removed non-specifically interacting mCherry, returning signal to background levels. Therefore, the CAR-Wash module succeeded in selectively enriching and separating GFP-H2B from mCherry and HeLa lysate components.

CONCLUSIONS

Combining simple, robust operation with high throughput and efficiency, the CAR-Wash platform changes the paradigm for in-droplet solid phase-mediated sample processing. We have characterized system performance in terms of bead loss and final droplet dilution for selected magnetic particles and flow conditions, showing excellent bead recovery and buffer exchange. In optimizing module design, we demonstrated that lengthening the magnetophoresis channel

provided a practical strategy for adapting the system to lower magnetite particles. We have also applied the approach in recovering enzyme activity by washing away a small molecule inhibitor and in selectively enriching a target fluorescent protein from cell lysate. The CAR-Wash platform represents an exciting advance in realizing the promise of droplet microfluidics by narrowing the technological gap between pre-existing droplet methodologies and important (bio)chemical techniques leveraging solid supports. Beyond these initial applications, we anticipate a breadth of downstream technologies capable of high throughput, miniaturized analogs for immunoassays, solid phase extraction, and many others.

ACKNOWLEDGEMENTS

We gratefully acknowledge financial support from the National Institutes of Health (NIH CA191186). S.R.D. was supported by a National Science Foundation Graduate Research Fellowship. The authors would like to thank Prof. Tamas Ordog and Dr. Jeong-Heon Lee from the Mayo Clinic Epigenomics Development Laboratory for providing the GFP-H2B expressing HeLa cell line. We also thank Prof. Robert Kennedy (University of Michigan) for access to microfabrication facilities and Nicolas Mesyngier (University of Michigan) for helpful discussions.

REFERENCES

1. T. Thorsen, R. W. Roberts, F. H. Arnold and S. R. Quake, *Physical Review Letters*, 2001, **86**, 4163-4166.
2. L. Shang, Y. Cheng and Y. Zhao, *Chemical Reviews*, 2017, **117**, 7964-8040.
3. S.-Y. Teh, R. Lin, L.-H. Hung and A. P. Lee, *Lab on a Chip*, 2008, **8**, 198-220.
4. E. Al-Hetlani and M. O. Amin, *Microchimica Acta*, 2019, **186**, 55.

5. H. Song, J. D. Tice and R. F. Ismagilov, *Angewandte Chemie International Edition*, 2003, **42**, 768-772.

6. J.-C. Baret, *Lab on a Chip*, 2012, **12**, 422-433.

7. N. Habib, I. Avraham-Davidi, A. Basu, T. Burks, K. Shekhar, M. Hofree, S. R. Choudhury, F. Aguet, E. Gelfand, K. Ardlie, D. A. Weitz, O. Rozenblatt-Rosen, F. Zhang and A. Regev, *Nature Methods*, 2017, **14**, 955-958.

8. Y. Xu, J.-H. Lee, Z. Li, L. Wang, T. Ordog and R. C. Bailey, *Lab on a Chip*, 2018, **18**, 2583-2592.

9. R. Obexer, A. Godina, X. Garrabou, P. R. E. Mittl, D. Baker, A. D. Griffiths and D. Hilvert, *Nature Chemistry*, 2017, **9**, 50-56.

10. S. M. Prakadan, A. K. Shalek and D. A. Weitz, *Nature Reviews Genetics*, 2017, **18**, 345-361.

11. Z. Zhu and C. J. Yang, *Accounts of Chemical Research*, 2017, **50**, 22-31.

12. T. Trantidou, M. Friddin, Y. Elani, N. J. Brooks, R. V. Law, J. M. Seddon and O. Ces, *ACS Nano*, 2017, **11**, 6549-6565.

13. M. Serra, D. Ferraro, I. Pereiro, J. L. Viovy and S. Descroix, *Lab on a Chip*, 2017, **17**, 3979-3999.

14. H. Lee, L. Xu and K. W. Oh, *Biomicrofluidics*, 2014, **8**, 044113.

15. A. Munaz, M. J. A. Shiddiky and N.-T. Nguyen, *Biomicrofluidics*, 2018, **12**, 031501.

16. M. A. M. Gijs, *Microfluidics and Nanofluidics*, 2004, **1**, 22-40.

17. R. Gao, Z. Cheng, A. J. deMello and J. Choo, *Lab on a Chip*, 2016, **16**, 1022-1029.

18. M. A. Booth, S. A. N. Gowers, C. L. Leong, M. L. Rogers, I. C. Samper, A. P. Wickham and M. G. Boutelle, *Analytical Chemistry*, 2018, **90**, 2-18.

19. C. D. M. Campos, S. S. T. Gamage, J. M. Jackson, M. A. Witek, D. S. Park, M. C. Murphy, A. K. Godwin and S. A. Soper, *Lab on a Chip*, 2018, **18**, 3459-3470.

20. V. Sahore, M. Sonker, A. V. Nielsen, R. Knob, S. Kumar and A. T. Woolley, *Analytical and Bioanalytical Chemistry*, 2018, **410**, 933-941.

21. C. A. G. N. Montalbetti and V. Falque, *Tetrahedron*, 2005, **61**, 10827-10852.

22. A. Q. Alorabi, M. D. Tarn, J. Gómez-Pastora, E. Bringas, I. Ortiz, V. N. Paunov and N. Pamme, *Lab on a Chip*, 2017, **17**, 3785-3795.

23. M. D. Tarn, M. J. Lopez-Martinez and N. Pamme, *Analytical and Bioanalytical Chemistry*, 2014, **406**, 139-161.

24. B. Teste, J. Champ, A. Londono-Vallejo, S. Descroix, L. Malaquin, J.-L. Viovy, I. Draskovic and G. Mottet, *Lab on a Chip*, 2017, **17**, 530-537.

25. A. Ali-Cherif, S. Begolo, S. Descroix, J.-L. Viovy and L. Malaquin, *Angewandte Chemie International Edition*, 2012, **51**, 10765-10769.

26. A. Ray, V. B. Varma, P. J. Jayaneel, N. M. Sudharsan, Z. P. Wang and R. V. Ramanujan, *Sensors and Actuators B: Chemical*, 2017, **242**, 760-768.

27. K. Zhang, Q. Liang, X. Ai, P. Hu, Y. Wang and G. Luo, *Lab on a Chip*, 2011, **11**, 1271-1275.

28. V. Sahore, S. R. Doonan and R. C. Bailey, *Analytical Methods*, 2018, **10**, 4264-4274.

29. P. Garstecki, M. J. Fuerstman, H. A. Stone and G. M. Whitesides, *Lab on a Chip*, 2006, **6**, 437-446.

30. A. R. Abate, T. Hung, P. Mary, J. J. Agresti and D. A. Weitz, *Proceedings of the National Academy of Sciences of the United States of America*, 2010, **107**, 19163-19166.

31. S. R. Doonan and R. C. Bailey, *Analytical Chemistry*, 2017, **89**, 4091-4099.

32. A. Shams Khorrami and P. Rezai, *Soft Matter*, 2018, **14**, 9870-9876.

33. E. Brouzes, T. Kruse, R. Kimmerling and H. H. Strey, *Lab on a Chip*, 2015, **15**, 908-919.

34. B. Verbruggen, T. Tóth, M. Cornaglia, R. Puers, M. A. M. Gijs and J. Lammertyn, *Microfluidics and Nanofluidics*, 2015, **18**, 91-102.

35. B. Verbruggen, K. Leirs, R. Puers and J. Lammertyn, *Microfluidics and Nanofluidics*, 2015, **18**, 293-303.

36. X. Pan, S. Zeng, Q. Zhang, B. Lin and J. Qin, *ELECTROPHORESIS*, 2011, **32**, 3399-3405.

37. D. Lombardi and P. S. Dittrich, *Analytical and Bioanalytical Chemistry*, 2011, **399**, 347-352.

38. S. Wang, K.-J. Sung, X. N. Lin and M. A. Burns, *PLOS ONE*, 2017, **12**, e0173479.

39. D. J. Guckenberger, H. M. Pezzi, M. C. Regier, S. M. Berry, K. Fawcett, K. Barrett and D. J. Beebe, *Analytical Chemistry*, 2016, **88**, 9902-9907.

40. J. Park, G. Destgeer, H. Kim, Y. Cho and H. J. Sung, *Lab on a Chip*, 2018, **18**, 2936-2945.

41. B. Seale, C. Lam, D. G. Rackus, M. D. Chamberlain, C. Liu and A. R. Wheeler, *Analytical Chemistry*, 2016, **88**, 10223-10230.

42. Y. Xia and G. M. Whitesides, *Angewandte Chemie International Edition*, 1998, **37**, 550-575.

43. A. Sciambi and A. R. Abate, *Lab on a Chip*, 2014, **14**, 2605-2609.

44. D. Lee, S. M. Nam, J.-a. Kim, D. Di Carlo and W. Lee, *Analytical Chemistry*, 2018, **90**, 2902-2911.

45. B. P. Ho and L. G. Leal, *Journal of Fluid Mechanics*, 1974, **65**, 365-400.

46. A. K. Price, A. B. MacConnell and B. M. Paegel, *Analytical chemistry*, 2014, **86**, 5039-5044.

47. M. T. Chung, D. Núñez, D. Cai and K. Kurabayashi, *Lab on a Chip*, 2017, **17**, 3664-3671.

SUPPLEMENTARY INFORMATION

The supplementary information in its original format (including videos) may be accessed online at doi: 10.1039/C9LC00125E.

Supplementary Movie SMV.1. CAR-Wash Operation. Input droplets (141 ± 1 pL each) electrocoalesce at 550 Hz with >98% 10 µm magnetic bead capture during droplet reformation at 560 Hz (189 ± 2 pL each).

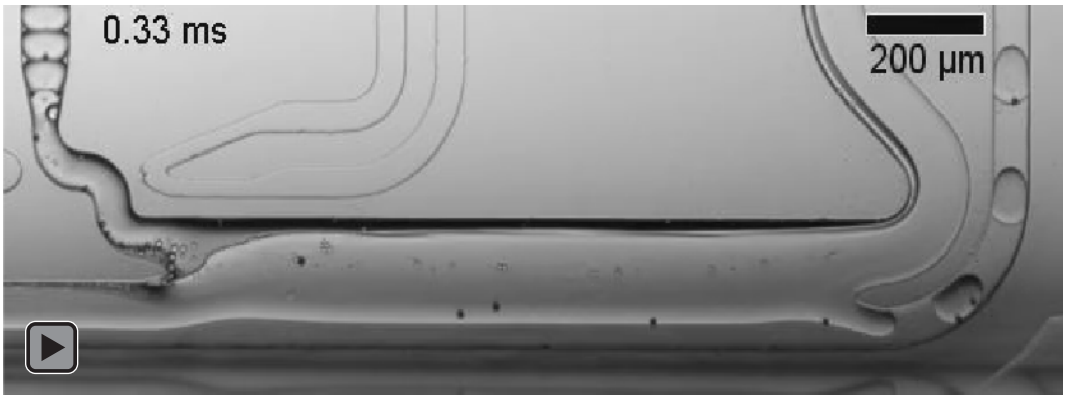

Supplementary Movie SMV.2. CAR-Wash Frequency Modulation. Reinjection of loosely packed droplets at 100 Hz with output droplet production at 500 Hz prevents coencapsulation of beads from different input droplets during resegmentation. This frequency mismatch also increases the proportion of empty droplets formed.

SUPPLEMENTARY FIGURE

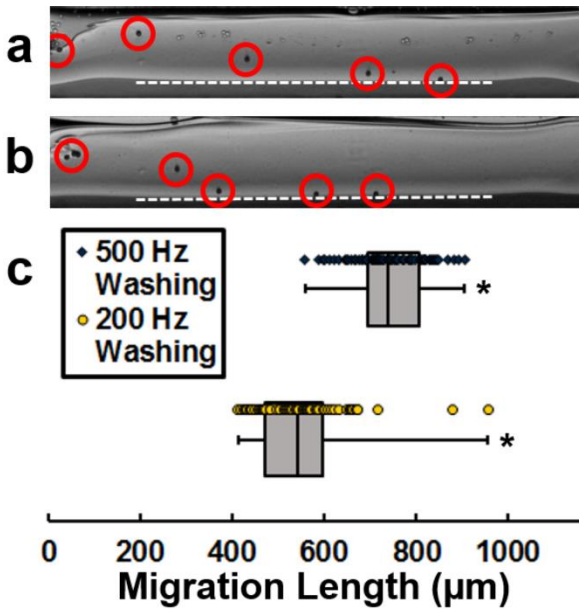

Figure V.S1. Magnetophoresis Flow Rate Dependence. a) Micrograph of the CAR-Wash magnetophoresis region during droplet processing at ~500 Hz input and output droplet frequencies. Approximate flow rates for each species are 75 µL/min for the washing buffer, 8.5 µL/min for the oil co-flow, and 4.5 µL/min for input droplets. Magnetic particles are circled in red, and the washing buffer-oil co-flow interface is highlighted with a white line. B) Micrograph of the same CAR-Wash magnetophoresis region during droplet processing at ~200 Hz input and output droplet frequencies. Approximate flow rates for each species are 60 µL/min for the washing buffer, 4 µL/min for the oil co-flow, and 2.5 µL/min for input droplets. c) Plot of particle migration lengths under each frequency condition. We define "migration length" as the distance each particle travels down the channel length before magnetically-driven orthogonal forces pull it into first contact with the washing buffer-oil co-flow interface. Decreasing frequencies and flow rates significantly decreases resulting migration lengths. Magnetic migration velocity in the direction of the flow interface (48 ± 2 mm/s at 500 Hz and 45 ± 4 mm/s at 200 Hz) did not differ significantly between frequency conditions. Significance was assessed at 95% confidence for N = 75 particles under each condition (evaluated in N = 5 bins based on distance from the co-flow interface when evaluating magnetic migration velocity). Micrographs are aligned and in scale with the plot's migration length axis.

Chapter VI

Chromatin Immunoprecipitation in Microfluidic Droplets: Toward Miniaturized and Automated Epigenetic Analysis

This work was performed with Gloria Diaz, Yi Xu, Vishal Sahore, Jeong-Heon Lee, Tamas Ordog, and Ryan C. Bailey. G. Diaz, Y. Xu, and V. Sahore (University of Michigan) participated in experimental design, microfluidic device design and fabrication, and data collection and analysis. J.-H. Lee and T. Ordog (The Mayo Clinic) provided indicated samples and reagents, participated in experimental design (especially in establishing biochemical protocols), and assisted in data analysis.

INTRODUCTION

Complicating the fundamental relationships of the Central Dogma of molecular biology, complex regulatory networks govern the transcription of DNA into RNA for translation into protein.[1] Epigenetic determinants, like non-coding RNAs, chemical modifications to DNA bases, and histone protein post-translational modifications (PTMs), provide a heritable and dynamically modifiable basis for regulating gene expression without inducing corresponding changes in the genome.[2-4] Of particular interest, epigenetic regulation and dysregulation by histone PTMs play major roles in development and health.[2, 5, 6] Correspondingly, they have provided a fertile area for the development of epigenetic therapies which commonly target histone-modifying enzymes (so-called epigenetic "writers" and "erasers") to reprogram dysregulated, often cancer-associated

pathways.[5, 7] Building on the promise of these initial successes, further maturity and depth of our understanding of epigenetic histone PTMs will almost certainly empower additional developments in treatment and diagnosis.

Epigenetic analysis of histone proteins seeks to profile the association of protein isoforms with DNA sequences. Histones organize DNA into nucleosome structures (typically with ~147 DNA base pairs per nucleosome), and chemical modifications like methylation and acetylation remodel the association between the histone and DNA as well as modulate the recruitment of and interactions with transcriptional machinery.[2, 6] To probe these interactions, Chromatin Immunoprecipitation (ChIP) uses an affinity separation to isolate and analyze DNA associated with a targeted histone PTM.[8-14] Supported by a growing knowledge base for the diversity of histone PTMs and their context-dependent transcriptional effects, ChIP with DNA sequencing (ChIP-seq) can *de novo* identify the transcriptional state of sequenced genes. For well-characterized relationships, ChIP with Quantitative Polymerase Chain Reaction (qPCR) provides a quantitative snapshot of the relative association of target genes with the modification of interest.[6, 15] Strategic use of these tools enables discovery of new epigenetic pathways, elucidates the regulatory state of target genes, and may be of interest in developing a quantitative diagnostic approach for epigenetic wellness.[7, 9]

As a critical barrier to widespread implementation, ChIP suffers from technical limitations. Assay protocols follow a laborious, user-dependent manual process to facilitate sample handling from input cells to final, enriched DNA. Due to poor robustness and sample loss at each phase, ChIP protocols rarely use fewer than 10^6 cells per assay, discouraging use on rare cell populations or with less-invasive patient biopsies.[9-11] Beyond technician variability, inconsistent reagent performance and antibody affinity during capture of targeted PTM-displaying nucleosomes further

hinder ChIP reproducibility.[9, 10] Extensive ChIP protocols have been developed with detailed guides to troubleshooting inconsistent results and for decreasing time and sample requirements, but further improvements are needed to realize the assay's full potential.[8-14]

Leveraging the capabilities of microfluidics, miniaturized devices have been developed to enable small sample, automated epigenetic analysis. Among the most successful examples, the Quake Group was first to establish a miniaturized, parallel platform for processing samples as small as few thousand cells for ChIP.[16, 17] While they showed good enrichment and effective DNA processing for sequencing analysis, the device featured a fixed-volume chamber which lost sample with each reagent addition and required precisely optimized assay conditions as a function of sample size. Next, the Lu Group developed a series of modules for effective ChIP down to a few 10s of cells and even integrated on-device sonication for chromatin shearing as well as expansion to non-histone immunoprecipitation targets.[18-21] Similarly, this platform was also limited to fixed sample size processing under precise assay conditions in a discrete microfluidic chamber. Most recently, the Weitz Group expanded the capabilities of droplet-enabled DNA barcoding to single cell ChIP.[22] Despite impressive single cell ChIP-seq capabilities, most of the ChIP assay after barcoding was performed manually, and processing was limited by both barcoding efficiency and number of unique barcodes. Nonetheless, these approaches have provided impressive examples of miniaturized ChIP and laid the groundwork for automated epigenetic analysis of rare cell populations.

In answering some of the existing limitations in bulk (large sample size, user dependence, etc.) and microfluidic (fixed sample size with intensive re-optimization) ChIP, droplet microfluidics presents exciting possibilities.[23, 24] By segmenting samples within a fluorinated oil and stabilizing volumes with fluorosurfactants, droplet systems enable high throughput serial

processing in which each portion of a bulk sample is processed as its own fL- to nL-scale reactor.[25-27] Thus, reaction conditions (reagent concentrations) do not require scaling with sample size. Instead, larger or smaller samples merely change the total number of droplets handled through uniform assay conditions. Sophisticated droplet technologies emulate manual sample handling steps at up to kHz rates for miniaturized volumes, and in-droplet physics promote rapid mass transfer for efficient chemical reactions. These approaches enable direct injection of reagents, in-droplet affinity purifications, and more, providing a basis for bioassay adaptation. [28-33]

The Bailey Lab's recent innovations in droplet-enabled chromatin preparation and droplet-based magnetic affinity separations established proof-of-concept for important ChIP unit operations.[32, 34] In this work, we extended those basic capabilities in more sophisticated devices and ultimately developed a microfluidic ChIP assay for serial processing of droplet-encapsulated cell samples. After biochemical optimization of ChIP on the bulk scale, we applied these conditions for droplet-enabled ChIP targeting H3K4me3 and H3K27me3 as representative activating and repressive histone PTMs. Critically, validation versus manual ChIP demonstrated effective, selective enrichment using the droplet method, if at reduced DNA yield, and it verified the potential of this technology for automated, non-deterministic epigenetic analysis.

EXPERIMENTAL SECTION

Device Preparation

Microfluidic devices were fabricated by adapting conventional soft lithography techniques.[35] In brief, devices were designed in AutoCAD (Autodesk, Inc.) and sourced in plastic with an ink emulsion (CAD/Art Services, Inc.). For master mold fabrication, all devices used SU8

2025 or SU8 2050 Negative Epoxy Photoresists (MicroChem Corp.) spun-coat onto 3 in diameter silicon wafers (University Wafer). All devices first used SU8 2025 at 40 μm feature height which was exposed via MJB3 Mask Aligner (SUSS MicroTec) with a high-pass optical filter (PL-360-LP, Omega Optical) after soft baking. Following exposure, devices were post-baked, developed in propylene glycol monomethyl ether acetate (Sigma Aldrich), and hard-baked for mechanical durability. For dual-layer devices (such as the cell encapsulation, cell lysis, chromatin digestion, and immunoprecipitation device), a layer of SU8 2050 was spun-coat over existing features to 160 μm feature height and processed with a second, complementary photomask following a similar procedure as for the first feature layer. After final development and hard-baking, all wafers were treated under vacuum with tridecafluoro-1,1,2,2-tetrahydrooctyl trichlorosilane (Gelest, Inc.) as a release aid.

Devices were fabricated from master molds using poly(dimethyl siloxane) PDMS in a 5:1 or 10:1 base: curing agent ratio (RTV615, Momentive, Inc.). After curing for at least 1 h in a 70 °C oven, PDMS stamps were removed from the master and cut to size. Devices were ported using needles (18 and 30 Ga) lubricated with Fluoroinert FC-40 (Sigma Aldrich). Finally, devices were bonded to glass slides (1 mm thickness, 75 mm x 50 mm, Thermo Fisher Scientific) or glass coverslips (No. 11/2, 22 mm x 40 mm, Sigma Aldrich) using oxygen plasma (PDC-32G, Harrick Plasma). After bonding, devices were baked at 70 °C overnight.

For the cell encapsulation, cell lysis, chromatin digestion, and immunoprecipitation device, devices were surface treated with Aquapel (Pittsburgh Glass Works) prior to use. Teflon tubing (#24 PTFE, Cole Parmer) was treated with 1% (w/v) Pluronic F127 (Sigma Aldrich) in PBS prior to use.

For integrated magnetic field devices, fabrication and preparation were modified as described previously.[29, 32] Briefly, designs included magnetic alignment features so that a magnet (Grade N52, 0.5 in x 0.25 in x 0.125 in, magnetized through thickness, K&J Magnetics, Inc.) was precisely positioned on the master prior to PDMS addition and curing. After curing, the magnet was removed, leaving a magnet port for later aligning the magnets in the assembled device (eight magnets total, arranged in a block of approximate dimensions: 0.5 in x 0.5 in x 0.5 in, direction of magnetization oriented toward the microchannel). Prior to use, magnetic devices (and bead-emulsifying devices) were surface treated with 1% (v/v) tridecafluoro-1,1,2,2-tetrahydrooctyl trichlorosilane in FC-40. For these devices, Teflon tubing (#24 PTFE, Cole Parmer) was used without modification.

Samples and Reagents

The continuous phase for droplet microfluidic operations was Novec 7500 (The 3M Company) with 1 or 2% (w/w) 008-Fluorosurfactant (RAN Biotechnologies, Inc.). All samples (except for cell and bead suspensions described below) were filtered via 0.2 µm nylon syringe filter (VWR International) prior to use on-device.

Cell samples were HeLa, typically suspended at a density of 7×10^6 cells mL^{-1} in PBS with 21.9% (v/v) Optiprep Density Gradient Medium (Sigma Aldrich) to decrease gravity-driven sedimentation. Samples were handled off-device or during bulk processing using DNA LoBind tubes (Thermo Fisher Scientific).

Cell lysis and chromatin digestion were mediated by Lysis Buffer, Digestion Buffer, and Quenching Buffer as described previously.[34] Lysis Buffer contained 10 mM HEPES, 1.5 mM $MgCl_2$, 10 mM KCl, and 0.5% (w/v) IGEPAL-CA630 (Sigma Aldrich) at pH 7.9. Digestion Buffer

contained 20 mM Tris-HCl, 15 mM NaCl, 60 mM KCl, 5 mM $CaCl_2$, 0.15 mM spermine, and 0.5 mM spermidine at pH 7.5. Quenching Buffer contained 100 mM Tris-HCl, 20 mM EDTA, 200 mM NaCl, 2% Triton-X 100, and 0.2% sodium dodecyl sulfate (SDS) at pH 8. To simplify processing, a single combined buffer was prepared for cell processing comprised of Lysis Buffer, Digestion Buffer, and Micrococcal Nuclease (MNase, 2000 GU μL^{-1}, New England Biolabs) at a ratio of 10:4:1, respectively.

Magnetic particles were Protein g Dynabeads (Thermo Fisher Scientific). Bead preparation began with manual magnetic washing and resuspension in 50 mM Tris-HCl, 10 mM EDTA, 100 mM NaCl, 1% Triton-X 100, and 0.1% SDS at pH 8. Next, ChIP-grade anti-H3K4me3 (produced by and generously provided by the Mayo Clinic) or anti-H3K27me3 (Cell Signaling Technologies, generously provided by the Mayo Clinic) antibodies were added to the particles so that the final titer was scaled as 1-8 µg with 30 µL beads for 4 x 10^6 cells (specific values indicated with data). Quantities were proportionally scaled for smaller samples. After 2 h of incubation with rotation at 4 °C, beads were manually magnetically washed in the same buffer before final resuspension in Quenching Buffer.

For sample washing after immunoprecipitation, Low Salt Washing Buffer, High Salt Washing Buffer, LiCl Washing Buffer, and Tris-EDTA (TE) Washing Buffer were used. Low Salt Washing Buffer contained 20 mM Tris-HCl, 2 mM EDTA, 150 mM NaCl, 0.1% SDS, and 1.0% Triton X-100 at pH 8.1. High Salt Washing Buffer contained 20 mM Tris-HCl, 2 mM EDTA, 500 mM NaCl, 0.1% SDS, and 1.0% Triton X-100 at pH 8.1. LiCl Washing Buffer contained 10 mM Tris-HCl, 1 mM EDTA, 250 mM LiCl, 1.0% Igepal-CA630, and 1.0% sodium deoxycholate at pH 8.1. Finally, TE Washing Buffer contained 10 mM Tris-HCl and 1 mM EDTA at pH 8.1.

For final purification and analysis, chemical coalescence of droplets was achieved with 1H,1H,2H,2H-perfluoro-1-octanol (Sigma Aldrich). Next, magnetic particles were exchanged into Elution Buffer, containing 20 mM Tris-HCl, 20 mM EDTA, 300 mM NaCl, and 2% SDS at pH 8.0. RNase A (1 h treatment at 65 °C, 2 µL at 10 mg mL^{-1} per sample, Sigma Aldrich) and Proteinase K (2 h treatment at 65 °C, 2 µL at 10 mg mL^{-1} per sample, Thermo Fisher Scientific) were used to degrade RNA and protein, respectively, during sample purification. Final DNA purification was performed using a QIAquick PCR purification kit (Qiagen) according to the manufacturer's instructions.

Microfluidic Device Operation

For the cell encapsulation, cell lysis, chromatin digestion, and immunoprecipitation device, devices were operated with syringe pumps (Pump 11 Pico Plus Elite, Harvard Apparatus) along guidelines from previous work.[34] Representative flow rates were 2 µL min^{-1} for the cell suspension, 2 µL min^{-1} for the combined Cell Lysis Buffer, Digestion Buffer, and MNase flow, 6 µL min^{-1} for the sample-encapsulating oil flow, 10 µL min^{-1} for the respacing oil flow, and 4 µL min^{-1} for the bead emulsion in Quenching Buffer.

For the integrated magnetic field washing devices and the bead-emulsifying devices, microfluidic devices were operated with pressure-driven flow as described previously.[29, 32] Briefly, this custom-assembled system distributed N_2 pressure from a gas cylinder through a custom manifold (VWR International) to individual two-stage regulators (VWR International) for selecting the pressure applied to each fluid line. Gas flowed through Tygon tubing (1/16 in ID x 1/8 in OD, Cole Parmer) through a solenoid valve (LHDA0531115H, The Lee Company) array and was interfaced via metal pins (New England Small Tube Corp.) through Teflon-silicone septa

(13 mm Autosampler Vial Septa, Thermo Fisher Scientific) into the headspace of solution-filled vials (Screw-Thread N-51A Borosilicate Glass Sample Vials, Thermo Fisher Scientific). The solenoid valve array provided digital control of individual pressure lines (turning them on or off) and was actuated by a custom LabView virtual instrument (National Instruments) communicating with a data acquisition device (NI PCIe-6251 Multifunction Data Acquisition Device with an SCB-68 Shielded I/O Connector Block, National Instruments). Tubing lengths (#30 PTFE, Cole Parmer) were typically fixed at 20 cm, but the droplet input for the integrated magnetic field washing devices used 25 cm for ease of use, and the bead suspension input for the bead-emulsifying devices used 5 cm from an inverted vial to minimize gravity-driven bead sedimentation.[36] Applied pressures were directly proportional to achieved flow rates. For the integrated magnetic field washing devices, representative pressures were 50 kPa for the input droplets, 55 kPa for the oil respacing the input droplets, 55 kPa for the Low Salt Washing Buffer, 65 kPa for the High Salt Washing Buffer, 65 kPa for the LiCl Washing Buffer, 40 kPa for the TE Washing Buffer, 55 kPa for the oil co-flowing with the washing buffers, 55 kPa for the oil resegmenting washed particles back into droplets, and 20 kPa for the waste collection outlet. For the bead-emulsifying devices, representative pressures were 55 kPa for the bead suspension and 85 kPa for the oil. Under these conditions, final flow rates were on the order of μL min^{-1}, and pressures were dynamically adjusted during operation as needed to achieve desired flow performance.

Electric field for all devices was mediated by a custom inverter to apply ~45 VAC (36 kHz) to the device. Electric field was typically supplied via on-device electrolyte-filled (3 M NaCl) channels connected to the inverters using syringes.[37] For integrated magnetic field washing devices, the electric field was connected via a submerged platinum wire in the Low Salt Washing Buffer reservoir, but the ground electrode was an electrolyte-filled channel as described above.

Imaging and Analysis

Device operation was monitored using an M80 Stereomicroscope (Leica Microsystems, Inc.) with a Phantom Miro Ex2 High Speed Camera (Vision Research, Inc.) or a DMi8 Microscope (Leica Microsystems) with a VEO 640L High Speed Camera (Vision Research, Inc.). Fluorescent imaging was performed on the DMi8 with the VEO 640L using a FITC fluorescence cube filter (Leica Microsystems). Image processing and analysis were performed using ImageJ software (National Institutes of Health). Droplet flow characteristics (size, frequency, velocity, etc.) were determined manually within the software from brightfield images, and analysis included at least N = 20 droplets for each conditions shown. Brightfield and fluorescent images were uniformly increased in brightness for ease of visualization, but quantitative data were obtained from the original, non-adjusted images.

Purified DNA was quantitatively evaluated across two primary metrics. DNA amount was measured with the Qubit dsDNA assay (Thermo Fisher Scientific) according to the manufacturer's protocol. DNA enrichment (indicating ChIP enrichment specificity) was measured using quantitative polymerase chain reaction (qPCR) performed on the 7900HT Fast Real-Time PCR System (Thermo Fisher Scientific), and this assay was performed by the DNA Sequencing Core (University of Michigan). For qPCR analysis, primer DNA sequences (see Table VI.1, Integrated DNA Technologies, Inc.) and master mix (Applied Biosystems™ PowerUp™ SYBR™ Green Master Mix, Thermo Fisher Scientific) were added to each sample prior to amplification. Evaluation of this data is described in the following sections, and, within each plot, the data represent parallel ChIP experiments with the same starting cell population. One of the datasets supplied a comparison for multiple parameters, alternately labeled as "60 ng," "Bound," and "Manual 60 ng" in Fig. VI.4a, VI.4c, and Fig. VI.5a, respectively.

Table VI.1. Primer Sequences Used in Quantitative Polymerase Chain Reaction Analysis of ChIP Enrichment.

Gene	Primer Direction	DNA Sequence (5' to 3')
BRG1	Forward	TTG GCG AAG CTG CGA TCG GG
	Reverse	AGG GGA CCG CTA ATG CCC GT
MYT1	Forward	CCT GCC GTG TGC TGT TTT T
	Reverse	CAC AAC ATG TCC CCT GGA ATC
hSAT	Forward	AAG GTC AAT GGC AGA AAA GAA
	Reverse	CAA CGA AGG CCA CAA GAT GTC
C19	Forward	AGC TTG TCT TTC CCA AGT TTA CTC
	Reverse	TAG CTG TCG CAC TTC AGA GGA

RESULTS AND DISCUSSION

Microfluidic Assay Design Principles

As a starting point, assay development initiated from two recent technologies developed by the Bailey Lab. First, Xu *et al.* described a droplet microfluidic method for chromatin preparation in an epigenetic context.[34] To profile nucleosome positioning as an indicator of the transcriptional state of proximal genes, the device compartmentalized cells into droplets at a co-flowing interface which simultaneously added cell lysis and chromatin digestion reagents (principally detergent and micrococcal nuclease, MNase, respectively). Following incubation through an extended delay channel network (the volume of which determined processing time), direct injection inhibited the Ca^{2+}-dependent MNase by adding EDTA into sample droplets as a chelator. Finally, droplets were collected from the device and processed for analysis of obtained DNA, including DNA yield, digested DNA fragment length, and DNA sequence. Overall, this method achieved effective automated processing across a range of sample sizes, and the combination of cell lysis and chromatin digestion elements (typically performed as separate,

discrete steps) proved an innovative approach to simplify the workflow. In the context of the ChIP assay, it represented much of the early stages of the assay: processing from input samples to digested chromatin.

The second supporting technology was very recently described by Doonan *et al*.[32] ChIP requires highly effective washing steps to exchange antibody-histone complexes through a series of detergent and ionic strength conditions for removal of off-target species. The Coalesce-Attract-Resegment Washing (CAR-Wash) module fused input droplets (containing magnetic particle-bound sample) with washing buffer flow. Next, a permanent magnet pulled particles across washing buffer streamlines to the opposite side of the channel as laminar flow confined the original, non-magnetic droplet material to its original flow path. Lastly, magnetic particles were re-encapsulated in new droplet volumes at the end of the device for further handling. Module characterization showed nearly complete particle capture and superior exclusion of starting waste volume compared to previous droplet microfluidic purification techniques. The CAR-Wash was originally deployed for proof-of-concept assays including a selective protein enrichment where, importantly, it was relatively insensitive to input droplet quality. This feature is particularly important for ChIP processing: continuing the ChIP assay through the washing stages requires robustly handling detergent-destabilized droplets (from both Lysis Buffer and washing buffer components).

These two examples prototyped features of the ChIP protocol, including cell processing through chromatin digestion and particle-mediated washing of captured chromatin complexes. Nonetheless, they omitted other crucial technical aspects of ChIP. First, bead and antibody addition must be delivered in controlled stoichiometry to promote specific enrichment of targets while minimizing background. Second, standard protocols wash immune complexes through a series of

washing buffers for efficient and selective ChIP, but the CAR-Wash only demonstrated single washing examples. Serially transferring sample through multiple iterations of the device will increase processing complexity, operation time, and sample loss. Overall, these technologies offered promising starting points for ChIP, but they required further adaptation before enabling the assay.

Expanding Microfluidic Device Functionality

Microfluidic devices were correspondingly altered to integrate additional ChIP functions. First, the core device described by Xu *et al.* was adapted to facilitate both robust processing of cells and terminal magnetic bead-bound antibody injection (Fig. VI.1a).[34] As before, cells were co-encapsulated with cell lysis and chromatin reagents to initiate chromatin preparation (137 ± 3 pL in volume each at 380 ± 30 Hz generation frequency for this example). This portion was only slightly adjusted to improve robustness against channel obstructions by decreasing the incidence of sharp channel bends in these relatively narrow channel regions (Fig. VI.1b). The delay channel region was left unchanged in geometry (and total storage volume) to ensure that slowly flowing droplets were processed according to previously optimized reaction duration (~210 s incubation, Fig. VI.1c). By maintaining the properties of these upstream features, the fundamental operating parameters and performance for well-established cell lysis and chromatin digestion functions were maintained.[34]

Downstream, the device was more significantly altered. After the incubation region, adding a respacing oil feature improved performance for terminal operations (Fig. VI.1d). Delay channels achieved droplet incubation using channels with large cross-sectional area to limit impractical increases in device hydraulic resistance.[33] Unfortunately, these channels gave droplets additional

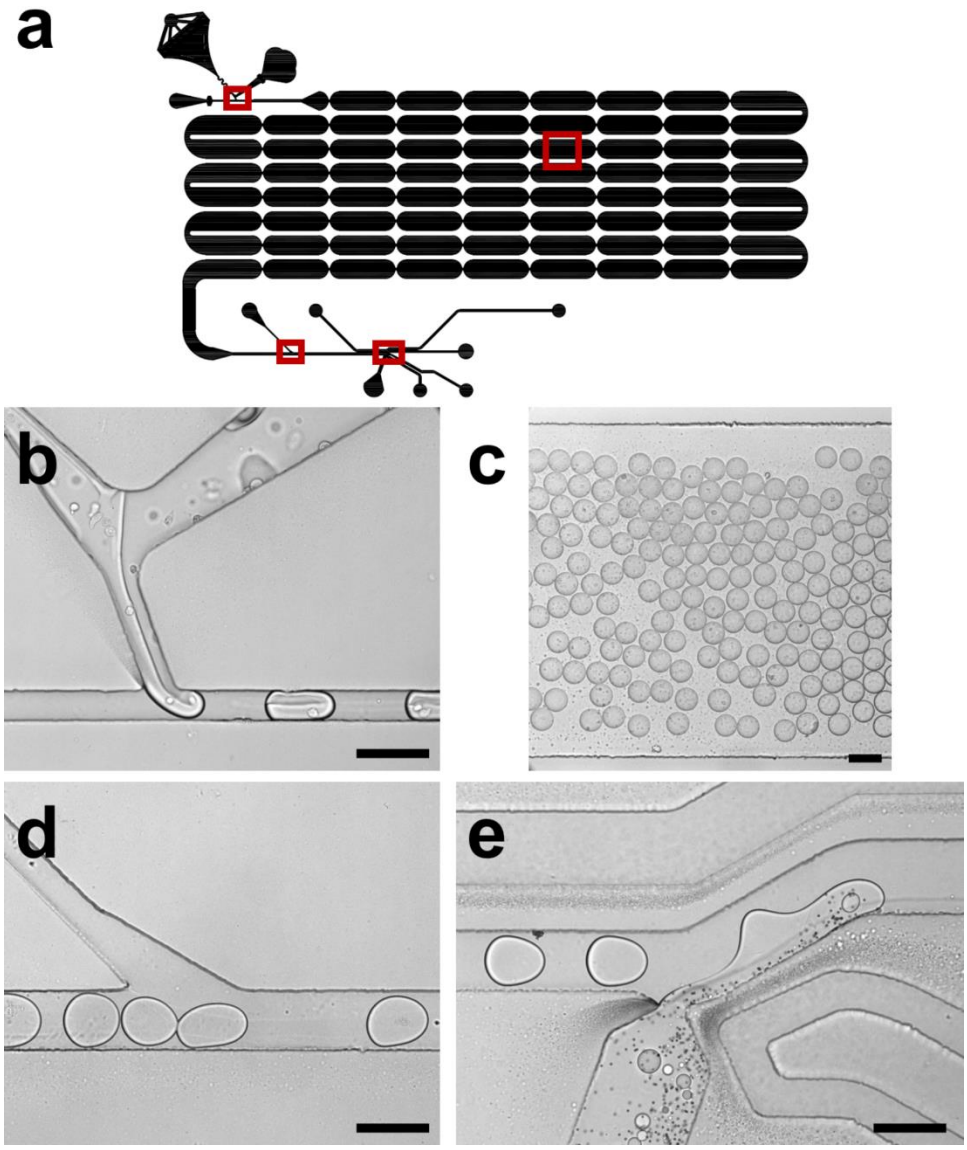

Figure VI.1. Schematic and Representative Micrographs for the Initial ChIP Module. a) Schematic of the microfluidic device with regions of interest (shown in later micrographs) indicated by red boxes. b) The cell suspension (left, cells visible as small, bright circles) and lysis and chromatin digestion stream (right) co-encapsulate into droplets under the influence of orthogonal, immiscible oil flow at the T-Junction. c) Cell lysis and chromatin digestion occurs during incubation in a serial network of large-volume channels. d) Oil respaces irregularly packed droplets after incubation. e) Direct injection under the destabilizing influence of electric field adds antibody-functionalized magnetic particles (visible as small, black objects in high abundance) and Quenching Buffer (to inhibit chromatin digestion) to respaced droplets. Flow is generally left to right, and all scale bars are 100 µm.

degrees of freedom (lateral and vertical) where they rearranged and shuffled within the continuous phase. Subsequent processing was hindered by random distribution of droplets, particularly for

droplet-spacing dependent direct injections. Thus, re-spacing the droplets further at the end of incubation helped to ensure all droplets received sufficient quenching buffer and antibody-magnetic bead addition, while avoiding total droplet destabilization and fusion with neighboring volumes (Fig. VI.1e). Bead and quenching buffer injection were further facilitated by rapid emulsion of the bead suspension as previously described (using a tabletop vortex mixer or simple droplet formation device).[32] Beneficially, this technique limited sedimentation of dense magnetic particles which might prevent uniform on-device loading during extended operation.[36] Two additional optimizations of the direct injection increased device robustness: (1) flow-through (instead of dead-end-filled) electrode channels required lower pressures to fill with electrolyte solution, improving ease of use and reducing the chance of total device mechanical failure during assay preparation, and (2) direct injection of the bead emulsion was interfaced at a less severe angle (40° instead of 90° relative to the intersecting flow channel). This redirection promoted more robust handling of the reinjected bead emulsion stream which was frequently subject to obstruction in the original design (by concentrated magnetic particles and incidental contaminants). These alterations added immunoprecipitation capabilities and decreased device sensitivity to channel obstructions.[34]

Next, the second device was expanded from the Dynabead particle washing module described by Doonan *et al*.[32] Here, the critical deficit in the original platform resided in the need for multiple washing phases supported by the consensus of ChIP protocols.[8-14] Experiments attempting serial reinjection for repeated washing of a single droplet population through different buffers were laborious and largely failed due to sample loss at each step (data not shown). On the other hand, interesting examples have demonstrated the potential of magnetically-mediated co-laminar sample processing.[38, 39] These microfluidic devices have been applied to bioassay and

material synthesis applications, achieving effective chemical manipulation of migrating particles during passage through orthogonal reagent streams. Therefore, the CAR-Wash principle was adapted to a co-laminar particle processing strategy for fully integrated ChIP washing (Fig. VI.2a). Droplets entering this device were frequently irregular due to detergent-driven instabilities and to variance in terminal quenching buffer-particle injection volume from the first module. After a simple oil respacing intersection, droplets were effectively electrocoalesced with the Low Salt Buffer stream (Fig. VI.2b). Lack of respacing increased the rate of coalescence failure when adjacent, closely packed droplets experiences disuniform flux of the electric field.. Upon fusion, particles rapidly migrated through the co-laminar streams (Low Salt Buffer, High Salt Buffer, LiCl Buffer, and TE Buffer). The fastest particles with highest magnetic content reached the TE Buffer-oil boundary (to restrict them from trapping at the channel wall) in as little as 10 ms, but a large fraction of the population did not completely migrate until flowing much further downstream. At the end of the co-flowing migration channel, beads were re-encapsulated into droplets (Fig. VI.2c). Precise flow conditions varied based on input droplet quality and magnetic alignment, and example input flow conditions approximated 200-500 Hz (estimated from total volume for coalesced input droplets) with output generation at up to 1500 Hz. More important than their exact values, flow conditions were dynamically selected to give effective droplet coalescence and magnetic particle capture while maximizing throughput.

The original CAR-Wash example physically and biochemically confirmed washing effectiveness in this format for a single buffer, and expanding this platform required profiling washing characteristics in the co-laminar format.[32] Fluorescently dying the first (Low Salt Buffer) and third (LiCl Buffer) washing buffers gave qualitative insight about the chemical environment of migrating magnetic particles at the beginning (Fig. VI.2d) and end (Fig. VI.2e) of the device.

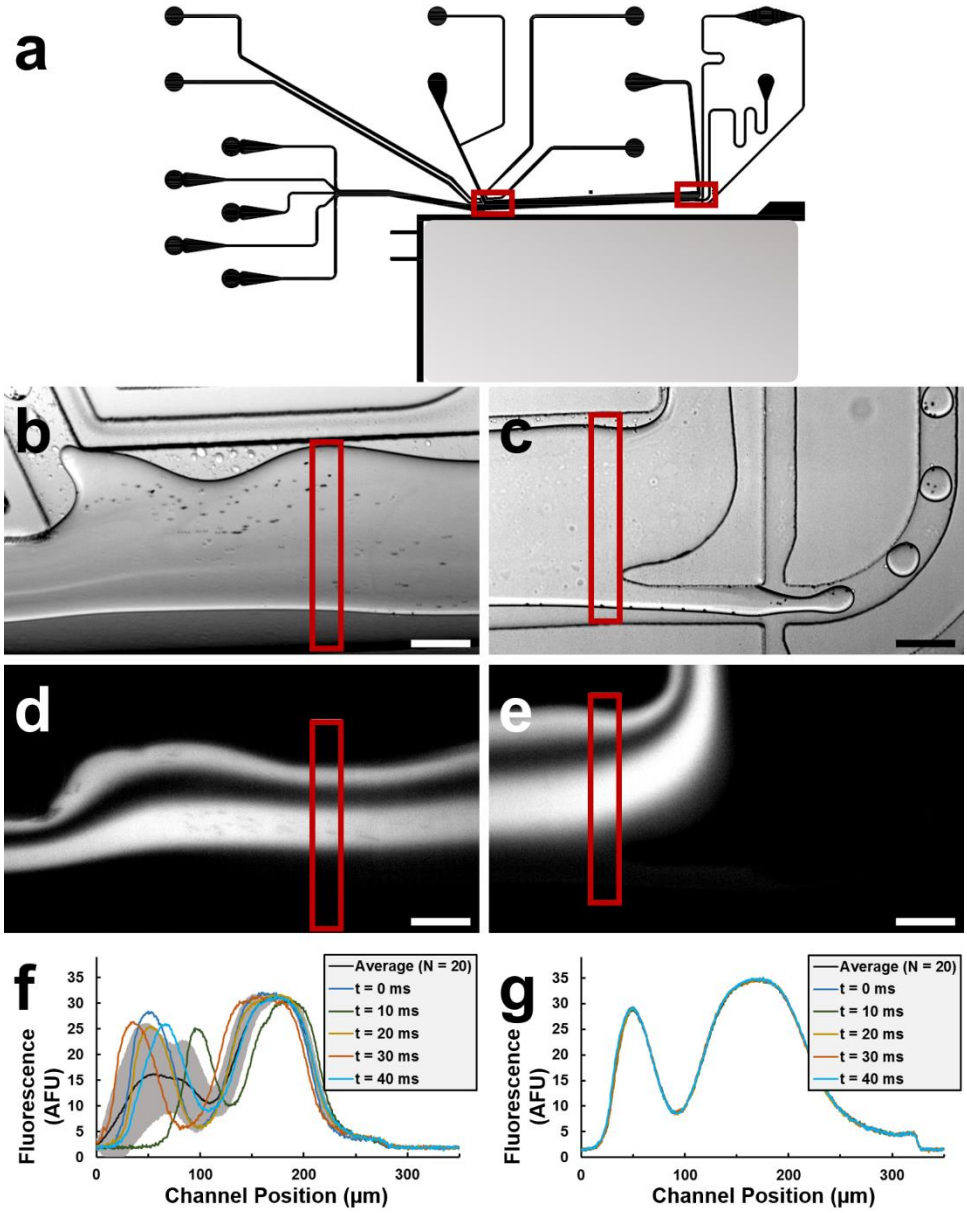

Figure VI.2. Schematic, Representative Micrographs, and Fluorescent Profiles for the Second ChIP Module. a) Schematic of the microfluidic device with regions of interest (shown in later micrographs) indicated by red boxes. The magnet is represented by the large gray rectangle. b) The oil-respaced sample droplets (often irregular due to detergent destabilization) are coalesced with the washing buffer coflow under the influence of directed electric field. Magnetic particles (visible as small, black objects in high abundance) are magnetically pulled across washing buffer streams until reaching the interface with the co-flowing oil stream. c) The majority of fully migrated particles are re-encapsulated in droplets of the terminal buffer stream, mediated by an orthogonal flow focusing interface. The remainder of channel volume flows to waste. Fluorescent imaging of d) the coalescence region and e) the re-encapsulation region demonstrates the localization of the four, co-flowing washing buffers. From top to bottom, these buffers were Low Salt Buffer (with 100 μM fluorescein and supplying the electric field), High Salt Buffer, LiCl Buffer (with 100 μM fluorescein), and TE Buffer. Fluorescence profiles of

each device region (regions of interest boxed in red in earlier images) demonstrate localization and mixing at f) the droplet coalescence and initial washing zone under destabilizing flow conditions and at g) the re-encapsulation zone under stabilized flow conditions. Each plot includes an average (black) with error bars (gray, representing the standard deviation) for 20 profiles as well as 5 example profiles from single timepoints (to indicate specific localization obscured by flow instabilities). Flow is generally left to right, and all scale bars are 100 μm.

Exact position of each buffer stream depended on the relative flow rates applied, and the disuniformity of input sample droplet flow generated instabilities in upstream profiles (Fig. VI.2f) which equilibrated after extended flow (Fig. VI.2g). Moreover, the lack of complete return to baseline in non-fluorescent washing buffers indicated the extent of convective (from the coalescence region's instabilities) and diffusive (from extended co-laminar flow) mixing. The device thus provided chemical gradients as particles migrate among streamlines, and we anticipate that the washing gradient could be adjusted as needed with buffer flow rates, co-laminar buffer channel length, and magnetophoresis channel width, among other strategies. Finally, variance in particle magnetic content could lead to very short interactions with each washing buffer (a few ms in duration across some tens of μm in lateral distance), but earlier CAR-Wash characterization showed highly efficient buffer exchange (100-fold dilution) at similar scales (~50 μm).[32] Later data in this work highlighting selective enrichment suggest that even these seemingly brief washing buffer interactions successfully recapitulate bulk ChIP washing effectiveness.

In combination of these two platforms, Fig. VI.3 summarizes this total droplet-based ChIP workflow: microfluidic droplet processing from original cells to purified nucleosomes (with manual final DNA recovery and analysis).

Manual ChIP Optimization and Analysis

The optimized microfluidic devices developed the mechanical capabilities for a streamlined ChIP protocol, and characterization in a manual format provided a useful strategy to

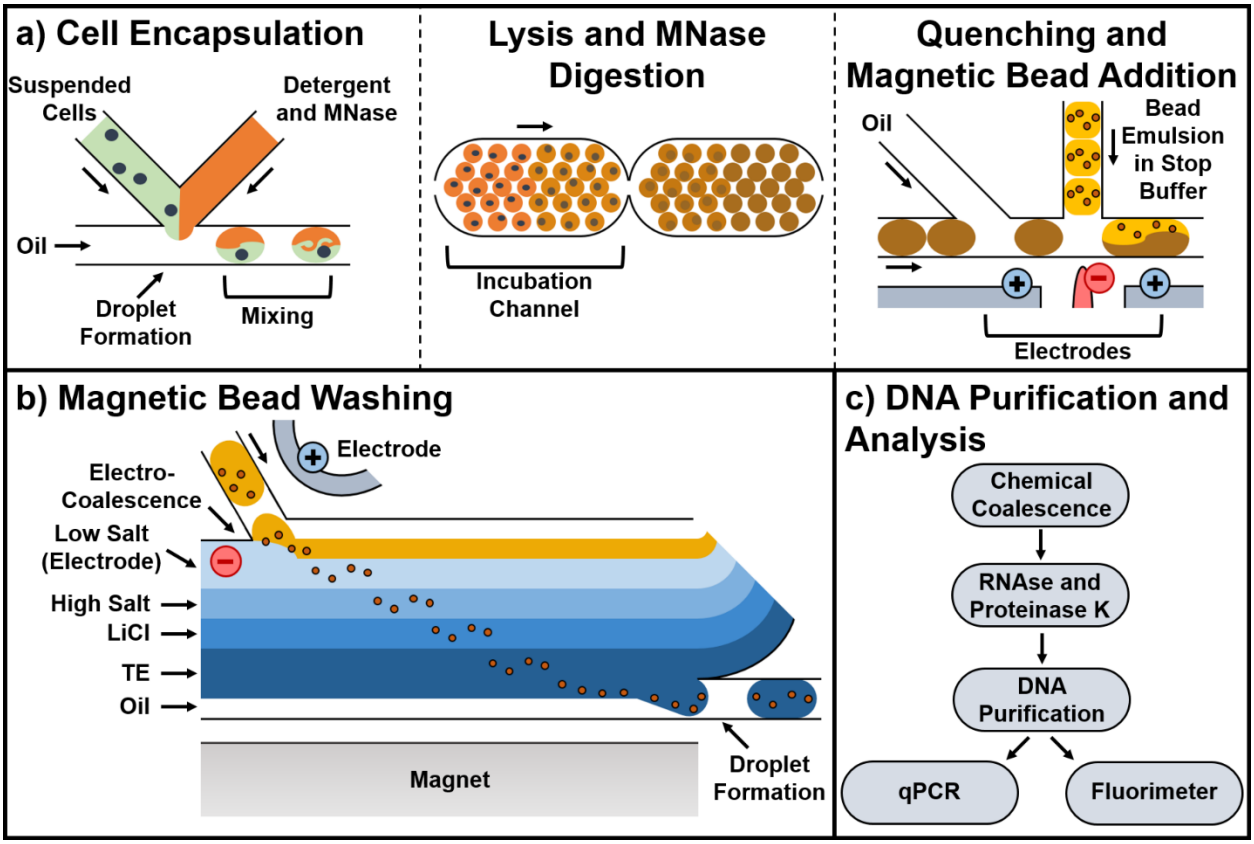

Figure VI.3. Chromatin Immunoprecipitation-in-Droplets Schematic. a) The first module of the workflow performed three key tasks: co-encapsulation of suspended cells with cell lysis and enzymatic (MNase) chromatin digestion components, reaction time for cell lysis and chromatin digestion during flow through large volume channels, and direct injection of antibody-conjugated magnetic particles in enzyme-quenching buffer. b) After antibody-histone target binding, droplets were reinjected onto the second module for washing. Upon electrical coalescence, the magnetic field from a channel-adjacent permanent magnet array attracted the magnetic particles through four miscible, co-flowing washing buffers: Low Salt Buffer (electrically charged), High Salt Buffer, LiCl Buffer, and Tris-EDTA (TE) Buffer. A co-flowing oil stream restricted particle motion from wall-bounded trapping and participated in re-encapsulation of washed particles in new droplets. c) After washing, final processing coalesced droplets for bead recovery followed by RNAse and proteinase treatment to elute DNA. Once purification was complete, DNA was analyzed with quantitative Polymerase Chain Reaction (qPCR) and fluorimetry. Arrows indicate flow directions of adjacent channel features. Electrically charged structures have polarity indicated. Features are not shown to scale.

optimize operating conditions. Briefly, the first module was designed to lyse cells, digest chromatin, and initiate immunoprecipitation. After incubation, the second module was designed to wash immunoprecipitated sample through the four washing buffers. Therefore, the manual ChIP protocol performed these key steps by (1) manually adding the lysis and digestion reagents

simultaneously, (2) injecting magnetic particles with antibody in Quenching Buffer after ~210 s incubation, and (3) performing manual magnetic washing after overnight incubation. Final DNA elution and analysis were performed manually in both on-device and manual samples.

To simplify microfluidic adaptation of ChIP, certain assay steps were combined or omitted. Prior characterization confirmed that the combined cell lysis and chromatin digestion (enzymatic only) were suitable for chromatin processing into mono-nucleosomes, even though other protocols performed these operations separately or even isolated nuclei before processing. [8-14, 34] Nonetheless, it was unclear as to how combining these steps followed by the addition of the immunoprecipitation solid phase during enzymatic quenching might affect enrichment. Further, our protocol did not use a clearing method (centrifugation or non-specific particle incubation) to remove insoluble chromatin and cell lysate components. [8-14] Such species might interfere with specific binding to antibodies and increase background during analysis. These discrepancies required evaluation prior to implementation of the microfluidic approach.

ChIP performance was primarily assessed using a fluorimeter to determine DNA yield and by using Quantitative Polymerase Chain Reaction (qPCR) to determine immunoprecipitation specificity. In particular, qPCR assayed the relative abundance of expected on- and off-target gene sequences for our well-characterized histone PTMs. The final analysis was performed using the ΔΔCt Method:[40]

$$\Delta\Delta Ct = (Ct_{GOI:IP} - Ct_{RG:IP}) - (Ct_{GOI:Input} - Ct_{RG:Input}) \quad \text{eq. 1}$$

Where the ΔΔCt is the change in the threshold cycle, Ct, for the gene of interest in the immunoprecipitated sample, GOI:IP, compared to the reference gene for the immunoprecipitated

sample, RG:IP, corrected by the same calculation for a non-immunoprecipitated input sample, GOI:Input and RG:Input, respectively. Compared to absolute ΔCt evaluation, the input correction reduces the effects from experimental variability in cell processing and qPCR performance.[40] Because qPCR functions on an approximate doubling of the amplified DNA target (within optimal cycle number), the enrichment of targeted DNA, described as the fold-change of target DNA sequence amount compared to reference DNA sequence amount, is:

$$= 2^{-\Delta\Delta Ct} \qquad \text{eq. 2}$$

For the assay, we selected a stringent 5-fold enrichment threshold for target DNA amount relative to the reference provides for positive enrichment (corresponding to $-\Delta\Delta Ct \approx 2.3$), but an enrichment threshold as low as 3-fold has been accepted previously.[15]

To demonstrate ChIP efficacy we chose to profile two well-characterized marks, one activating for associated DNA and the other repressive. Trimethylation of lysine 4 on histone H3 (H3K4me3) was the activating target, trimethylation of lysine 27 on histone H3 (H3K27me) was the repressing target, and genes for qPCR analysis were correspondingly selected.[14, 41] The BRG1 Transcription Start Site (TSS) was actively expressed in the context of ATP-dependent chromatin remodeling and was expected to associate with H3K4me3.[42] Next, the MYT1 TSS was repressed by the Polycomb Repressive Complex 2 (PRC2) and was expected to associate with H3K27me3.[9] A constitutive heterochromatin site, hSAT, was also included and not expected to associate with either modified histone.[43] Finally, an intergenic region, C19, was used as the reference gene not associated with either modification.[9]

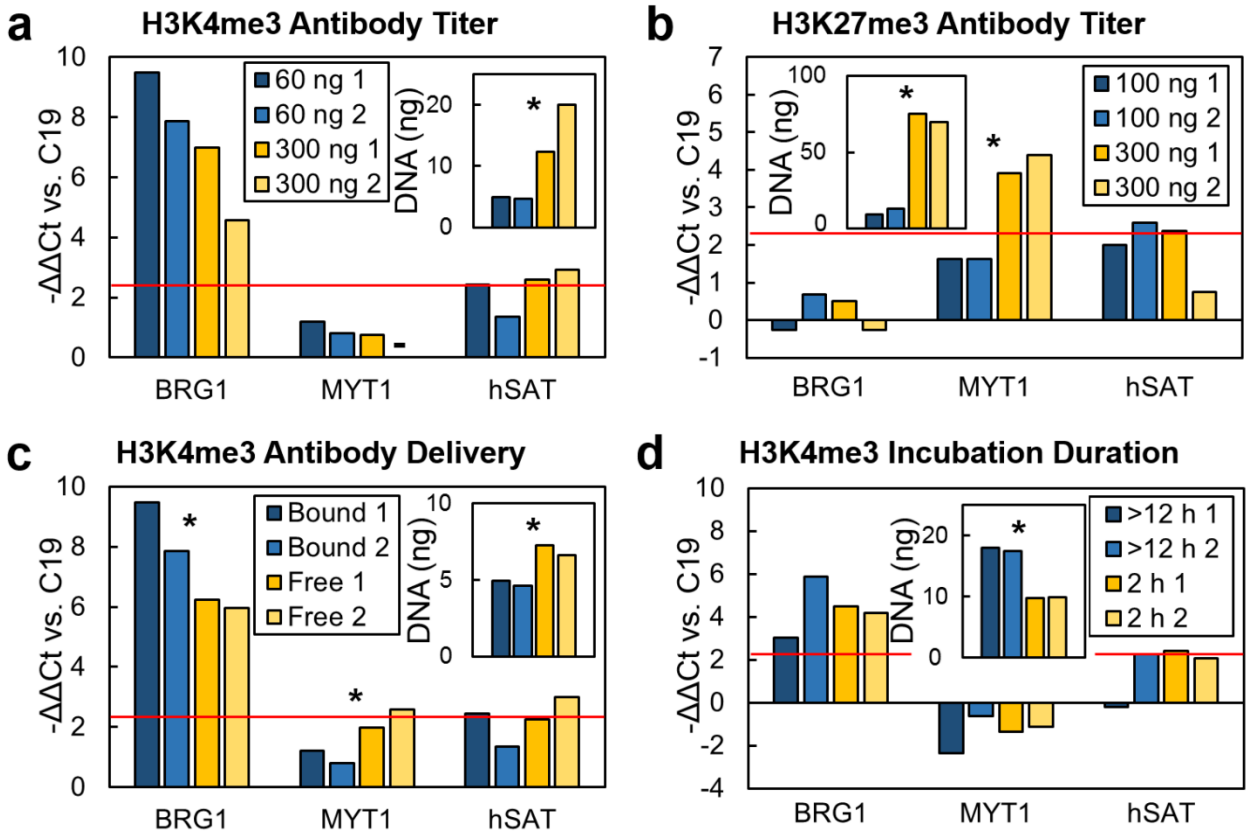

Figure VI.4. Manual ChIP Characterization for 250,000 HeLa Cells. a) For lower antibody titer (60 ng), H3K4me3 shows a (not statistically significant) increase in strongly H3K4me3-associated BRG1 enrichment with no change in off-target MYT1 or hSAT. DNA yield (inset) is significantly higher with higher antibody titer. b) For higher antibody titer (300 ng), H3K27me3 shows a significant increase in strongly H3K27me3-associated MYT1 enrichment with no change in off-target BRG1 or hSAT. DNA yield (inset) is significantly higher with higher antibody titer. c) For pre-treating magnetic beads with 60 ng anti-H3K4me3 antibody ("Bound"), BRG1 shows significantly higher specific enrichment, MYT1 shows significantly lower non-specific enrichment, and DNA yield was significantly lower compared to adding the free antibody (60 ng) in the lysis and digestion reagent followed by adding the magnetic beads during enzymatic quenching ("Free"). There was no change in hSAT enrichment. d) Overnight (>12 h) and short (2 h) incubation show no significant difference in enrichment for any of the gene loci, but overnight incubation significantly increased DNA yield. A "-" indicated the data was unavailable (qPCR well failure). A "*" indicated statistical significance (Student's t-Test at 95% confidence), but limited replicates limit statistical power. The red line indicated the threshold for positive enrichment (at least a 5-fold change in the gene of interest vs. reference sequence C19).

Fig. VI.4 shows example ChIP characterization and optimization data. First, we optimized antibody titer for H3K4me3 (Fig. VI.4a) and H3K27me3 (Fig. VI.4b). In both cases, DNA yield increased significantly with titer due to increased specific binding capacity but, perhaps, also due

to increased non-specific interactions with a higher antibody loading on the bead surface. In fact, our data supports both possibilities. Anti-H3K4me3 at higher titer showed lower specific interactions with BRG1 (Fig. VI.4a), but anti-H3K27me3 at higher titer showed significantly higher specific enrichment for MYT1 (Fig. VI.4b). Next, antibody loading method was evaluated (Fig. VI.4c). Antibodies were typically applied to the bead surface and magnetically washed before introduction with the quenching buffer. On the other hand, we anticipated that variance in the microfluidic operation's terminal direct injection of beads and antibody (due to inconsistent droplet spacing after incubation) might interfere with antibody-target stoichiometry. Therefore, this study tested adding the free antibody with the lysis and digestion reagent to take advantage of the robustness and reproducibility of upstream microfluidic operation. Nonetheless, for H3K4me3, we saw significantly reduced BRG1 specific enrichment with significantly higher non-specific MYT1 enrichment and DNA yield. Therefore, this approach increased non-specific binding because it did not pre-coating the particles with antibody prior to interactions with non-specific lysate and chromatin components. Lastly, immunoprecipitation incubation time was evaluated (Fig. VI.4d). For overnight and 2 h incubation (terminated by manual particle washing), enrichment did not differ significantly, but overnight incubation obtained significantly higher DNA yield.

Generally, these data showed positive enrichment of specific loci with only inconsistent, slight enrichment of off-target sequences (primarily hSAT). Higher yield for H3K27me3 ChIP also conforms to expectations of high target abundance.[14] Unfortunately, biological replicates of similar conditions (such as 60 ng particle-bound anti-H3K4me3 with overnight incubation) showed enrichment and DNA yield inconsistencies (for example, spanning 5 ng to nearly 20 ng, Fig. VI.4a,d). These data emphasize the challenges of reproducibility in manual ChIP protocols

and the clear need for a robust, automated assay. Finally, low replicate numbers limit the statistical power of these results, but the promising trends provide proof-of-principle for implementing the modified method into droplet platform.

ChIP in Droplets

Finally, the ChIP assay was performed using the droplet microfluidic modules (with side-by-side manual experiments for validation). Optimized antibody titers and bead amounts were doubled for droplet experiments to conserve stoichiometry by taking into account the ~50% of droplets formed that did not encapsulate any cells. In line with manual characterization, cell lysis and chromatin digestion were performed simultaneously, and the digestion was quenched simultaneously with antibody-coated particle addition. After overnight incubation, droplets were reinjected for co-laminar magnetic particle washing. Washed droplets were coalesced for final manual DNA purification and analysis.

Fig. VI.5 shows representative ChIP results from the full droplet-enabled assay. Manual processing directly provided a standard for comparison for microfluidic performance, and including a manually-processed control group without antibody further confirmed ChIP enrichment specificity. For the activating mark H3K4me3, both droplet and manual ChIP showed good enrichment of BRG1, significantly higher than the no antibody control, and non-specific enrichment of off-target genes was generally low (Fig. VI.5a). While positive enrichment of BRG1 did not differ significantly among droplet and manual trials, DNA yield was significantly lower for the droplet system. For the repressing mark H3K27me3, both droplet and manual samples show enrichment of MYT1, significantly higher than for the no-antibody control (Fig. VI.5b). Non-specific enrichment of other genes for this target was similarly low for most trials, and we obtained

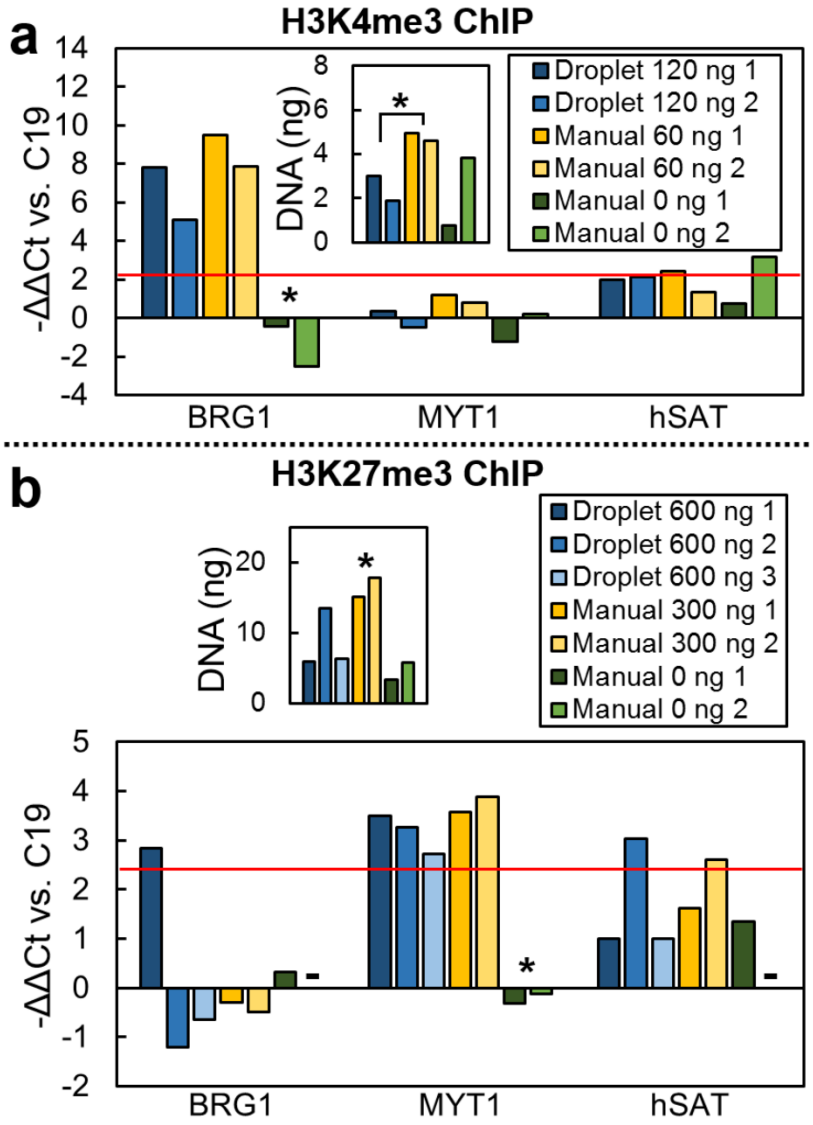

Figure VI.5. Comparison of ChIP in Droplet and Manual Formats for 250,000 HeLa Cells. a) H3K4me3 capture for droplet ("Droplet 120 ng") and manual ("Manual 60 ng") ChIP showed highly effective enrichment of the H3K4me3-associated BRG1 locus, significantly higher than for the no antibody control ("Manual 0 ng"). Off-target MYT1 and hSAT showed little enrichment with no significant differences among groups. Manual processing did, however, show significantly higher DNA yield than the droplet assay. b) H3K27me3 capture for droplet ("Droplet 600 ng") and manual ("Manual 300 ng") ChIP showed effective enrichment of the H3K27me3-associated MYT1 locus, significantly higher than for the no antibody control ("Manual 0 ng"). Off-target BRG1 and hSAT generally showed little enrichment with no significant differences between droplet and manual ChIP. Manual processing showed significantly higher DNA yield than for the droplet assay and no antibody conditions. A "-" indicated the data was unavailable for this gene locus. A "*" indicated statistical significance (Student's t-Test at 95% confidence), but limited replicates limit statistical power. The red line indicated the threshold for positive enrichment (at least a 5-fold change in the gene of interest vs. reference sequence C19). Legends indicated the antibody titer.

significantly higher DNA yields for manual ChIP (this time compared to both droplet and no antibody control values).

Overall, our microfluidic ChIP assay showed convincing positive enrichment of corresponding genes for activating H3K4me3 and repressing H3K27me3 with minimal non-specific enrichment using the ΔΔCt Method.[15] Importantly, validating microfluidic performance with parallel manual processing confirmed no significant difference in enrichment as a function of assay format. Lower DNA yields for the microfluidic assay may also be improved by technical optimization in the future: more robust cell loading onto the first device, improved droplet transfer onto the washing device, or higher efficiency magnetic bead capture during washing. Compared to other microfluidic ChIP assays, we have not yet scaled down to very small cell numbers (100 to 10,000 cells) or achieved single cell resolution.[16-20, 22] We have, however, shown serial droplet-by-droplet ChIP operations, opening the possibility for variable sample size by serially processing more or fewer droplets without needing intensive re-optimization of reagent concentrations. For evaluating enrichment, microfluidic ChIP assays have taken a range of approaches or provided DNA sequencing data, obscuring direct comparisons in some cases.[16-20, 22] Nonetheless, we have demonstrated comparable enrichment, if for different targets, relative to those directly providing fold change values.[18, 19] Future expansion of our assay to include DNA sequencing will empower broader comparisons while enhancing its scope and information yield.

CONCLUSIONS

In summary, this work established a proof-of-concept implementation for droplet-based microfluidic ChIP. Promisingly, DNA enrichment for both an activating (H3K4me3) and a repressing (H3K27me3) histone isoform showed expected correlations with analyzed DNA targets

and did not differ significantly from manual processing in this exploratory study. Future work will optimize DNA yield and expand processing to additional histone targets and to dynamic sample sizes. More generally, this work lays out an unprecedented advance in droplet microfluidic technologies, demonstrating a complex, multistep bioassay with integrated functions for cell processing and affinity-based purification at a previously unrealized scale. We anticipate that, in addition to ChIP, these technical innovations will empower a host of other droplet-enabled bioassays.

ACKNOWLEDGEMENTS

We gratefully acknowledge financial support from the National Institutes of Health (NIH CA191186). S.R.D. was also supported by the National Science Foundation Graduate Research Fellowship Program. Please see the Chapter VI title page (177) for additional detail on contributions from team members and from collaborators.

REFERENCES

1. F. H. Crick, *Symposia of the Society for Experimental Biology*, 1958, **12**, 138-163.
2. T. Chen and S. Y. R. Dent, *Nature Reviews Genetics*, 2013, **15**, 93.
3. M. L. Suvà, N. Riggi and B. E. Bernstein, *Science*, 2013, **339**, 1567-1570.
4. E. Heard and Robert A. Martienssen, *Cell*, 2014, **157**, 95-109.
5. P. Chi, C. D. Allis and G. G. Wang, *Nat Rev Cancer*, 2010, **10**, 457-469.
6. A. J. Bannister and T. Kouzarides, *Cell Res*, 2011, **21**, 381-395.
7. K. J. Falkenberg and R. W. Johnstone, *Nat Rev Drug Discov*, 2014, **13**, 673-691.
8. J. D. Nelson, O. Denisenko and K. Bomsztyk, *Nature Protocols*, 2006, **1**, 179-185.
9. J. Zhong, Z. Ye, S. W. Lenz, C. R. Clark, A. Bharucha, G. Farrugia, K. D. Robertson, Z. Zhang, T. Ordog and J.-H. Lee, *BMC genomics*, 2017, **18**, 985-985.

10. M. Adli and B. E. Bernstein, *Nature Protocols*, 2011, **6**, 1656.

11. J. A. Dahl and P. Collas, in *Chromatin Immunoprecipitation Assays: Methods and Protocols*, ed. P. Collas, Humana Press, Totowa, NJ, 2009, DOI: 10.1007/978-1-60327-414-2_4, pp. 59-74.

12. J. A. Dahl and P. Collas, *Nat. Protocols*, 2008, **3**, 1032-1045.

13. G. D. Gilfillan, T. Hughes, Y. Sheng, H. S. Hjorthaug, T. Straub, K. Gervin, J. R. Harris, D. E. Undlien and R. Lyle, *BMC Genomics*, 2012, **13**, 645.

14. S. Bonn, R. P. Zinzen, A. Perez-Gonzalez, A. Riddell, A.-C. Gavin and E. E. M. Furlong, *Nature Protocols*, 2012, **7**, 978.

15. T. Sandmann, J. S. Jakobsen and E. E. M. Furlong, *Nature Protocols*, 2007, **1**, 2839.

16. A. R. Wu, J. B. Hiatt, R. Lu, J. L. Attema, N. A. Lobo, I. L. Weissman, M. F. Clarke and S. R. Quake, *Lab on a Chip*, 2009, **9**, 1365-1370.

17. A. R. Wu, T. L. A. Kawahara, N. A. Rapicavoli, J. v. Riggelen, E. H. Shroff, L. Xu, D. W. Felsher, H. Y. Chang and S. R. Quake, *Lab on a Chip*, 2012, **12**, 2190-2198.

18. Z. Cao, C. Chen, B. He, K. Tan and C. Lu, *Nature methods*, 2015, **12**, 959-962.

19. Z. Cao and C. Lu, *Analytical Chemistry*, 2016, **88**, 1965-1972.

20. S. Ma, Y.-P. Hsieh, J. Ma and C. Lu, *Science Advances*, 2018, **4**, eaar8187.

21. Y. Zhu, Z. Cao and C. Lu, *Analyst*, 2019, **144**, 1904-1915.

22. A. Rotem, O. Ram, N. Shoresh, R. A. Sperling, A. Goren, D. A. Weitz and B. E. Bernstein, *Nature Biotechnology*, 2015, **33**, 1165.

23. T. Thorsen, R. W. Roberts, F. H. Arnold and S. R. Quake, *Physical Review Letters*, 2001, **86**, 4163-4166.

24. H. Song, J. D. Tice and R. F. Ismagilov, *Angewandte Chemie International Edition*, 2003, **42**, 768-772.

25. L. Shang, Y. Cheng and Y. Zhao, *Chemical Reviews*, 2017, **117**, 7964-8040.

26. M. Serra, D. Ferraro, I. Pereiro, J. L. Viovy and S. Descroix, *Lab on a Chip*, 2017, **17**, 3979-3999.

27. J.-C. Baret, *Lab on a Chip*, 2012, **12**, 422-433.

28. A. R. Abate, T. Hung, P. Mary, J. J. Agresti and D. A. Weitz, *Proceedings of the National Academy of Sciences of the United States of America*, 2010, **107**, 19163-19166.

29. S. R. Doonan and R. C. Bailey, *Analytical Chemistry*, 2017, **89**, 4091-4099.

30. D. Lombardi and P. S. Dittrich, *Analytical and Bioanalytical Chemistry*, 2011, **399**, 347-352.

31. E. Brouzes, T. Kruse, R. Kimmerling and H. H. Strey, *Lab on a Chip*, 2015, **15**, 908-919.

32. S. R. Doonan, M. Lin and R. C. Bailey, *Lab on a Chip*, 2019, **19**, 1589-1598.

33. L. Frenz, K. Blank, E. Brouzes and A. D. Griffiths, *Lab Chip*, 2009, **9**, 1344-1348.

34. Y. Xu, J.-H. Lee, Z. Li, L. Wang, T. Ordog and R. C. Bailey, *Lab on a Chip*, 2018, **18**, 2583-2592.

35. Y. Xia and G. M. Whitesides, *Angewandte Chemie International Edition*, 1998, **37**, 550-575.

36. A. K. Price, A. B. MacConnell and B. M. Paegel, *Analytical Chemistry*, 2014, **86**, 5039-5044.

37. A. Sciambi and A. R. Abate, *Lab on a Chip*, 2014, **14**, 2605-2609.

38. M. D. Tarn and N. Pamme, in *Microchip Diagnostics: Methods and Protocols*, eds. V. Taly, J.-L. Viovy and S. Descroix, Springer New York, New York, NY, 2017, DOI: 10.1007/978-1-4939-6734-6_6, pp. 69-83.

39. A. Q. Alorabi, M. D. Tarn, J. Gómez-Pastora, E. Bringas, I. Ortiz, V. N. Paunov and N. Pamme, *Lab on a Chip*, 2017, **17**, 3785-3795.

40. K. J. Livak and T. D. Schmittgen, *Methods*, 2001, **25**, 402-408.

41. X. Liu, C. Wang, W. Liu, J. Li, C. Li, X. Kou, J. Chen, Y. Zhao, H. Gao, H. Wang, Y. Zhang, Y. Gao and S. Gao, *Nature*, 2016, **537**, 558.

42. K. W. Trotter and T. K. Archer, *Nuclear receptor signaling*, 2008, **6**, e004-e004.

43. J. S. Becker, D. Nicetto and K. S. Zaret, *Trends in Genetics*, 2016, **32**, 29-41.

Chapter VII

Conclusions and Future Directions

DISSERTATION SUMMARY

This work summarized five years of effort toward developing a droplet microfluidic-based chromatin immunoprecipitation (ChIP) assay. Chapter I began by providing a broad overview of the epigenome from the context of precision medicine. After surveying epigenetic analysis techniques, it discussed impressive advances in clinically-driven microfluidic platforms for assay automation and miniaturization as well as ongoing research directions which may empower future deployment of these methods. Next, it contextualized the goal of addressing deficiencies in ChIP by exploring the core challenges associated with miniaturizing the technique into a droplet-based format. In particular, it profiled the state-of-the-art for microdroplet manipulations and identified areas of need, particularly in magnetic particle-enabled affinity separations.

Next, Chapter II described an initial technological development for improving droplet microfluidic capabilities, the K-channel.[1] This approach provided a new standard for versatility in droplet manipulation by using a single architecture for droplet generation, direct injection, and magnetic extraction. Operation was primarily dictated by applied conditions, not channel geometry, although specialized examples showed promise in serial operations for magnetic affinity purification. Chapter III included the K-channel and related technologies in demonstrating the applicability of thermoplastic-based hot embossing to mass-production of droplet microfluidic devices.[2] Importantly, it showed initial examples of secondary droplet operations like direct

injection and droplet splitting with integrated electric and magnetic fields, confirming that these materials did not interrupt fundamental performance characteristics. Chapter IV coupled the K-channel to a new module, the Counter-Current Continuous Phase Extraction (C^3PE) system. Similarly to the K-channel, this platform provided effective droplet handling across a wide range of conditions (this time for control over droplet packing fraction), and exact results were dynamically adjustable. Overall, the coupling of this extraction module with the K-channel enabled high temporal resolution analysis of droplet incubation conditions in the context of time-sensitive biochemistry.

Chapter V described a paradigm shift in droplet-based affinity purifications, the Coalesce-Attract-Resegment Washing (CAR-Wash module).[3] Compared to generally inefficient and input-sensitive magnetically-biased droplet splitting methods, the CAR-Wash empowered nearly complete fluid exchange for particle washing at much higher throughput, and applications to reversing enzyme inhibition and protein enrichment demonstrated its robustness and versatility. Finally, Chapter VI innovated on the CAR-Wash concept and another Bailey Lab droplet technology for chromatin preparation to realize droplet microfluidic ChIP.[3, 4] This semi-automated workflow processed from cells to affinity-purified DNA-histone protein complexes, including droplet-based immunoprecipitation and multistage washing. Early data showed good enrichment for selected activating and repressive histone isoforms, comparable to example microfluidic ChIP workflows and validated by parallel, manually-processed controls.

FUTURE DIRECTIONS

The droplet-based workflow successfully achieved ChIP with convincing enrichment and DNA yield for two targets, but additional work must improve the platform. Technologically,

droplet processing at particular stages could be irregular, such as in bead and antibody addition after in-droplet chromatin digestion and during washing coalescence and particle capture. Thus, the technology will benefit from further refinement to standardize operating conditions and increase robustness, perhaps by adapting strategies for synchronizing and uniformly guiding droplet populations.[5] Additional work may even simplify operational requirements (such as the number of actively controlled flow lines for the washing device) by using hydraulic circuit-based approaches for driving multiple fluids (like the washing buffers) at desired flow rates using a single source for pressure generation.[6] Lastly, the mature technology should handle small droplet populations with reduced sample loss, especially from device-to-device transfers, and dynamic adjustment to larger sample sizes may be best achieved by parallelizing processing through networks of identical device units.

Other areas for improvement depend on biochemical optimization of microfluidic ChIP. Fully characterizing immunoprecipitation in the small scale and rapid mass transfer regimes of flowing droplets may reveal fundamentally altered enrichment results and timescale. Thus, it may be possible to combine the chromatin preparation and the washing modules into a single, integrated device with only brief immunoprecipitation time. Likewise, post-processing of recovered nucleosome complexes (through DNA elution, purification, and, perhaps, analysis by in-droplet polymerase chain reaction) may also benefit from microfluidic automation to decrease user dependence, sample loss, and processing time. These optimizations must also extend the assay to additional histone, transcription factor, and modified DNA targets to fully realize the capabilities of epigenetic immunoprecipitation. Preliminary studies of other captures (including H3K4me, H3K27ac, and CTCF transcription factor) for HeLa and other cell lines were initially unsuccessful (data not shown). Adaptation to these species may require not only antibody titer and incubation

optimization but also the integration of other ChIP stages like sonication for chromatin shearing, chemical crosslinking for stabilizing transient associations, and clearing of insoluble, off-target chromatin and lysate components for decreasing background.[7] These features may require re-engineering devices, for example, with direct injection of non-magnetic particles in high abundance (which will be eliminated during magnetic washing) to provide excess surface area for non-specific precipitation. The overall goal of these aims must be to extend the applicability of the droplet-based ChIP method, but, admittedly, they will not address the fundamental challenge of developing high affinity ChIP antibodies.

In the longer term, the single cell handling capabilities of droplet microfluidic offer an exciting direction. Ongoing work in the Bailey Lab seeks to adapt active cell detection and droplet sorting as well as inertial ordering methods to compartmentalizing a single cell in nearly every droplet.[8, 9] Therefore, the next step would be in adapting DNA barcoding and/or single cell DNA sequencing library preparation methods to facilitate single cell analysis (pending cost and throughput limitations).[10] Particularly for rare and heterogeneous cell populations, single cell ChIP-seq may give additional insights into important epigenetic phenomena confounded by conventional, ensemble-limited analysis, but the limited copy number of target genes may raise challenges in establishing the validity of this workflow.[11]

Finally, the technology development to enable ChIP should be generalized to other applications. Recent, innovative epigenetic workflows like Cleavage Under Targets and Release Using Nuclease (CUT&RUN) and the Assay for Transposase Accessible Chromatin (ATAC-seq) may be adapted within the Bailey Lab's existing technologies.[12, 13] Thus, the lessons and strategies from ChIP assay development will translate to alternative means of chromatin mapping to yield complementary epigenetic information. More broadly speaking, these droplet manipulation and

washing technologies are also well-poised to performing heterogeneous phase protein immunoassays and other solid phase-enabled manipulations (for the first time in a high efficiency, high throughput droplet format).[14]

CONCLUDING REMARKS

In closing, this work has contributed to the fields of droplet microfluidics and miniaturized epigenetic analysis by adapting the complex, multistep ChIP protocol into a highly sophisticated droplet-enabled platform. Establishing this integrated system required technical innovations, particularly in magnetically-actuated affinity purification, which will drive the overall direction of microfluidic droplet assay development. Future implementations of these platforms will push the limits of automated and miniaturized bioanalytical measurements, and I look forward to seeing mature droplet technologies validated in a widespread clinical context.

REFERENCES

1. S. R. Doonan and R. C. Bailey, *Analytical Chemistry*, 2017, **89**, 4091-4099.
2. V. Sahore, S. R. Doonan and R. C. Bailey, *Analytical Methods*, 2018, **10**, 4264-4274.
3. S. R. Doonan, M. Lin and R. C. Bailey, *Lab on a Chip*, 2019, **19**, 1589-1598.
4. Y. Xu, J.-H. Lee, Z. Li, L. Wang, T. Ordog and R. C. Bailey, *Lab on a Chip*, 2018, **18**, 2583-2592.
5. B. Ahn, K. Lee, H. Lee, R. Panchapakesan and K. W. Oh, *Lab on a Chip*, 2011, **11**, 3956-3962.
6. K. W. Oh, K. Lee, B. Ahn and E. P. Furlani, *Lab on a Chip*, 2012, **12**, 515-545.
7. J. D. Nelson, O. Denisenko and K. Bomsztyk, *Nature Protocols*, 2006, **1**, 179-185.
8. A. Sciambi and A. R. Abate, *Lab on a chip*, 2015, **15**, 47-51.
9. D. Di Carlo, *Lab on a Chip*, 2009, **9**, 3038-3046.

10. R. Zilionis, J. Nainys, A. Veres, V. Savova, D. Zemmour, A. M. Klein and L. Mazutis, *Nature Protocols*, 2016, **12**, 44.

11. A. Rotem, O. Ram, N. Shoresh, R. A. Sperling, A. Goren, D. A. Weitz and B. E. Bernstein, *Nature Biotechnology*, 2015, **33**, 1165.

12. P. J. Skene and S. Henikoff, *eLife*, 2017, **6**, e21856.

13. J. D. Buenrostro, B. Wu, H. Y. Chang and W. J. Greenleaf, *Current protocols in molecular biology*, 2015, **109**, 21.29.21-21.29.29.

14. M. Serra, D. Ferraro, I. Pereiro, J. L. Viovy and S. Descroix, *Lab on a Chip*, 2017, **17**, 3979-3999.

APPENDIX A

Integrated Magnetic Field Device Fabrication and Assembly

INTRODUCTION

This appendix provides an overview of the procedure for fabricating and using the integrated magnet microfluidic devices featured in this work. In brief, it offers guidelines for photomask design, master fabrication, device preparation, and final device assembly. The process of microfluidic device fabrication for polydimethylsiloxane (PDMS, RTV615, Momentive, Inc.) devices has been well established by the literature,[1] and this appendix provides a specialized protocol.

PHOTOMASK DESIGN

First, the photomask was designed using a suitable computer-aided-drafting program (AutoCAD, Autodesk, Inc.). This fabrication used a negative photoresist, so features were transparent to ultraviolet (UV) light on the photomask. Besides conventional flow channel, electrode channel, and tubing port feature inclusions, these designs also included magnetic alignment structures. Such features delineated the boundary positions for the magnet in the final device by providing thick (>100 μm wide) photoresist barriers in direct contact with the magnet during later processing. Alignment structures were typically separated at least 100 μm from the nearest adjacent features to promote a strong, leak-free bond between the poly(dimethyl siloxane) (PDMS) and glass layers in the final device. The plastic photomask was printed with the emulsion

down (ink on the side in contact with the coated wafer) for best feature resolution in final devices (CAD/Art Services, Inc.). Example photomasks are shown in APPENDIX B.

MASTER FABRICATION

After obtaining the photomask, master mold fabrication was performed. To obtain 40 μm height features using SU8 2025 Negative Epoxy Photoresist (MicroChem, Corp.), the following representative procedure was used:

A 3 in diameter silicon wafer (<100>, test grade, University Wafer) was rinsed with acetone followed by isopropanol. The wafer was dried with air or nitrogen flow. The wafer was baked in an oven at 70 °C for 5 minutes to ensure complete solvent removal then left to cool at room temperature for 5 minutes. After cooling, 2-5 mL SU8 2025 negative epoxy photoresist was poured onto the center of the polished side of the silicon wafer. The wafer was processed via spin coater at 500 rpm for 10 s then at 2000 rpm for 30 s with a ramp of 300 rpm/s. The wafer was soft baked on a pre-heated hotplate at 65 °C for 3 minutes then transferred to a 95 °C hotplate for an additional 6-10 minutes of baking. Then, the wafer was removed from heat and left to cool to room temperature for 5 minutes. Prior to wafer processing, equipment like the spin coater, hot plates, and other work surfaces were lined with aluminum foil to contain photoresist waste.

The photomask (secured by tape to a Mask Plate, 4 in, Soda Lime Glass, 90 mil Thick, 5300 A*, Low Reflect Chrome, Nanofilm) and the wafer were loaded into the MJB3 Mask Aligner (SUSS MicroTec) at power setting “3” with the cooling fan enabled, with contact distance “9.00,” in soft contact mode, and with the high pass UV filter (PL-360-LP, Omega Optical). Exposure was conducted for 66 s. The wafer was removed from the aligner and let rest at room temperature for 10 minutes. The wafer was post baked on a pre-heated hotplate at 65 °C for 1 minute then

transferred to a 95 °C hotplate for an additional 6 minutes of baking. At this point, device features were visible on the wafer surface. The wafer was removed from heat and left to cool to room temperature for 5 minutes.

After cooling, the wafer was submerged in propylene glycol monomethyl ether acetate (PGMEA, Sigma Aldrich) for 3 minutes for development. PGMEA provided an organic solvent selective for dissolving unpolymerized SU8 negative epoxy photoresist at short development times. Then, the wafer was removed from the solvent bath and rinsed with PGMEA followed by isopropanol. The wafer was dried with air or nitrogen flow. White streaks on the wafer, particularly near device features, indicated underdevelopment. Additional rinsing with PGMEA followed by isopropanol then drying was necessary. Channel features lifting off the surface indicated overdevelopment or underexposure. For overdevelopment, PGMEA development time was reduced in future wafer processing. For underexposure, the UV exposure time was increased in future wafer processing.

Fabrication quality was optically inspected under a brightfield microscope. Inspection revealed underdevelopment if photoresist was visible beyond device features, overdevelopment if channel features lifted off the wafer surface, or underexposure if features were lost. These problems were addressed as discussed above. After letting the wafer rest at room temperature for 5 minutes, it was baked for 5 minutes on a pre-heated hotplate at 65 °C, and then the temperature was ramped to 150 °C for 15 minutes. For this hard bake step, the photoresist slightly reflowed to anneal defects and yield higher mechanical strength in the final result. The hotplate was returned to 65 °C for 5 minutes before turning off the heat. 30 minutes was allowed for gradual cooling to room temperature. Abrupt temperature changes resulted in feature failure, especially in delaminating features from the wafer surface. After cooling, the wafer was placed in a vacuum

vessel with 20 µL tridecafluoro-1,1,2,2-tetrahydrooctyl trichlorosilane (Gelest, Inc.). After evacuating via house supplied-vacuum, the wafer was left in the vaporized silane atmosphere for 45 minutes. The wafer was recovered after carefully releasing the vacuum. Care was taken in handling the toxic and water-reactive silane in the chemical fume hood, and an aqueous trap was used to neutralize hazardous trichlorosilane vapors during evacuation. The master mold was then ready to use.

PDMS DEVICE ASSEMBLY

After fabricating the master mold, device fabrication from the master was performed. Wafers were stored in 3 in diameter petri dishes to cover them from contamination as well as to contain pre-cured PDMS. For magnetic device fabrication, N52 magnets (0.5 in x 0.25 in x 0.125 in, magnetized through thickness, KJ Magnetics, Inc.) were positioned in contact with the wafer prior to PDMS addition. To accomplish this, the magnetized face of a magnet was carefully placed on the wafer surface, then a second magnet was slowly placed underneath the petri dish to interact with the first magnet's magnetic field. This second magnet held the first securely in position. Then, the paired magnet assembly was carefully pushed across wafer and petri dish surfaces until it stopped in contact with the raised magnetic alignment feature patterned onto the wafer surface. Too much pressure during assembly and alignment caused the magnets to damage the alignment features. After all magnets were aligned, PDMS mixed and degassed in a 5:1 base: curing agent ratio was poured over the wafer. PDMS pouring was oriented from the channel side towards each magnet assembly to reduce the incidence of trapping bubbles at the magnet over channel regions. PDMS was cured at 70 °C for 1 hour in the oven, with care taken to keep magnets isolated from magnetic oven racks and walls.

Once the PDMS was fully cured, the devices were ready for final preparation and assembly. After removal from the oven, the magnet(s) were carefully removed from the underside of each master. Then, a scalpel or razor blade was used to cut the PDMS on the wafer surface to delineate the outline of each device. Each in-device magnet was gently pushed away from the alignment and channel features to free them from direct contact with the wafer surface, then all integrated magnet PDMS devices were removed from the wafer surface. Devices still containing magnets were isolated from each other during subsequent processing to prevent accidental damage to devices and masters. Also, care was taken to avoid hazardous attractions between magnets and metal blades or needles during subsequent processing.

On a soft surface (like a rubber stopper), a blade was used to cut away the corner of the PDMS device containing the magnet, cutting parallel but 2-4 mm away from the position of the actual alignment features. The magnet was then removed through this cutaway portion. Magnets used during fabrication were not used during device operation due to loss of magnetization from oven heating and incidental damage incurred to magnets during fabrication.

After cleaning PDMS surfaces and the working surface (rubber stopper) with tape, PDMS ports were punched at designated channel areas using a needle (30 ga for later interface with #30 PTFE tubing, Cole Parmer). For best results, the needle had a rounded (not tapered) but well-sharpened edge, and it was lubricated with inert oil (Fluoroinert FC-40, Sigma Aldrich). Punching was performed from the channel side of the PDMS, and a narrow inner diameter metal wire was used to remove the PDMS core before removing the needle. These steps, in combination with rigid, well-cured 5:1 PDMS, helped promote accurate and reasonably fragment-free port creation to prevent future operating failures. Once all ports were punched, a blade was used to trim the PDMS device to its final size. Particularly, any extra PDMS near the magnet alignment region was

removed so that it would not interfere with final magnet insertion. Once the devices were fully ported and shaped, they were cleaned with tape once more. Next, a vacuum line with a trap was used to pull deionized water through each flow port from the channel side for additional cleaning, and the devices were dried thoroughly with air or nitrogen flow.

Devices were now ready for oxygen plasma bonding. The following were cleaned with tape: the PDMS device, a glass coverslip (No. 11/2, 22 mm x 40 mm, Sigma Aldrich), and a roughened glass sample-holding slide. The glass coverslip was placed in the plasma oven (PDC-32G, Harrick Plasma), as was the PDMS device (on top of the rough glass sample holder, channel side up). The plasma chamber door and inlet valve were closed, then the vacuum line was opened to pump down the chamber to 1.0 Torr. The needle valve on the door was adjusted to throttle the air intake for tuning the final chamber pressure. The device was exposed to plasma on "high" for 30 seconds. The vacuum was isolated, and then the chamber was slowly re-pressurized the chamber using the valve on the door. All components were quickly recovered from the plasma oven, and the PDMS device was dropped (channel side down) onto the clean side of the glass coverslip. Successful bonding was indicated by the PDMS lying flat without air bubbles on the glass. Bonded devices were baked in the oven at 70 °C overnight.

MAGNET ARRAY POSITIONING

For each device, eight magnets were assembled into two separate blocks of four magnets each, with adjacent magnets in contact in the direction of magnetization. The two blocks were connected to each other orthogonal to the direction of magnetization with a cleanroom wipe separating them, and the magnets were manually adjusted as needed to promote straight alignment. The final magnet block had dimensions of approximately 0.5 in x 0.5 in x 0.5 in. All tubing and

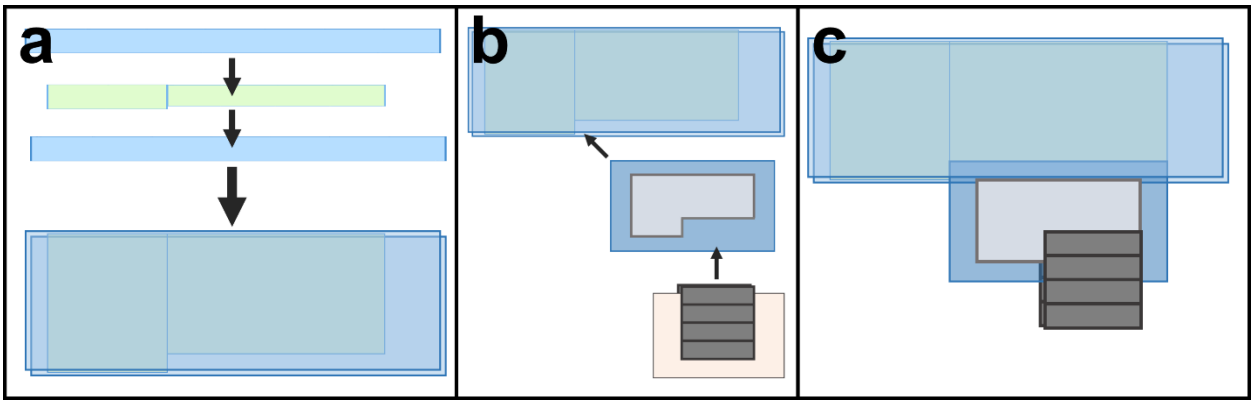

Figure A.1. Integrated Magnetic Device Assembly. a) The magnetic device holder was assembled by securing two glass coverslips (of identical thickness to the glass used for the microfluidic device) between two thicker glass slides to form a right-angled groove. Epoxy or another suitable adhesive was ensured a strong bond among layers. b) The microfluidic device was nested in the groove of the magnetic device holder to provide support while adding the magnet array. The magnet array was pushed onto the device glass coverslip while the cleanroom wipe separating the two halves of the array was simultaneously removed. c) Assembly was complete when the magnet array was fully positioned within the integrated magnetic device alignment region.

other interfacing materials were inserted into the PDMS-glass device before magnet introduction. For loading the magnet onto the integrated device, the PDMS-glass device was first secured by a simple holder assembled from sandwiching glass coverslips partway between two thicker glass slides (Fig. A.1a). The inner coverslips were positioned such that they left a vacant corner between the thicker slides into which the free leading edge of the device coverslip was be securely held against laterally-directed forces. This holder also reduced the hazard of personal injury in the event of broken glass from the device. Immediately prior to magnet loading onto the device, the cleanroom wipe was partly withdrawn from between the halves of the final magnet block so that a small portion of the leading magnet edges were free. The lagging edge of the device coverslip was inserted into this free region. Then, the magnet block was pushed onto the coverslip while simultaneously retracting the cleanroom wipe (Fig. A.1b). Force was not applied perpendicularly to the coverslip to avoid device coverslip fracture. This operation was most effective with a well-aligned set of smooth magnets, as any defects created pressure points. Once the magnet assembly

was fully on the coverslip, it was pushed carefully against the PDMS boundaries in the magnetic alignment region (Fig. A.1c). Pushing the magnet too far with too much force distorted or delaminated the PDMS to cause device failure.

CONCLUSIONS

While this photomask design and master fabrication strategy provide specific adaptations of general protocols, device preparation and final assembly include critical details for this class of integrated magnet designs. Ultimately, these processes are crucial to obtaining the high on-chip magnetic fields necessary for novel magnetic droplet operations. Future work may optimize these processes, particularly final assembly with the magnet array, to increase successful device yield and decrease user-dependence in assay operation.

REFERENCE

1. Y. Xia and G. M. Whitesides, *Angewandte Chemie International Edition*, 1998, **37**, 550-575.

APPENDIX B

Microfluidic Device Photomask Designs

INTRODUCTION

These images show photomasks at actual size (3 in diameter) representing the core devices used for this work. Some photomasks pictured include multiple copies of the same device. Additional designs related to these elements were also used. Photomasks were designed for use with negative photoresists and for fabrication at 40 μm feature height unless otherwise indicated. White features were transparent on the physical mask, and black features were opaque. Plastic photomasks were manufactured with the ink emulsion down (on the wafer-oriented side). An original file containing these designs is stored within Box at U-M cloud storage via "Bailey Lab Internals/Alumni Data/Steven Doonan/Device Photomasks.dwg" and may be made available by Prof. Ryan Bailey upon request.

PHOTOMASKS

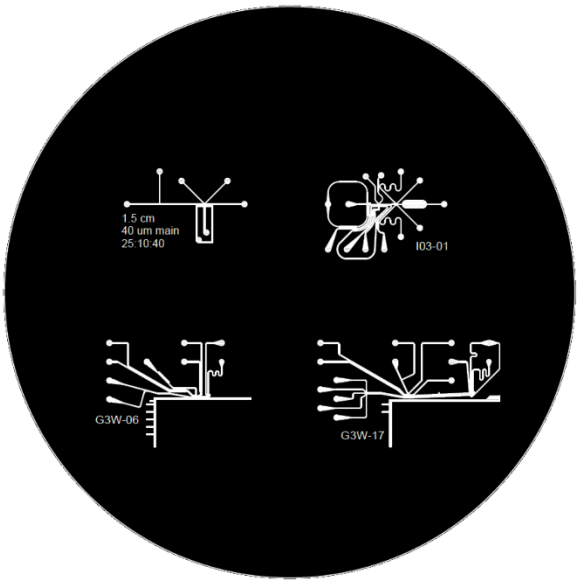

Figure B.1. Representative mask for novel droplet technologies. K-channel design for direct injection, fluid extraction, droplet splitting, and droplet formation (top left, index: "25:10:40"). C^3PE design for time-controlled dye injection into droplets, continuous phase extraction, and incubation monitoring (top right, index: "I03-01"). CAR-Wash design for droplet-mediated 10 µm magnetic particle washing (bottom left, index: "G3W-06"). Multilaminar CAR-Wash design for droplet-mediated washing of 2.8 µm magnetic dynabeads through four co-flowing buffers (bottom right, index "G3W-17").

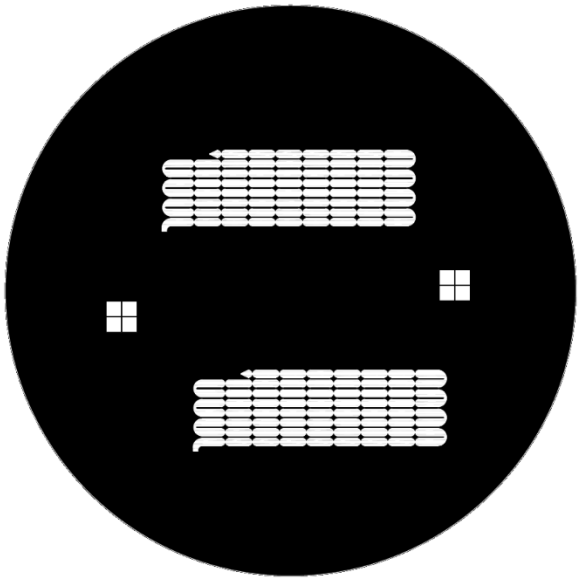

Figure B.2. Delay channel elements for droplet incubation (index: “ChIP1-01”). These features were fabricated at 160 μm feature height and aligned with the the aid of the square alignment features. This mask includes features for two separate, identical devices.

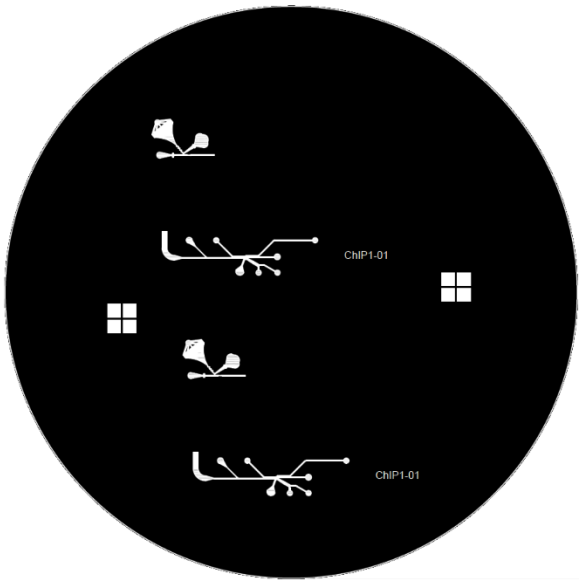

Figure B.3. Droplet formation, droplet respacing, and bead injection elements (index: "ChIP1-01"). These features were aligned with the the aid of the square alignment features. This mask includes features for two separate, identical devices.

APPENDIX C

Pressure-Driven Flow Control

INTRODUCTION

Flow control for the majority of microfluidic droplet techniques demonstrated herein was achieved via pressure-driven flow. The flow controller was assembled from a combination of custom-fabricated and commercially available components.

PRESSURE MANIFOLD

Primarily, each flow controller (providing up to four individually addressable fluid lines) was supplied from a nitrogen gas cylinder. This cylinder was connected to a custom manifold (VWR International) which delivered the high pressure to up to four two-stage regulators (55850-420, VWR International, Fig. C.1a). Each regulator controlled the specific lower pressure supplied to its connected fluid line (Fig. C.1b). Using barbed fittings (NPT Male Pipe Adapter, 316 SS, 1/4 in NPT(M) x 1/16 in, Cole Parmer) and couples (Female Threaded Straight Coupling, 1/4 in NPT(F), 316 SS, Cole Parmer), regulators were connected to flexible Tygon tubing (1/16 in ID x 1/8 in OD, Cole Parmer), and this carried the pressure to the solenoid valve array (Fig. C.2a). Caution was exercised when working with high pressure cylinders, which were always capped or connected to pressure regulating equipment. Cylinders were also secured to walls or laser tables during use and only moved when secured to an approved cylinder cart. The custom manifold was professionally fabricated to safely handle high pressures.

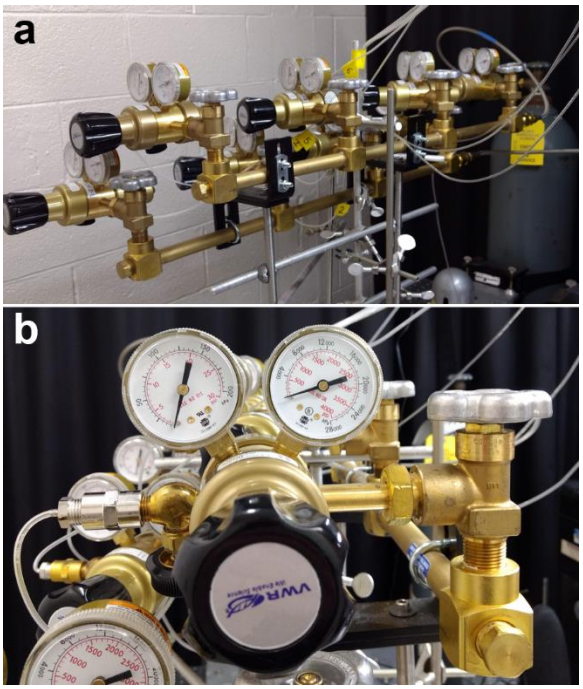

Figure C.1. Pressure Manifold. a) Two manifolds pressured by two compressed nitrogen cylinders provided four pressure lines for fluid delivery each. b) Each pressure line was controlled by a two-stage regulator connected to a valve on the manifold. A barbed adapter and couple linked the regulator assembly to soft tubing for delivery to the solenoid valve array.

SOLENOID VALVE ARRAY

Each fluid line was controlled by a pair of three-port solenoid valves (LHDA0531115H, The Lee Company, Fig. C.2b) actuated by a LabView program (National Instruments). When the 5 V signal from LabView (National Instruments) was received at the gate of the transistor (IRF520) corresponding to each valve pair, the current from each USB power supply (5 V, 110 mA) could pass through each solenoid valve and through the transistor drain and source (grounded). Therefore, the addition of the LabView signal switched the valves from the normally open (N.O.) position to the normally closed (N.C.) position (Fig. C.2c). The circuit was assembled so that each valve was connected to a spliced 5 V USB power supply, and the path to ground for the solenoid valve's circuit passed between drain and source of a shared transistor. The transistor gate was connected to the specific control line on the data acquisition device (DAQ, NI PCIe-6251

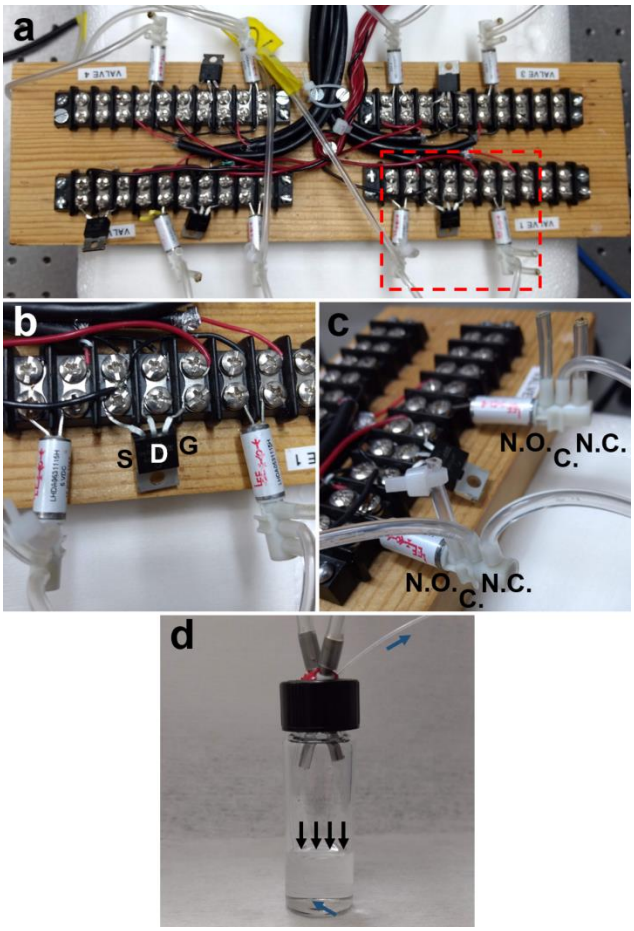

Figure C.2. Solenoid Valve Array Interface. a) Each valve array was assembled with four pairs of solenoid valves. Each solenoid valve pair with transistor represented the minimum functional unit of this array (red box). b) All valves were connected to their own USB power supplies, but grounding for each valve pair was routed through a transistor drain (D) and source (S) controlled by a LabView signal to the gate (G). The LabView 5 V signal was also connected to the ground at S. c) For each valve pair, the normally open (N.O.) port of the first valve was unsealed, the common (C.) port was connected to the regulator for pressure delivery, and the normally closed (N.C.) port supplied pressure to the fluid vial. For the second valve, the N.O. port was unsealed, the C. port received pressure from the fluid vial, and the N.C. port was sealed. d) Pressure was mediated from the valve array by soft tubing connected to stainless steel pins through the Teflon-silicone septum in the vial cap. Pressure in the vial headspace (black arrows) drove fluid into the opening of the PTFE tubing submerged in fluid toward the microfluidic device (blue arrows).

Multifunction Data Acquisition Device with an SCB-68 Shielded I/O Connector Block, National Instruments) corresponding to the LabView program. The transistor source was connected to the USB power supply grounds and to a digital ground on the DAQ.

Actuating the valves to the N.C. position supplied pressure to the corresponding fluid lines, and removing the signal to restore the N.O. position removed and vented pressure to atmosphere. Pressure was delivered into the headspace of fluid-containing glass vials via stainless steel pins (New England Small Tube Corp.) piercing a Teflon-silicone septum (13 mm Autosampler Vial Septa, Fisher Scientific) in the cap of each vial (Screw-Thread N-51A Borosilicate Glass Sample Vials, Fisher Scientific, Fig. C.2d). Pins were connected to solenoid valves via the same flexible Tygon tubing which connected the valves to the regulator assembly. Polytetrafluoroethylene (PTFE) tubing (#30 PTFE, Cole Parmer) submerged in each fluid was inserted directly into inlet ports in microfluidic devices and passed through the Teflon-silicone septum. Therefore, pressurizing the vial exerted a pressure on the fluid which drove it through the PTFE tubing into the microfluidic device. Achieved fluid flow rates depended on tubing length and inner diameter, sample fluid physical properties, and microfluidic device architecture.

For each valve pair, the first valve received pressure from the regulator through the Common (C.) port. The N.O. port was left with a short length of open flexible tubing, and the N.C. port was connected to the fluid vial. The operation of this valve thus diverted input pressure to atmosphere until actuation led to pressure delivery into the fluid vial. For the second valve in each pair, the C. port was connected to the fluid vial. The N.O. port was left with a short length of open flexible tubing, and the N.C. port was connected to a short length of heat-sealed flexible tubing. Thus, this second valve equilibrated the fluid vial with atmospheric pressure in the absence of signal and sealed the pressurized volume (including the fluid vial) when receiving the LabView signal. In summary, the actuation delivered pressure via the first valve and sealed the system via the second valve. Removing signal diverted input pressure via the first valve and released fluid vial pressure via the second valve.

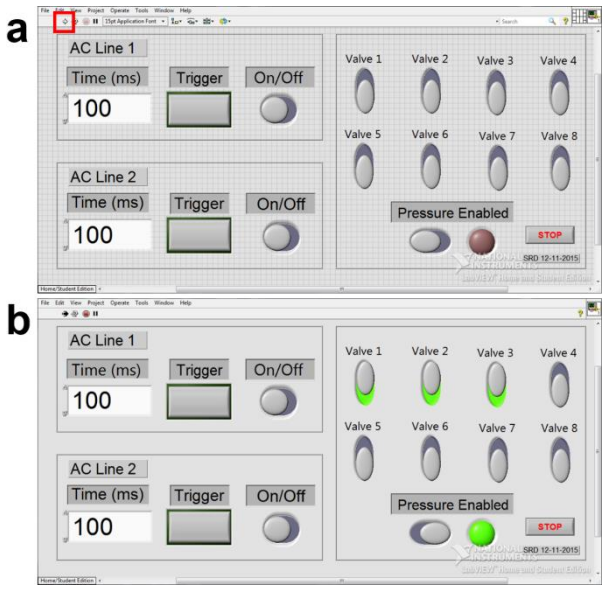

Figure C.3. LabView Front Panel. a) The LabView program was initiated by pressing the "Run" arrow (highlighted by the red box). b) Electric field control was included on the left side of the virtual instrument, and pressure control for flow was mediated by the right side. For electric field control, the corresponding LabView 5 V signal line (analog or digital used as analog) controlled the gate of a transistor interrupting the path to ground for the electric field inverter's 12 V power supply. Using the "On/Off" switch provided continuous electric field, or setting a time and using the "Trigger" function provided a transient electric field for the duration selected. For pressure-driven flow control, selecting "Pressure Enabled" provided the master control necessary for actuating any of the valves. Combining "Pressure Enabled" with the corresponding switch actuated the desired valve pair. The program was terminated using the "STOP" button. This example showed valve pairs 1, 2, and 3 active with pressure enabled. Valve pairs 4-8 were inactive, and the timer-enabled electric field power supply control was also inactive.

LABVIEW PROGRAM

See Fig. C.3 for the LabView user interface and Fig. C.4 for the LabView programming and additional details. An original file containing this virtual instrument (VI) is stored in the Box at U-M cloud storage via "Bailey Lab Internals/Alumni Data/Steven Doonan/PressureControl.vi" and may be made available by Prof. Ryan Bailey upon request. In summary, the VI mediated electrical signals to transistor gates, and these transistors controlled the operation of solenoid valves (and electric field power supply elements). By providing a simple network of Boolean logic

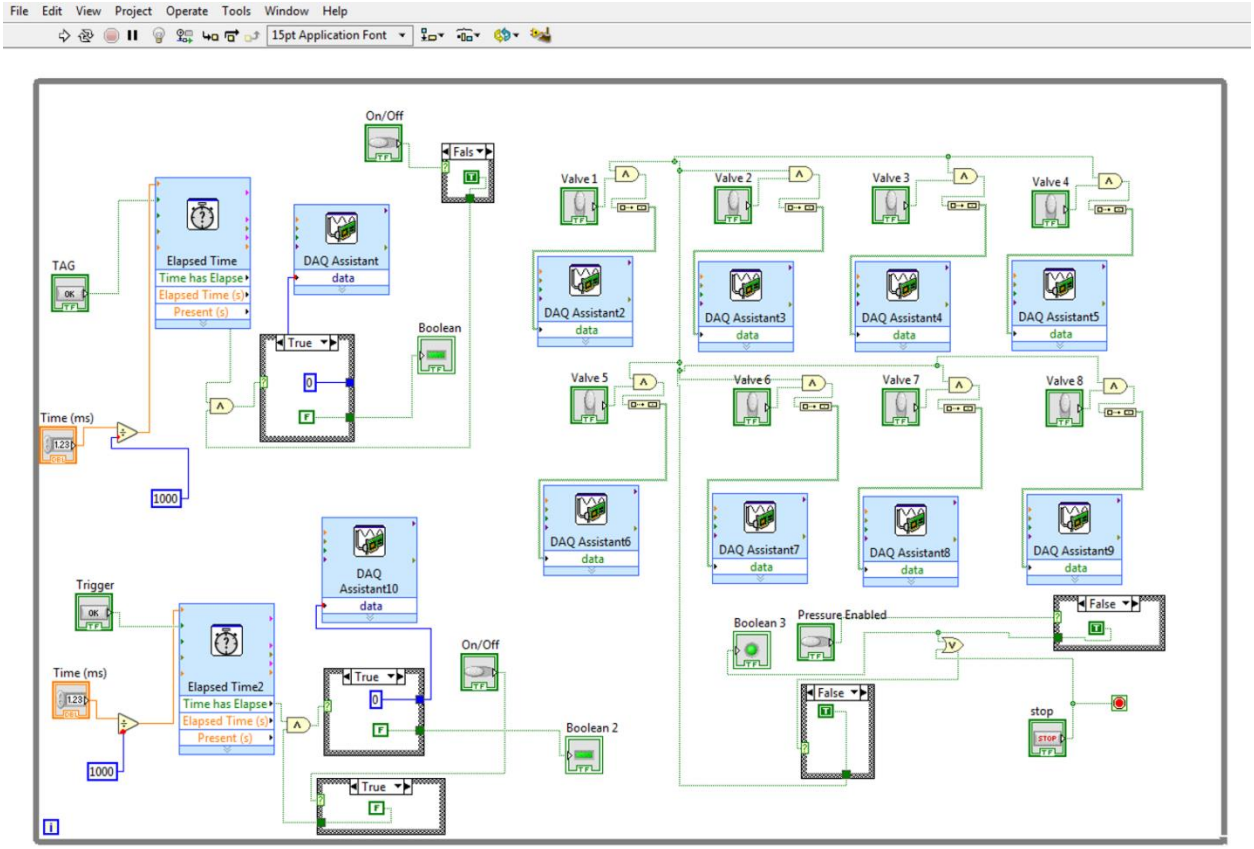

Figure C.4. LabView Block Diagram. The left side of the block diagram mediated electric field power supply control, and the right side of the block diagram mediated pressure control for microfluidic flow. Wiring lines connect elements in a virtual circuit, and the virtual instrument was operated within a "while loop." For each functional unit (capable of actuating a valve pair or an electric field element), a similar logical structure in the virtual instrument produced a 5 V analog (or digital used as analog) signal. First, some logical element (switch or elapsed time function) provided a Boolean signal which interacted with other Boolean and numerical signals via logic elements like "and" and "or." Then a "build array" element transduced the Boolean signal for receipt by a "DAQ Assistant" element. Receipt of a "True" signal was configured to trigger an electrical signal from the data acquisition device at the specified pinout connection, and this signal was supplied to the gate of a specific physical transistor interfaced to a valve pair or electric field power supply. Additional Boolean indicators were provided in the virtual instrument to improve the user interface on the front panel.

operations, the LabView program allowed switching of flow and electric field elements to control microfluidic device function.

EXAMPLE STANDARD OPERATING PROCEDURE

Before the experiment, several features of the flow controller were checked. First, the connections between the transistors in the solenoid valve array were confirmed. Specifically, each transistor gate was connected to the corresponding digital line (P0.#, where # = valve pair index – 1), and at least one transistor source per flow controlling solenoid valve array was connected to a digital ground. The electrical connections of each valve in the array were also verified. Then, the power cables for the USB power supply hubs were connected to power the solenoid valve array. Next, the LabView program was enabled, and the operation of each valve pair was confirmed.

After verifying correct performance of the LabView-controlled solenoid valve array, the pressure lines were joined to each valve pair by connecting the corresponding regulator-attached soft tubing line to the C. port of the first valve in each pair. Before opening the gas cylinder valve to pressurize the system, the manifold valves for each regulator were closed, and each regulator was set to minimum delivery pressure. After opening the gas cylinder valve, the manifold valve for each regulator was also opened. Then, the regulator was adjusted to desired pressures for device operation. The needle valves on each regulator after pressure regulation were left open unless gas flow was to be temporarily restricted without pressure adjustment. Delivered gas pressures were calibrated with a pressure sensor as needed to account for inaccuracies and hysteresis in individual regulator performance. Gas pressures were never set above 15 psi, the pressure limit for the solenoid valves used.

Finally, the flow controller was interfaced to the microfluidic device. After removing the storage glass vial from each fluid vial assembly, the plastic cap, Teflon-silicone septum, and stainless steel pins were cleaned with deionized water on a cleanroom wipe to remove soluble contaminants. Then, they were cleaned with tape to remove contaminating particles. At this stage, the cleaned cap assembly was screwed onto the sample fluid-containing vial. Precise lengths of

PTFE soft tubing (typically #30, 20 cm length, Cole Parmer) were cut perpendicular to the tubing length with a sharp blade. After cleaning the PTFE tubing with tape, it was inserted through the Teflon-silicone septum into the fluid in the vial. Finally, the opposite end of the tubing was cleaned with tape then inserted into an inlet fluid port in the microfluidic device. This process was repeated for all flow lines, and device waste lines generally used PTFE tubing connected to a waste collection tube instead of a fluid vial.

Once all lines were fully connected, the flow control system was ready for microfluidic device operation. During operation, flow rates were changed by proportionally increasing or decreasing the pressure delivered by the corresponding regulator. When decreasing pressure, it was critical to pulse the LabView signal to that solenoid valve pair in order to vent higher pressure trapped in the fluid vial. To compensate for regulator error and hysteresis, experimental notes recorded both the pressure readings and the index for each regulator used.

After operation, proper cleaning and storage reduced the chance of flow controller contamination and damage. First, the gas cylinder valve was closed, and the residual pressure in the manifold and regulators vented. The flow controller was never left under pressure to prevent hazards from users unknowingly interacting with a high pressure system. After pressure dissipation, the manifold valves to each regulator were closed, and the regulators were set to minimum pressure. Then, the USB power supply hubs for the solenoid valves were unplugged, and the LabView program was stopped and closed. The PFTE tubing was disconnected from the microfluidic device, removed from the fluid vials, and discarded. After removing sample fluid vials from each fluid vial assembly, the plastic cap, Teflon-silicone septum, and stainless steel pins were cleaned with deionized water on a cleanroom wipe to remove soluble contaminants. The storage glass vials were replaced onto each assembly.

CONCLUSIONS

This appendix describes the basic components and operation of a custom pressure-driven flow controller, and this method was successfully applied to many of the microfluidic techniques described in this work. Alternatives for pressure-driven flow, some commercial, are also possible, and flow control may also use other methods like syringe pumps, peristaltic pumps, or gravity-driven flow. For any flow approach chosen, proper precautions should be taken, particularly for high pressure systems.